Wire Arc Additive Manufacturing (WAAM)

Department of Mechanics, Mathematics and Management
MECHANICAL AND MANAGEMENT ENGINEERING
Ph.D. Program
SSD: IIND-04/A MANUFACTURING TECHNOLOGIES AND SYSTEMS

Final Dissertation

Wire Arc Additive Manufacturing (WAAM)

by

Mojtaba Karamimoghadam

Bari-18/12/2025

Referees:

Prof. Antonio M. Mateo

Prof. Matteo Villa

Supervisor:

Prof. Giuseppe Casalino

Coordinator of Ph.D Program:

Prof. Giuseppe Casalino

Course n°38, 01/11/2022-31/10/2025

Department of Mechanics, Mathematics and Management
MECHANICAL AND MANAGEMENT ENGINEERING
Ph.D. Program
SSD: IIND-04/A MANUFACTURING TECHNOLOGIES AND SYSTEMS

Final Dissertation

Wire Arc Additive Manufacturing (WAAM)

---

by
Mojtaba Karamimoghadam

Supervisor:

Prof. Giuseppe Casalino

Coordinator of Ph.D. Program:
Prof. Giuseppe Casalino

Course n°38, 01/11/2022-31/10/2025

Acknowledgments

First and foremost, I would like to express my deepest gratitude to my distinguished supervisor, **Professor Giuseppe Casalino**, for his invaluable guidance, wisdom, and continuous support throughout my doctoral journey. His exceptional mentorship, scientific insight, and unwavering encouragement have profoundly shaped my academic and professional growth. Working under his supervision has been both an honor and an inspiration, his dedication to excellence and his genuine passion for research have left an enduring mark on my career and character.

I would like to express my profound and heartfelt gratitude to the love of my life, my angel, best friend, and soul mate, **Negar Khorshidi**. Throughout the many years of this journey, her patience, love, and faith in me have been the pillars that sustained my spirit and determination. In moments of exhaustion and doubt, when the challenges seemed insurmountable, her warmth, wisdom, and constant encouragement became my guiding light, reminding me of my purpose and strength. Every page of this thesis carries traces of her sacrifices, her gentle words of reassurance, and her belief that I could overcome every obstacle. Without her presence, this achievement would not have been possible, this journey is as much hers as it is mine.

I am deeply grateful to my family, whose unconditional love, sacrifices, and encouragement have been the foundation of every success I have achieved. Their faith in me has always been a source of motivation and comfort, no matter the distance or difficulty. I would also like to extend my sincere thanks to my friends and colleagues, whose support, collaboration, and companionship made this journey memorable and fulfilling. The discussions, laughter, and shared efforts in the lab and beyond have enriched this experience beyond measure.

Finally, I wish to express my profound gratitude to **myself**, for the perseverance, dedication, and commitment that kept me moving forward through every obstacle. This journey has been a testament to resilience, self-belief, and the power of persistence.

Table of Contents

Abstract 8
Chapter 1 10
Introduction and Literature Review 10
1.1. Additive Manufacturing 10
1.1.1. Powder Bed Fusion (PBF) 10
1.1.2. Directed Energy Deposition (DED) 11
1.1.3. Wire Laser Additive Manufacturing (WLAM) 11
1.1.4. Wire Arc Additive Manufacturing (WAAM) 11
1.2. Wire Additive Manufacturing 12
1.2.1. Fundamentals of WAAM 12
1.3. Critical Process Parameters and Their Influence 16
1.3.1 Thermal and Energy Parameters 16
1.3.2 Geometrical and Kinematic Parameters 17
1.3.3 The Quest for Optimal Bead Geometry: Aspect Ratio and Wetting Angle 17
1.4. Materials for WAAM 18
1.4.1 Steels 18
1.4.2 Aluminum Alloys 19
1.4.3 Titanium Alloys 19
1.4.4 Nickel-Based Superalloys 19
1.4.5 Copper-Based Alloys and Bimetallic Structures 19
1.5. Wire Laser Additive Manufacturing (WLAM) 25
1.6. Laser Arc Hybrid Wire Manufacturing (LAHWM) 29
1.7. Applications and Benefits of WAAM Across Sectors 32
1.7.1 Aerospace and Aviation 32
1.7.2 Automotive and Transportation 33
Chapter 2 35
WAAM Investigation on AISI 308L Stainless Steel Wire Feed Rate 35
2.1. Materials and Equipment 35
2.2. Microstructural Characterization 35
2.3. Microstructural Analysis 37
2.4. Surface Roughness 39
2.5. Microhardness 40
2.6 Oxide Layer and Process Defects 41
Chapter 3 44
WAAM Investigation on ER70S-6 Wire Feeder Rate 44
3.1. Material Fabrication 44
3.2. Characterization Method 45
3.3. Microstructure 45

3.4. Microstructure Influence on Microhardness....49
3.5. Interface EBSD Analysis....52
Chapter 4....55
Numerical Modeling of WAAM Fabrication of AISI 308L Stainless Steel....55
4.1. Deposition Strategy....55
4.2. Specimen Examination....56
4.3. Statistical Analysis....57
4.4. Numerical Model....57
4.5. Constitutive Equations....58
4.6. Phase-Field Equations....59
4.7. Thermal Modelling....60
4.8. Phase Change Interface....60
4.9. Solid Mechanics Model....61
4.10. Coupling Phenomena....61
4.11. Boundary Conditions....62
4.12. Meshing Strategy....63
4.13. Geometry of Transverse Sections....64
4.14. Statistical Analysis....67
4.15. Thermal History....68
4.16. Bead Formation....73
Chapter 5....79
Numerical Modeling of WAAM Fabrication of ER70S-6....79
5.1. Experimental Deposition Methodology....79
5.2. Thermal Examination....79
5.3. Geometry Characterization of Deposited Beads....79
5.4. Statistical Analysis and Process Optimization....80
5.5. Numerical Model....80
5.6. Overall Bead Appearance....83
5.7. Aspect Ratio, Bead Width, and Bead Height....84
5.8. Wetting Angle....85
5.9. Temperature Profile During WAAM Deposition....87
5.10. Effects of Arc Power and Deposition Speed on the Geometrical Characteristics of Deposited Beads....90
5.11. Identification of the Optimal Processing Window for Desired Geometrical Characteristics....93
Chapter 6....96
WAAM Fabrication of CuAl8 and ER70S-6 Cubic Structure....96
6.1. Manufacturing Process of WAAM Samples....96
6.2. Characterization....97
6.3. Microstructural Characterization....98

6.3.1. Wall Samples 98
6.3.2. Interface Characterization 105
6.4. Mechanical Characterization 110
6.4.1. Uniaxial Tensile Testing 110
6.4.2. Surface Roughness and Microhardness 112
Chapter 7 117
Laser Hybrid Arc Welding of WAAMed ER70S-6/AISI 308L SS Plates with AISI 316L SS 117
7.1. Materials and Fabrication 117
7.1.1. Base Materials and WAAM Fabrication 117
7.1.2. Pre-Weld Preparation 118
7.2. Laser Hybrid Welding Process 118
7.3. Material Characterization and Mechanical Testing 120
7.3.1. Microstructural Analysis 120
7.3.2. Mechanical Testing 120
7.4. Discussion 120
7.4.1. Microstructural Analysis of the Weld Zone 120
7.4.1.1. Weld Bead Morphology and Ferrite Formation 120
7.4.1.2. Columnar Grain Growth 121
7.4.1.3. Phase Transformation Analysis via XRD 121
7.4.1.4. Microstructural Variations Across the Weld 122
7.4.1.5. Defect Formation and Analysis 123
7.4.2. Crystallographic and Interfacial Analysis 124
7.4.2.1. AISI 316L/AISI 308L Interface 124
7.4.2.2. AISI 316L/ER70S-6 Interface 125
7.4.2.3. Phase and Elemental Distribution 126
7.4.3. Microhardness Profile 127
7.4.4. Uniaxial Tensile Strength 128
Chapter 8 131
Conclusions and Recommendations 131
8.1. Process parameter microstructure correlation 131
8.2. Microstructural evolution and mechanical performance 131
8.3. Numerical and statistical modeling 132
8.4. Advanced joining via Laser Hybrid Welding (LHW) 132
8.5. Integrated understanding and technological impact 132
8.6. Outlook and future perspectives 133
References 135
Appendix 156
Publications 156
Metal Wire Additive Manufacturing: A Comparison between Arc Laser and Laser/Arc Heat Sources 157

Experimental, statistical and numerical study of the single laser spot condition and influence parameters of a Neodymium-Doped Yttrium Lithium Fluoride laser 159

Analysis of wire arc additive manufacturing of ER70S-6 steel beads through experimental, statistical, and numerical analysis 160

Wire arc additive manufacturing of low alloyed steels, copper aluminum alloys, and their bimetals 161

Impact of feed rate and arc power in wire arc additive manufacturing of AISI 308L stainless steel 162

Effect of wire feed rate on ER70S-6 microstructure of wire arc additive manufacturing process 163

Laser Hybrid Welding of WAAM-Fabricated Dissimilar Steels: Microstructural Evolution and Mechanical Performance of AISI 308L and ER70S-6 Joints with 316L Filler 165

Effect of manufacturing strategy on microstructure of a low-carbon steel alloy fabricated with wire-arc additive manufacturing 166

Abstract

This thesis presents an extensive experimental and numerical investigation into Wire Arc Additive Manufacturing (WAAM) and its integration with advanced joining and simulation strategies for steels and bimetallic alloys. The research encompasses the development, optimization, and characterization of WAAM processes for AISI 308L stainless steel, ER70S-6 low-alloy steel, and CuAl8 copper-based alloy, as well as hybrid laser welding of dissimilar WAAM-fabricated plates. Using Cold Metal Transfer (CMT) as the deposition technique, process parameters, including arc power, wire feed rate, and deposition speed, were systematically studied through full-factorial Design of Experiments (DOE) and validated via thermal imaging, microstructural, and mechanical analyses. The results show that optimal combinations of deposition speed (5–9 mm/s) and arc power (1200–1700 W for stainless steels; 1600–2800 W for low-alloy steels) significantly affect bead geometry, wetting angle, and aspect ratio, achieving values consistent with ideal ranges (aspect ratio ≈ 2.5, wetting ≈ 60°). Finite Element and Computational Fluid Dynamics (CFD) simulations, coupled with phase-field modeling, were developed to predict thermal distribution, melt pool dynamics, and residual stress fields. The models demonstrated strong agreement with experimental measurements, providing a robust predictive framework for multi-scale WAAM simulations. Microstructural analyses using SEM, EBSD, and XRD revealed refined dendritic morphologies and δ-ferrite/γ-austenite transformations in AISI 308L and ER70S-6 deposits, with grain sizes ranging from 5 μm in the heat-affected zone to 16 μm in weld centers. The CuAl8 and ER70S-6 bimetallic structures exhibited distinct phase transitions (α and β phases) with peak microhardness values of 137 HV (CuAl8) and 259 HV (ER70S-6), while hybrid laser welding of WAAM-fabricated dissimilar plates using 316L filler achieved enhanced interfacial bonding, maximum microhardness of 303 HV, and improved tensile performance with up to 43% strength increase at optimized parameters. Overall, this research advances the understanding of process–structure–property relationships in WAAM and laser-hybrid welded steels and bimetals. The integration of experimental, statistical, and numerical methods provides new insights into thermal-mechanical behavior and solidification phenomena, contributing to the design of defect-free, high-strength, and corrosion-resistant components for energy, aerospace, and marine applications.

Keywords: Wire Arc Additive Manufacturing; Cold Metal Transfer; AISI 308L; ER70S-6; CuAl8; Laser Hybrid Welding; Phase Field Simulation; Microstructure; Mechanical Properties; Process Optimization; Dissimilar Metals; Bimetallic Structures.

Chapter 1

Introduction & Literature Review

Chapter 1

Introduction and Literature Review

1.1. Additive Manufacturing

The evolution of manufacturing has been marked by a continuous pursuit of efficiency, precision, and flexibility. In recent decades, Additive Manufacturing (AM), commonly known as 3D printing, has emerged as a transformative technology that challenges conventional subtractive and formative manufacturing paradigms [1]. Unlike traditional methods that remove material from a larger block or shape it using molds, AM constructs parts layer-by-layer directly from a digital model (CAD). This fundamental shift offers a host of unique advantages, including unparalleled design freedom for creating complex internal geometries and lightweight lattice structures, significant reduction in material waste, rapid prototyping capabilities that drastically shorten development cycles, and the ability to produce custom, one-of-a-kind parts without the need for expensive tooling [2, 3].

The initial development of AM technologies, dating back to the 1980s, was primarily focused on polymers for prototyping purposes [4]. However, the potential of creating functional, load-bearing metal components soon drove intensive research and development into metal AM processes. The early 2000s saw a limited market for industrial laser sources suitable for AM, but the subsequent decade witnessed exponential growth, fueled by the laser beam's high thermal stability and efficiency, which helped reduce material waste [5, 6]. Today, metal AM is no longer confined to rapid prototyping but is extensively used for fabricating end-use parts, tooling, and complex components across a diverse range of industries [7, 8]. Metal AM technologies can be broadly categorized based on the feedstock material and the energy source used. The two predominant categories are:

1.1.1. Powder Bed Fusion (PBF)

This includes processes like Selective Laser Melting (SLM) and Electron Beam Melting (EBM). In PBF, a thin layer of metal powder is spread across a build platform, and a high-energy source (laser or electron beam) selectively fuses the powder according to the cross-section of the part. The platform is then lowered, a new powder layer is applied, and the process repeats. PBF is renowned for its high resolution and ability to produce intricate features with excellent surface finish, making it ideal for small, complex components [9, 10].

1.1.2. Directed Energy Deposition (DED)

In DED processes, focused thermal energy, typically from a laser, electron beam, or electric arc is used to melt material as it is being deposited. The feedstock, which can be in powder or wire form, is fed into the melt pool created on the substrate. DED systems are often mounted on multi-axis robotic arms, allowing for greater flexibility in building or repairing large-scale components. The key differentiator of DED is its ability to fabricate large parts and add features to existing components, albeit generally with a lower resolution compared to PBF [11, 12]. The choice between powder and wire feedstock presents a critical trade-off. Powder-based systems (both PBF and some DED) offer fine resolution but can be associated with higher material costs, potential health and safety concerns due to powder handling, and lower material deposition rates. In contrast, wire feedstock is generally more cost-effective, safer to handle, and enables significantly higher deposition rates, making it particularly attractive for large-part manufacturing [13, 14]. Within the domain of wire-based DED, the primary differentiation lies in the energy source used to melt the wire. The two most common techniques are Wire Laser Additive Manufacturing (WLAM) and Wire Arc Additive Manufacturing (WAAM).

1.1.3. Wire Laser Additive Manufacturing (WLAM)

This process utilizes a high-power laser beam to create a melt pool on the substrate into which the metal wire is fed [13, 14]. WLAM offers high precision and control, enabling the fabrication of medium to small features with near-net-shape characteristics. The concentrated heat source allows for deep penetration and high welding speeds. The adoption of fiber lasers has been a significant advancement, as they are highly efficient and capable of processing reflective metals like aluminum, copper, and brass, which are challenging for CO_2 or Nd:YAG lasers due to back-reflection issues [15].

1.1.4. Wire Arc Additive Manufacturing (WAAM)

WAAM employs an electric arc as the heat source to melt the wire feedstock. The arc is generated between the wire electrode and the substrate, creating a molten pool that solidifies as the torch moves, depositing material along a predetermined path [4, 16]. WAAM is characterized by its very high deposition rates (often several kilograms per hour), making it one of the most efficient AM processes for producing large-volume components. While its precision and surface finish are typically inferior to those of WLAM or PBF processes, its unparalleled deposition efficiency and cost-effectiveness for large parts have established its niche in industries such as shipbuilding, construction, and aerospace [17, 18]. A hybrid

approach, known as Laser Arc Hybrid Wire Deposition (LAHWD), combines the WAAM and laser processes. In LAHWD, a laser is used to melt the wire feedstock while an arc is employed to stabilize the melt pool. This synergy can result in a higher deposition rate, improved surface quality, and better mechanical properties compared to either process alone, though it introduces greater complexity and cost [19, 20].

1.2. Wire Additive Manufacturing

Wire Additive Manufacturing (WAM) is an advanced additive process that employs metallic wire as the primary feedstock material for fabricating components. When analyzing this process, it is essential to account for various factors, including material composition, geometric configuration, and physical properties, as each can significantly influence the final build quality (Figure 1) [21].

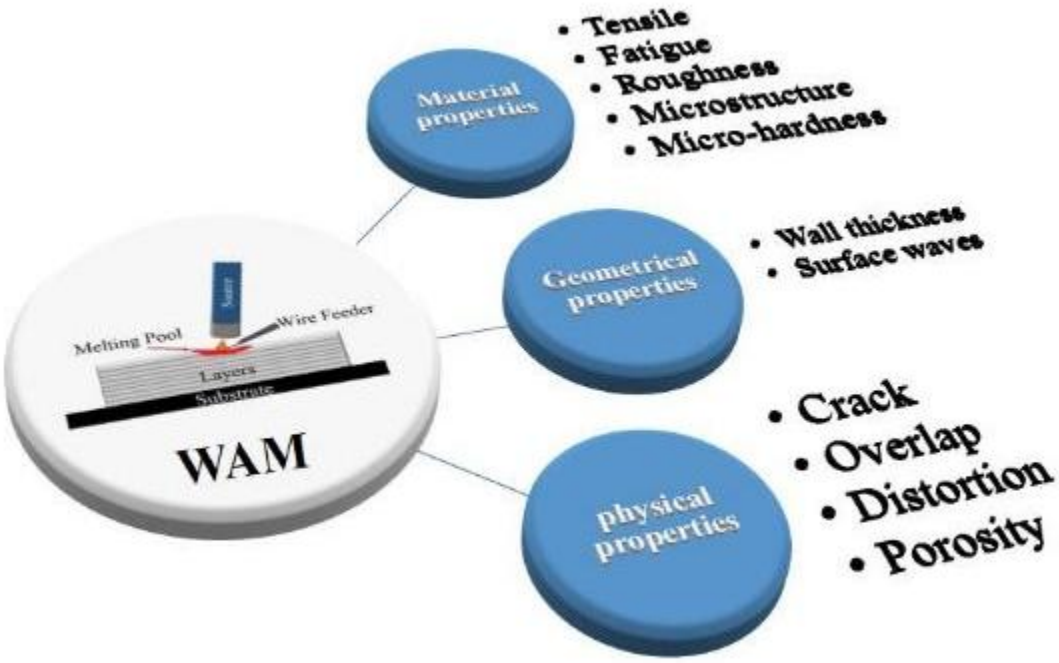

Figure 1-1. Wire additive manufacturing scheme.

Effective control of input parameters is crucial in minimizing defects during WAM processing. Variations in these parameters directly affect phase formation, leading to distinct morphological and structural outcomes in the deposited material [22].

1.2.1. Fundamentals of WAAM

1.2.1.1 Process Principle and Setup

Wire Arc Additive Manufacturing is a directed energy deposition process that builds three-dimensional components through the layer-by-layer deposition of weld beads. The

fundamental setup, as illustrated in Figure 1, typically consists of several key components [12, 18]:

1. **Power Source and Welding Torch:** A standard arc welding power source (e.g., for GMAW, GTAW, or PAW) generates the electric arc. The torch is responsible for delivering the current and, in the case of GMAW, the wire feedstock.
2. **Wire Feeder:** A precision system that continuously feeds the metal wire from a spool to the welding torch at a controlled rate (Wire Feed Rate - WFR).
3. **Robotic Manipulator:** A multi-axis robot or a CNC gantry system that moves the welding torch along a pre-programmed path, defining the geometry of each layer.
4. **Substrate/Base Plate:** The foundation upon which the part is built. The substrate is often made of a material similar to the wire to ensure good metallurgical bonding.
5. **Shielding Gas System:** To protect the molten metal from atmospheric contamination (oxygen and nitrogen), an inert or semi-inert gas (e.g., argon, helium, or mixtures) is directed onto the weld pool.

To date, numerous techniques have been applied in additive manufacturing (AM), each presenting its own advantages and limitations depending on the experimental setup, material type, and equipment used. Given the increasing demand for unique and customized components across various industries, AM technologies have evolved to address specific 3D printing challenges and achieve optimal productivity. Among these, WAAM and WLAM are two prominent wire-based AM processes. The fundamental distinction between them lies in their heat sources: WAAM employs an electric arc, whereas WLAM utilizes a laser beam. WAAM generally offers higher deposition rates and efficiency, while WLAM provides superior dimensional accuracy and surface finish. Moreover, WLAM exhibits greater versatility in processing various materials, whereas WAAM is mainly suitable for aluminum alloys [6, 23].

Despite these advantages, laser-based material processing faces significant challenges, particularly regarding the precise preparation of part edges and the minimization of defects caused by the small laser focal spot. This precision is essential to ensure proper beam formation during processing. Furthermore, attempts to bridge large gaps or fabricate sizable components cannot rely solely on defocusing the laser beam, since the associated decrease in power density promotes conduction-mode welding, which limits penetration depth. To

overcome these issues, some studies have proposed introducing beam oscillation or combining the laser system with WAAM to enhance deposition efficiency and joint quality [3, 5].

The emerging WLAM process, often using fiber, CO_2, or YAG lasers, has been recognized as a promising method for fabricating large metallic components using various wire materials [3, 23]. Consequently, both WAAM and WLAM represent powerful techniques for wire-based additive manufacturing. Their effectiveness can be further improved through process optimization and systematic material characterization across diverse metals, arc types, and laser sources [6, 24]. In the early 2000s, the availability of laser sources for welding and AM applications was relatively limited. However, in the past decade, the global market for Laser Additive Manufacturing (LAM) has expanded substantially, driven by the high thermal stability of laser beams, which helps minimize material waste. Hybrid-AM technologies have also emerged, combining concentrated, high-intensity heat sources that enable deep and localized welds at elevated build rates. The increasing adoption of laser-based systems beyond the automotive sector,particularly in aerospace, medical, electronics, and jewelry manufacturing, has significantly fueled market growth. With continuous innovations in materials, equipment, and processing methods, the demand for LAM products is expected to rise further.

Among various laser technologies, fiber lasers are projected to dominate the LAM market due to their capacity to process highly reflective metals such as brass, aluminum, copper, gold, and silver. In contrast, CO_2 and Nd:YAG lasers are more prone to damage from reflected beams during the processing of such bright metals [14]. Fiber lasers, however, provide a reliable means to weld reflective materials for diverse applications, including aircraft and automotive structures, copper joints, shape-memory alloys, and precious metals [15, 24]. A key objective of wire-based additive manufacturing strategies is to minimize production time and cost while maintaining high performance and precision. This approach reduces overall processing time and enables the fabrication of large, geometrically complex components with excellent accuracy. Additionally, WAM methods facilitate cost-effective repair of damaged parts, making them highly attractive in industrial applications. Through AM, multi-material or composite components can also be fabricated with precise control over individual material proportions, allowing designers to tailor properties such as strength, weight, flexibility, and reflectivity [19, 21, 24].

To ensure the mechanical integrity of printed components, various testing methods are used to assess sample quality. Recent studies also highlight that accurate numerical simulations can effectively predict and optimize WAM process parameters [25–30]. In both WAAM and WLAM, the wire feedstock is melted at the heat source,typically delivered by robotic systems that provide motion and control [31–43].

A comparative analysis of WAAM and WLAM reveals their respective advantages and limitations in terms of microstructural development, mechanical behavior, and overall manufacturing quality. These processes have found applications across multiple industries, including food production, aerospace, and shipbuilding. In this study, the authors aim to categorize and compare the microstructural and mechanical characteristics of components produced by these two methods, providing a structured understanding of their capabilities. Defects in fabricated parts are influenced by factors such as material composition, equipment conditions, and environmental variables. Previous research has explored how input parameters and material properties affect these outcomes, ultimately contributing to enhanced device performance and more reliable manufacturing [1, 43]. The process begins with the generation of an electric arc between the wire tip and the substrate, creating a molten pool. The wire is fed into this pool, melting and depositing material. The robot then moves the torch, laying down a bead of solidified metal. After a complete layer is deposited, the torch is raised by a predefined layer height, and the process repeats for the subsequent layer, adhering to the sliced CAD model [5, 12].

1.2.1.2 Arc Variants in WAAM

The characteristics of the WAAM process are heavily influenced by the type of arc welding process employed. The most common variants include:

- **Gas Metal Arc Welding (GMAW)-based WAAM:** This is one of the most prevalent forms of WAAM. In GMAW, the wire electrode is consumable and forms part of the electrical circuit. Metal transfer modes in GMAW, such as spray, globular, and short-circuit, can significantly affect spatter, stability, and heat input [42].
- **Cold Metal Transfer (CMT)-based WAAM:** Developed by Fronius, CMT is an advanced variant of GMAW that has gained immense popularity in WAAM due to its exceptional process stability and low heat input [8, 10]. The CMT process is characterized by a digitally controlled, high-frequency retraction of the wire. When the wire short-circuits with the melt pool, the current drops to nearly zero, and the

wire is retracted, detaching the droplet with minimal force. This results in essentially spatter-free material transfer and significantly reduced thermal input compared to conventional GMAW [10, 17]. The low heat input is particularly beneficial for managing residual stresses and distortion in thin-walled structures.

- **Gas Tungsten Arc Welding (GTAW)-based WAAM:** In GTAW (or TIG), a non-consumable tungsten electrode generates the arc, and the wire is fed separately into the weld pool. This allows for independent control of the heat input and wire feed rate, often leading to superior bead shape control and surface finish, though at a generally lower deposition rate than GMAW [4, 43].
- **Plasma Arc Welding (PAW)-based WAAM:** PAW uses a constricted arc and a separate orifice gas, resulting in a highly concentrated and stable heat source with greater penetration and higher energy density than GTAW. This can be advantageous for certain materials and geometries [11, 23].

1.3. Critical Process Parameters and Their Influence

The quality, geometry, microstructure, and mechanical properties of WAAM-fabricated components are profoundly influenced by a complex interplay of process parameters. Understanding and optimizing these parameters is crucial for achieving reproducible and high-quality parts [9, 19, 24]. The key parameters can be categorized into thermal, geometrical, and material-related factors.

1.3.1 Thermal and Energy Parameters

- **Arc Power (Current and Voltage):** Arc power, determined by the welding current and voltage, is a primary factor controlling the heat input into the substrate and the deposited material. Higher arc power increases the melting rate of the wire and the size of the molten pool, leading to wider and flatter beads [24, 32]. As demonstrated in studies on AISI 308L and ER70S-6, increasing arc power enhances melt pool fluidity and spreading, which improves the wetting angle and aspect ratio of the bead, contributing to better interlayer bonding [34, 44]. However, excessive heat input can lead to issues such as excessive dilution with the substrate, increased residual stresses, distortion, coarser microstructures, and potential evaporation of alloying elements [18, 38].
- **Heat Input:** Heat input is a calculated parameter (often as Voltage × Current / Travel Speed) that provides a comprehensive measure of the energy delivered per unit length

of deposit. It directly affects the thermal history, including peak temperatures, cooling rates, and solidification behavior [38, 45]. High heat input generally results in slower cooling rates, promoting the formation of coarser microstructures and potentially reducing mechanical strength, while low heat input leads to faster cooling and finer microstructures [25, 46].

1.3.2 Geometrical and Kinematic Parameters

- **Deposition Speed (Travel Speed):** This is the speed at which the welding torch moves relative to the substrate. Deposition speed has a direct inverse relationship with heat input per unit length. Higher travel speeds reduce the linear heat input, resulting in a smaller melt pool, narrower bead width, and potentially higher bead height [11, 32]. Optimizing travel speed is essential; too high a speed can lead to lack of fusion between layers or insufficient wetting, while too low a speed can cause excessive heat accumulation, leading to sagging and geometrical inaccuracies [19, 34].

- **Wire Feed Rate (WFR):** The wire feed rate controls the volume of material deposited per unit time. It must be balanced with the thermal energy provided by the arc. An optimal WFR ensures stable transfer of molten droplets into the melt pool. If the WFR is too high for a given current, incomplete melting or stubbing of the wire can occur. Conversely, a WFR that is too low can lead to an unstable arc and irregular deposition [28, 29]. Research on AISI 308L and ER70S-6 has shown that increasing the WFR can lead to a decrease in surface roughness and a more uniform deposition, as it helps maintain a consistent melt pool volume [24, 33].

- **Layer Height and Bead Overlap:** The vertical step increment between layers (layer height) and the lateral overlap between adjacent beads (in multi-bead structures) are critical for determining the surface roughness and dimensional accuracy of the final part. The layer height is typically set as a percentage of the bead height from the previous layer. Proper bead overlap is necessary to avoid valleys or grooves between beads, which can act as stress concentrators [15, 47].

1.3.3 The Quest for Optimal Bead Geometry: Aspect Ratio and Wetting Angle

- **Aspect Ratio (Width/Height):** A bead with an aspect ratio between 2 and 3 is generally considered ideal for WAAM [16]. A ratio that is too low (a tall, narrow bead) can lead to poor stability between layers and an uneven surface, making

subsequent layers difficult to deposit accurately. A ratio that is too high (a wide, flat bead) may not provide sufficient build-up rate and can lead to excessive remelting of previous layers.

- **Wetting Angle (θ):** This is the angle at which the deposited bead wets the substrate or previous layer. A wetting angle close to 60° is often targeted, as it promotes excellent interlayer bonding and minimizes the entrapment of defects between layers [14, 15]. Poor wetting (high contact angle) can create gaps and lack-of-fusion defects.

Statistical methods like Design of Experiments (DOE), Analysis of Variance (ANOVA), and Response Surface Methodology (RSM) are extensively used to model the relationship between process parameters and these geometrical responses, enabling the optimization of the WAAM process for specific materials [9, 22, 48].

1.4. Materials for WAAM

WAAM's versatility is demonstrated by its compatibility with a wide range of metallic alloys. The choice of material is dictated by the intended application and the required mechanical, corrosion, or thermal properties.

1.4.1 Steels

- **Low-Carbon Steels (e.g., ER70S-6):** These are among the most commonly used materials in WAAM due to their good weldability, strength, and low cost. They are widely employed in structural applications. The microstructure of as-deposited ER70S-6 typically consists of polygonal ferrite, Widmanstätten ferrite, and non-lamellar pearlite, with grain size varying from the finer grains in the high-cooling-rate dilution zone (3-5.6 μm) to coarser grains in the middle of the bead (8.6-11.6 μm) [49-53]. Microhardness values for WAAM ER70S-6 can reach up to 300 HV, influenced by the cooling conditions and resulting microstructure [21].

- **Stainless Steels (e.g., AISI 308L, 316L):** Austenitic stainless steels are valued for their excellent corrosion resistance and toughness. WAAM of 308L and 316L has been successfully demonstrated for various applications. The microstructure is predominantly austenitic, often with some amount of δ-ferrite present to prevent solidification cracking [11, 54-56]. Process parameters significantly affect the oxidation and surface roughness of these materials, with higher wire feed rates generally leading to smoother surfaces [24]. Microhardness in the heat-affected zone (HAZ) of 308L parts can reach up to 310 HV [24].

1.4.2 Aluminum Alloys

Aluminum alloys present challenges for WAAM due to their high thermal conductivity, reflectivity (for laser-based processes), and susceptibility to oxidation and solidification cracking. However, alloys like Al-5Mg (5356) and Al-Si (4043) have been successfully processed using WAAM, particularly with the low-heat-input CMT process [10, 11]. The controlled heat input helps manage the thermal cycle, reducing porosity and cracking tendencies.

1.4.3 Titanium Alloys

Titanium alloys, such as Ti-6Al-4V, are highly sought after in aerospace and biomedical industries for their high strength-to-weight ratio and excellent corrosion resistance. WAAM of Ti-6Al-4V requires stringent atmospheric control, often using a local argon chamber or trailing shields to prevent oxygen and nitrogen contamination, which can embrittle the material. The microstructure is typically a mixture of α and β phases, with prior β columnar grains growing epitaxially across multiple layers. Post-processing heat treatments are often employed to modify the microstructure and achieve desired mechanical properties [2, 11].

1.4.4 Nickel-Based Superalloys

Nickel superalloys like Inconel 625 and 718 are used in high-temperature applications, such as turbine components. WAAM offers a viable route for repairing and manufacturing these expensive parts. The process must be carefully controlled to avoid the formation of deleterious phases (e.g., Laves phase in Inconel 718) and to manage the high residual stresses. Studies have shown that WAAM-fabricated Inconel 625 can exhibit comparable or superior mechanical properties to cast counterparts, with a fine, dendritic microstructure [10, 11, 57-64].

1.4.5 Copper-Based Alloys and Bimetallic Structures

Copper and its alloys, such as CuAl8 (aluminum bronze), are known for their high thermal and electrical conductivity. WAAM of pure copper is challenging due to its very high thermal conductivity, but alloys like CuAl8 are more readily processed [13, 65-68]. A particularly exciting application of WAAM is the fabrication of bimetallic or functionally graded materials (FGMs). This involves depositing one material onto another, creating a component with graded properties. For example, depositing a corrosion-resistant nickel-aluminum bronze (NAB) or CuAl8 onto a high-strength steel substrate creates a part that combines the surface properties of the former with the structural integrity of the latter, which is highly valuable for marine components like propellers [34, 68-75]. The interface is critical,

and studies have shown that with proper parameter control, defect-free interfaces with a smooth gradient in composition and hardness can be achieved [69, 76]. The maximum failure load for such bimetallic specimens has been reported to reach 4726 N for steel-steel and 1939 N for CuAl8-steel samples [34].

In WAAM, metal wire is melted by an electric arc and deposited layer by layer to produce three-dimensional geometries. This section discusses the application of WAAM for different metallic wires and reviews the corresponding microstructural and mechanical characteristics, such as microhardness, tensile strength, and fracture behavior, of the fabricated parts. Figure 2 illustrates a general schematic of the WAAM process. Due to the rapid deposition rates and ambient cooling conditions, WAAM components may exhibit certain defects [44–46]. Although large and heavy AM parts can experience issues such as cracking, porosity, incomplete fusion, and weak interlayer bonding, these problems can be mitigated through optimization of process parameters and hardware configurations [47–51].

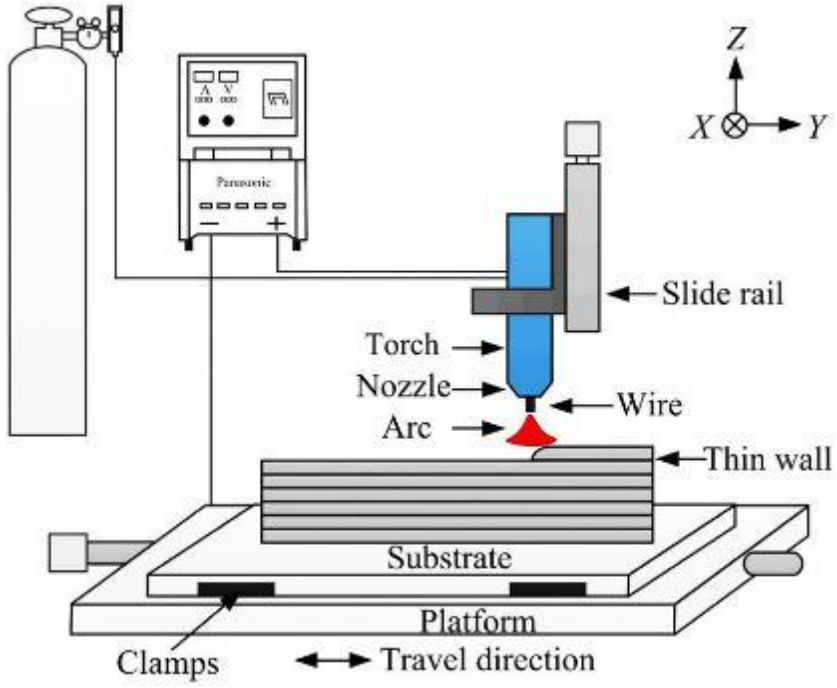

Figure 1-2. Schematic of the WAAM process.

Figure 3(a) presents SEM images of a WAAM-manufactured sample using TC4-DT alloy wire (0.6 mm in diameter) [44]. After air cooling and etching with HF + 10% HNO_3 + 86% H_2O, cracks were observed along α′ structures (Figure 3(b)). The cooling rate plays a critical role, excessively rapid air cooling may transfer heat into adjacent layers, reducing formability. Therefore, achieving a balance between rapid solidification and proper layer formation is essential.

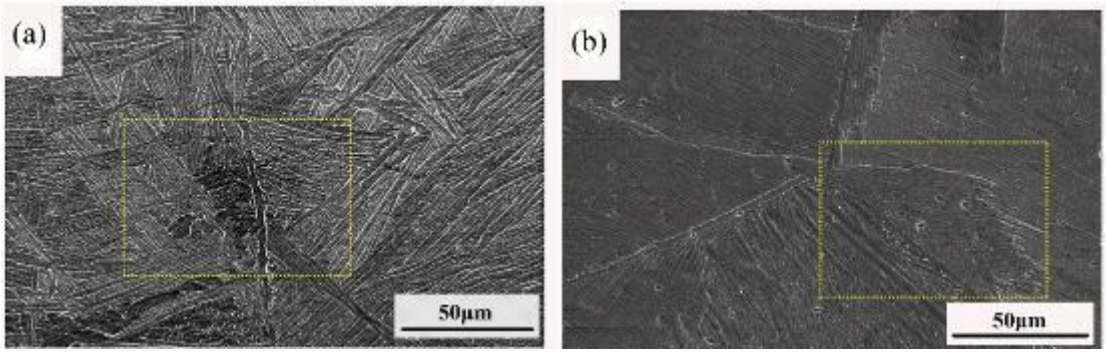

Figure 1-3. Crack morphology: (a) microstructure of the first crack, (b) microstructure of the second crack. Reproduced from ref. [44] with permission from *Journal of Materials Research and Technology.*

Figure 4(a) shows a crack in a nickel-based Alloy 718 sample fabricated via WAAM [52]. Crack propagation occurred after air cooling, as confirmed through EBSD mapping (Figure 4(b–c)).

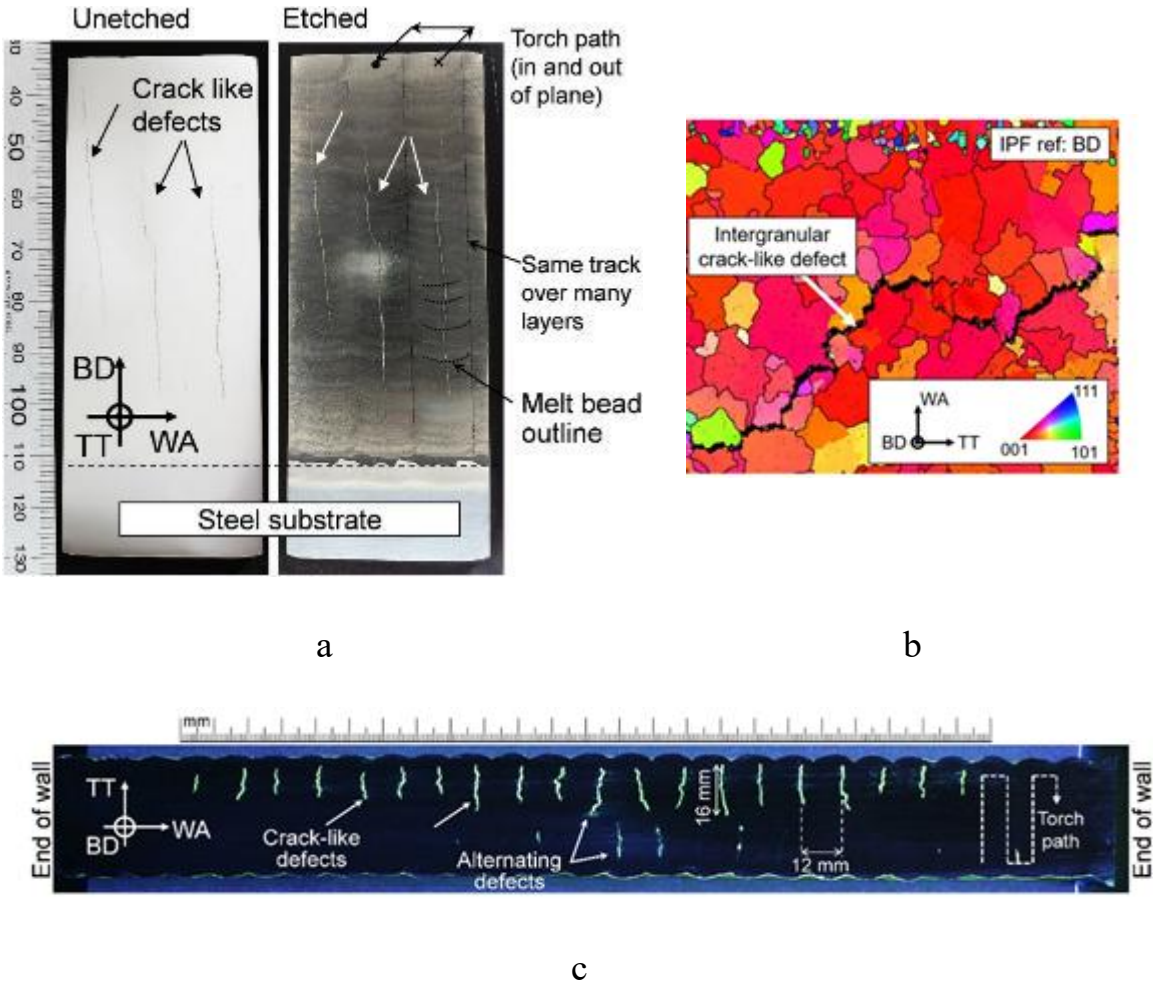

Figure 1-4. Cracking in WAAM-built Alloy 718. Reproduced from ref. [52].

A simulation of crack growth using a non-destructive ultrasonic testing (UT) approach combined with finite element analysis in COMSOL Multiphysics is shown in Figure 5 [53].

The laser beam induced a heat-affected zone in the metal, with R-waves corresponding to high input energy, while L- and S-waves represented ultrasonic signal variations. By detecting these signals (RS and R waves), the UT simulation revealed the internal crack morphology.

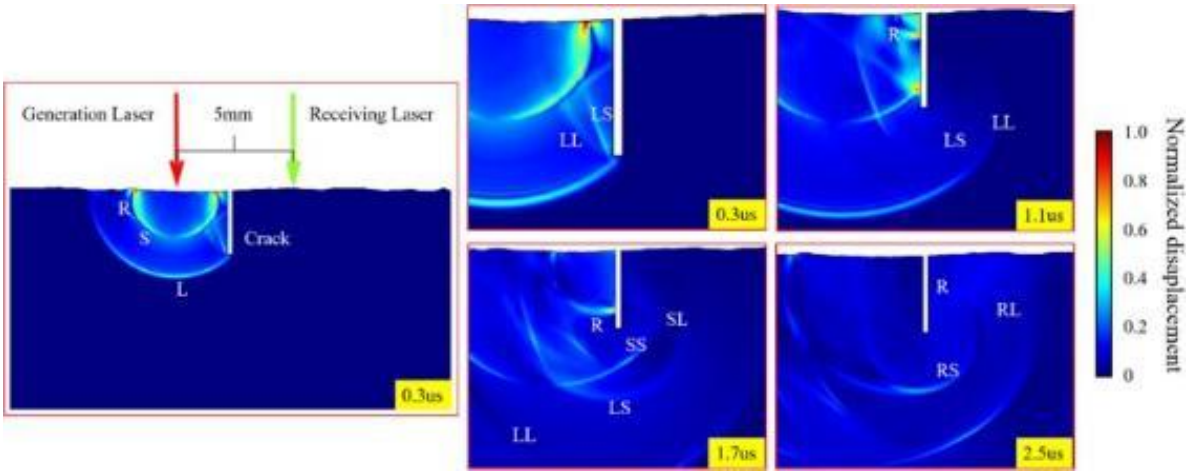

Figure 1-5. Simulation of crack propagation in the WAAM process using UT. Reproduced from ref. [53] with permission from *Ultrasonics.*

A study also investigated the correlation between shielding gas flow rate and porosity formation in aluminum WAAM samples. The findings revealed that higher gas flow rates led to increased porosity. This occurs because excessive gas flow entraps oxygen within the molten pool, preventing uniform solidification and leading to localized pore formation (Figure 6) [54].

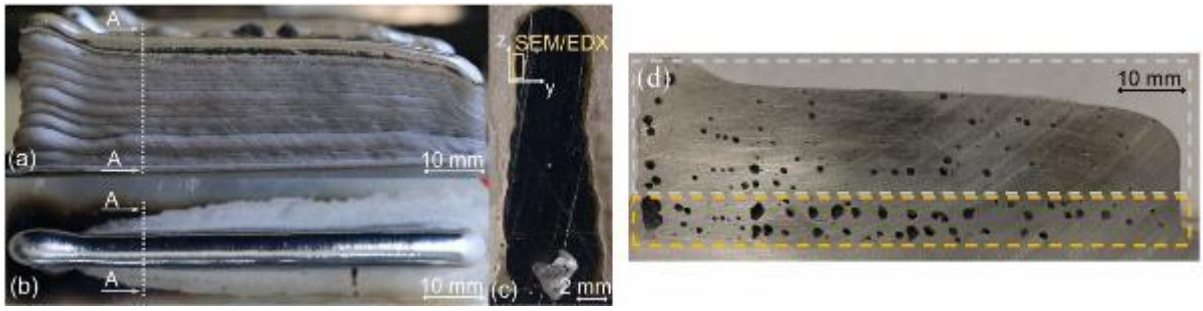

Figure 1-6. Cross-sections of aluminum samples fabricated under varying shielding gas flow rates: (a–d) 10, 8, 6.1, and 10 L/min. Reproduced from ref. [54] with permission from *Additive Manufacturing.*

Gierth et al. [55] conducted a systematic study on the AlMg5Mn aluminum alloy fabricated via gas-shielded WAAM using low-energy, controlled short-arc techniques. The investigation compared three arc modes, CMT, CMT Advanced (CMT-ADV), and CMT-Pulse Advanced (CMT-PADV), focusing on energy input per unit length, thermal cycles, and resulting microstructural and mechanical characteristics. Selecting an appropriate arc mode

was shown to be vital for producing high-quality, large-scale parts. The study optimized process parameters such as wire feed rate and deposition speed and analyzed porosity, surface contour, and overall sample integrity. Results indicated that optimal parameter combinations enable superior part quality with predictable mechanical performance. Similarly, Wang et al. [56] explored variable symmetry and double-pulse techniques in GTAW welding of aluminum alloy 2124. Their results demonstrated that the advanced double-pulse approach significantly reduced coarse dendritic grains and promoted a more uniform distribution of precipitates, leading to a finer equiaxed grain structure. Despite certain drawbacks, WAAM exhibits notable advantages in fabricating large, complex structures with adjustable wire diameters and a wide range of metallic materials. Table 1 summarizes key findings from recent WAAM research.

To better understand process behavior, finite element simulations are often used to model wall deposition, mechanical response, and strain distribution using Hooke's law. Ding et al. [57] applied this approach to simulate thermal behavior in WAAM of mild steel, as illustrated in Figure 7.

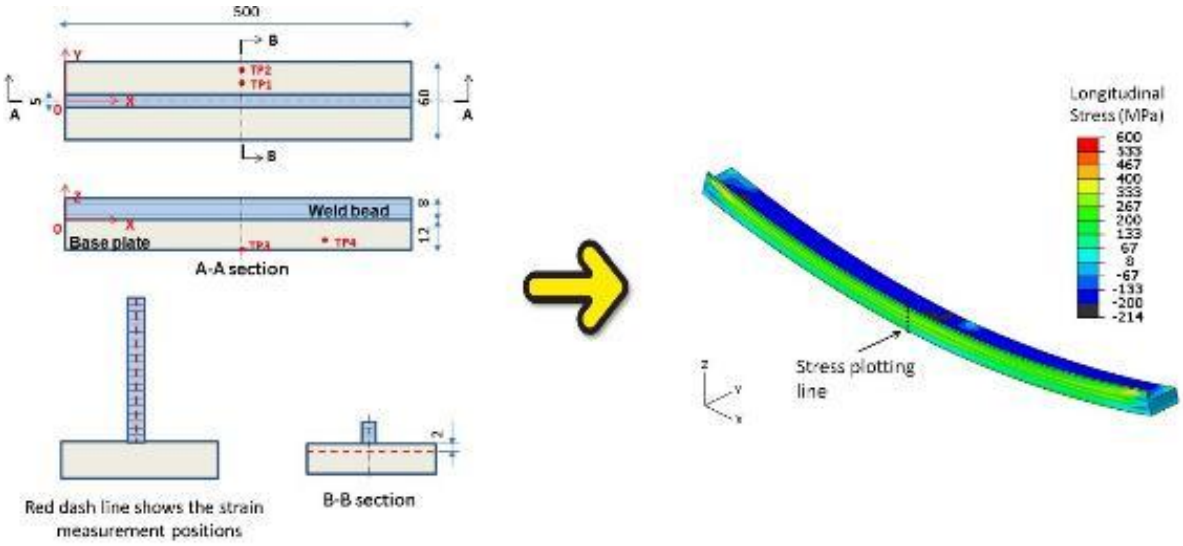

Figure 1-7. Thermal simulation of a mild-steel WAAM component. Reproduced from ref. [57] with permission from *Computational Materials Science.*

Table 1. Summary of recent research on WAAM process outcomes.

Materials	Input parameters	Tests	Wire diameter	Ref. (year)
Mild-steel S355JR-AR	Welding speed: 8.33 mm/s The welding process heat input is 269.5 J/ mm Dwelling time: 400 s	Thermo-mechanical analysis	1.2 mm	[57] (2011)
Ti,6Al-4V	Wire feed speed: 1.8 m/min Average voltage: 12 V Layer height: 1.2 mm Average current: 99A Peak current: 180 A Base current: 45 A	Microstructure Fatigue Tensile	1.2 mm	[58] (2012)
Tool steel	Welding speed: 800 mm/min Shielding gas: 82% argon and 18% CO2 Flow rate: 22L/min	Strategy of additive patterns	1.2 mm	[59] (2014)
DH36 Low carbon steel	The arc length: 3.5 mm Average Current: 140 A Average Voltage: 12.7 V Welding speed: 100 mm/min Wire feed speed: 1000 mm/min	Microstructure EDS XRD Micro-hardness Tensile Yield strength (0.2% offset)	0.9 mm	[60] (2015)
Ni-Al Bronze (NES 747)	Wire feed speed: 5.4-8 m/min Welding Speed: 400 mm/min Average Current: 175.5-256.1 A Average Voltage: 24.8-29 V Heat input: 653-1114 J/mm	Microstructure XRD Micro-hardness	1.2 mm	[61] (2016)
Grade 1080 aluminum Cu-9	Average Current: 160 A Wire feed speed of Al: 311 mm/min Wire feed speed of Cu: 1300 mm/min Average deposition energy: 20.2 kJ/g Welding speed: 95 mm/min Gas flow rate: 9 L/min Inter-pass temperature: 673 K	Microstructure XRD Micro-hardness Tensile	0.9 mm	[62] (2017)
2Cr13 martensitic stainless steel	Welding speed: 0.4 m/min Wire feed angle: 90 Dwelling time: 120 s Stand-off distance: 4.1 mm Average voltage: 12.9 V Average current: 96 A Wire feed speed: 5.2 m/min Arc length correction factor: 7%	Microstructure XRD EBSD maps Pole figure Tensile Fractography	1.2 mm	[63] (2018)
G4Si1 (1.5130) Steel AZ31 magnesium	Wire feed speed: 2.5–5.0 m/min Welding speed: 40 cm/min Half width: 2-3 mm Layer thickness: 2-3 mm The offset per layer:1.7 mm	Thermo-physical properties Young's modules Flow stress	1.2 mm	[64] (2018)
Ti6Al4V alloy	Shielded welding gas graded: 99.995% argon Average Current: 110 A Average voltage: 12 V Welding speed: 95 mm/min Wire feed speed: 1000 mm/min Dwelling time: 125 s	Microstructure XRD EDS	1.2 mm	[65] (2018)
Al-5Mg and Al-3Si alloys	Average Voltage: 15.2-18 V Average Current: 115-177 A Welding speed: 6-8 mm/s Dwelling time: 120 s	Heat source management Tensile	0.9 mm	[66] (2019)
Inconel 625	Wire feed speed: 6.5 m/min Welding speed: 8-10 mm/s Average Current: 148 A Average Voltage: 14.6 V Heat input: 216-270 J/mm	Microstructure Tensile Micro-hardness Fracture surface EDS	1.2 mm	[67] (2019)
Ti-6Al-4V alloy	Average Current: 120 A Average Voltage: 14 V Wire feed rate: 10 m/min Layer thickness: 3.3 mm Argon flow rate: 15 l/min.	Microstructure Tensile Yield strength	1 mm	[68] (2020)

Al-Zn-Mg-Cu alloys	Average Current: 220 A Welding speed: 10 cm/min Wire feed speed: 130 cm/min Inter-pass temperature: 80℃	Microstructure Tensile EBSD XRD TEM EDS mapping Micro-Hardness	1.2 mm	[69] (2020)
EN AW-5754A H111 (substrate) S Al 5556 (welding wire)	Welding speed: 0.3-0.6 m/min Wire feed speed: 9.45 m/min Shielding gas: Argon/Helium Average Current: 60-180 A Average Voltage: 0-23 V	Geometrical Properties Optically observed porosity Buildup Time Tensile strength Microstructural analysis Micro-Hardness Elongation to fracture	1 mm	[55] (2020)
Titanium-6Al4V Stainless-Steel-316 Inconel-718 Aluminum 5356	Wire feed speed: 5-12 m/min Energy: 300-1080 J/mm Overlapped walls rate: 65 % Shielding gas: Argon	Monitored energy Microstructural analysis Tensile strength	1.2 mm	[70] (2021)
ER70S-6 Q235	Shielding gas: Argon (80 %) and CO2 (20 %) Welding speed: 0.1-0.6 m/min Wire feed speed: 1-5 m/min Nozzle to work distance: 5-21 mm	Weld bead geometries	0.9 mm	[71] (2021)
$Ni_{50.8}Ti$	Shielding gas: 30% He and Argon Welding speed: 4 mm/s Average Current: 110-130 A Average Voltage: 14.7-14.9 V Wire feed speed: 7.4-8.9 m/min	Macro morphology Microstructure Phase identification XRD patterns Micro-hardness Tensile	1 mm	[72] (2022)

Furthermore, Ding et al. [59] demonstrated that modifying scanning strategies can reduce surface roughness in WAAM parts. The roughness parameter R_a was determined using Equation 1:

$$R_a = \frac{1}{n}\sum_{i=1}^{n}\left|h_i - \bar{h}\right| \quad (1)$$

where $\bar{h}$is the average surface height and $h_i$is the absolute height of each surface point.

1.5. Wire Laser Additive Manufacturing (WLAM)

In WLAM, metallic wire feedstock is melted by a focused laser beam and deposited in a linear path to build components with complex geometries (Figure 8).

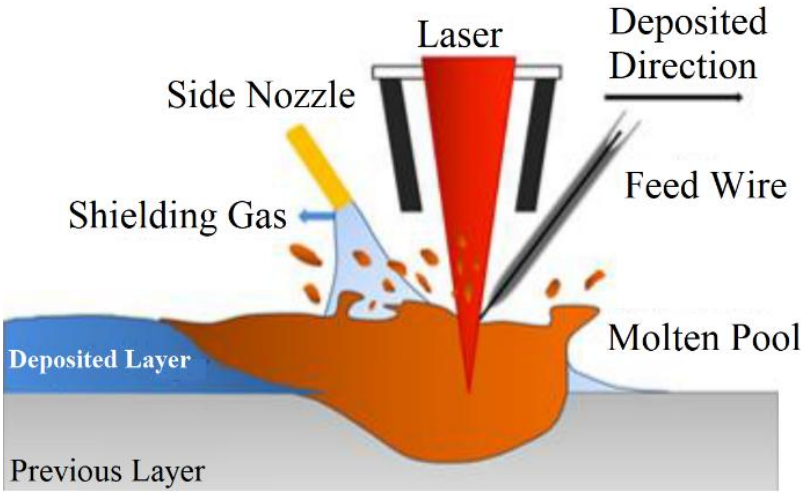

Figure 1-8. Schematic of the WLAM process.

The process parameters, particularly the laser power, scanning speed, and deposition pattern, play a crucial role in determining the final part quality [73-76]. Although the technique is capable of producing dense and precise components, certain types of defects may still arise during or after fabrication [77-83]. Due to the high melting rate and rapid solidification associated with WLAM, porosity formation is one of the most common issues [84–88].

During the process, entrapped air or shielding gases can become trapped inside the molten pool, resulting in porosities distributed throughout the structure. Figure 9 presents the WLAM deposition of stainless steel 316L wire, in which various porosities formed during processing [89]. These voids often occur between dendritic microstructures because of the extremely high cooling rate of the molten 316L wire, which limits sufficient time for austenite matrix formation alongside ferritic phases, leaving air trapped at phase boundaries (Figure 9 a, b). Additionally, porosities may appear between deposition tracks due to incomplete fusion of successive layers. This happens when the molten metal fails to fully spread over the preceding bead, whose irregular surface, resembling sea waves, prevents uniform wetting and bonding, ultimately leading to lack-of-fusion defects (Figure 9 c, d).

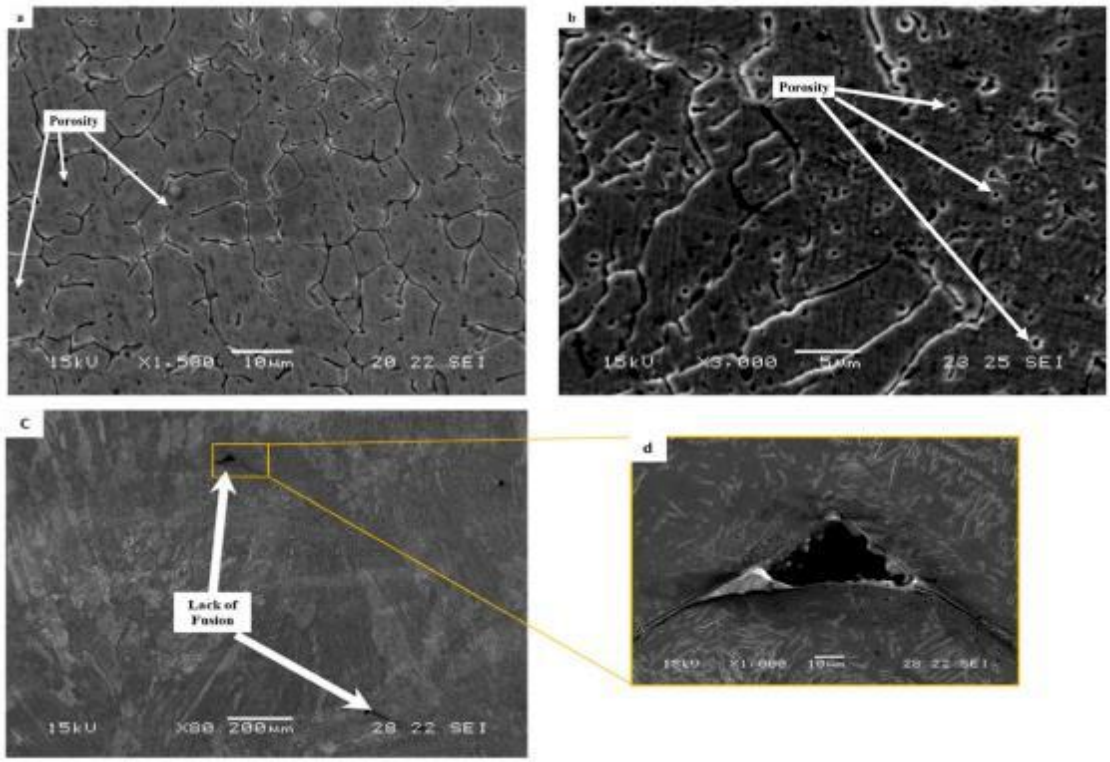

Figure 1-9. Microstructure of WLAM-fabricated 316L samples: (a, b) porosity within austenitic and ferritic phases; (c, d) lack-of-fusion porosity. Reproduced from ref. [89] with permission from *Metals.*

A summary of recent studies on WLAM, including mechanical property assessments and laser parameter effects, is presented in Table 2.

Table 2. Summary of WLAM research outcomes.

Materials	Input parameters	Type of laser	Tests	Ref. (year)
Ti–6Al–4V	Laser power: 2.6-3.5 kW Laser scanning speed: 7.5-10 mm/s Feeding angle: 55° Wire-feed speed: 30-40 mm/s Diameter of optical fibre: 0.4 mm Focal plane diameter: 0.56 mm Focal length of optics: 140 mm wire diameter: 1.2 mm	3.5 kW Nd:YAG laser	Tensile Microstructure	[81] (2011)
Ti-6Al-4V	Laser power: 1.75-3.5 kW Laser scanning speed: 7.5-40 mm/s Wire-feed speed: 15-160 mm/s Focal length of optics: 140 mm Focal plane diameter: 056 mm Focal length of optics: 140 mm wire diameter: 1.2 mm	3.5 kW Nd:YAG laser	Micro-hardness Microstructure	[82] (2012)

Ti-6Al-4V	Wire feed angle: 55° Deposit spacing: 3mm Layer thickness: 0.8 mm Wire-feed speed: 2200 mm/min Laser power: 1.65 kW Deposition speed: 500 mm/min Wire diameter: 1.2 mm Diameter of laser beam mm 3	Not reported	Tensile Macrostructure	[83] (2017)
AISI 301	wire diameter: 0.3-0.5 mm spot diameter: 0.3 mm Laser power: 150 W Pulse duration: 6–12 ms Pulse energy: 9-12 J Wire feeding speed: 900 mm/min Wire feeding angle: 30° Shielding gas type- rate: Argon at 0.8 bar Laser scanning speed: 90-180 mm/min	5 kW Nd:YAG laser	Micro-hardness Tensile test Macro-structure	[84] (2018)
308L	wire diameter: 1.1 mm Laser power: 0.4-1600 kW Laser scanning speed: 1.2 m/min Spot size: 2mm Deposition rate: 0.7 kg/h Shielding gas: Argon Wire feeding speed: 1.5 m/min Number of Layers: 45 Bead Overlap: 47%	5 kW Diode laser	Micro-hardness Tensile Microstructure Macro-structure	[85] (2019)
ER321	Laser power: 2 kW wire diameter: 1.2 mm Laser scanning speed: 4.5 mm/s Wire feeding speed: 20 mm/s Shield gas flow rate: 15 L/min	3 kW Fiber laser	Microstructure Micro-hardness Tensile	[86] (2021)
Ti-6Al-4V	Laser power: 1200 W Deposition speed: 2 mm/s Wire feed rate: 10 mm/s Shield gas flow rate: 15 L/min Laser beam size: 2.6 mm Laser scanning speed: 120 mm/min	Not reported	Ultrasonic vibration Microstructure Grain size Statistical distributions	[87] (2021)
Ti-6Al-4V	Laser focus radius: 0.2 mm Spot radius: 1.5 mm Wire diameter: 1 mm Width of the deposit: 2-4 mm Laser power: 3 kW Scanning speed: 20 mm/s Wire feeding speed: 30 mm/s	Not reported	Simulation	[88] (2021)
316L	Feeding rate: 8.3 mm/s Laser scanning speed: 6.5 mm/s Deposition rate: 250 g/h Wire diameter: 1.2 mm Laser power: 1.5 kW	Not reported	Microstructure Tensile Corrosion Resistance Roughness XRD Fracture surface analysis	[89] (2021)
Ti-6Al-4V	Laser power: 2.5-3 kW Laser scanning speed: 10 mm/s Wire diameter: 1.2 mm Cooling rate: 20 K/s Laser radius: 7.5 mm	3 kW Fiber laser	Microstructures Simulation of phases	[90] (2021)
316L	Wire diameter: 1.2 mm Shielding gas flow rate: 20 L/min Wire feeding speed: 3-7 m/min Laser power: 1.5-5 kW	5 kW Fiber laser	Micro-hardness Visual test Drop deposition from	[91] (2021)

Al alloy 5A06	Wire diameter: 1.2 mm Optical fiber diameter: 600 µm Focal length: 0.26 mm Shielding gas flow rate: 15 L/min Wire feeding angles: 15-75˚ Laser power: 2.6-3.2 kW Laser scanning speed: 1-2.5 m/min Wire feeding speed: 2-5 m/min	4 kW Fiber laser	Macro structure Microstructures DOE	[92] (2021)
Ti6-Al-4V	Core diameter: 0.15 mm Beam waist: 0.3 mm Laser power: 200-1000 W Beam spot diameter: 1, 1.4–2 mm Travel speed: 5, 8, 10 mm/s Wire feed speed: 10, 13, 15 mm/s	3 kW Fiber laser	Microstructures Micro-hardness Macro-structure	[93] (2021)
Ti6-Al-4V	Wire diameter: 1.5 mm Laser power: 4-6 kW Laser scanning speed: 3.5-10 mm/s Wire feed rate: 40-71.3 mm/s Hot wire power: 300 W	6 kW fiber laser	Microstructure Molten pool processing	[94] (2022)
Ti6-Al-4V	Laser scanning speed: 1-30 mm/s Laser power: 1-1.8 kW Peak temperature: 3125 K.	3 kW Fiber laser	The model of melting pool Microstructure Macro-structure	[95] (2022)
Inconel 625	Wire diameter: 1.2 mm Deposition rates: 10m/min Nitrogen flow rate: 20 L/min Deposition layer thickness:1.0–1.1 mm Laser power: 2000 W Scanning rate: 45 mm/s Wire-feeding rate: 55 mm/s Focal length: 27 mm	2 kW Fiber laser	Corrosion resistance Microstructure EBSD XRD EPMA TEM	[96] (2022)
ER2319	Wire diameter: 1.2 mm Focal length: 200 and 300 mm spot diameter: 0.3 mm Laser Power: 1900-2400 W Laser scanning speed: 1.2 m/min Wire scanning speed: 1.2 m/min	3 kW Fiber laser	Tensile Micro-hardness Macro structure Microstructure XRD EBSD Fracture morphology	[97] (2022)

1.6. Laser Arc Hybrid Wire Manufacturing (LAHWM)

Laser Arc Hybrid Wire Manufacturing (LAHWM) is a combined process that integrates the principles of WAAM and Laser Additive Manufacturing (Figure 10). In this hybrid approach, the laser serves as the primary heat source to melt the wire feedstock, while the electric arc stabilizes the melt pool, leading to higher deposition rates, improved surface finish, and enhanced mechanical performance [98, 99].

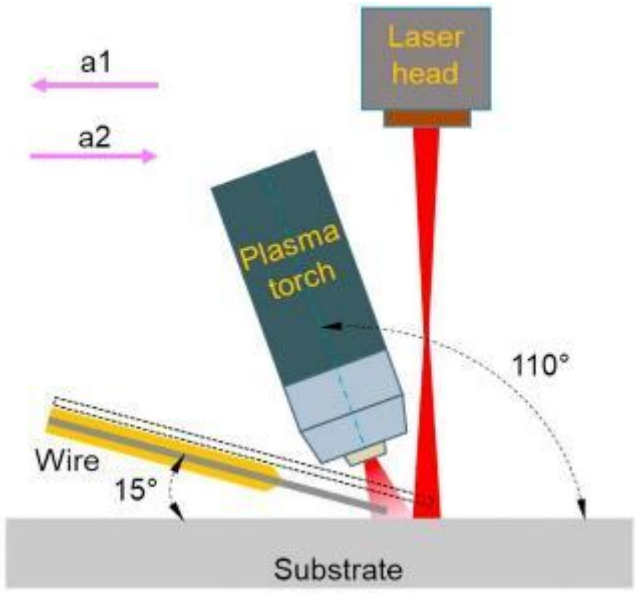

Figure 1-10. Schematic of LAHWM. Reproduced from ref. [99] with permission from *Journal of Materials Processing Technology.*

LAHWM has been successfully utilized to produce high-performance components for aerospace, automotive, and biomedical applications [100-103]. This process can handle a wide range of materials, including aluminum, titanium, and stainless steel, while offering exceptional dimensional precision and surface quality. Despite these benefits, LAHWM remains an emerging technology with challenges such as optimizing process control, minimizing residual stresses, and developing suitable post-processing techniques to further refine mechanical properties [104-106]. Nonetheless, the hybrid process shows considerable potential for delivering high-quality components in a cost-efficient and productive manner. With continued research and technological advancement, LAHWM is expected to gain greater prominence across multiple industrial sectors [103]. A summary of the latest studies is provided in Table 3.

Table 3. Summary of LAHWM research outcomes.

Materials	Input parameters	Type of laser	Tests	Ref. (year)
316L-Si Stainless steel	Laser scanning speed: 35 mm/s Wire-feed speed: 6.7 m/min Wire diameter: 1.2 mm Focal length of optics: 250 mm Focal plane diameter: 3 mm Layer height: 0.8-1.2 mm Average current: 170 A Average voltage: 18.5 V Angle of arc torch to the workpiece: 90° Angle of laser to the workpiece: 30°	3.5 kW Fiber laser	EDX Macro-image Simulation RTI	[107] 2019

ER316 L	Laser power: 2 kW Laser scanning speed: 0.3 1.2 m/min Wire-feed speed: 6 m/min Wire diameter: 1 mm Heat input: 175-289 J/mm Layer length: 160 mm Average current: 112 A Average voltage: 13.3 V Shielding gas flow rate: 25 L/min Angle of arc torch to the workpiece: 60̊ Angle of laser to the workpiece: 90̊ Laser-arc distance: 2 mm	6 kW Fiber laser	Surface accuracy Microstructure Tensile Macro-image RTI XRD EBSD Fractographies	[108] 2020
ER4043 and 6061	Laser power: 200-400 W Scanning speed: 1000 mm/min Wire-feed speed: 250 mm/min Average current: 80-160 A Average voltage: 13.3 V Wire diameter: 1.2 mm	Nd:YAG	Micro-hardness Tensile Macrostructure Backscattered image XRD Tensile	[109] 2021
ER316L	Laser power: 500-2000 W Average current: 147 A Average voltage: 14.2 V Angle of arc torch to the workpiece: 55° Angle of laser to the workpiece: 90̊ Wire-feed speed: 0.6 m/min Heat input: 259-409 J/mm Focal plane diameter: 0.4 mm Wire diameter: 1 mm	6 kW Fiber laser	Tensile Surface accuracy Macro-structure EBSD Micro-hardness	[110] 2021
Al-6Mg-0.3Sc alloy	Laser power: 750 W Focal plane diameter: 0.4 mm Angle of arc torch to the workpiece: 45° Angle of laser to the workpiece: 45° Oscillation frequency: 200 Hz Average current: 30 A Average voltage: 13.8 V wire diameter:1.2 mm	10 kW Fiber laser	Micro-hardness EBSD Tensile Microstructure Fractographies Macro-structure	[111] 2022

Expanding the predictive framework for assessing various material and mechanical properties in multilayer WAAM remains a significant challenge. Although the WAAM process has been developed and refined over recent years, obtaining a comprehensive understanding of the mechanical behavior of additively manufactured components still requires extensive investigation [16]. An advanced predictive framework would enable real-time estimation of microstructural features in printed components and facilitate direct comparisons among different WAAM techniques. To achieve this, process parameters could be dynamically adjusted in a closed-loop feedback system, aligning estimated and desired microstructural properties for optimized fabrication outcomes [67].

Future research could benefit from implementing in-situ monitoring systems that analyze the microstructure of multi-material WAAM deposits in real time. Closed-loop feedback from molten pool monitoring, both during and after solidification, would offer valuable insights into phase transformation mechanisms. Current literature on indirect process control assumes that modifying microstructural characteristics requires a deep understanding of molten pool geometry and temperature distribution, both of which are strongly influenced by

process variables. Moreover, conducting comprehensive mechanical and surface characterizations, including wear resistance, surface roughness, corrosion resistance, tensile strength, fatigue performance, and impact testing, can help correlate simulation results and experimental outcomes for process optimization [62]. Image and video analyses using high-speed cameras also provide crucial data on metal melting behavior. Such visual data can be integrated into image-processing algorithms to improve WAAM process modeling and serve as a foundation for machine learning applications in process control [57].

The molten pool region, generated by the continuous melting of the wire, is one of the most critical zones in WAAM. Due to the high deposition rate and narrow HAZ typical of laser-assisted processes, various thermal and structural defects may arise during or after deposition [65]. Integrating thermal cameras and temperature sensors can record real-time heat generation data, allowing for optimized parameter control to significantly reduce these defects [22]. An emerging and highly promising direction is the application of WAAM for biomedical and tissue engineering purposes. Using fine-diameter wires, such as magnesium-based alloys, enables precise fabrication of biodegradable structures with potential medical applications [52]. These components could serve as implants or structural reinforcements within the human or animal body, reducing the need for invasive replacements and minimizing associated healthcare costs [73]. Beyond biomedical uses, WAAM has potential applications in the electronics industry, where fine metallic wires can be selectively melted to form micro-scale conductive paths or weld delicate components, contributing to the miniaturization and enhancement of electronic devices [70]. The WAM represents a rapidly advancing technology poised to transform manufacturing practices across numerous industries. The three main WAM variants WAAM, WLAM, and WLAHM each offer distinct advantages and trade-offs. WAAM is recognized for its high deposition rate, low cost, and material flexibility.

1.7. Applications and Benefits of WAAM Across Sectors

The unique capabilities of WAAM have led to its adoption and exploration across a wide spectrum of industries. Its benefits are most pronounced in applications involving large, customized, or high-value components.

1.7.1 Aerospace and Aviation

The aerospace industry demands high-performance, lightweight components, often made from expensive materials like titanium and nickel-based superalloys. WAAM is used for:

- **Manufacturing Large Structural Components:** Fabricating large brackets, fuselage frames, and wing spars that would be difficult and wasteful to machine from a solid forging [46, 47].
- **Repair and Refurbishment:** One of the most economically compelling applications is repairing worn or damaged parts, such as turbine blades and engine casings. WAAM can be used to add material precisely to the damaged area, which is then machined back to specification, extending the component's life at a fraction of the replacement cost [1, 3].

Benefit: WAAM enables significant cost savings and reduced lead times for producing and maintaining large, complex aerospace parts, while also minimizing material waste.

1.7.2 Automotive and Transportation

In the automotive sector, WAAM is explored for:

- **Rapid Prototyping of Large Tools and Dies:** Manufacturing large stamping dies and molds directly from CAD data, accelerating development cycles [30].
- **Customized Components:** Producing bespoke parts for luxury vehicles, racing cars, or heavy-duty machinery.

Benefit: WAAM provides design flexibility and agile manufacturing for prototypes and low-volume production runs, avoiding the high cost and long lead times of traditional tooling.

Chapter 2

WAAM Investigation on AISI 308L Stainless Steel Wire Feeder Rate

Chapter 2

WAAM Investigation on AISI 308L Stainless Steel Wire Feed Rate

2.1. Materials and Equipment

In this study, AISI 308L stainless steel wire with a 1 mm diameter was utilized for the WAAM process. Its chemical composition is listed in Table 1. High-purity argon gas (99.9999%) served as the shielding medium to enhance arc stability and minimize the formation of defects such as porosity. Once the desired voltage and current were selected in the generator, the PC controller initiated the process using CAD-based programmed paths. Each deposition track measured 10 cm in length, built upon a 10 mm-thick low-alloy steel substrate. The substrate was securely clamped to prevent distortion induced by the high temperatures of the molten pool. Since the deposition mode was Cold Metal Transfer (CMT), the material was deposited in a semi-solid state, allowing for controlled cooling between layers. This resulted in crack- and waviness-free beads, though a minor surface roughness was still observed on the upper layers.

Table 1. Chemical composition of AISI 308L wire (wt. %).

Elements	C	Cu	Ni	Cr	Si	P	Mo	Mn	Fe
%	0.02	0.75	10.00	20.15	0.45	0.02	0.4	1.5	Bal.

The key process parameters included wire feed rates (WFR) between 3.5–7.0 m/min, currents from 72–115 A, and voltages between 11.1–12.6 V. Table 2 summarizes the operating parameters and the corresponding bead geometries for the eight fabricated samples, characterized at 2× magnification using the MS/SFX Series instrument.

Table 2. Process parameters and geometric characteristics of AISI 308L deposited beads.

	Voltage (V)	Current (A)	Power (W)	WFR (m/min)	Width (mm)
#1	11.1	72	799	3.5	2.9
#2	11.2	78	874	4.0	3.8
#3	11.3	85	961	4.5	4.2
#4	11.3	92	1040	5.0	5.1
#5	11.4	99	1129	5.5	5.3
#6	11.8	104	1227	6.0	5.6
#7	12.2	110	1342	6.5	5.9
#8	12.6	115	1449	7.0	6.2

2.2. Microstructural Characterization

Microstructural investigations were carried out using a Carl Zeiss Merlin SEM (Jena,

Germany) coupled with an Oxford Instruments INCA-350 EDX detector (Abingdon, UK). Additional surface and cross-sectional analyses were performed with an Olympus LEXT OLS3000 optical microscope (Tokyo, Japan). For optical microscopy, specimens were etched using Carpenter's reagent (a mixture of ferric chloride, cupric chloride, alcohol, hydrochloric acid, and nitric acid) following ASM standards [112]. Prior to SEM examination, the cross-sections were etched in Nital for 10 s and rinsed immediately with distilled water. Backscattered electron imaging (BSE) was employed to identify microstructural phases and detect any process-induced defects. Figure 1(a) displays the optical micrographs, Figure 1(b) depicts the deposition direction and track arrangement, and Figure 1(c) outlines the bead geometry and oxide layer region used for oxidation analysis.

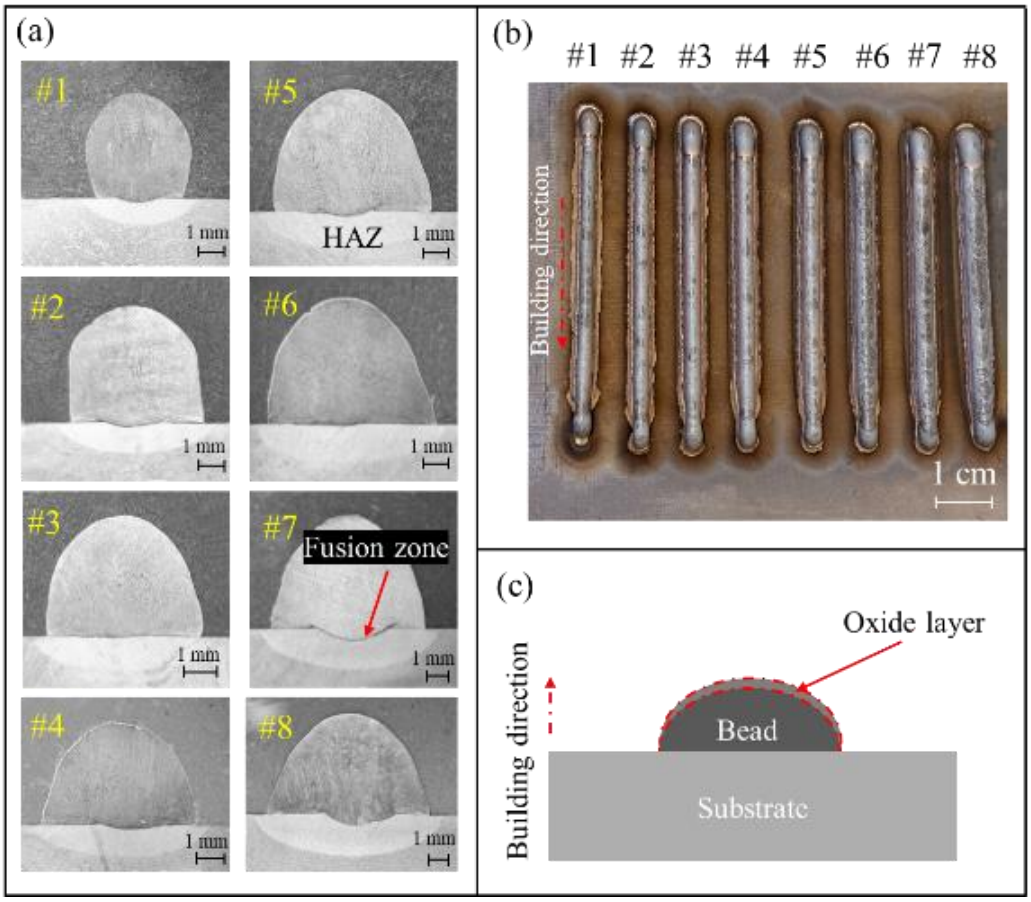

Figure 2-1. (a) Optical micrograph of WAAM cross-section, (b) deposition path and orientation, (c) geometry of deposited beads.

For Electron Backscatter Diffraction (EBSD), a TESCAN AMBER X microscope was used at a 70° tilt angle. Analyses covered regions spanning the substrate boundary through the deposited beads to examine grain morphology and phase transitions. Energy Dispersive X-ray (EDX) measurements were also obtained from various regions, substrate interface, mid-bead, and bead peaks, to evaluate elemental diffusion. ATEX software was used to

derive inverse pole figure (IPF) maps and grain size distributions.

2.3. Microstructural Analysis

Figure 3 compares SEM micrographs of samples #8 and #1, which correspond to the highest and lowest process parameter values, respectively. δ-ferrite (appearing white) is clearly visible in all regions. In Figures 2(a, d), corresponding to the right sides of the deposited beads, sample #8, with its smaller bead width (2.9 mm) and lower cooling rate, shows a greater fraction of austenite compared to sample #1, whose bead width exceeded 6 mm. In the mid-sections (Figures 2b and 3e), chromium segregation within δ-ferrite was observed due to differential diffusion during solidification. The composition and cooling conditions largely govern the solidification mode and final phase distribution, determining the δ-ferrite morphology at room temperature. Figures 2(c, f) illustrate that the CMT thermal cycle strongly influences the diffusion-controlled δ→γ transformation. In austenitic stainless steels produced via AM, δ-ferrite nucleates at interdendritic boundaries during solidification. Owing to the lower diffusion rate in FCC austenite compared to BCC ferrite, steep elemental segregation gradients occur [113].

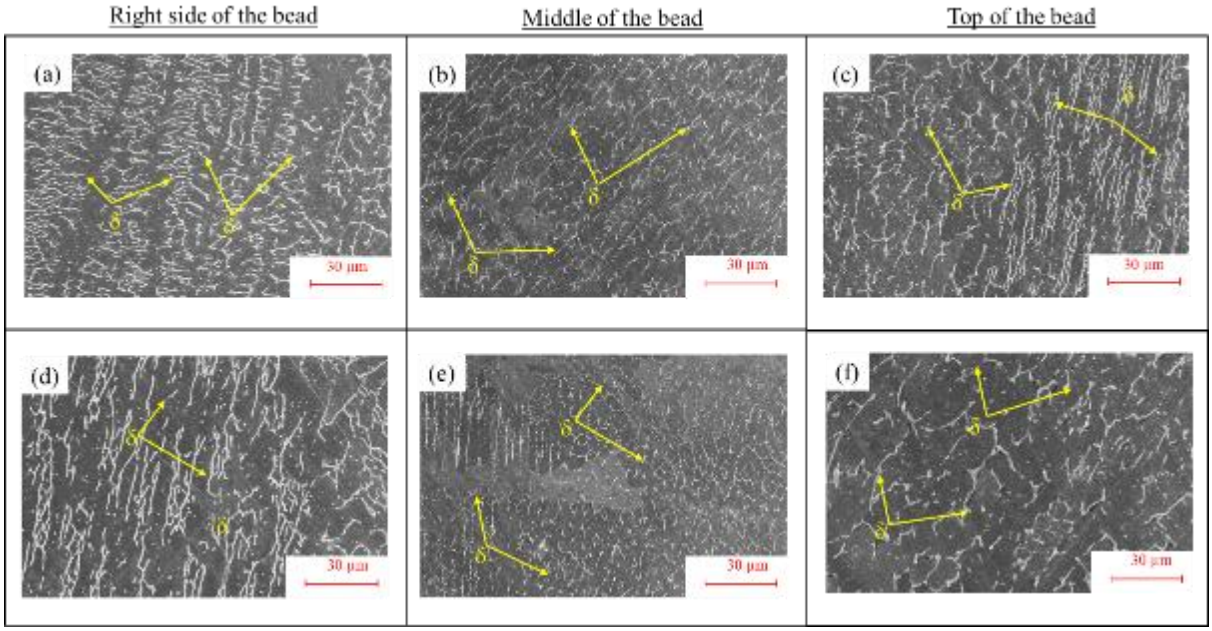

Figure 2-2. SEM micrographs of AISI 308L WAAM deposits for (a–c) sample #8 and (d–f) sample #1. a) the right side of the deposited bead sample #8, b) the Middle of the deposited bead sample #8, c) the Top of the bead's peak of sample #8 (Voltage=12.6 V, Current=115 A, and feeder rate= 7 m/min), d) the right side of the deposited bead sample #1, be the middle of the deposited bead sample #1, and f) top of the bead's peak of sample #1 (Voltage=11.1 V, Current=71 A, and feeder rate= 3.5 m/min).

To further assess fusion quality, the dilution zone of sample #4 was examined (Figure 3). The EDS spectra in Zone 1 (Figures 3a–b) reveal high chromium concentrations, indicating ferrite-rich regions. In contrast, Zone 2 (Figures 3d–e) near the base metal interface showed

negligible chromium peaks, confirming dominance of the low-alloy steel substrate within this region.

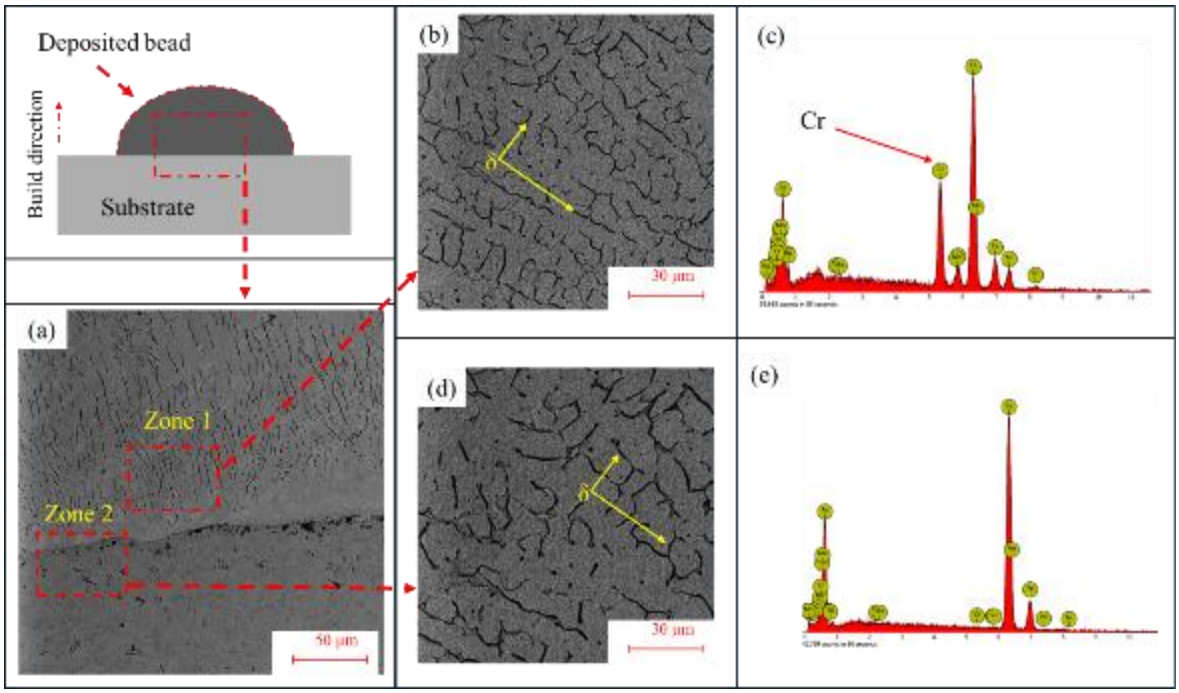

Figure 2-3. EDS elemental mapping of sample #4 (V=11.3 V, I=92 A, WFR=5 m/min). a) Large scale of the EDS target zones, b) Middle of the sample, c) Elements distribution diagram, d) boundary of the deposition and base metal e) Elements distribution diagram for the boundary of the deposition and base metal.

The substrate exhibited a ferrite–pearlite microstructure. As shown in Figure 4(a–g), the HAZ directly below the fusion boundary displayed finer grains than the base metal. Columnar austenitic dendrites grew along the heat flow direction (Figure 4b–c), while the center of the fusion zone showed a transition microstructure. Regions farther from the fusion boundary possessed coarser grains, confirming the gradient in thermal exposure.

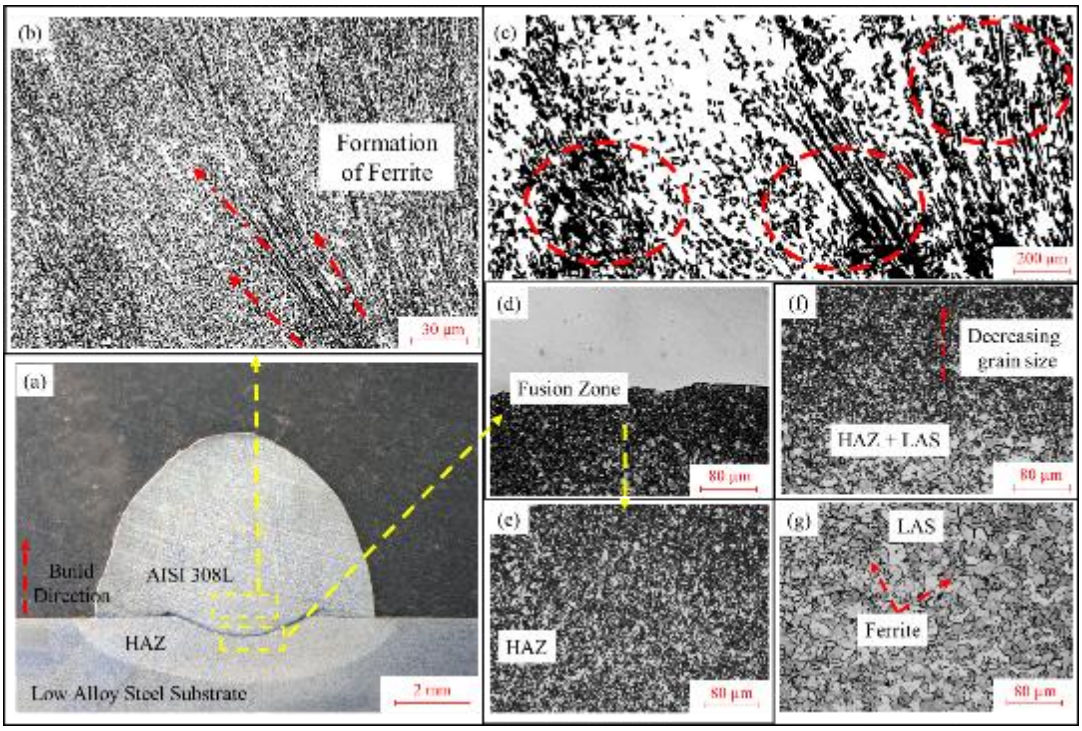

Figure 2-4. Microstructural evolution in the substrate and HAZ of AISI 308L WAAM layers. a) Defined the zones b) microstructure of AISI 308L on top of the boundary c) Massive distribution of δ ferrite d) The boundary between fabricated layer and substrate e) HAZ of the substrate f) HAZ and LAS boundary g) base metal microstructure.

2.4. Surface Roughness

A smooth deposition surface is essential in WAAM to prevent voids, gaps, or porosity between subsequent layers. The peaks of each bead, acting as nucleation points for the next track, were analyzed via laser profilometry, using Ra as the response parameter. Figure 5(a) presents the Ra values for all eight samples, while Figure 5(b) compares arc signal patterns of samples #1 and #8. The longer arc-on period in sample #8 enabled greater metal transfer per pulse, producing wider, more uniform beads. Figure 6 demonstrates that surface roughness inversely correlates with current, higher current (115 A) produced the lowest Ra (~20 µm) for AISI 308L.

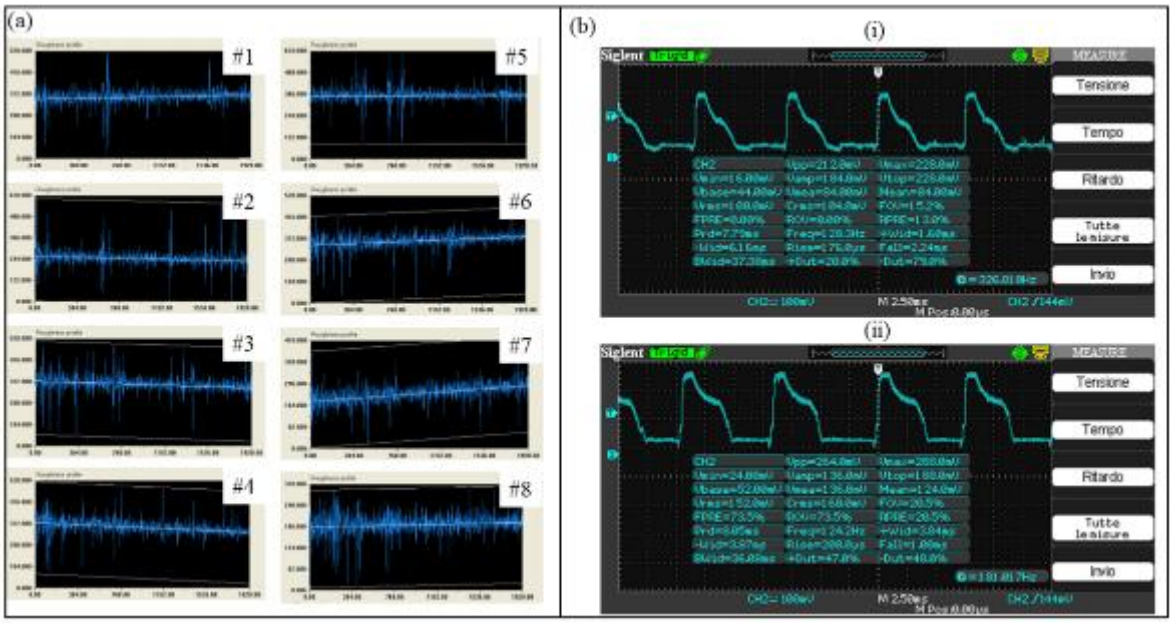

Figure 2-5. (a) Surface roughness results; (b) arc signal comparison for samples #1 and #8.

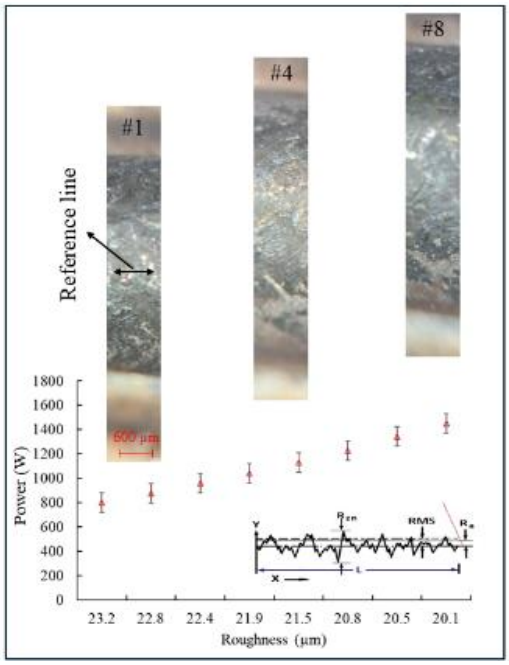

Figure 2-6. Roughness trends across fabricated WAAM samples.

2.5. Microhardness

Due to the non-uniform cooling paths and heat dissipation into both the substrate and ambient air, the grain morphology varied along the bead height. Near the fusion boundary, finer grains formed, while coarser grains were observed toward the bead top. EBSD analysis of sample #4 (Figure 7) confirmed deposition alignment along the <111> crystallographic direction. The grain size mapping revealed a gradual refinement from ~13–14 µm near the substrate to ~5–6 µm within the deposited bead. Due to Figure 8, microhardness peaked at the fusion center (290–310 HV) and decreased toward the bead edges (250–260 HV). This

defect-free bonding between substrate and deposited metal demonstrates the suitability of CMT-WAAM for repairing or reinforcing components.

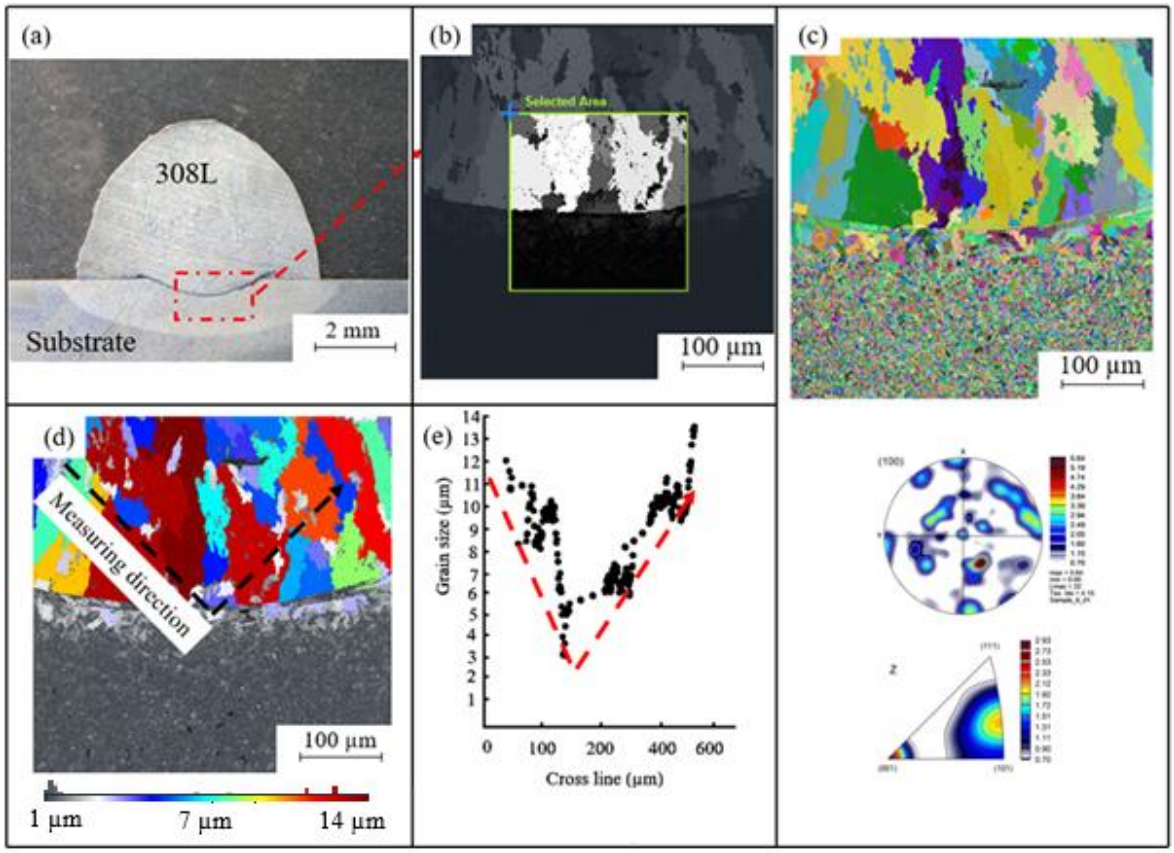

Figure 2-7. EBSD and grain size analysis of sample #4. a) EBSD selection area b) Fixed area of EBSD c) IPF image and pole figure from deposited bead and LAS substrate d) Map of the grain size by the V direction e) graph of the grain size from V direction.

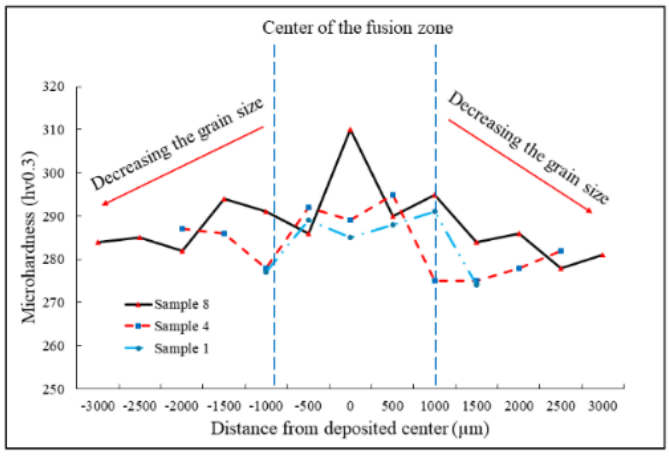

Figure 2-8. Microhardness distribution for samples #1, #4, and #8.

2.6 Oxide Layer and Process Defects

Oxidation of bead peaks is a critical factor in WAAM, as oxides can entrap within subsequent layers and compromise mechanical integrity. During deposition, oxide films from the substrate surface may detach and mix with the molten pool, eventually accumulating

near bead summits. Using the FIB technique, sample #5 was examined to characterize this oxidation layer (Figure 9). After trenching and platinum deposition, a 945 nm-thick oxide layer was observed (Figure 9-f). EDS results (Figure 9-g) indicated chromium enrichment, suggesting that corrosion resistance remained largely preserved post-solidification.

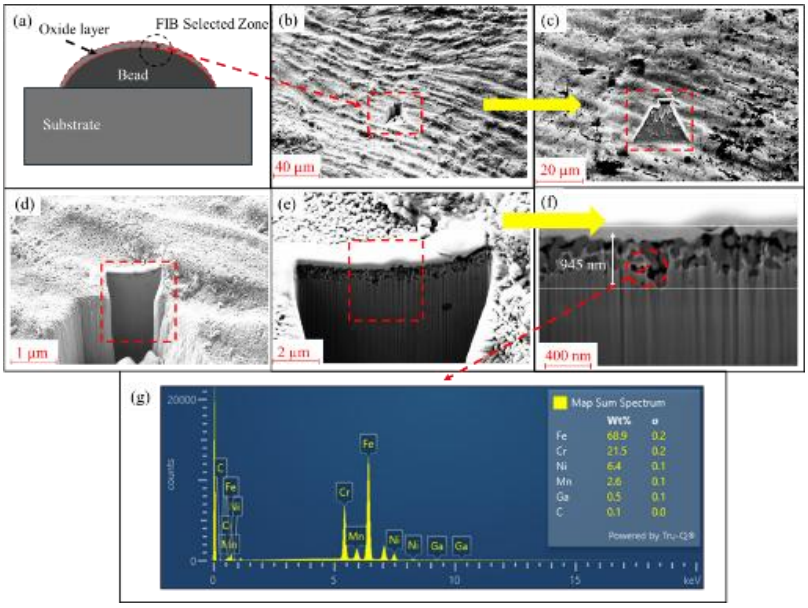

Figure 2-9. FIB and EDS characterization of the oxide layer in sample #5. a) Schematic of the selected zone for FIB analysis b) surface processing selection by FIB c) FIB removal of the AISI 308L SS, d) platinum deposition e) selecting the area for analysis f) Oxid layer height and EDS selection g) EDS analysis from red zone in Figure d.

Further FIB analysis of sample #1, fabricated at the lowest wire feed rate, revealed micropores (105–271 nm) localized at bead peaks (Figure 10). Elemental mapping confirmed these voids as non-material regions, i.e., true pores. Such porosity was exclusive to low-parameter samples, reinforcing the importance of optimized current and feed rate to ensure defect-free WAAM deposits.

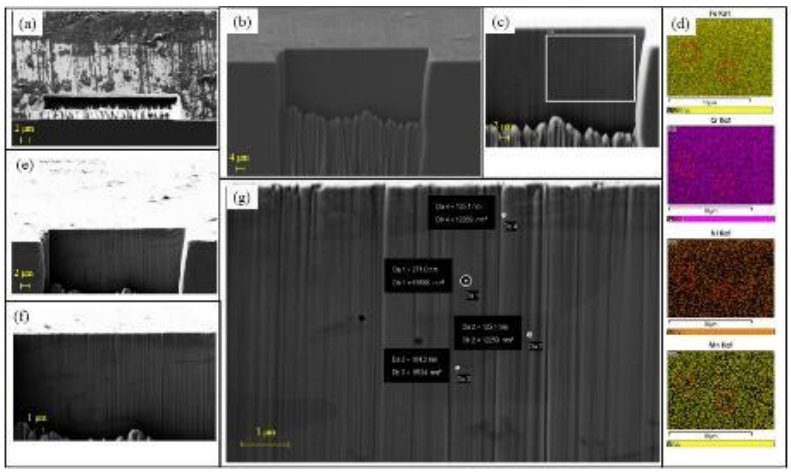

Figure 2-10. FIB examination of pores on sample #1. a) Top view of the FIB analysis b) front view of the FIB area c) Selecting zone for Map analysis d) Map of the elements e) backscattered of the FIB area f) Selecting zone g) porosities dimensions.

Chapter 3

WAAM Investigation on ER70S-6 Wire Feed Rate

Chapter 3

WAAM Investigation on ER70S-6 Wire Feeder Rate

3.1. Material Fabrication

In this study, ER70S-6 low-alloy steel wire with a diameter of 1 mm was employed to fabricate WAAM specimens on a St 37 steel substrate. The system was computer-controlled, and sample geometries were generated using reference code programming (Figure 1-a). The chemical compositions of both the ER70S-6 wire and substrate are listed in Table 1.

Table 1. Chemical composition of ER70S-6 wire and substrate plate (wt.%)

Element	Fe	C	Cu	Mn	Si	P	S	Ni	Cr	V	Nb	Ti	S
Wire: ER70S-6	Bal.	0.15	0.2	0.9	-	0.035	0.04	0.2	0.15	0.008	0.008	0.025	-
Substrate: St37 steel	Bal.	0.16	-	0.35	0.18	-	-	-	-		-	-	0.05

Process parameters summarized in Table 2 included a wire feed rate of 4.5–6.5 m/min, a current of 125–167 A, and a voltage of 14.8–16.5 V. A total of five specimens were produced using the WAAM system (Figure 1-b) at a constant travel speed of 7 m/min. Each deposition track measured 100 mm in length.

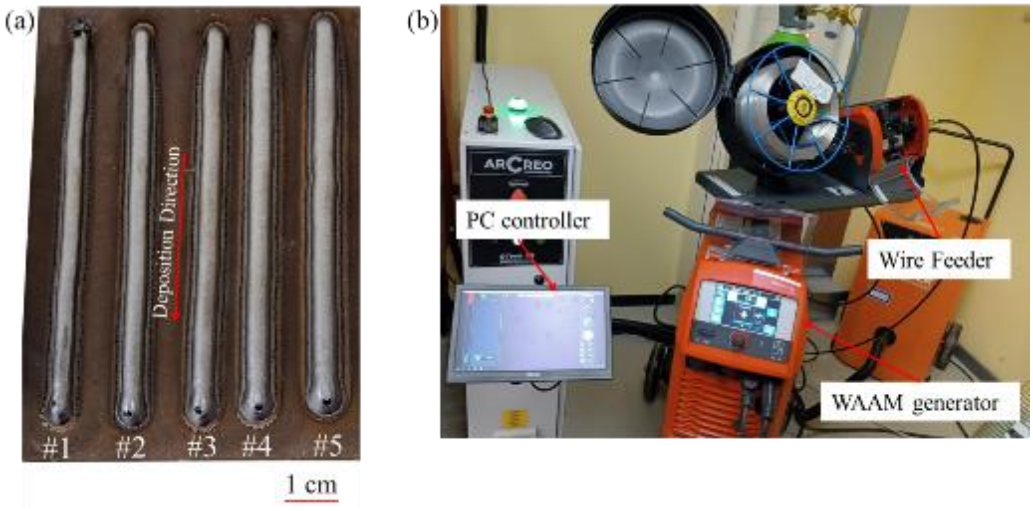

Figure 3-1. (a) WAAM setup used in this study; (b) single-bead WAAM samples.

Table 2. Process parameters for Wire Arc Additive Manufacturing of St 52 low-alloy steel

Sample Number	Wire feeder (m/min)	Current (A)	Voltage (V)	Robot Speed (m/min)	Bead's Width (mm)
#1	4.5	125	14.8	7	5.25
#2	5	135	15.1	7	5.97
#3	5.5	145	15.4	7	6.33
#4	6	155	15.7	7	6.89
#5	6.5	159	16.0	7	7.32

3.2. Characterization Method

Microstructural evaluation was conducted using a Carl Zeiss Merlin SEM (Jena, Germany) equipped with an Oxford Instruments INCA-350 EDX system (Abingdon, UK). Additionally, an Olympus LEXT OLS3000 confocal microscope (Tokyo, Japan) was used for optical observation. For optical microscopy, specimens were etched with 5% Nital (a solution of 5 vol% nitric acid in 95 vol% ethanol) in accordance with standard metallographic procedures. The etched cross-sections were immersed in the reagent for 10 s, then rinsed thoroughly with distilled water and acetone. SEM analyses employed secondary and backscattered electron imaging to reveal microstructural morphology. For Electron Backscatter Diffraction (EBSD), a TESCAN AMBER X system was used at a 70° tilt angle to examine grain orientation near the substrate-deposit interface. Energy Dispersive X-ray Spectroscopy (EDX) measurements were performed on the fusion boundary, intermediate zones, and bead peaks to assess elemental diffusion across these regions. Microhardness measurements were carried out using a DuraScan G5 universal tester (EMCO-TEST Prüfmaschinen GmbH, Austria) under a 200 g load applied for 15 s per indentation. Indentations were made at 500 μm intervals along the cross-section to evaluate hardness gradients across the substrate–deposit interface.

3.3. Microstructure

Figure 2 shows cross-sectional views of the ER70S-6 WAAM deposits, illustrating the overall morphology and the regions analyzed for microstructural evaluation. The examined zones included the fusion interface, bead boundary, and HAZ, which were also subjected to EBSD and microhardness analyses. During the CMT-WAAM process, the ER70S-6 wire melted and solidified on the low-alloy steel substrate. The cooling rate and heat transfer into the substrate and surroundings strongly influenced the resulting microstructure [114].

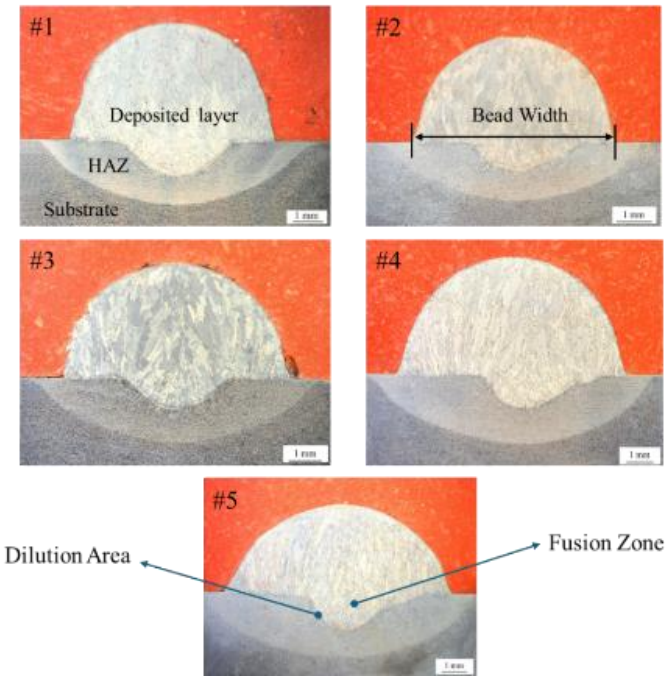

Figure 3-2. Cross-sections of WAAM-fabricated ER70S-6 samples (#1–#5).

As the molten ER70S-6 cooled, austenite transformed into ferrite and pearlite, while slower cooling promoted the formation of Widmanstätten ferrite (Figure 3-b), a plate-like structure that develops along specific austenite planes [115]. Carbide precipitation occurred during cooling, particularly at grain boundaries or within ferrite matrices [116], enhancing hardness and wear resistance (Figure 3-c). The dilution zone between the deposited metal and the substrate is critical, as it governs metallurgical bonding and elemental redistribution. The high temperature gradient during cooling promotes Widmanstätten ferrite nucleation, which may grow into the substrate because of the compositional differences between ER70S-6 and St 37 steels [117, 118]. This microstructure affects mechanical performance: although Widmanstätten ferrite increases strength and hardness, its coarse plate morphology can act as a crack initiation site, reducing toughness and ductility [119, 120]. The cooling rate also affects grain size and phase morphology. Faster cooling produces finer ferrite and pearlite grains, improving mechanical strength via the Hall–Petch effect [121, 122]. Conversely, slow cooling favors coarser structures and non-uniform phase distribution.

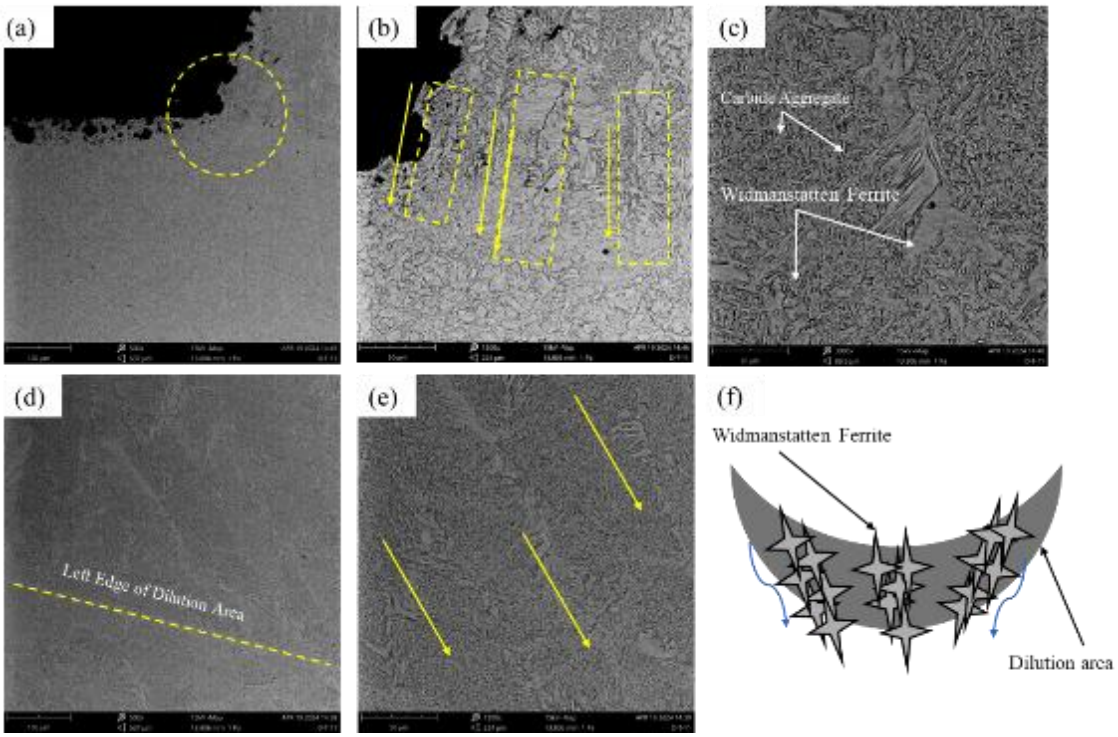

Figure 3-3. Interface between deposited ER70S-6 and St 37 substrate (WFR = 5.5 m/min; I = 145 A; V = 15.4 V; travel speed = 7 m/min): (a) 500× macro view; (b) Widmanstätten ferrite plates; (c) carbide aggregates; (d–f) edge and schematic of ferrite formation.

Figure 4 presents the microstructure of sample #2, showing penetration of the molten zone into the substrate and microstructural variations across the bead height. The substrate exhibited a concave profile post-deposition (Figure 4-a). Finer microstructures were observed at the bottom and edges of the bead (Figures 4-b,c) due to faster heat dissipation, whereas coarser grains formed at the top (Figures 4-d–f) because of slower cooling [123, 124]. While higher heat input can refine grains and enhance hardness, excessive thermal energy may cause grain coarsening or phase transformations detrimental to mechanical properties [125, 126].

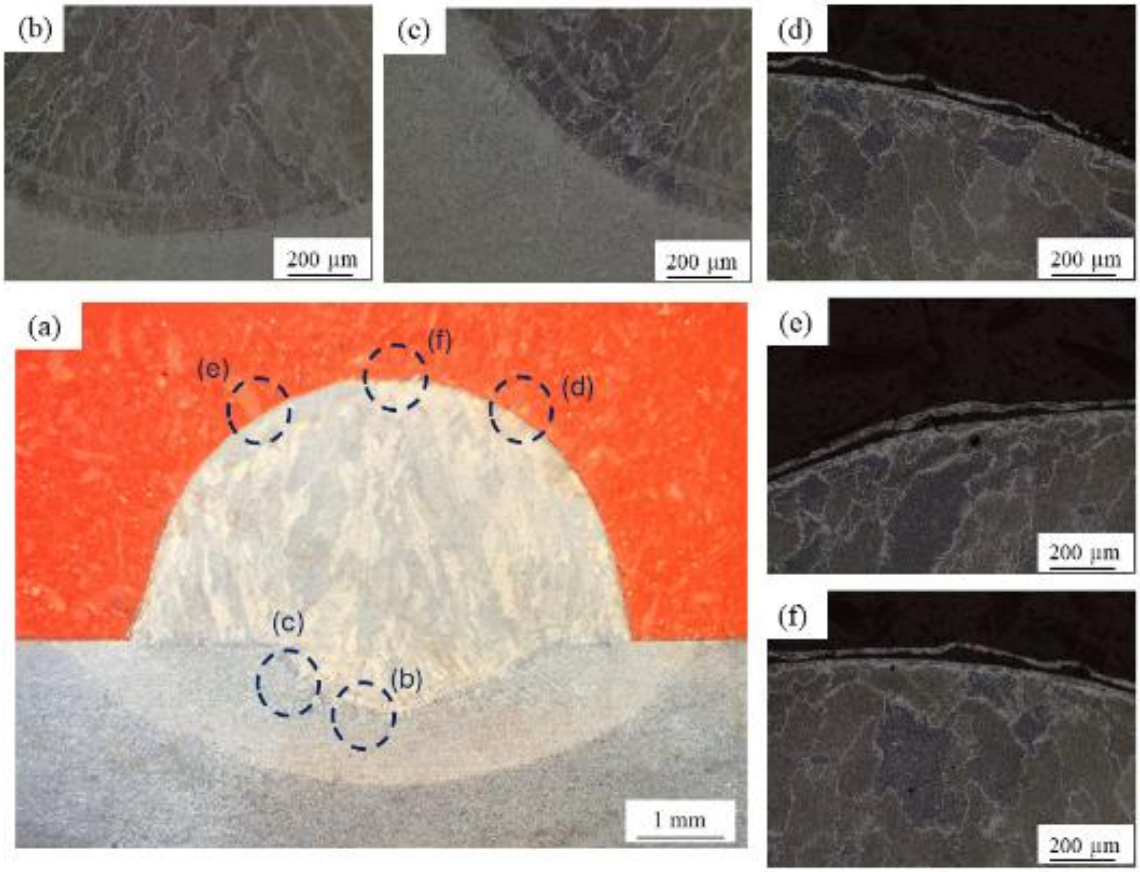

Figure 3-4. Microstructure of sample #2: (a) macrostructure; (b,c) dilution zone; (d–f) upper bead regions.

At the bead peaks (Figure 5-a), significant Widmanstätten ferrite (~20 %) was detected (Figure 5-b), attributed to slower cooling at the top surface [127, 128]. This phase improves strength and interlayer bonding for subsequent depositions [129]. Wire feed rate notably influences bead geometry and HAZ width. At 4.5 m/min, the bead width was 5.25 mm with a smaller HAZ and coarser microstructure. Increasing the rate to 6.5 m/min expanded the bead width to 7.32 mm and produced finer columnar dendrites, yielding microhardness values near 300 ± 15 HV [115]. The angle of Widmanstätten ferrite plates also varied from ~75° at 4.5 m/min to ~63° at 6.5 m/min, indicating faster solidification in narrower beads [34, 36, 39]. XRD patterns (Figure 5-d) revealed ferrite (α-Fe) peaks at ~44.5°, 65°, and 82° (BCC, ICDD 00-006-0696) for sample D-5-4, while sample #2 showed additional austenite (γ-Fe, FCC, ~50°, ICDD 00-033-0397) peaks, signifying retained austenite caused by slower cooling. Sample #4 displayed broader peaks from overlapping α-Fe/γ-Fe phases, suggesting Widmanstätten ferrite formation [130, 131]. These findings confirm that heat input and cooling rate strongly dictate phase composition and stability in WAAM-processed steels [132, 133].

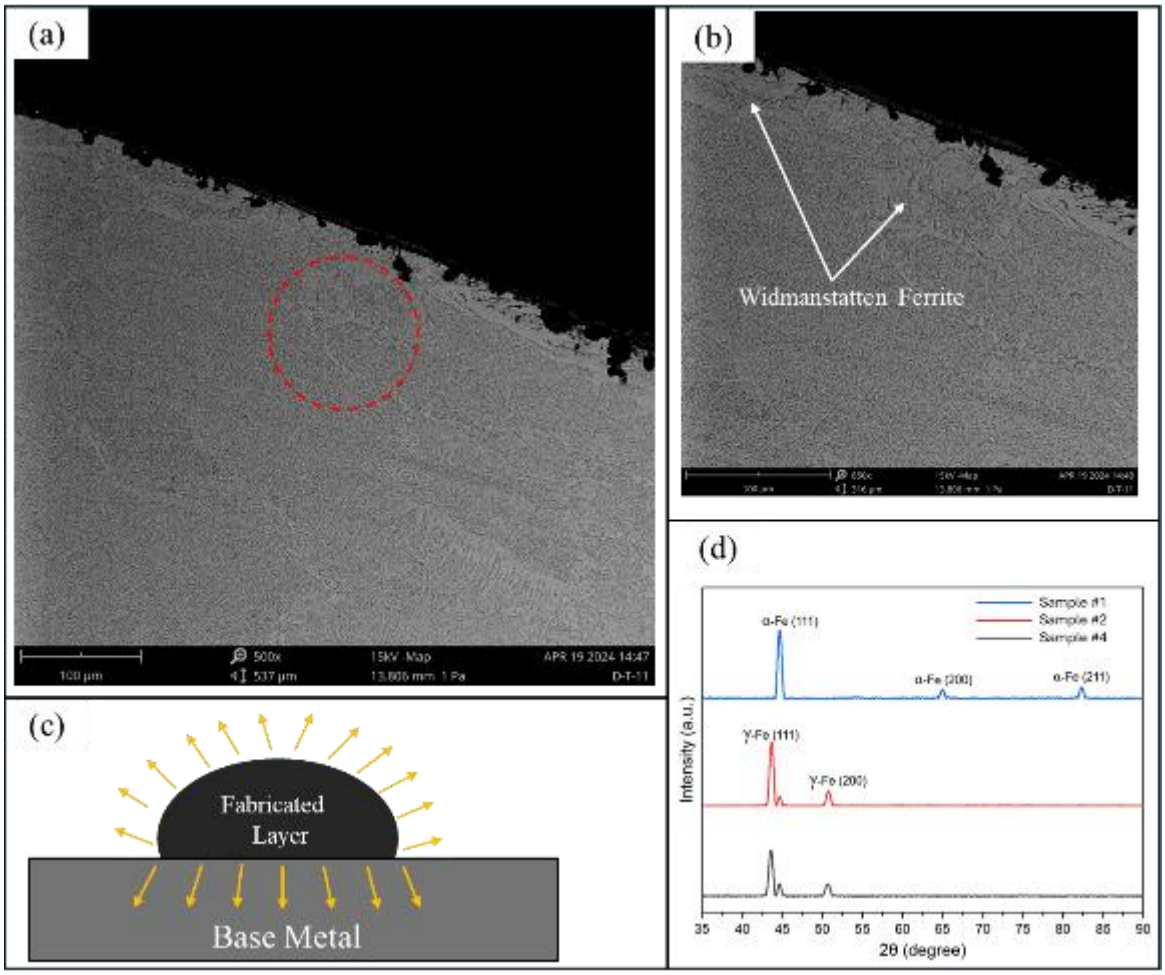

Figure 3-5. Peak microstructure of sample #2: (a) top-right region; (b) Widmanstätten ferrite; (c) cooling schematic; (d) XRD patterns of samples #1, #2, and #4.

3.4. Microstructure Influence on Microhardness

Figure 6 displays the Vickers microhardness profiles of samples #1–#5, highlighting hardness variations across the substrate, HAZ, and deposited region. Indentations (200 g load, 15 s dwell, 500 µm spacing) revealed that hardness increased from the substrate upward into the HAZ and deposited layer. Figures 7(a–c) show that the upper HAZ contained finer grains, consistent with the elevated hardness in this region. A higher wire feed rate (6.5 m/min) deposited more material per pass, creating a broader 8.5 mm melted zone and an expanded 7.4 mm HAZ, compared to 4.5 m/min in sample #1. Wetting angles decreased from 94° (sample #1) to 65° (sample #4), producing smoother bead transitions and more uniform cooling. This refined microstructure within the dilution region significantly enhanced hardness and structural stability [134, 135].

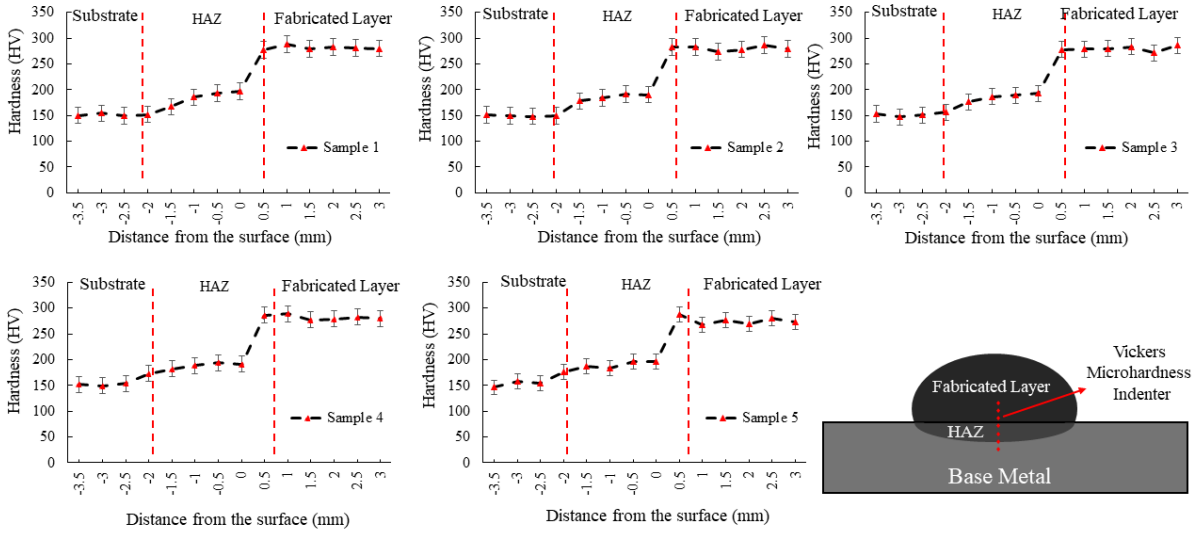

Figure 3-6. Vickers microhardness profiles for WAAM samples #1–#5.

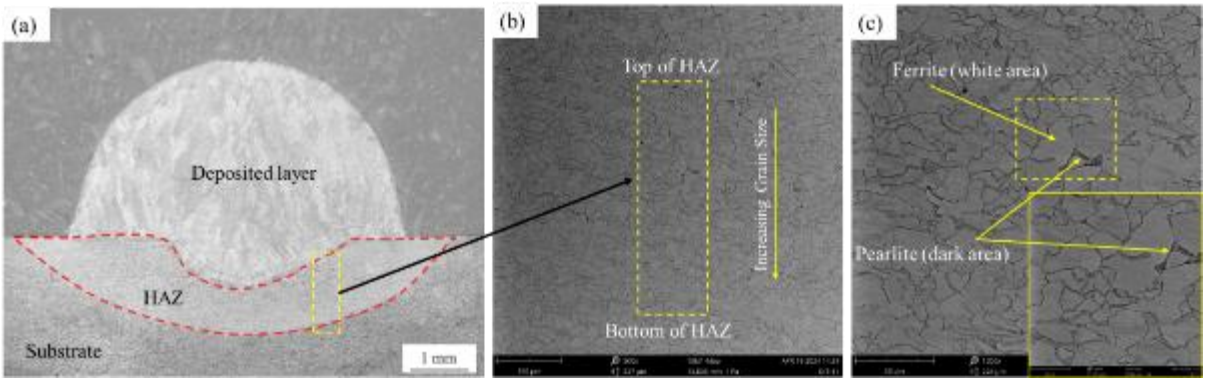

Figure 3-7. (a) HAZ analysis area; (b) microstructure near HAZ; (c) 3 k× magnified view showing fine grains.

EBSD analysis of sample #5 (Figure 8-a) fabricated at 6.5 m/min, 159 A, and 16 V, confirmed grain refinement within the dilution zone. The average grain size decreased from 8.6–11.6 µm to 3–5.6 µm, representing up to 210 % refinement near the substrate interface. Grain coarsening toward the surface (Figure 8-b) reflects reduced thermal gradients at the upper regions. Microhardness results from zones P1 and P2 (Figure 8-c) showed similar hardness to the substrate in localized areas, implying partial substrate entrapment within the fusion boundary during deposition. Dislocation mapping (Figure 8-d) and interface morphology (Figure 8-e) indicate strong substrate–deposit interactions, especially in high-deposition-rate conditions. At the P1/P2 interface (Figure 9-a), limited plastic deformation was observed, consistent with cold-substrate bonding and Widmanstätten ferrite formation at the interface. EDS results revealed Mn content of 1.86 % near the substrate and 1.43 % at the interface, confirming elemental redistribution between ER70S-6 and the base steel during solidification.

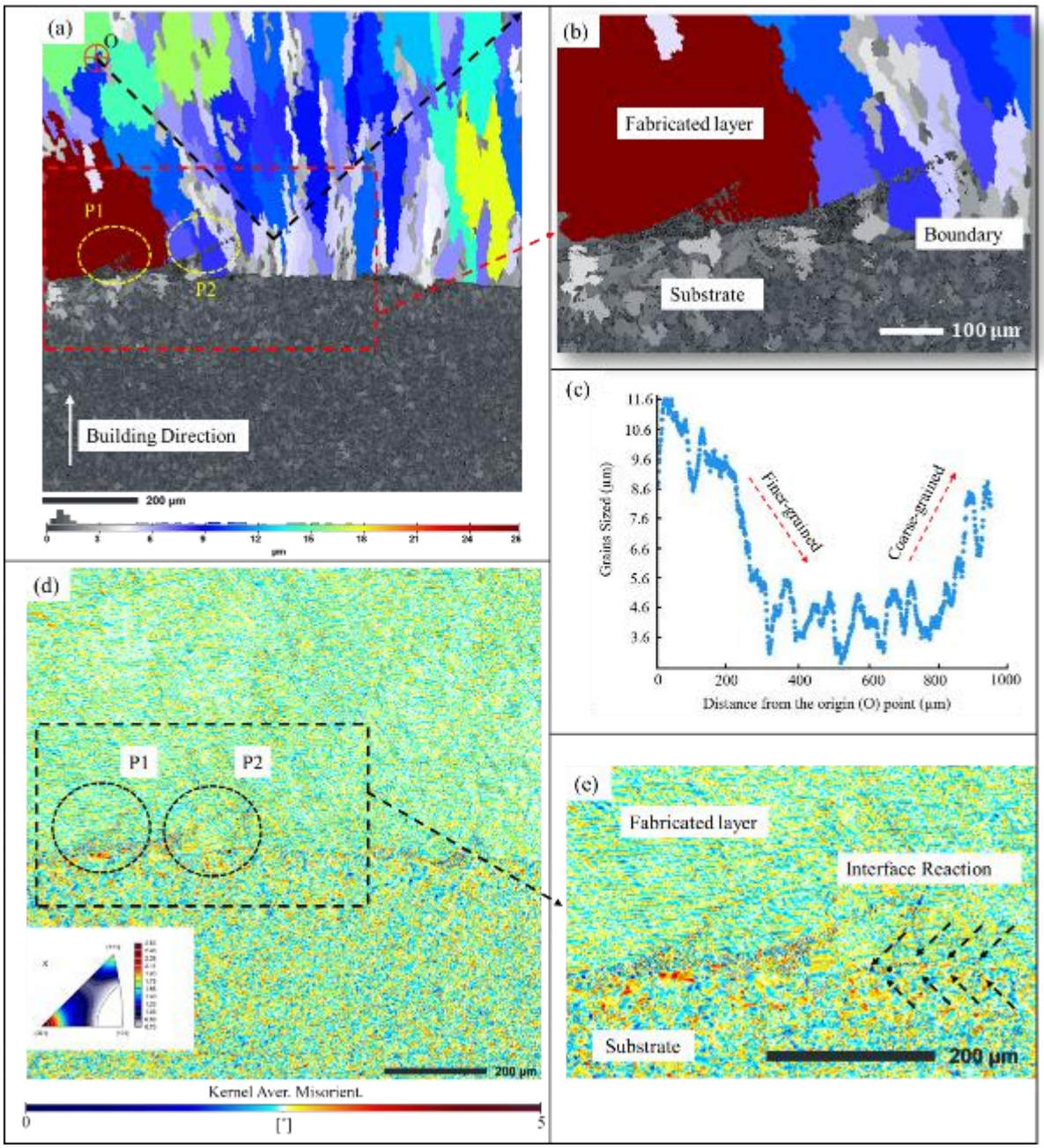

Figure 3-8. (a) EBSD grain map of sample #5 (V direction); (b–c) grain distribution; (d) dislocation density map; (e) substrate–deposit interface.

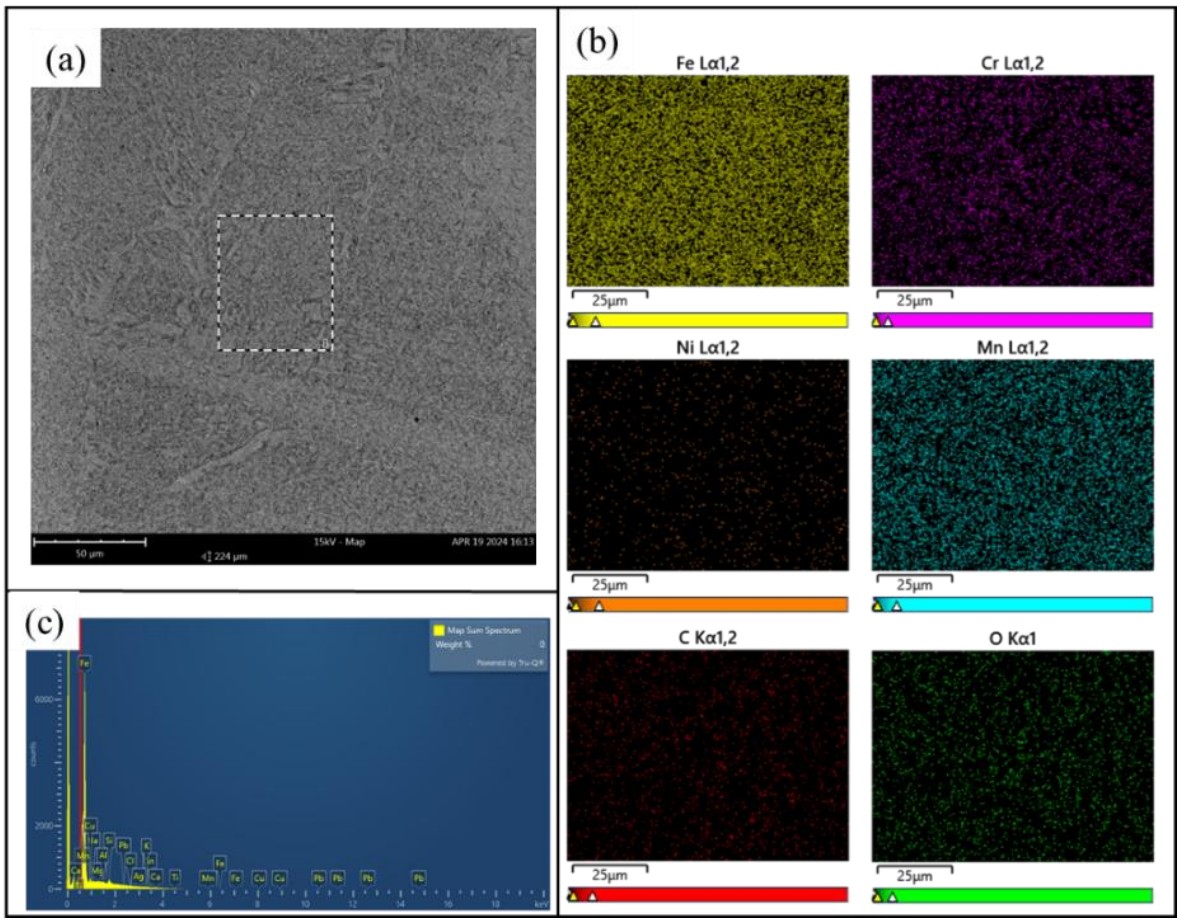

Figure 3-9. (a) EDS of P1; (b) EDS 50 µm below joint; (c) elemental maps of bead/substrate boundary.

3.5. Interface EBSD Analysis

Figure 10 presents the EBSD inverse pole figure (IPF) map for sample #5, illustrating grain orientation at the substrate–deposit boundary. Rapid surface cooling led to columnar grain alignment along the Z-axis. When the molten ER70S-6 contacted the substrate, partial melting and intermixing occurred, producing a hybrid zone of ER70S-6 + St 37. Upon air cooling, ferrite phases developed along the Y-direction, enhancing the mechanical stability of the first deposited layer. EBSD–EDS correlation also showed an increase in Mn concentration at the dilution interface, which likely improves hardenability. Microhardness tests confirmed that the high-temperature exposure transformed ST37 austenite into ferrite upon cooling, consistent with TTT diagram predictions.

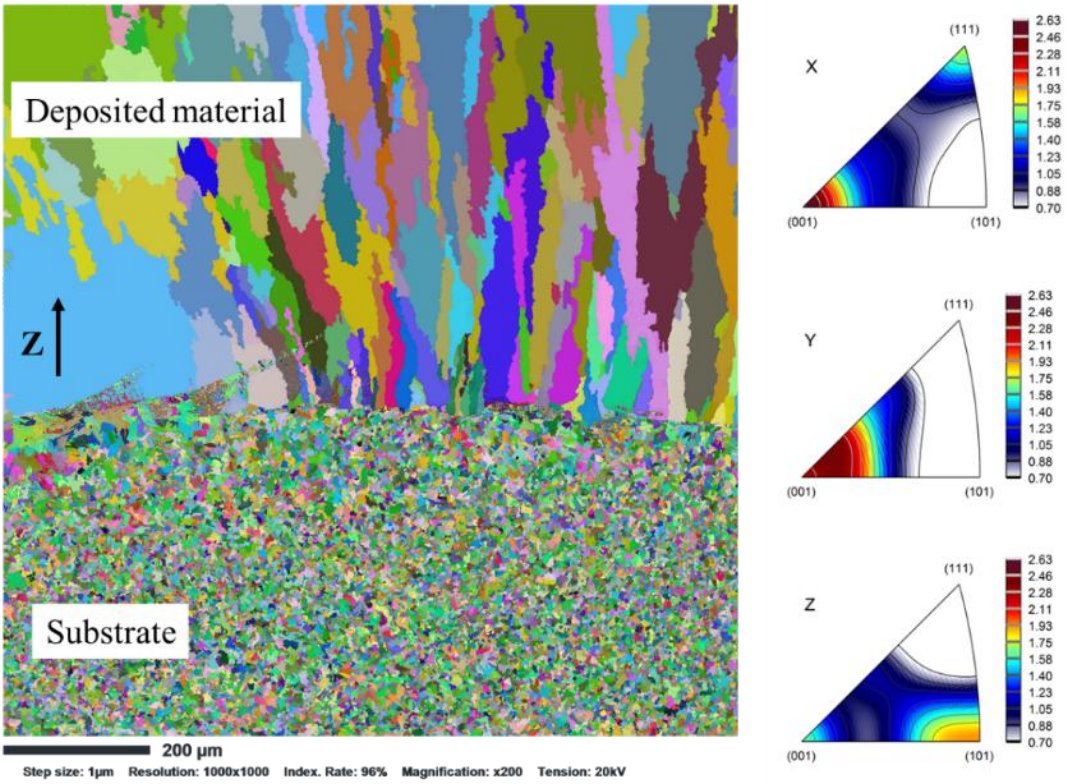

Figure 3-10. EBSD inverse pole figure map of WAAM-fabricated ER70S-6 sample #5.

Chapter 4

Numerical Modeling of WAAM Fabrication of AISI 308L Stainless Steel

Chapter 4

Numerical Modeling of WAAM Fabrication of AISI 308L Stainless Steel

4.1. Deposition Strategy

In this study, nine single-string, single-layer AISI 308L stainless-steel beads were deposited onto ST37 steel substrates under varying process conditions. The feedstock material was supplied in wire form with a diameter of 1.2 mm. The experimental parameters were defined based on a Design of Experiments (DOE) approach using a full factorial plan (2^3) that incorporated two main factors: deposition speed and arc power. The arc power (P) was calculated as the product of the current (I) and voltage (U), as described by Equation (1):

$$P = U \times I \tag{1}$$

Each input factor was examined at three levels, as detailed in Table 1. Consequently, the full factorial plan yielded nine experimental runs, each characterized by a unique combination of deposition speed and arc power (Table 2). The selected process parameter ranges were determined from preliminary trials and aligned with the equipment manufacturer's recommendations to ensure process stability, minimize bead discontinuities, and avoid excessive spatter formation. To ensure experimental repeatability, each deposition condition was replicated three times. Other parameters remained constant throughout all trials, specifically, a wire feed rate of 7 m/min was maintained.

Table 1. Full factorial design of experiments (DOE) for the WAAM process.

	Levels		
factors	**-1**	**0**	**1**
Deposition speed v_r [mm/s]	5	7	9
Arc power P [W]	875	1230	1700

Table 2. WAAM processing parameters used in the study.

	Specimen								
	1	**2**	**3**	**4**	**5**	**6**	**7**	**8**	**9**
Deposition speed v_r [mm/s]	5	5	5	7	7	7	9	9	9
Arc power P [W]	875	1230	1700	875	1230	1700	875	1230	1700

The deposition process was carried out using a Cold Metal Transfer (CMT) system (Fronius, Austria) integrated with a collaborative robot arm (Omron, Japan). A shielding gas mixture containing 92% argon and 8% carbon dioxide was supplied at a flow rate of 19 L/min to protect the molten pool from atmospheric contamination. The complete WAAM setup

included a workbench, cobot arm, CMT power source, wire feeder, ventilation system, argon gas supply, and control unit. Each bead was designed to have a length of 120 mm and was deposited in the same direction to maintain consistency. To prevent heat accumulation between successive depositions, each new bead was deposited only after the previous one had cooled to room temperature.

4.2. Specimen Examination

Following deposition and natural cooling, the fabricated beads were sectioned at their mid-length for analysis (Figure 1). The cross-sections were mechanically polished using 100, 600, 1200, and 2500 grit abrasive papers to remove surface irregularities and eliminate cutting-induced defects before macrographic observation. The polished specimens were examined using a Zeiss AXIO Imager M1m optical microscope at 3× and 4× magnifications, depending on sample size. High-resolution micrographs of the transverse cross-sections were captured and subsequently processed using ImageJ software to quantify the geometrical features of the deposited layers, specifically, height, width, and wetting angle. The measured geometrical parameters are schematically represented in Figure 2, and the applied evaluation methodology followed the procedures described in references [28, 29].

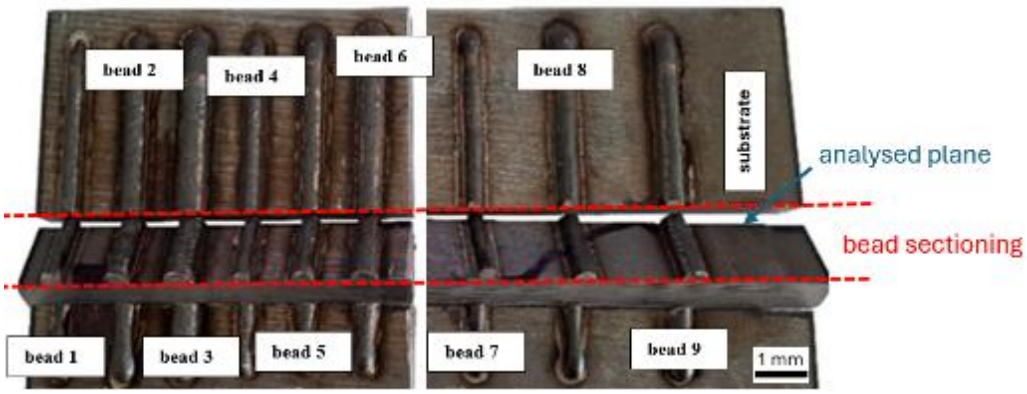

Figure 4-1. Deposited WAAM beads after transverse cutting.

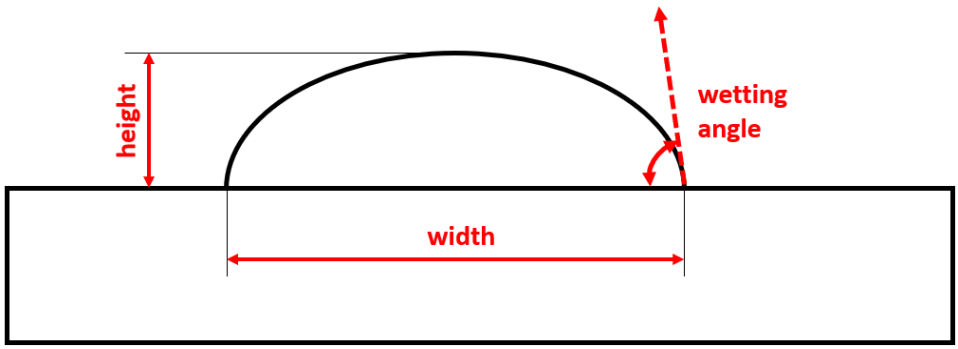

Figure 4-2. Schematic representation of geometrical measurements (height, width, and wetting angle).

The deposition process was further analyzed using thermography. Thermal monitoring was

performed with a Flir T1020 bolometric thermal camera, equipped with an IR lens offering a 28° field of view and a 36 mm focal length. The camera specifications include a 1024 × 768 resolution, low noise, and a frame rate of 30 Hz, with the minimum detectable temperature difference of 20 mK. Each deposition process was thermally observed at three predefined measurement points, as illustrated in Figure 3, maintaining a 70 cm distance between the camera and the specimen surface.

Figure 4-3. Position of measurement points for thermal investigation.

4.3. Statistical Analysis

As previously noted, the methodology of this study was structured following a Design of Experiments (DOE) framework, applying a 2^3 full factorial design with two factors, each examined at three levels, and three repetitions per experimental run. Initially, the reproducibility of the experiments was verified by evaluating the variance among specimens produced under identical process conditions, resulting in a repeatability coefficient of 95%. Upon confirmation of reproducibility, the mean value of the three replicates was used as the representative result. This systematic design allowed for the statistical evaluation of the influence of input parameters ,namely arc power and deposition speed ,on the output responses, including bead width, height, wetting angle, and aspect ratio. The Response Surface Methodology (RSM) was employed to interpret the data, while Analysis of Variance (ANOVA) was conducted to determine the statistical significance of the observed effects. The significance threshold (p-value) was set to 0.05.

4.4. Numerical Model

To complement the experimental investigation, numerical simulations were performed using a custom-developed model that integrated macro- and mesoscale approaches within a phase-field modeling framework. The 3D numerical model simulated heat and mass transfer during the WAAM process, capturing the resulting thermal history, distortions, and residual stresses of the deposited beads under various process parameters. All simulations were implemented in COMSOL Multiphysics, where the computational analyses were conducted. Figure 4 presents a schematic illustration of the computational domains utilized in the proposed model.

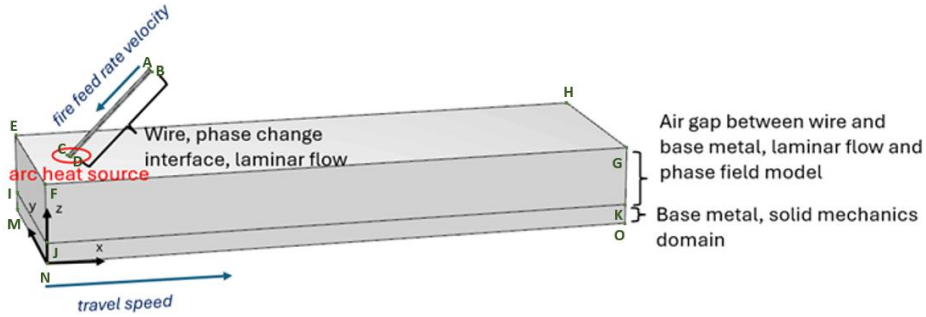

Figure 4-4. Schematic representation of the computational domains.

4.5. Constitutive Equations

Since the principal objective of the developed numerical model was to analyze the melt pool dynamics, the focus was placed on the molten state of the deposited metal, which was modeled as an incompressible Newtonian fluid. Accordingly, the Computational Fluid Dynamics (CFD) model was governed by the fundamental conservation equations of mass, momentum, and energy, as defined in Equations (2)–(5) [30, 31]:

$$\rho\frac{\partial \mathbf{u}}{\partial t} + \rho(\mathbf{u}.\nabla)\mathbf{u} = \nabla.[-p\mathbf{I} + \mathbf{K}] \tag{2}$$

$$\frac{\partial \rho}{\partial t} + \nabla.(\rho\mathbf{u}) = 0 \tag{3}$$

$$\rho C_p\frac{\partial T}{\partial t} + \rho C_p\mathbf{u}.\nabla T + \nabla\mathbf{q} = Q \tag{4}$$

$$\mathbf{q} = -k\nabla T \tag{5}$$

where:

- ρ , density of the fluid,
- u , velocity vector,
- t , time,
- p , pressure,
- I , identity matrix,
- T , temperature,
- C_p , specific heat capacity,
- q , heat flux,
- Q , heat source term,
- k , thermal conductivity.

These equations describe the momentum balance under the influence of pressure and viscous forces, the continuity of mass, and the transport of thermal energy within the molten pool during the WAAM process.

4.6. Phase-Field Equations

The interaction between the molten metal and the solid substrate was modeled through a fluid–structure interaction (FSI) framework (Eq. 6), while the surrounding air region and the melt–air interface were treated using phase-field modeling coupled with a two-phase flow approach (Eqs. 7–13):

$$\boldsymbol{F}_A = [-p\boldsymbol{I} + \boldsymbol{K}].\boldsymbol{n} \tag{6}$$

$$\nabla GI \cdot \nabla GI + \sigma_w GI \nabla \cdot \nabla GI = (1 + 2\sigma_w) GI \tag{7}$$

$$F_{st} = \left(\frac{\lambda}{\epsilon_{pf}^2}\psi - \frac{\partial f}{\partial \emptyset}\right)\nabla \emptyset \tag{8}$$

$$\rho = \rho_1 v_{f.1} + \rho_2 v_{f.2} \tag{9}$$

$$\mu = \mu_1 v_{f.1} + \mu_2 v_{f.2} \tag{10}$$

$$v_{f.1} = \frac{1 - \emptyset}{2} \tag{11}$$

$$v_{f.2} = \frac{1 + \emptyset}{2} \tag{12}$$

$$v_{f.1} + v_{f.2} = 1 \tag{13}$$

where:

- F_A , body force acting on the fluid,
- n , unit normal vector at the interface boundary,
- GI , reciprocal initial interface distance,
- σ_w , surface tension coefficient,
- λ , coupling coefficient,
- ϵ_{pf} , interface thickness control parameter,
- ψ , auxiliary phase-field variable,
- ϕ , phase-field order parameter,
- F_{st} , surface tension force,
- ρ_1, ρ_2 , densities of the first and second fluid phases, respectively,
- μ_1, μ_2 , dynamic viscosities of the two fluids,
- v_{f1}, v_{f2} , volume fractions of the first and second fluids.

The phase-field method effectively captures the evolution of the fluid–gas interface, accounting for surface tension effects, interface curvature, and multiphase flow dynamics during deposition. This approach allows a smooth transition between the molten metal and surrounding gas, providing a robust description of interface motion, droplet coalescence, and melt pool surface deformation in the WAAM process.

The free surface of the molten pool was influenced by both gravitational and buoyancy forces, with the latter modeled using the Boussinesq approximation. Additionally, the

Marangoni effect and arc pressure were incorporated as key driving forces acting on the molten metal. The resulting body force from the arc pressure was expressed as follows (Eq. 14):

$$\mathbf{F_a} = p_a \nabla F \frac{F\rho + (1-F)\rho_{gas}}{0.5(\rho + \rho_{gas})} \tag{14}$$

where $F_a$denotes the body force originating from the arc pressure p_a.

4.7. Thermal Modelling

To accurately represent the heat input from the arc, the model employed a boundary heat source, formulated in Eq. (15). The heat transfer between the deposited beads and the base plate was accounted for through thermal fluxes at the upper surface of the substrate. Furthermore, heat losses to the surrounding environment were modeled via radiation and natural/forced convection from all exposed surfaces, as described in Eqs. (16), (17):

$$Q = \eta UI - \frac{4\pi}{3} R_a^3 \mathbf{q_m} \tag{15}$$

$$-k\frac{\partial T}{\partial \mathbf{n}} = h_s(T - T_{amb}) \tag{16}$$

$$h_s = h_c + \varepsilon k_b \frac{(T^4 - T_{amb}^4)}{(T - T_{amb})} \tag{17}$$

where $\eta$is the heat source efficiency, $U$the voltage, $I$the current, $R_a$the effective arc radius, and $q_m$the heat of the deposited material. The term $n$represents the normal vector to the surface, $h_s$the overall heat transfer coefficient, $h_c$the convective heat transfer coefficient, $\varepsilon$the emissivity coefficient, and $T_{amb}$the ambient temperature.

4.8. Phase Change Interface

Temperature variations during the process led to phase transformations, modeled through the latent heat of fusion, as defined in Eq. (18). The corresponding thermophysical properties within the mushy zone were calculated using Eqs. (19)–(22):

$$h = \int C_p dT + l_f \tag{18}$$

$$\rho = \rho_s \theta_s + \rho_l \theta_l \tag{19}$$

$$C_p = \frac{1}{\rho}\left(C_{ps}\rho_s\theta_s + C_{pl}\rho_s\theta_s\right) + l_f \frac{\partial a_m}{\partial T} \tag{20}$$

$$k = k_s\theta_s + k_l\theta_l \tag{21}$$

$$a_m = \frac{1}{2}\frac{\rho_l\theta_l - \rho_s\theta_s}{\rho_s\theta_s + \rho_l\theta_l} \tag{22}$$

where $h$is the enthalpy, $l_f$the latent heat of fusion, and $C_p$the specific heat capacity. The parameters ρ_s, C_{ps}, k_srepresent the density, heat capacity, and thermal conductivity of

the solid phase, while ρ_l, C_{pl}, k_lcorrespond to those of the liquid phase. The variables $\theta_s$and $\theta_l$denote the solid and liquid phase fractions, respectively, and $a_m$represents the mass fraction of the mushy region. The mushy zone was modeled as a porous medium, incorporating the Carman–Kozeny equation. Considering the typical temperature range achieved during the WAAM process, evaporation effects were neglected in the present model.

4.9. Solid Mechanics Model

The solidified material was represented as an elastoplastic medium, characterized by the von Mises yield criterion and the Johnson–Cook constitutive model, as formulated in Eqs. (23)–(27):

$$\rho \frac{\partial^2 \boldsymbol{u}}{\partial^2 t} = \nabla .\ \mathrm{S} + \mathbf{F}\mathrm{v} \tag{23}$$

$$\mathrm{S} = \mathrm{S}_{inel} + \mathrm{S}_{el} \tag{24}$$

$$\epsilon = \frac{1}{2}[(\nabla \mathbf{u})^T + \nabla \mathbf{u}] \tag{25}$$

$$\sigma_{ys} = (\sigma_{ys0} + k(\varepsilon_{pe})^n)(1 + C\log(\frac{\dot{\varepsilon}_{pe}}{\dot{\varepsilon}_0}))(1 - T_h^m) \tag{26}$$

$$T_h = \frac{T - T_{ref}}{T_m - T_{ref}} \tag{27}$$

where $F_v$is the deformation gradient, and $S$is the second Piola–Kirchhoff stress tensor, composed of elastic (S_{el}) and inelastic (S_{inel}) components. The yield stress σ_{ys}depends on the initial yield stress σ_{ys0}, strength coefficient k, effective plastic strain ε_{pe}, hardening exponent n, and strain-rate sensitivity coefficient C. Here, $\dot{\varepsilon}_{pe}$represents the equivalent plastic strain rate, $\dot{\varepsilon}_0$the reference strain rate, $m$the thermal softening exponent, $T_{ref}$the reference temperature, and $T_m$the melting temperature.

4.10. Coupling Phenomena

The developed numerical model was fully coupled, ensuring the interaction between all physical fields involved in the WAAM process. Specifically, the Marangoni flow represented the coupling mechanism between heat transfer and laminar flow, while thermal expansion served as the link between structural mechanics and heat transfer. The fluid–structure interaction (FSI) node established the connection between fluid flow and structural dynamics, whereas the two-phase flow module provided the coupling between the phase-field and laminar flow models.

4.11. Boundary Conditions

The boundary conditions were defined to closely replicate the experimental conditions observed during the deposition process. A schematic representation of the computational domains and the corresponding physical phenomena is presented in Figure 4. To simulate the mechanical clamping of the base plate, the bottom surface of the solid domain was assigned a zero-displacement constraint. The initial temperature was assumed to be uniform across all domains, set at 20 °C. All exposed surfaces of the substrate, except the bottom face, were subjected to heat flux boundary conditions, accounting for natural and forced convection as well as radiative heat losses, as described in Section 3.3 of this study. The complete list of boundary conditions for the solid domain is summarized in Table 3.

Table 3. Boundary conditions in the solid domain

	Temperature	**Displacement**
MNOP	$in\ t = 0s\ T = 293.15\ K$	$\boldsymbol{u} = 0\ mm$
IMNJ, NJOK, KLPO, IMPO	$in\ t = 0s\ T = 293.15K$ $q_{loss} = -h_{conv}(T - T_{ref}) - \varepsilon\sigma(T^4 - T_{ref}^4)$ (27)	

The wire domain was treated as a phase-change medium, where the melting temperature defined the transition threshold between solid and liquid phases. The lower boundary of the wire domain was continuously exposed to the heat source, as detailed in Section 3.3. The flow of molten metal was modeled as laminar, moving with a constant velocity equivalent to the wire feed rate. Accordingly, the entire wire domain was assigned a prescribed velocity boundary condition, reproducing the translational motion of the wire over the substrate at a constant deposition speed. The boundary conditions for the wire domain are summarized in Table 4.

Table 4. Boundary conditions in the wire domain

	Flow properties	**temperature**	**velocity**	**phase**
AB	inlet	$in\ t = 0s\ T = 293.15K$	$in\ t = 0s\ v = 0\ mm/s$	$\theta_s = 1, \theta_l = 0$
CD	outlet	$if\ t = 0s\ T = 293.15\ K$ $if\ t > 0s\ Eq.(14)$	$v = wire\ feed\ rate = 7\ m/min$	$\theta_s = 0, \theta_l = 1$
ABCD	laminate	$if\ t = 0s\ T = 293.15\ K$ $if\ t > 0s\ Q - q_{loss}$	$v = wire\ feed\ rate = 7\ m/min$	$T > 1683.15\ K$ $\theta_s = 0, \theta_l = 1$ $T < 1663.15\ K$ $\theta_s = 0, \theta_l = 1$ $\theta_s + \theta_l = 1$

As the molten metal traveled through the air gap, the model accounted for gravitational, arc pressure, and buoyancy forces. Upon contact with the solid substrate, the Marangoni effect was activated to simulate surface-tension-driven flow. The boundary conditions

applied to the air gap domain are summarized in Table 5.

Table 5. Boundary conditions in the air gap domain

	phase	temperature	pressure and surface tension
EFGHIJKL	$t = 0s\ v_{air} = 1, \quad v_{metal} = 0$	$if\ t = 0s\ T = 293.15\ K$	$-P + 2\mu\frac{\partial v_n}{\partial n} = -P_{arc} + \frac{\gamma}{R}$
	$t > 0s\ v_{air} + v_{metal} = 1$	$if\ t > 0s\ Q - q_{loss}$	
EFGH	$v_{air} + v_{metal} = 1$	$if\ t > 0s\ Q - q_{loss}$	$P = P_{atm} + P_{arc}$
IJKL	$v_{air} + v_{metal} = 1$	$if\ t > 0s\ Q - q_{loss}$	$P_{st} = \gamma k$ $-\mu\frac{\partial v_t}{\partial n} = \frac{\partial \gamma}{\partial T}\frac{\partial T}{\partial S}$

4.12. Meshing Strategy

The numerical simulations were performed using COMSOL Multiphysics, which employs physics-controlled meshing to automatically determine optimal mesh densities and solver sequences for each physics interface. The meshing strategy varied depending on the nature of each computational domain. The solid domain (representing the base plate) was discretized using hexahedral mesh elements with a “normal” mesh size, as illustrated in Figure 5-a. The single-phase fluid domain (representing the molten wire) was assigned a “finer” mesh size (Figure 5-b) to better capture the rapid thermal and flow dynamics occurring within this region, thereby improving numerical stability and solution convergence. In contrast, the multiphase fluid domain, corresponding to the molten filler metal traveling through the air gap, required a more sophisticated computational approach (Figure 5-c). To enable the free movement of molten material between the wire and the substrate, the Arbitrary Lagrangian–Eulerian (ALE) formulation was applied, allowing mesh deformation within the phase-field domain. This region was thus modeled as a deforming mesh, with mesh motion governed by the Yeoh mesh-smoothing algorithm [32]. Despite this flexibility, the initial mesh in this domain remained significantly finer than that employed for the solid region.

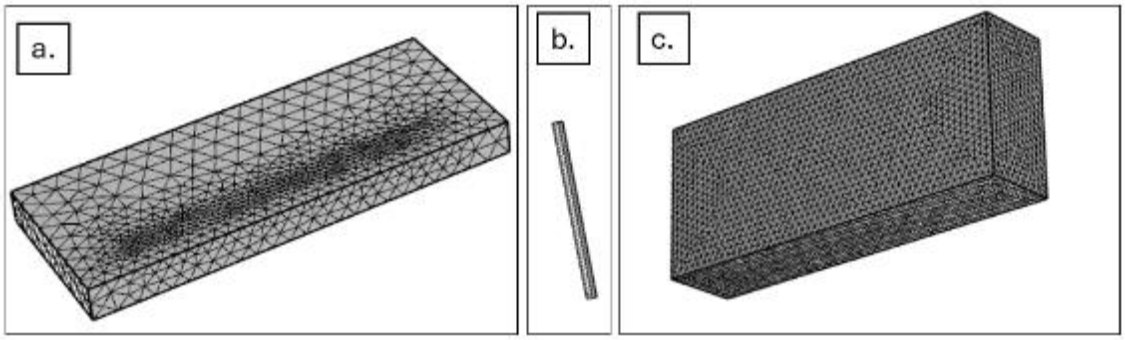

Figure 4-5. Mesh representation in (a) solid domain, (b) liquid domain, and (c) air gap domain.

Additionally, the mesh was refined along all interfacial boundaries between computational domains. This refinement was automatically handled by the software based on the local physical interactions. The refinement zone shown in Figure 5-a corresponds to the interface between the solid base plate and the liquid domain (fluid 1), where the molten filler material first makes contact during deposition.

4.13. Geometry of Transverse Sections

As shown in Figure 1, the deposition process produced relatively uniform and continuous beads across all investigated process conditions. Minor irregularities were primarily observed at the lateral edges of the beads, where the material exhibited narrow transitional zones followed by broader, lower-height endings. In contrast, the central regions of the beads appeared smooth, consistent, and without noticeable geometrical deviations. Table 6 presents the experimentally measured geometrical features ,including bead height, width, and wetting angle ,for the central transverse sections of AISI 308L specimens deposited under varying processing parameters. The aspect ratio (defined as the width-to-height ratio) was also calculated to evaluate bead morphology and deposition precision. The geometrical profiles of the transverse sections obtained at different travel speeds and arc powers are illustrated in Figure 6.

Table 6. Experimentally measured width, height, and wetting angle of beads deposited under different processing conditions

	Bead								
	1	**2**	**3**	**4**	**5**	**6**	**7**	**8**	**9**
Width [mm]	2.05	4.03	5.88	2.93	4.06	6.48	2.72	2.64	5.22
Height [mm]	2.65	3.11	3.46	2.11	2.01	3.41	2.12	3.41	2.54
Wetting angle [°]	94.9	91.4	76.8	92.9	84.7	69.1	88.4	100.9	60.8
Aspect ratio [-]	0.77	1.30	1.70	1.39	2.02	1.90	1.28	0.77	2.06

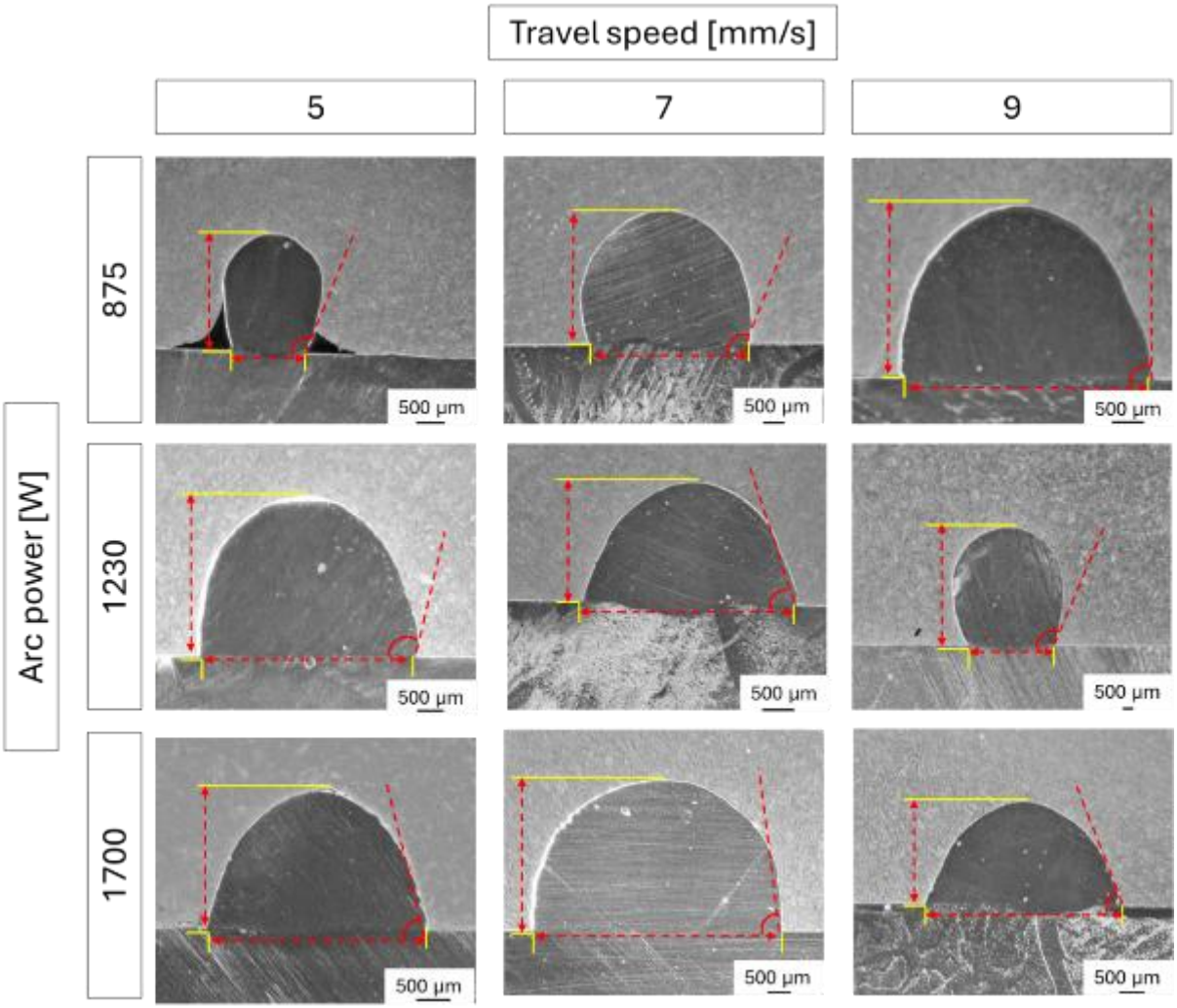

Figure 4-6. Transverse sections of deposited beads produced with various travel speeds and arc powers.

The transverse profiles of the beads exhibited semi-cylindrical geometries, typical of the WAAM process. However, significant variations were observed in bead height, width, wetting angle, and aspect ratio, indicating a strong dependency of bead geometry and deposition accuracy on the process parameters. As depicted in Figure 6, wetting angles below 95° ,generally regarded as desirable due to improved spreading and layer adhesion ,were achieved when using an arc power of 1700 W. The influence of process parameters on bead geometry (height, width, wetting angle, and aspect ratio) is further analyzed in Section 4.2. Previous studies indicate that wetting angles between 55° and 95° yield the most geometrically stable and dimensionally accurate deposits, combining high surface quality and effective layer formation [33–35].

- Lower wetting angles (<55°) indicate excessive spreading, resulting in insufficient layer buildup and reduced dimensional precision.

- Higher wetting angles (>95°) are unfavorable, as they limit the spreading of molten material and reduce bonding quality with either the substrate or the previously deposited layers.

Although Cold Metal Transfer (CMT) technology ,owing to its controlled heat input ,can significantly reduce dilution, it cannot fully eliminate it. In multi-material WAAM, dilution is often considered a defect, yet a moderate level of dilution may actually reduce surface tension differences at the substrate–deposit interface, enhancing wettability and reducing the wetting angle. Moreover, in multilayer components, proper dilution ensures strong interlayer bonding, which is essential for maintaining the mechanical integrity and dimensional stability of the build. Inadequate interlayer fusion can, conversely, result in poor adhesion and potential structural collapse [36, 37].

Considering these factors, the CMT process with a higher arc power (1700 W) demonstrated the most favorable bead geometry. The increased power produced higher arc and molten pool temperatures, leading to improved dilution, enhanced metal fluidity, and controlled solidification rates. These conditions collectively promoted better spreading behavior and reduced surface tension, thereby improving the overall bead morphology [38]. The aspect ratio (width-to-height ratio) is another key geometric parameter that reflects bead stability and surface uniformity. According to the literature, an optimal aspect ratio between 2 and 3 ensures consistent mechanical performance, minimizes defects, and enhances dimensional accuracy of the deposited parts [39].

- Low aspect ratios can result in poor continuity, increased surface roughness, and reduced mechanical strength [40, 41].

- Excessively high aspect ratios, conversely, indicate over-spreading, leading to weak layer definition and increased post-processing requirements [38, 40].

As presented in Table 6, the optimal aspect ratios were achieved for beads 5 and 9, both produced under higher deposition speeds and elevated arc powers. Increasing the arc power enhanced the temperature and flowability of the molten filler metal, while higher deposition speeds influenced the flow dynamics, particularly the velocity and direction of molten metal spreading across the substrate before solidification [42].

4.14. Statistical Analysis

The statistical analysis confirmed that arc power had a significant effect on the width and wetting angle of the deposited beads, whereas height and aspect ratio were not notably influenced by either of the investigated parameters. These findings are illustrated in the Pareto charts shown in Figure 7. The Response Surface Methodology (RSM) identified arc power as the only statistically significant factor affecting bead width and wetting angle, with corresponding p-values of 0.004 and 0.04, respectively. In contrast, the deposition speed showed no statistically significant effect on any of the measured geometric parameters. This lack of correlation could be attributed to the complex fluid dynamics of molten metal flow, which may not be adequately captured by the second-order polynomial model employed in RSM.

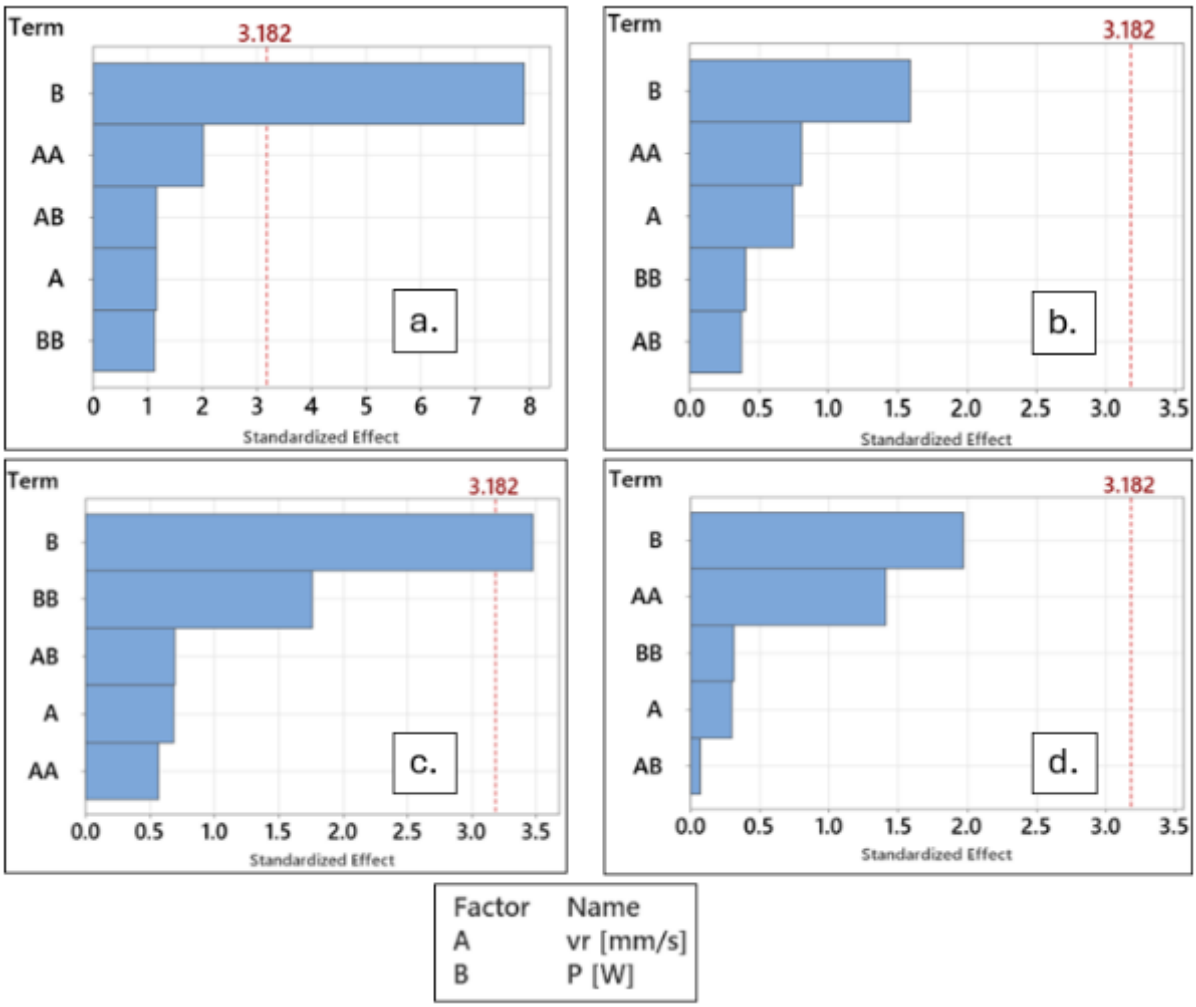

Figure 4-7. Pareto charts representing the significance of the investigated process parameters on (a) bead width, (b) bead height, (c) wetting angle, and (d) aspect ratio.

Consistent with previous studies [136, 137], the height of WAAM-deposited beads is primarily governed by the wire feed rate, with additional influence from the dynamic

behavior of molten metal during deposition [138]. In the present work, the wire feed rate and arc power were interdependent due to the inherent characteristics of the machine's operational curve. Consequently, bead formation was influenced by several factors, including deposition speed, mass input, arc temperature, and temperature-dependent viscosity of the molten metal.

Given the complex interplay of underlying physical phenomena ,such as phase change, Marangoni convection, and non-isothermal fluid flow ,it is reasonable to infer that the mechanisms affecting bead height are too nonlinear to be fully represented by the second-order polynomial approximation used in RSM. On the other hand, RSM revealed a quasi-linear relationship between arc power and bead width (Figure 8-a), while the correlation between arc power and wetting angle exhibited an inverse proportionality with a nonlinear trend (Figure 8-b). Both the increase in bead width and reduction in wetting angle at higher arc powers are consistent with the elevated heat input and the corresponding higher melting rate. Greater melting rates generate larger molten volumes, resulting in bigger molten droplets at the wire tip. Upon impacting the substrate, these larger droplets spread more extensively, thereby increasing the bead width and decreasing the wetting angle [139].

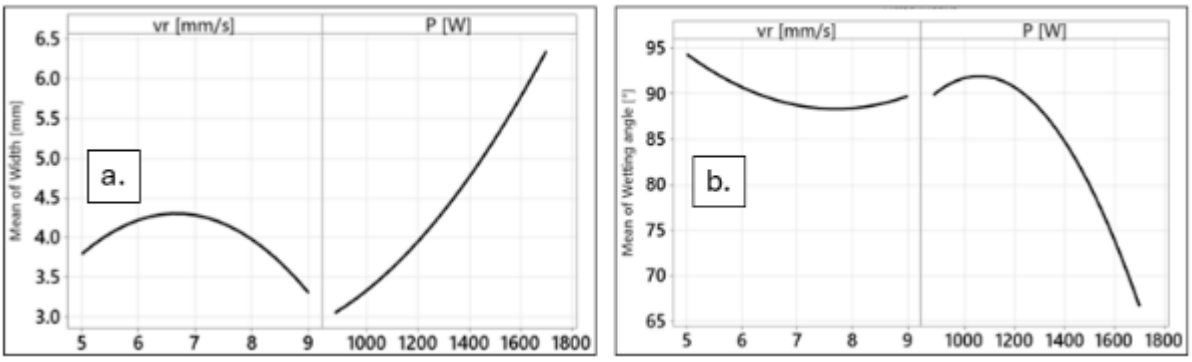

Figure 4-8. Main effects plots showing the influence of deposition speed and arc power on (a) bead width and (b) wetting angle of WAAM-deposited specimens.

4.15. Thermal History

Figure 9 compares the experimental and numerically simulated thermal histories recorded at the three predefined measurement points (1, 2, and 3; positions detailed in Section 2.2) during the deposition process. The experiments were performed using an arc power of 1230 W and travel speeds of 5, 7, and 9 mm/s, corresponding to beads 2, 5, and 8, respectively.

The closest agreement between experimental and simulated temperature curves was

achieved when the arc efficiency in the numerical model was set to 0.68, as illustrated in Figure 9. This efficiency value was therefore used consistently across all subsequent numerical simulations. A strong correlation was observed between the simulated and measured thermal profiles, particularly during the initial heating and first cooling stages. Minor discrepancies were noted during the secondary heating phase and steady-state region, likely resulting from slight deviations between the actual material properties (thermal conductivity and specific heat capacity) and the values defined in the numerical model, especially at elevated temperatures. A more noticeable difference appeared at measurement point 3 for bead 5 (Figure 9-b), where the numerical model did not reproduce an additional temperature peak observed experimentally. Nevertheless, the overall deviations between the simulated and measured temperatures did not exceed 10 °C, demonstrating the high accuracy and reliability of the developed numerical model, and validating its effectiveness in reproducing the thermal behavior during the WAAM process.

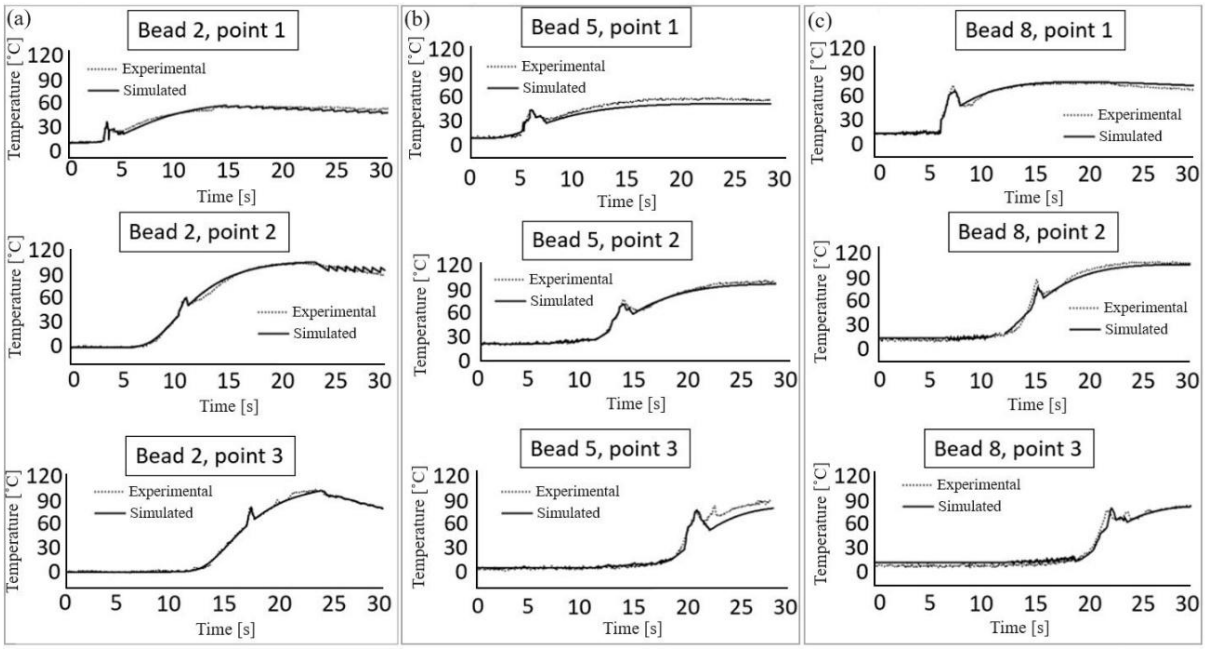

Figure 4-9. Comparison between experimental and simulated thermal curves in (a) bead 2, (b) bead 5, and (c) bead 8.

As shown in Figure 9-a–c, the temperature evolution recorded at measuring point 1 for specimens deposited at travel speeds of 5, 7, and 9 mm/s, respectively, exhibited an initial steep temperature rise. This rapid temperature increase corresponds to the impact of molten filler droplets striking the substrate surface [140]. Due to convective cooling and the relatively small volume of freshly deposited molten metal, the temperature at the measuring point subsequently dropped sharply. As the deposition process continued, the temperature

rose again, albeit with a less pronounced gradient, before eventually reaching a steady-state condition [141]. This general pattern of temperature evolution at point 1 was consistent across all examined beads, regardless of deposition speed.

In contrast, the temperature evolution at measuring point 2 exhibited a gentler initial increase, as the temperature in this region began to rise prior to the actual deposition of molten metal [142]. This preheating effect of the substrate influenced the local thermal gradients, which may have contributed to distinct microstructural variations in this area [143, 144]. Once the molten filler reached the base plate, the temperature at point 2 attained its maximum value, followed by a brief rapid cooling stage. As additional layers of molten metal accumulated, the temperature gradually increased again and then stabilized. Notably, the maximum temperatures at point 2 were significantly higher than those at point 1. This difference can be attributed to the combined effects of substrate preheating and variations in thermal exposure: the region around point 1 was more exposed to ambient conditions and therefore experienced greater cooling losses [145].

A similar preheating trend was also observed at measuring point 3, where the temperature began to rise before the deposition occurred. As shown in Figure 8, the steepness of this initial temperature increase was inversely related to the deposition speed ,slower travel speeds resulted in less steep temperature rises but higher overall temperatures at the measurement location. This phenomenon is attributed to the prolonged exposure time of the substrate to the thermal energy input from the arc at lower deposition speeds [146, 147]. After the initial heating phase, all samples exhibited a short but intense cooling stage at point 3. The observed temperature peaks likely correspond to localized cooling beneath the arc, associated with thermal flux variations in the melt pool depression region, further intensified by convective heat exchange with the shielding gas. The subsequent secondary temperature peak can be linked to the arrival of new molten material, temporarily reheating the analyzed zone [148, 149]. Figure 10 presents the temperature–time curves recorded under different process parameters for the predefined measuring points. All simulated thermal profiles displayed minor irregularities near their maximum temperatures, closely resembling those observed in the experimental measurements.

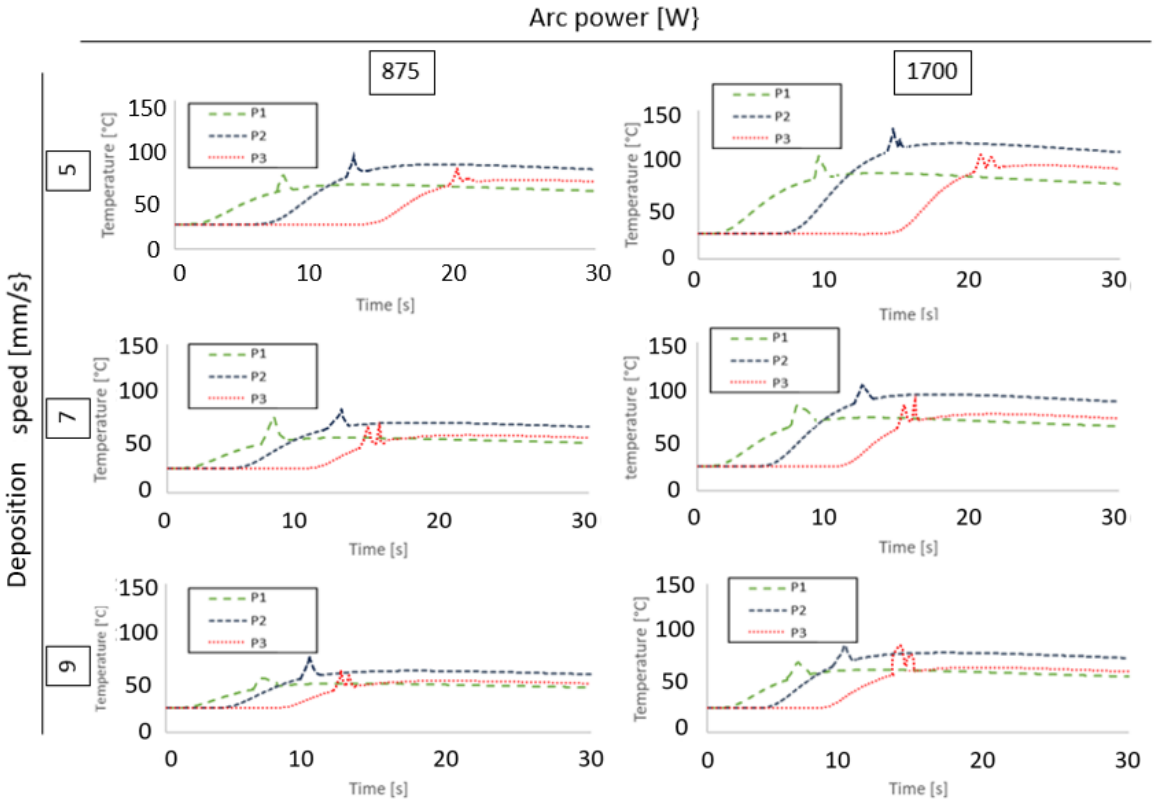

Figure 4-10. Thermal curves of beads deposited under different process conditions at predefined measuring points.

A distinctive feature observed in the thermal curves at measuring point 3 was the presence of a double-peak pattern. This behavior is likely related to the increasing spatial separation between the arc plasma and the region of material deposition as the process progresses [150]. The first peak can be attributed to direct heating by the arc, whereas the second peak corresponds to localized reheating from newly deposited material. The intermediate cooling phase between these peaks may result from the shielding gas flow, which enhances heat dissipation, or from temporary depressions in the molten pool caused by arc pressure and flow instabilities. Thermal imaging data obtained with the infrared camera further corroborate these phenomena (Figure 11). The captured thermographs identified distinct thermal zones, including:

- Wire heating (Area 1),
- Substrate preheating prior to deposition (Area 2), 3–4. Two separate high-temperature regions within the molten pool, separated by a slightly cooler band, and
- Intense cooling of the previously deposited material along the single-track region.

These observations confirm the multistage and non-uniform thermal behavior of the

WAAM process, illustrating how complex thermal gradients and localized heat transfer govern melt pool evolution and solidification dynamics.

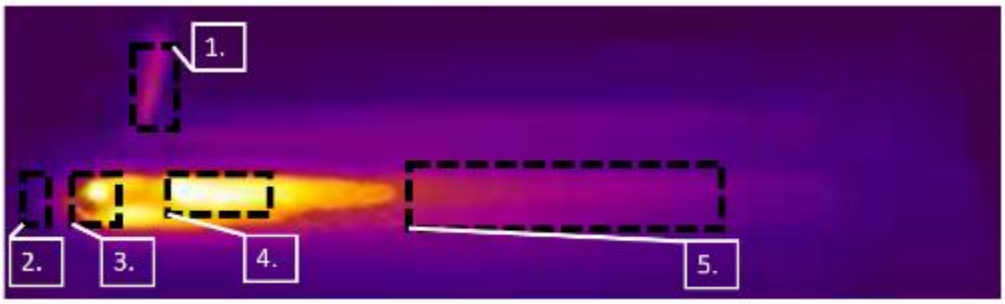

Figure 4-11. Thermographic capture of the deposition process highlighting five thermally active regions: (1) wire heating, (2) substrate preheating, (3–4) two high-temperature melt pool zones separated by a cooler region, and (5) rapid cooling of deposited material.

The analysis of thermal curves obtained during deposition under varying processing parameters (see Figures 9 and 10) revealed that the maximum temperature recorded at the measured points was primarily governed by the applied arc power. Specifically, regions exposed to higher arc power exhibited significantly elevated peak temperatures compared to those processed under lower arc power conditions. In addition, the deposition speed was found to play a crucial role in determining the temperature distribution across the central and lateral regions of the bead. As illustrated in Figure 12-a, beads deposited at lower travel speeds retained higher temperatures at their extremities for a longer duration compared to those deposited at higher speeds under the same arc power (Figure 12-b). Although both thermographs were captured five seconds after the end of deposition, the warmest region in the bead produced at lower speed was observed closer to the central area, whereas in the bead deposited at higher speed, the maximum temperature zone had already shifted outward.

This behavior can be attributed to the enhanced preheating effect of the substrate at lower deposition speeds. The longer interaction time between the heat source and the base plate allowed for greater thermal energy absorption, thereby intensifying the temperature gradients across the bead [151]. Such gradients may contribute to the development of anisotropic microstructures, as localized differences in cooling rates can promote non-uniform grain morphology. Conversely, the more uniform thermal profile observed in specimens deposited at higher velocities favors the formation of a homogeneous microstructure, characterized by more consistent cooling and solidification conditions [152].

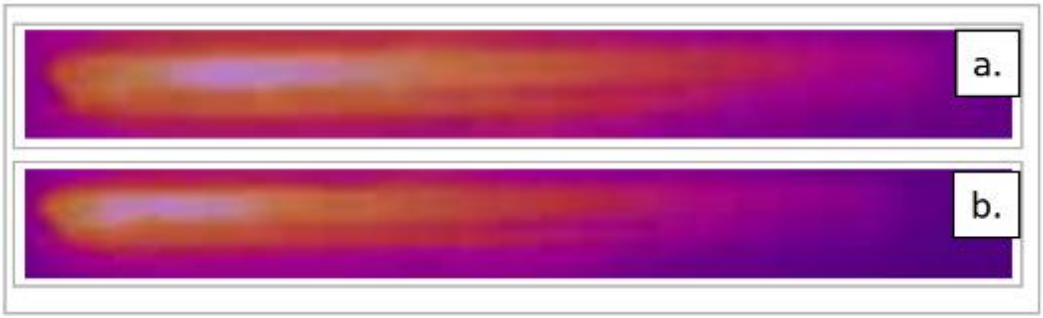

Figure 4-12. Thermographs recorded five seconds after deposition in specimens fabricated with an arc power of 1700 W and travel speeds of (a) 5 mm/s and (b) 7 mm/s.

4.16. Bead Formation

The process of bead formation can be conceptually divided into three distinct stages. The first stage involves the formation of molten droplets at the tip of the heated wire. As illustrated in Figure 13-a, the molten wire initially develops two necking zones; however, the continuous supply of feed material promotes the growth of the lower droplet, which eventually becomes dominant, suppressing the formation of the upper droplet. As the mass of the dominant droplet increases, the combined effects of gravity, surface tension, and inertial forces intensify the necking near the wire tip (Figure 13-b), ultimately leading to droplet detachment. During its downward travel through the air gap, a new droplet begins to form almost immediately at the wire tip, ensuring the continuity of the metal transfer process (Figure 13-c).

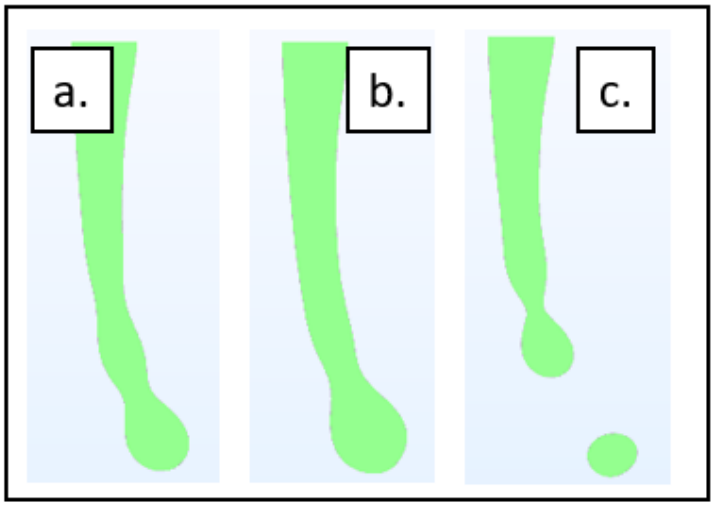

Figure 4-13. Stages of droplet formation: (a) initial necking at two points, (b) growth of dominant droplet and enhanced necking, and (c) droplet detachment with new droplet initiation.

According to previous studies, the early stages of droplet formation are primarily governed by surface tension, which promotes the development of quasi-spherical droplets [153]. As melting progresses and the droplet mass increases, gravitational forces begin to

dominate, causing the droplet to elongate and deform [139]. The slight bending of the necked wire observed in Figure 13 is likely influenced by the motion dynamics of the cobot arm, which may further facilitate droplet detachment.

Upon impact with the substrate, the initially spherical droplet undergoes significant deformation, as shown in Figure 14-a. The viscous molten metal, aided by the residual heat input from the arc, spreads across the substrate, enhancing wetting behavior and forming a more uniform deposit (Figure 14-b). As deposition continues, successive droplets merge, and the bead gradually spreads, assuming its final geometric profile. Concurrently, the ongoing droplet formation shortens the distance between the wire tip and the melt pool, while the melt pool itself expands in the direction of deposition (Figure 14-c).

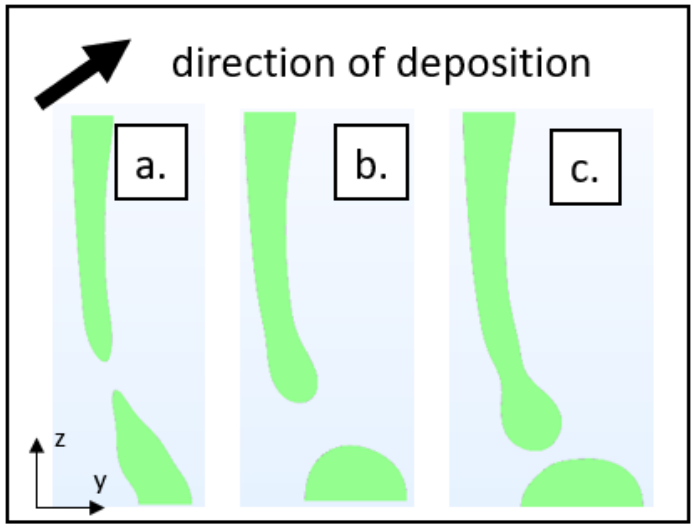

Figure 4-14. Melt pool formation: (a) droplet deformation upon substrate impact, (b) droplet spreading, and (c) final bead shape with new droplet detachment.

As the deposition process progressed, the melt pool continued to expand, while additional wire feed sustained the formation of new molten material. This progression occasionally resulted in brief contact between the wire tip and the melt pool surface (Figure 15-a). In the context of Cold Metal Transfer (CMT), this event constitutes a short-circuit phase, during which intense heat transfer occurs, melting the wire tip and forming a fresh droplet. Immediately after the short circuit, the CMT system retracts the wire (Figure 15-b), breaking the molten bridge. However, this sudden backward motion not only aids detachment but also disturbs the melt pool dynamics, generating localized surface waves and transient flow irregularities (Figure 15-c).

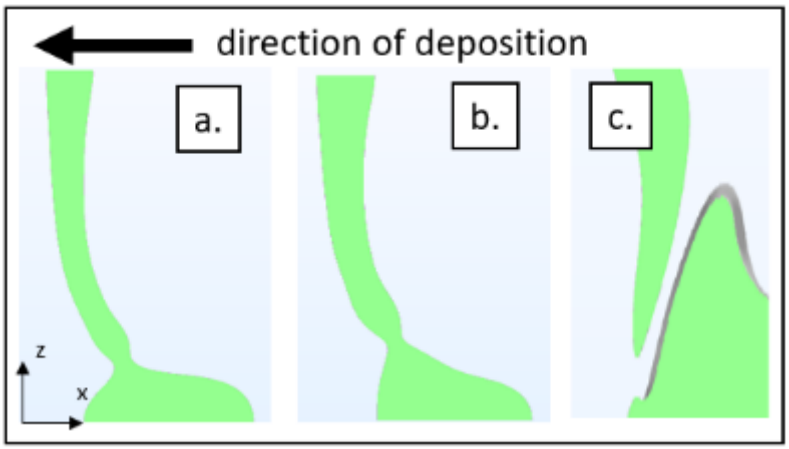

Figure 4-15. (a) Wire–melt pool contact, (b) wire retraction phase, and (c) wire retraction–induced flow disturbances in the melt pool.

Consistent with these experimental observations, the numerical simulations also indicated the formation of a melt pool depression directly beneath the arc (Figure 16). According to previous studies [154], such depressions typically result from the combined influence of arc pressure and electromagnetic forces. However, in the present model, only arc pressure was incorporated. The simulations revealed that larger depressions occurred at lower deposition speeds, which can be explained by the longer exposure time of the melt pool to the arc pressure at any given point. This localized deformation altered the melt flow direction, initially driving the material downward and backward, followed by forward flow to compensate for the displaced volume as the arc advanced.

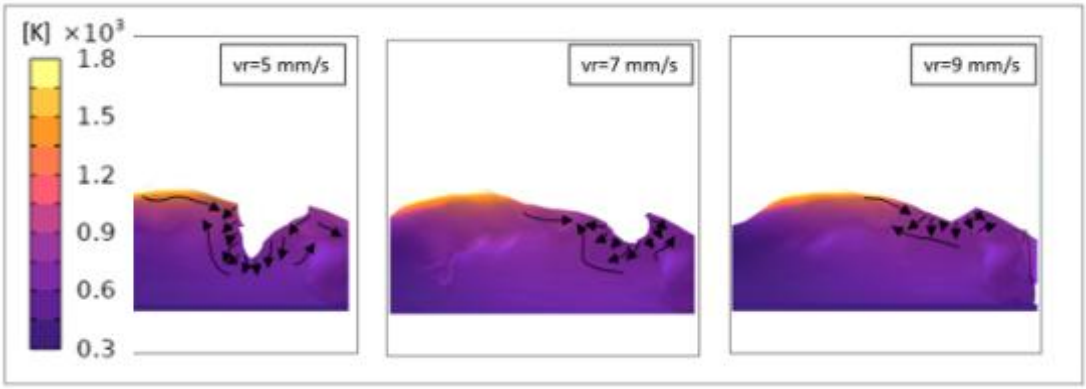

Figure 4-16. Melt pool depression observed during deposition with fixed arc power and varying travel speeds.

The numerical results also demonstrated that the droplet formation process was primarily influenced by the arc power, which directly correlated with the temperature of the wire tip (Figure 17-a). Even with a constant wire feed rate, the higher thermal input associated with increased arc power led to greater melting of the filler material, resulting in the formation of larger droplets (Figure 17-b). This occurs because, under constant feed conditions, higher arc

power proportionally enhances the melting rate, thereby producing a larger molten volume within the same time interval compared to lower power settings [155].

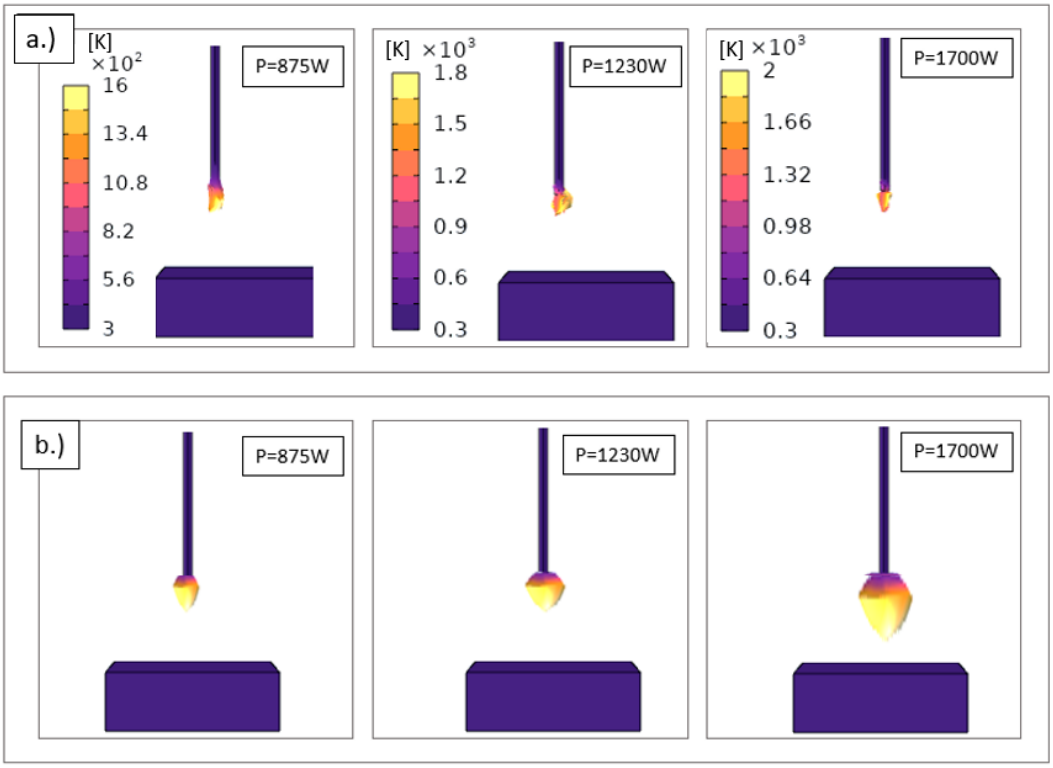

Figure 4-17. Comparison of (a) wire tip temperature at t = 0.028 s and (b) molten droplet morphology at t = 0.055 s during WAAM under different arc powers.

The simulations further confirmed that the final geometry of the deposited bead was governed by several interacting factors:

- The amount of molten material produced and transferred during deposition,
- The compensatory flow induced by arc pressure–driven depressions, and
- The transient flow disturbances resulting from wire retraction.

Although deposition speed did not exhibit statistical significance in earlier analyses, the simulations suggested that it nonetheless influenced bead height by controlling the residence time of the arc within the melt pool and, consequently, the heat distribution during deposition. The accuracy and reliability of the proposed numerical model were validated through the close agreement between the simulated and experimentally observed bead transverse sections.

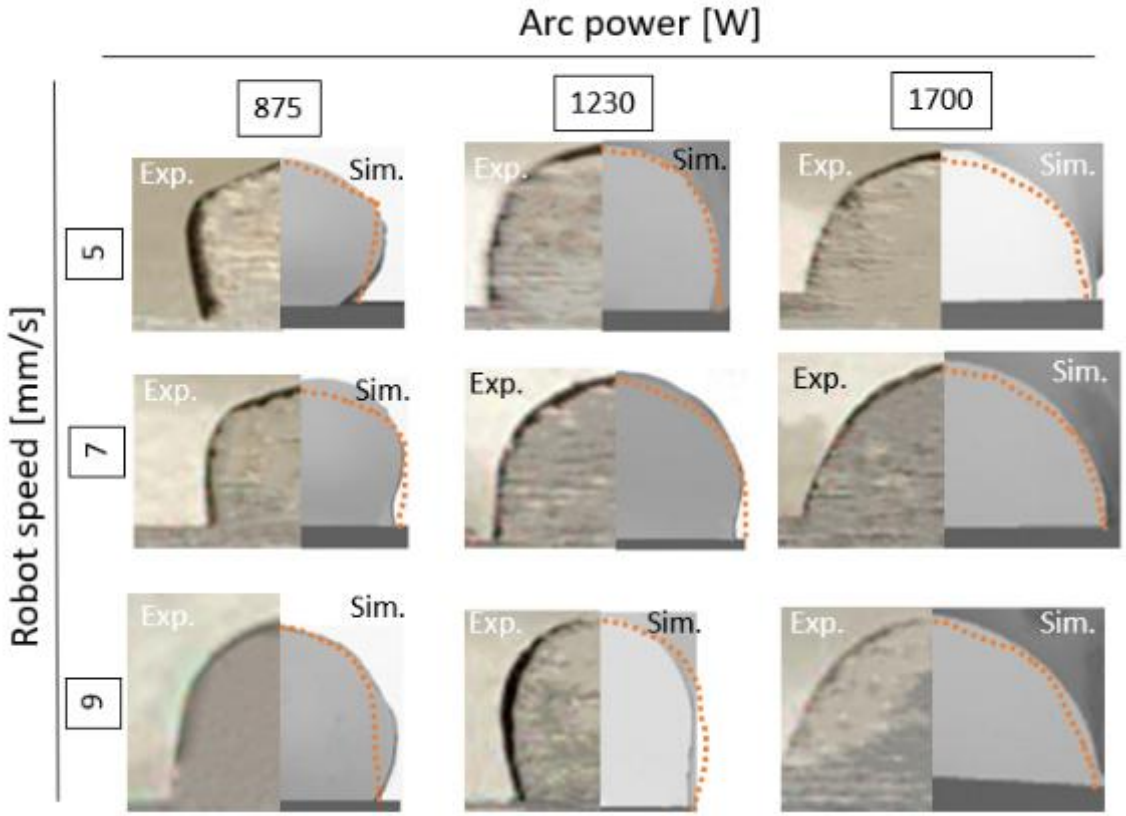

Figure 4-18. Comparison between experimental and simulated transverse sections of beads deposited under different processing parameters.

Chapter 5

Numerical Modeling of WAAM Fabrication of ER70S-6

Chapter 5

Numerical Modeling of WAAM Fabrication of ER70S-6

5.1. Experimental Deposition Methodology

The process parameters for bead deposition were defined following the Design of Experiments (DOE) approach. Two primary factors, arc power and deposition speed, were investigated, each at three levels. The arc power levels were set at 1616 W, 2434 W, and 2839 W, while the deposition speed was varied at 5 mm/s, 7 mm/s, and 9 mm/s, as listed in Table 2. This design yielded a total of nine experimental runs.

Table 2. Investigated factors and their corresponding levels

	level		
	1	**2**	**3**
v_r [mm/s]	5	7	9
P [W]	1616	2434	2839

5.2. Thermal Examination

Thermal tomography analysis of the deposition process was conducted using a FLIR T1020 bolometer thermal camera equipped with a 28° infrared lens (36 mm focal length). The camera offers a resolution of 1024 × 768 pixels, a frame rate of 30 Hz, and low thermal noise sensitivity. Each deposition trial was monitored at three predefined points, as indicated in Figure 1, with the camera positioned at a constant distance of 70 cm from the specimens.

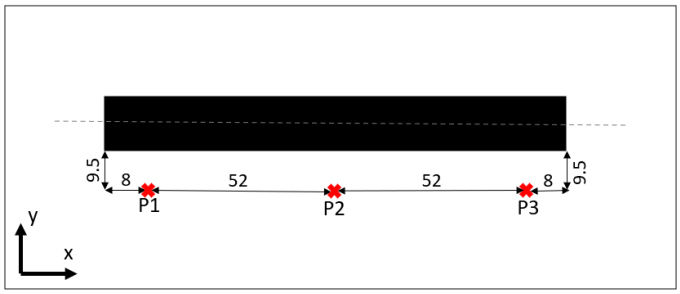

Figure 5-1. Location of measurement points used for thermal tomography analysis.

5.3. Geometry Characterization of Deposited Beads

After fabrication, the deposited specimens were sectioned transversely at their mid-lengths for geometric analysis. High-resolution images of the cross-sections were captured and processed using ImageJ software. The analysis involved measuring the bead width, height, and wetting angle, as schematically illustrated in Figure 2. The aspect ratio of each bead was subsequently determined by dividing its width by height.

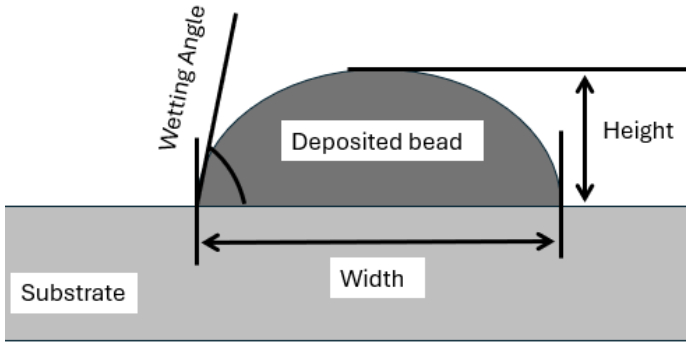

Figure 5-2. Schematic representation of the geometrical parameters evaluated.

5.4. Statistical Analysis and Process Optimization

The effects of the selected process parameters, namely deposition speed and arc power, on the geometrical features (width, height, aspect ratio, and wetting angle) of the deposited beads were statistically evaluated using Analysis of Variance (ANOVA) and Response Surface Methodology (RSM). These analyses were performed using the statistical software Minitab, allowing for optimization and correlation assessment between process parameters and bead morphology.

5.5. Numerical Model

The experimental results were reproduced numerically using a multi-scale model that integrates macroscale computational fluid dynamics (CFD) with mesoscale phase-field modeling. The CFD portion of the model was governed by the conservation equations of mass, momentum, and energy [156]. Following the principles of phase-field modeling, the interaction between the liquid filler (fluid domain) and the solid substrate (solid domain) was described by Equation (1):

$$\boldsymbol{F_A} = [-p\boldsymbol{I} + \boldsymbol{K}].\boldsymbol{n} \tag{1}$$

where $F_A$represents the volume force acting on the fluid, $I$is the unit diagonal matrix, and $n$denotes the normal vector at the boundary surface. The interaction between the molten filler metal and the surrounding gas was characterized by two-phase field coupling, as represented in Equations (2–8) [157, 158]:

$$\nabla GI \cdot \nabla GI + \sigma_w GI \nabla \cdot \nabla GI = (1 + 2\sigma_w)GI \tag{2}$$

$$F_{st} = \left(\frac{\lambda}{\epsilon_{pf}^2}\psi - \frac{\partial f}{\partial \emptyset}\right)\nabla \emptyset \tag{3}$$

$$\rho = \rho_1 v_{f.1} + \rho_2 v_{f.2} \tag{4}$$

$$\mu = \mu_1 v_{f.1} + \mu_2 v_{f.2} \tag{5}$$

$$v_{f.1} = \frac{1 - \emptyset}{2} \tag{6}$$

$$v_{f.2} = \frac{1 + \emptyset}{2} \tag{7}$$

$$v_{f.1} + v_{f.2} = 1 \tag{8}$$

Here, GIdenotes the reciprocal of the initial interface distance, $\psi$is the phase-field auxiliary variable, and ϕrepresents the phase-field order parameter. The coefficient $\sigma_w$corresponds to the surface tension, while ε_{pf}defines the interface thickness. $F_{st}$is the surface tension force, $\rho_1$and $\rho_2$are the densities of the two phases, and $\mu_1$and $\mu_2$denote their respective dynamic viscosities. The volume fractions of each fluid phase are represented by $v_{f,1}$and $v_{f,2}$. The numerical model accounted for gravitational and buoyancy forces, as well as arc pressure acting on the free surface of the molten pool. The Marangoni effect was implemented as the coupling mechanism between the solid and liquid domains. The heat input from the arc was modeled through a boundary heat source, as described by Equation (9). Heat transfer from the deposited beads to the substrate was simulated using thermal fluxes applied to the upper surface of the base metal. The cooling process was modeled by incorporating radiative heat losses and convective heat transfer with the surrounding atmosphere, expressed by Equations (10) and (11):

$$Q = \eta UI - \frac{4\pi}{3} R_a^3 q_m \tag{9}$$

$$-k\frac{\partial T}{\partial \boldsymbol{n}} = h_s(T - T_{amb}) \tag{10}$$

$$h_s = h_c + \varepsilon k_b \frac{\left(T^4 - T_{amb}^4\right)}{(T - T_{amb})} \tag{11}$$

where $Q$is the total heat input, ηrepresen Notably, in Equations (9–11), ηrepresents the heat source efficiency, Udenotes the voltage, $I$is the current, $R_a$corresponds to the radius of the heat input, and $q_m$refers to the heat of the deposited metal. Furthermore, $h_s$indicates the overall heat transfer coefficient, which combines the convective heat transfer coefficient (h_c) and the radiative component determined by the emissivity coefficient (ε). The parameter T_{amb}represents the ambient temperature. The solid domain in the numerical model was treated as an elastoplastic material, modeled using the von Mises yield criterion and the Johnson–Cook constitutive model [159]. The temperature-dependent thermophysical properties of molten ER70S-6 are illustrated in Figure 3, while the additional parameters implemented in the numerical simulation are summarized in Table 3.

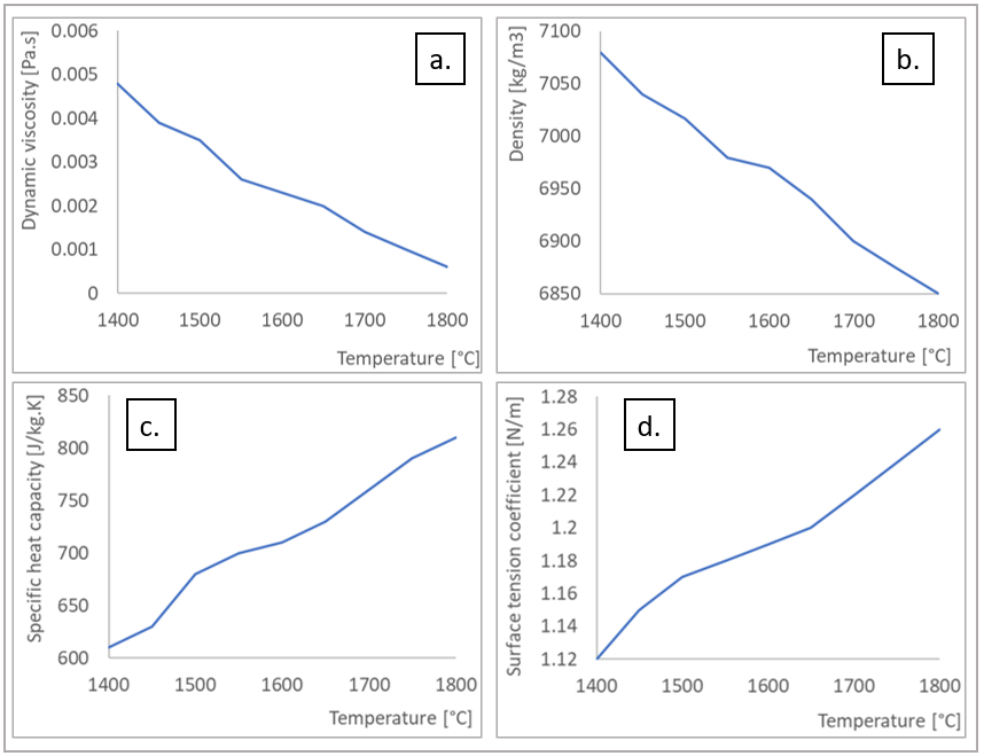

Figure 5-3. Temperature-dependent material properties of molten ER70S-6: (a) dynamic viscosity, (b) density, (c) specific heat capacity, (d) surface tension coefficient.

Table 3. Selected material parameters of ER70S-6 and air, and other relevant physical constants.

Parameter [unit]	value
ER70S-6	
Solidus temperature [°C]	1490
Liquidus temperature [°C]	1510
Density at ambient temperature [kg/m^3]	7850
Coefficient of heat expansion [1/K]	9.3x10^{-6}
Radiation emissivity [-]	0.6
Air	
Density [kg/m^3]	1.184
Dynamic viscosity [Pa.s]	1.85x10^{-5}
Specific heat capacity [J/kg.K]	1005
Thermal conductivity [W/m.K]	0.0262
others	
Atmospheric pressure [N/m^2]	101300
Stefan-Boltzmann constant [W/m^{2}K^4]	5.67x10^{-8}

The coupling between the thermal field and the CFD model was achieved through non-isothermal fluid flow, while the thermal expansion node facilitated the interaction between the heat source and the solid region. The boundary conditions were designed to replicate the actual experimental environment during deposition. Accordingly, the ambient temperature reflected the laboratory conditions, the air gap was defined under atmospheric pressure, and the prescribed thermal and mass inputs corresponded to those listed in Table 2. To enable the unrestricted flow of molten metal through the air gap separating the filler material and

the substrate, the Arbitrary Lagrangian–Eulerian (ALE) numerical framework was implemented to overcome mesh deformation challenges inherent to the phase-field domain. Within this framework, the phase-field region was modeled as a deforming mesh, allowing dynamic grid movement using Yeoh mesh smoothing techniques [160]. The remaining computational domains were discretized into standard mesh elements to ensure numerical accuracy and stability throughout the simulations.

5.6. Overall Bead Appearance

As shown in Figure 4-a, the variation in processing parameters resulted in distinct geometrical profiles among the deposited ER70S-6 beads. Despite the differences in bead width and length, all samples exhibited continuous deposition tracks with slightly widened extremities. The lateral widening observed at the start and end of the deposition tracks is typically associated with changes in torch velocity and torch-to-substrate distance during these stages of the process [161]. This effect becomes more pronounced at higher arc power levels, which can be attributed to modifications in wetting behavior. At elevated power inputs, the increased heat energy raises the temperature of the molten pool, leading to a reduction in viscosity [162]. Consequently, the molten material becomes more fluid and therefore more responsive to variations in torch movement or positional changes, resulting in the observed widening near the bead extremities.

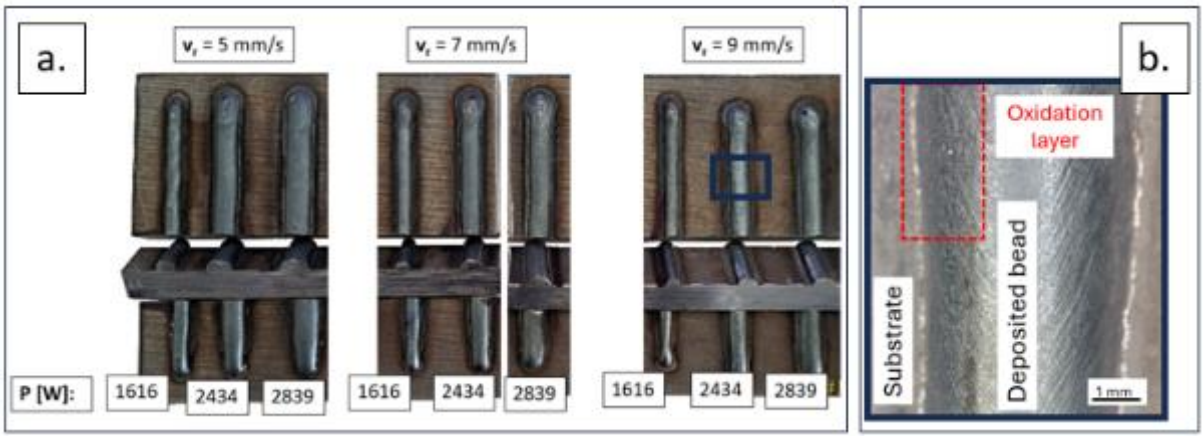

Figure 5-4. (a) Overall appearance of ER70S-6 beads deposited under different processing parameters; (b) detailed view showing oxidation traces.

The darkened and tinted coloration visible on both the beads and the surrounding substrate area (Figure 4-b) indicates the formation of oxide layers. The occurrence of oxidation, despite the use of shielding gas, has been previously reported by Dinovitzer et al. [163], who explained that oxide films predominantly form after deposition, during the cooling phase, when the beads are exposed to natural convection in the absence of shielding

protection.

5.7. Aspect Ratio, Bead Width, and Bead Height

The measured widths, heights, and the corresponding aspect ratios of beads produced under various processing conditions are summarized in Table 4. The results demonstrate that bead geometry is highly sensitive to the applied processing parameters. The aspect ratio, representing the combined influence of bead width and height, is a key indicator for achieving defect-free geometry in both single-layer and multi-layer depositions. Most of the evaluated bead sections exhibited aspect ratios within the optimal range of 2–3. However, beads deposited at lower arc power (1616 W) displayed noticeably lower aspect ratios. This observation is consistent with previous studies [163], which associate reduced aspect ratios with diminished bead continuity and a higher likelihood of geometric irregularities or defects.

Table 4. Measured widths, heights, and aspect ratios of beads deposited under various processing conditions.

v_r [mm/s]		**5**	**5**	**5**	**7**	**7**	**7**	**9**	**9**	**9**
P [W]		**1616**	**2434**	**2839**	**1616**	**2434**	**2839**	**1616**	**2434**	**2839**
width [mm]	**Exp.**	4.82	6.74	8.39	4.04	5.91	8.12	3.64	5.52	6.64
	Sim.	5.02	6.96	8.62	4.47	6.18	8.42	3.86	5.64	6.68
height [mm]	**Exp.**	3.12	3.06	3.37	2.41	2.62	3.12	2.32	2.32	2.43
	Sim.	3.26	3.08	3.45	2.51	2.70	3.34	2.34	2.46	2.52
aspect ratio	**Exp.**	1.55	2.20	2.49	1.68	2.26	2.60	1.57	2.38	2.73
	Sim.	1.54	2.26	2.50	1.78	2.29	2.52	1.65	2.29	2.65
relat. error [%]	**width**	4.15	3.26	2.74	10.64	4.57	3.69	6.04	2.17	0.60
	height	4.49	0.65	2.37	4.15	3.05	7.05	0.86	6.03	3.70
	as. r.	-0.65	2.72	0.34	6.00	1.28	-3.04	5.07	-3.67	-2.90

The numerical simulations showed strong agreement with the experimental measurements, confirmed by the low relative error across most process conditions. The highest relative error, 10.64%, occurred for the bead produced with an arc power of 1616 W and deposition speed of 7 mm/s. However, this higher percentage was primarily due to the small absolute width of the bead, as the absolute error was only 0.43 mm. These results validate the predictive reliability of the simulation model. The simulations further revealed that the aspect ratio of the deposited beads is strongly influenced by the spreading dynamics of molten droplets immediately after deposition. Under low arc power, the direction of molten metal flow remained largely perpendicular to the substrate (Figure 5-a). As the arc power increased, the flow direction angle between the molten metal and the substrate surface also increased (Figure 5-b–c). A smaller flow angle produced taller and narrower beads, whereas an increased angle resulted in wider and flatter bead profiles. Even at constant

deposition speeds, higher arc power enhanced the fluidity of the molten metal, leading to occasional spattering due to excessive flowability (Figure 5-c).

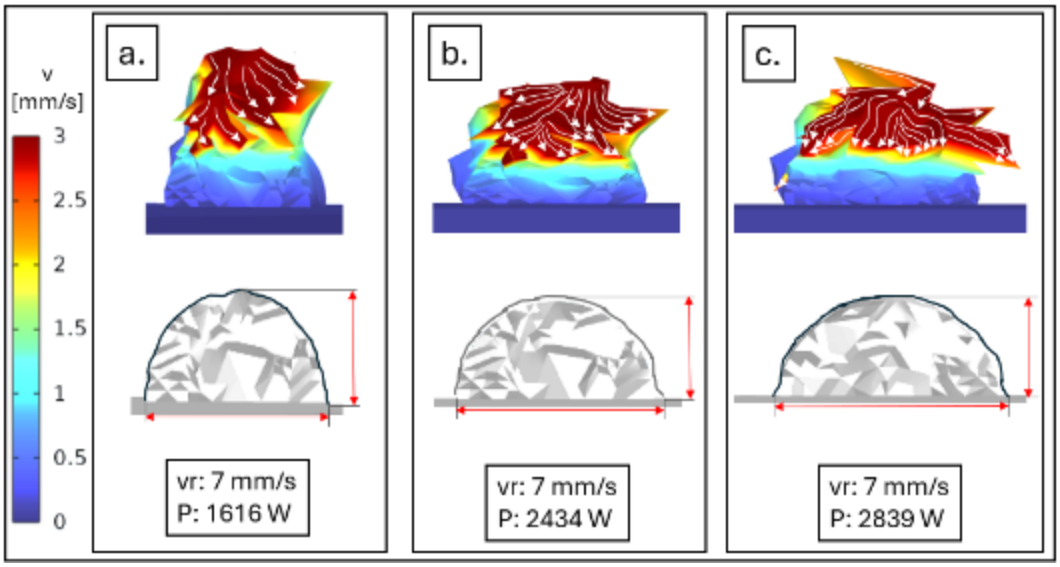

Figure 5-5. Correlation between bead geometry and molten metal flow behavior under a constant deposition speed of 7 mm/s and varying arc powers: (a) 1616 W, (b) 2434 W, (c) 2839 W.

Consistent with the previously discussed improvement in spreading behavior at higher arc powers, the findings in Figure 5 indicate that the temperature-induced enhancement of flow dynamics contributes to flow asymmetry during deposition. This phenomenon is evident from the non-uniform final bead shapes observed at elevated power levels (Figure 5-b–c). This behavior can be attributed to the increased droplet mass resulting from higher arc temperatures. Under a constant wire feed rate, an increase in arc power enhances the melting rate of the filler wire, thereby producing larger molten droplets. These heavier droplets attain higher flight velocities, generating non-uniform flow dynamics upon impact with the substrate. Furthermore, the higher arc power elevates the melt pool temperature, which modifies the viscosity and surface tension of the molten material. The increased fluid mobility amplifies the dynamic response of the pool to successive droplet impacts, ultimately causing asymmetric splattering and geometric irregularities in the final bead profile.

5.8. Wetting Angle

The measured wetting angles of the beads deposited under different processing conditions are listed in Table 5. Among all examined samples, the bead exhibiting a wetting angle closest to the optimal value of 60° was obtained at a deposition speed of 7 mm/s and an arc power of 2839 W. In contrast, only one specimen, deposited at 9 mm/s with the same arc power, displayed a wetting angle below 60°. All other samples showed substantially

higher wetting angles, indicating a tendency toward overspreading of the molten material.

Table 5. Wetting angles of beads deposited under different processing parameters.

v_r [mm/s]		5	5	5	7	7	7	9	9	9
P [W]		1616	2434	2839	1616	2434	2839	1616	2434	2839
wetting angle [°]	**Exp.**	82	77.7	73.8	82.3	65.4	61.7	73.6	67.3	54.7
	Sim.	79.8	74.8	71.9	84.6	67.3	59.4	68.4	64.9	53.5
Relative error [%]		-2.7	-3.7	-2.6	2.8	2.9	-3.7	-7.1	-3.6	-2.2

Figure 6 presents the transverse cross-sections of the deposited specimens, highlighting variations in bead height, width, and wetting angle under different processing conditions. The close agreement between experimental measurements and simulated predictions, supported by generally low relative errors, confirms the accuracy and robustness of the developed numerical model.

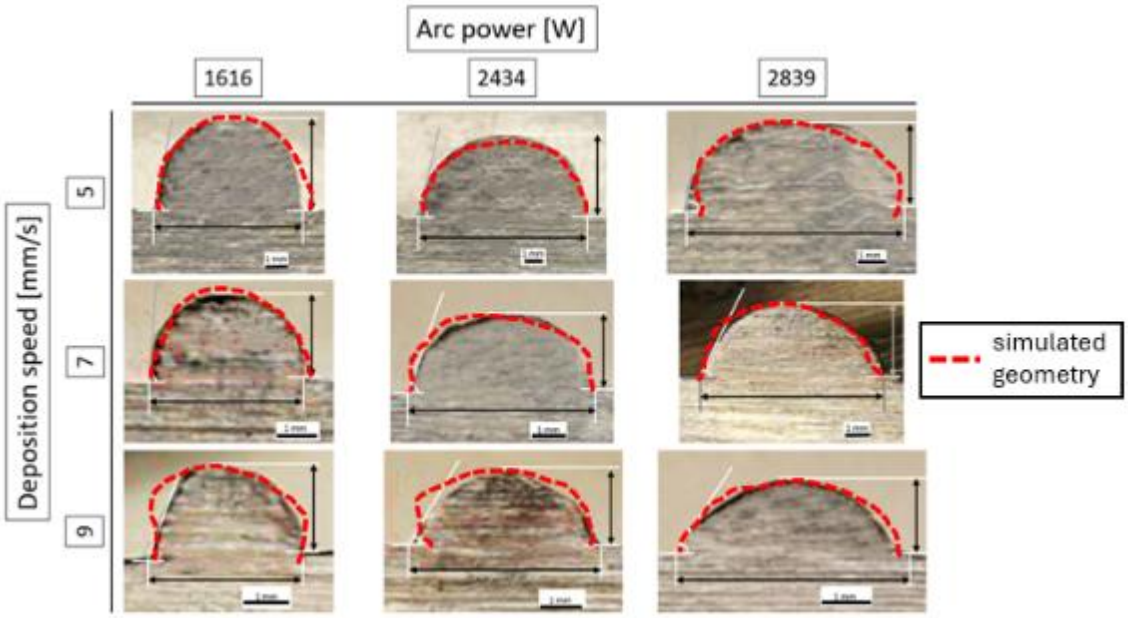

Figure 5-6. Transverse sections of beads deposited under different processing conditions.

In contrast to the previously discussed flow asymmetry caused by increased arc power at a constant deposition speed, the present findings suggest that deposition speed is the dominant factor influencing flow asymmetry. As shown in Figure 6, all specimens produced at a deposition speed of 9 mm/s exhibit a higher degree of asymmetry compared to those fabricated at lower speeds. This can be attributed to the faster solidification rate of the molten pool, which reduces the available time for stabilization through surface tension and Marangoni-driven flow. The accelerated solidification also promotes directional solidification, while the rapid displacement of molten material can cause uneven droplet ejection and result in asymmetric flow patterns. As illustrated in Figure 7, higher wetting angles are observed when the material flow vector forms a larger angle with the base plate,

whereas smaller angles between these vectors correspond to lower wetting angles. A combination of low arc power and low deposition speed produced the highest wetting angles, whereas lower wetting angles were achieved under higher arc power and higher deposition speeds. The reduction in wetting angle at elevated arc powers is attributed to enhanced flowability caused by a decrease in fluid viscosity, while at higher deposition speeds, the wetting angle is more strongly influenced by the droplet trajectory and impact dynamics. Simulation results further indicate that, although a correlation exists between the wetting angle and the angle formed by the material flow vector and base plate, the two are not identical. This discrepancy likely arises from non-uniform cooling, thermal shrinkage variations, and spattering phenomena. Therefore, accurate control of bead geometry requires considering WAAM deposition as a complex, dynamic process, where thermal, fluid, and geometric factors interact continuously and influence one another.

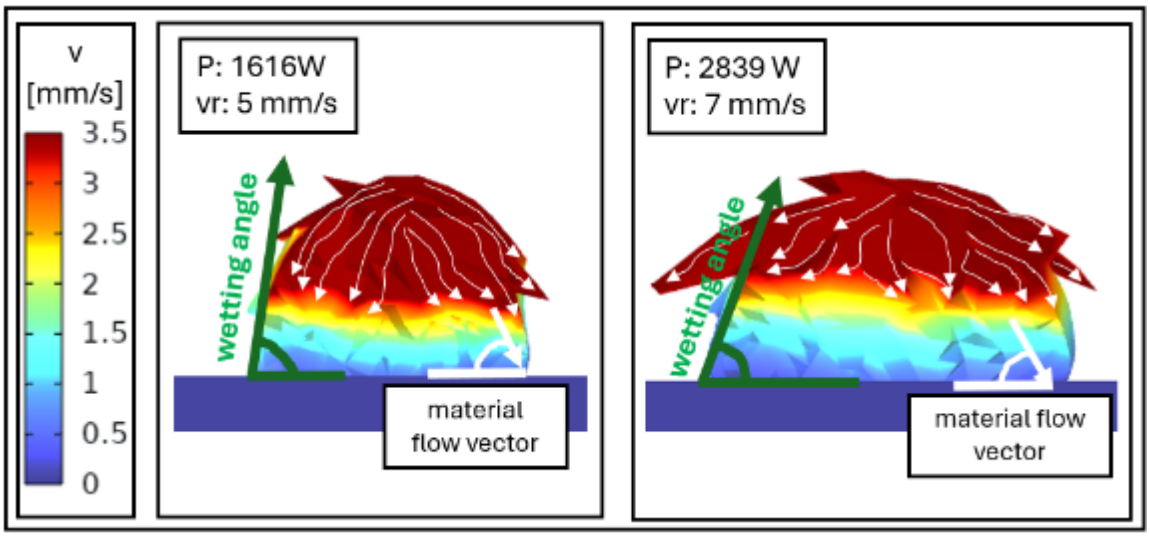

Figure 5-7. Comparison between wetting angles and angles between material flow vector and base plate in specimens deposited under different processing conditions.

5.9. Temperature Profile During WAAM Deposition

The temperature evolution during deposition plays a crucial role in determining both the wetting behavior and the final geometry of WAAM-deposited beads. As illustrated in Figure 8, the recorded temperature profiles at predefined measurement points were significantly influenced by deposition speed. The curves labeled p1, p2, and p3 represent the thermal histories recorded at measurement points 1, 2, and 3, respectively, as defined in Section 2.4. At higher deposition speeds, the overall temperature decreased due to limited heat accumulation time, resulting in altered cooling rates and variations in heat input [164]. The thermal curves for beads deposited at speeds above 5 mm/s display an additional peak corresponding to the initial interaction between the torch (heat source) and the base plate,

where the thermal sensors were positioned. Moreover, the strong agreement between the experimental and simulated temperature curves at all measurement points further validates the reliability of the numerical model.

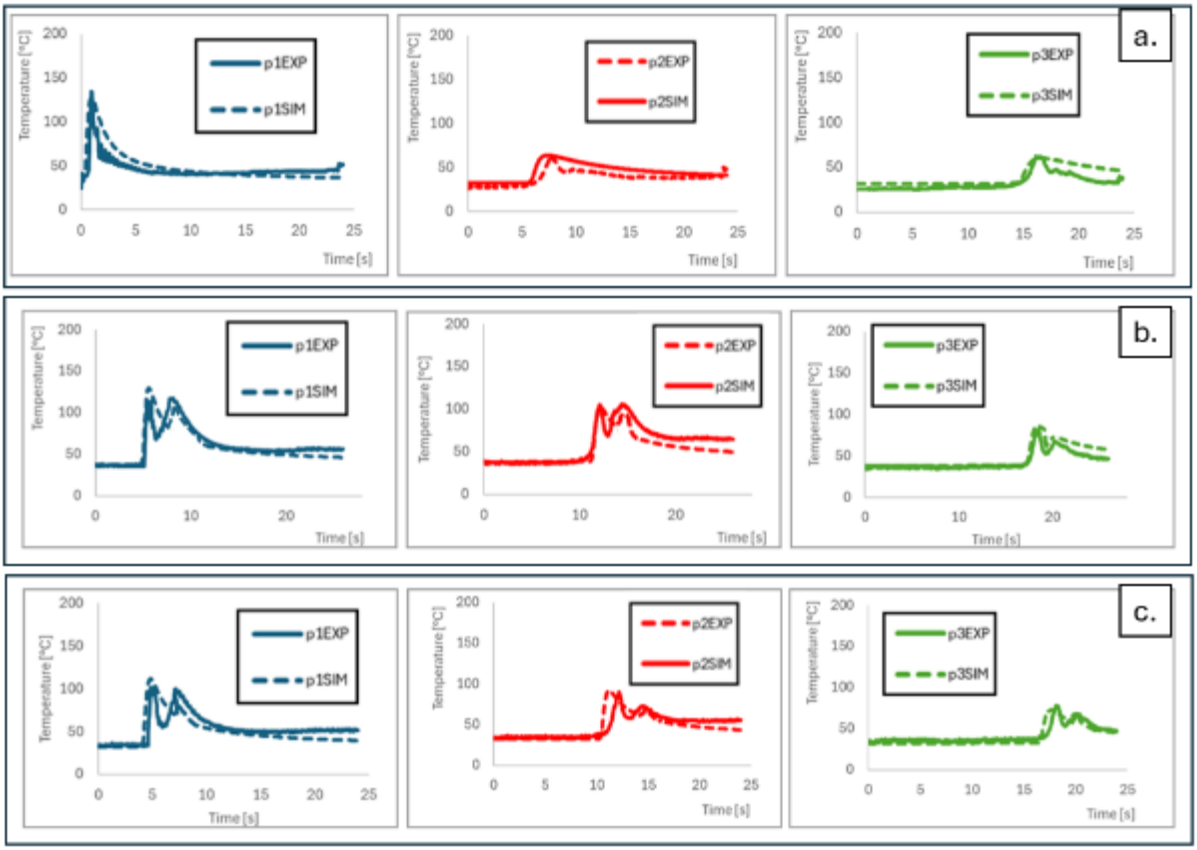

Figure 5-8. Comparison of experimental and simulated thermal curves recorded at predefined measuring points during deposition using an arc power of 2434 W and deposition speeds of (a) 5 mm/s, (b) 7 mm/s, and (c) 9 mm/s.

The specimens deposited at a velocity of 5 mm/s exhibit a distinct single thermal peak, characterized by a rapid temperature rise as the torch traverses the monitored region. The first measurement point (p1) recorded a markedly steeper temperature gradient compared to points p2 and p3, primarily due to its closer proximity to the torch path. Additionally, heat accumulation within the base plate caused a temperature increase even prior to direct torch contact, influencing the initial thermal response. Previous studies [165, 166] have reported similar findings, emphasizing the impact of base-plate heat accumulation on thermal gradients and cooling rates, which subsequently affect microstructural heterogeneity.

In contrast, the thermal curves obtained during deposition at 7 mm/s and 9 mm/s displayed a distinctive double-peak profile. This phenomenon is likely associated with the injection of an additional molten droplet into the melt pool shortly after the first droplet impact (Figure 9-a). Simulation results show that this secondary droplet enters the melt pool while it remains at elevated temperature, and the previous droplet location is still thermally

distinguishable. Consequently, the melt pool forms an elongated shape with two hot centers connected by a slightly cooler molten bridge. A similar configuration was confirmed through thermal tomography analysis in the experimental observations (Figure 9-b).

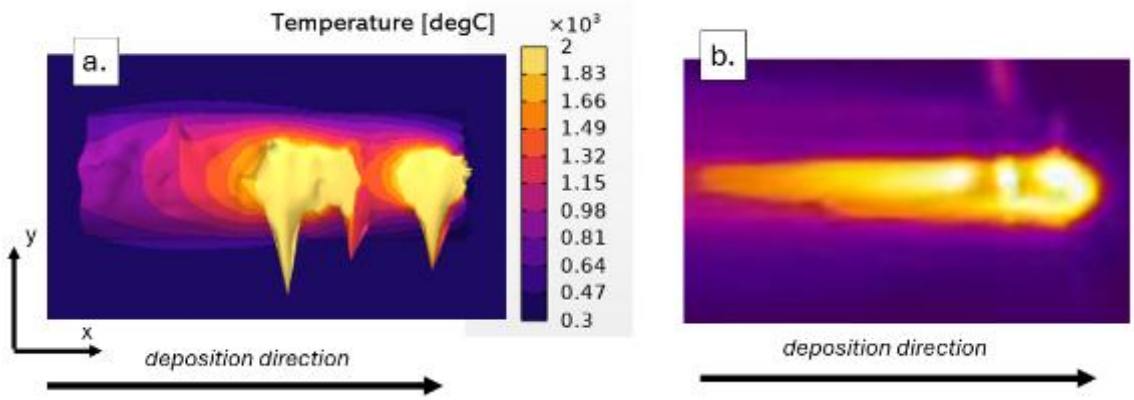

Figure 5-9. (a) Simulated and (b) experimental melt pools showing two hot centers during deposition at a speed of 9 mm/s and an arc power of 2434 W.

As shown in Figure 10, which presents the thermal curves obtained at measurement points p1, p2, and p3 for beads deposited under different process parameters, the arc power exerts a pronounced influence on the shape and magnitude of the thermal peaks, whereas the deposition speed primarily affects the temporal spacing between successive peaks. Consistent with the reasoning and experimental observations previously discussed in Figure 8, an increase in deposition speed beyond 5 mm/s introduces an additional peak following the initial deposition event. This secondary peak corresponds to the entry of a new molten droplet into the melt pool. Conversely, simulation results indicate that a deposition speed of 5 mm/s allows sufficient time for the melt pool to stabilize before subsequent material deposition occurs. A further increase in deposition velocity consistently results in a larger time interval between the two peaks, independent of the applied arc power. This phenomenon aligns with the findings of Voropaev et al. [168], who established a relationship between deposition speed and arc stability, leading to variations in metal transfer dynamics. Their study suggests that a higher volume of molten droplets entering the melt pool prolongs its liquid phase, thereby enhancing the spreading behavior of the molten material.

In contrast, the present study reveals that a lower droplet volume, associated with higher relative velocities, induces repeated thermal cycling of the melt pool. This repeated heating modifies both the material properties of the deposited metal and the cooling kinetics of the melt pool, effectively extending the time available for spreading and influencing the overall solidification behavior. Additionally, changes in the droplet ejection dynamics, caused by

variations in deposition speed, result in temporal and spatial inconsistencies in the molten metal's contact with the substrate. These variations contribute to differences in the geometry of the thermal curves, including alterations in peak slope, spacing, and overall peak symmetry.

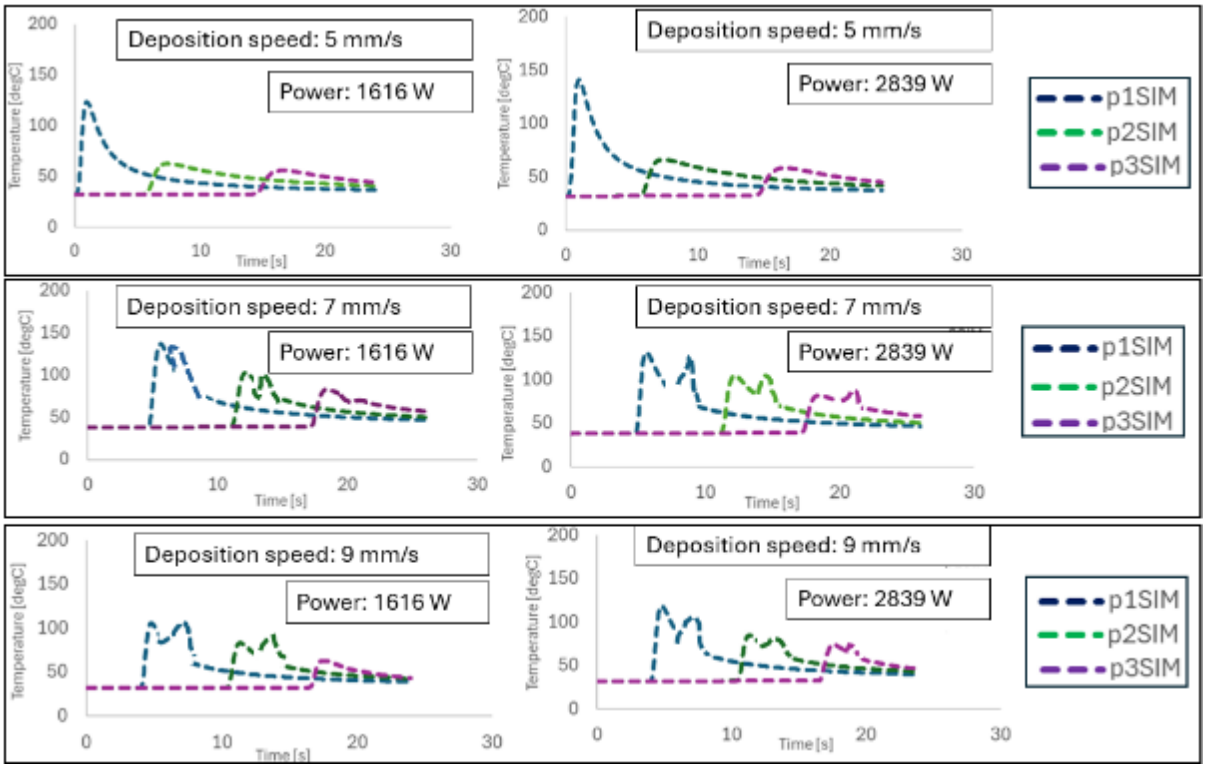

Figure 5-10. Thermal curves of beads deposited under varying process parameters.

5.10. Effects of Arc Power and Deposition Speed on the Geometrical Characteristics of Deposited Beads

The statistical analysis revealed a significant effect of arc power on the aspect ratio of the deposited beads, as indicated by a p-value of 0.000, confirming its strong influence. In contrast, the deposition speed did not exhibit a statistically significant effect, with a p-value of 0.058. As discussed in Sections 3.2 and 3.3, the limited influence of deposition speed on aspect ratio may stem from flow asymmetry observed at higher speeds. Additionally, the Response Surface Methodology (RSM), constrained to a second-order polynomial model, may not fully capture the complex relationship between deposition speed and aspect ratio. Conversely, the arc power demonstrated a clear linear correlation with the aspect ratio, as shown in Figure 11-a. The aspect ratio increased with higher arc power, which is likely related to dilution effects, more prominent under high-power conditions, and their direct impact on bead height. Furthermore, an aspect ratio within the optimal range of 2–3 can be

consistently achieved when the arc power exceeds 1930 W, irrespective of deposition speed, as illustrated in Figure 11-b. This outcome simplifies process control, since maintaining precise control over deposition speed is inherently more challenging due to its complex interaction with melt flow symmetry.

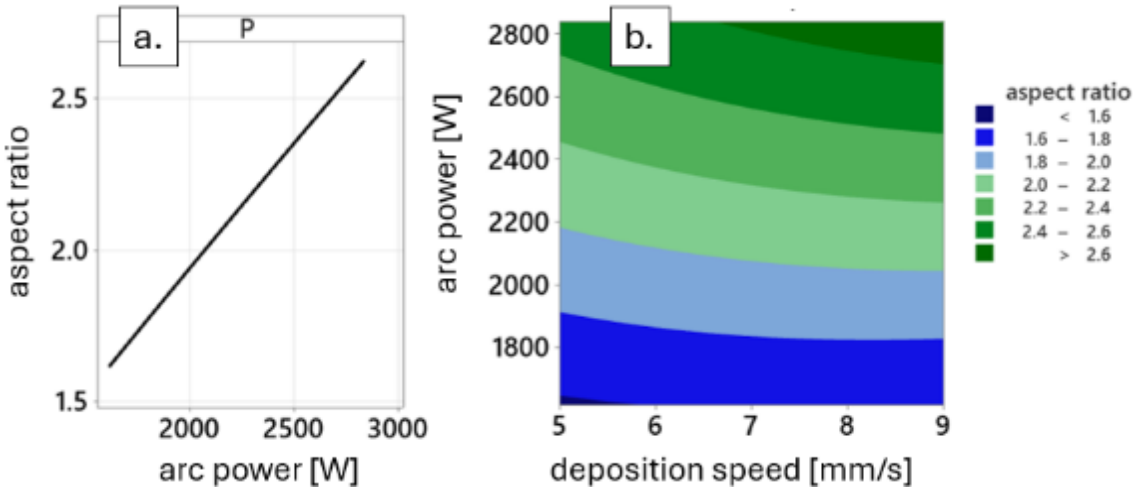

Figure 5-11. (a) Factorial plot and (b) contour plot summarizing the effects of the examined process parameters on the aspect ratio of deposited beads.

The ANOVA results also confirmed that both deposition speed and arc power significantly affect the wetting angle, with respective p-values of 0.041 and 0.019. Similar to the aspect ratio, arc power was identified as the dominant influencing factor, whereas the effect of deposition speed appeared secondary. The results revealed a nearly linear inverse relationship between both process parameters and the wetting angle, as shown in Figure 12-a. Specifically, wetting angles below 60° were obtained for beads produced at a deposition speed of 9 mm/s and arc power of 2839 W, indicating optimal wetting conditions. Conversely, any reduction in either process parameter resulted in increased wetting angles, reflecting poorer spreading behavior, as illustrated in Figure 12-b.

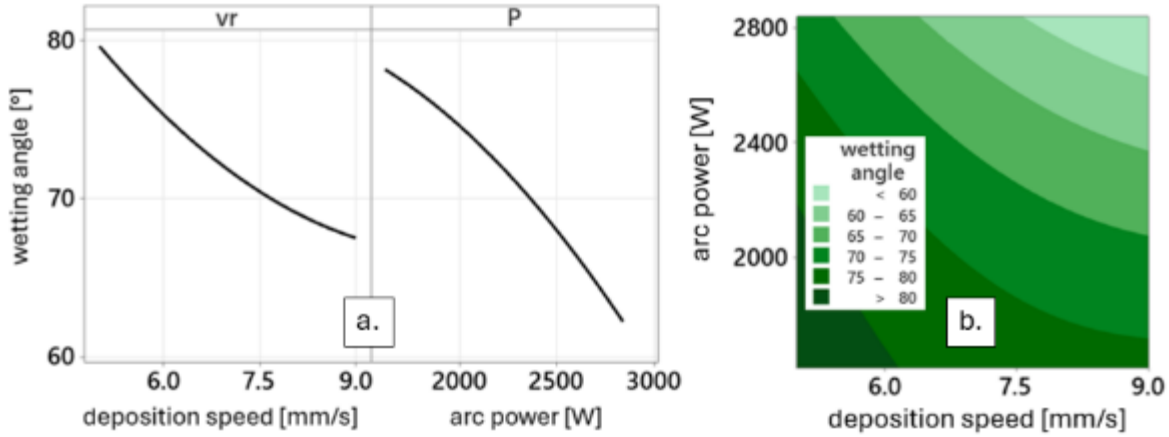

Figure 5-12. (a) Factorial plot and (b) contour plot summarizing the effects of processing parameters on the wetting angle of deposited beads.

The influence of arc power on the aspect ratio is substantial, primarily due to the increased thermal energy input delivered to the melt pool during deposition [169]. This elevated heat input promotes more extensive melting of the filler material [170], thereby increasing the mass of molten metal transferred into the melt pool [171]. As the droplet mass increases, the influence of gravitational forces becomes more pronounced, causing a stronger impact upon contact and enhancing lateral spreading along the melt pool boundaries [172]. Additionally, the higher melt pool temperature lowers the viscosity of the molten filler, further facilitating its flow and spreadability [173].

Several studies [174–177] have shown that the thermal effects associated with deposition speed in the WAAM process exhibit an inverse relationship to those observed with arc power. According to Muller et al. [178], this relationship arises because higher deposition speeds allow less time for the molten pool to spread before solidification occurs. This difference can be attributed to the crucial role of deposition speed in governing molten metal flow dynamics, which are fundamental to the spreading and wetting behavior of the melt pool. Since this fluid motion is typically non-laminar [179], the thermal–fluid interactions in WAAM are highly complex and nonlinear, making it difficult to describe the relationship between process parameters and geometric outcomes through simple linear correlations. As a result, the apparent weaker influence of deposition speed, relative to arc power, may reflect the limitations of linear models rather than an actual lack of physical significance, as supported by the observed variations in bead width and aspect ratio [180].

Graf [181] emphasized that wetting behavior in WAAM is strongly influenced by the temperature-dependent viscosity of the molten filler material. As energy input increases, the molten metal temperature rises, leading to a reduction in viscosity and promoting more effective wetting and spreading. Conversely, Bonn et al. [182] demonstrated that the wetting angle of liquid metals on smooth surfaces depends primarily on the surface tension at the solid–liquid and liquid–gas interfaces. While material properties and temperature are critical factors influencing surface tension [177], several additional variables contribute to this behavior. These include the metal transfer mode, droplet size, gravitational effects on the molten droplets [51], and environmental conditions, such as the shielding gas composition, which can affect the formation of oxide layers [183]. The presence of oxidized films, observed on all deposited beads (see Section 3.1), likely creates interfacial barriers that hinder optimal contact between the molten metal and the substrate. This phenomenon

adversely affects wetting efficiency [180] and consequently alters the geometric quality of the deposited beads.

5.11. Identification of the Optimal Processing Window for Desired Geometrical Characteristics

The identification of the optimal processing window was based on the statistical optimization performed within the same analytical environment used for the preceding evaluations. Target values were set for the bead characteristics as follows: an aspect ratio of 2.5 and a wetting angle of 60°. These targets were selected based on previous studies which identify these values as optimal for achieving defect-free components with enhanced dimensional accuracy and strong interlayer bonding.

During the optimization analysis, both response variables, aspect ratio and wetting angle, were assigned equal weighting to ensure a balanced evaluation of process performance. The composite desirability function was then calculated to quantify the overall optimization efficiency, integrating both predicted and experimental outcomes. The predicted values were subsequently validated by comparison with the experimental data obtained from specimens produced under the identified optimal conditions. Table 6 summarizes the results of the statistical–analytical optimization process. The optimal deposition parameters, deposition speed of 9 mm/s and arc power of 2592 W, produced bead geometries closely matching the target characteristics. The predicted wetting angle (60.79°) and aspect ratio (2.50) corresponded closely with the experimental measurements (58.80° and 2.70, respectively). The model's robustness is further supported by the composite desirability value of 98.22%, confirming the high accuracy and predictive capability of the applied optimization framework. Accordingly, the statistical–analytical methodology employed in this work can be considered validated, offering a reliable basis for predicting and controlling the geometrical outcomes of the WAAM process.

Table 6. Results of the optimization process.

	Identified v_r [mm/s]	**P** [W]	**Wetting angle** [°]	**Aspect ratio**	**Composite desirability** [%]
Predicted outcome	9	2592	60.79	2.50	98.22
Real outcome			58.80	2.70	
Relative error [%]			-3.38	7.41	

The specimen fabricated under the identified optimal processing parameters exhibits a

uniform and symmetrical bead geometry, characterized by a notable penetration of material into the substrate, forming a distinct melt-through (dilution) zone. This dilution occurs as a result of adequate heating of the base material, which becomes sufficiently softened during deposition. When subjected to the combined effects of arc pressure and the impact of the newly deposited molten filler, the softened substrate tends to form a shallow cavity, subsequently filled with molten metal.

The dilution zone is predominantly located beneath the central region of the bead, where the majority of the deposited material accumulates. This concentration of mass increases both the local weight and the pressure exerted on the substrate, promoting its localized deformation. The penetration of molten filler into the substrate or previously deposited layers enhances metallurgical bonding, which can lead to superior mechanical integrity in WAAM-fabricated components [184]. According to previous studies [184–186], dilution is one of the most influential parameters in determining the geometrical features of WAAM-deposited beads. Higher dilution, typically resulting from increased heat input and enhanced mixing between the substrate and filler materials, produces wider and flatter beads [184]. This geometry corresponds to a higher degree of material fluidity and improved lateral spreading under elevated thermal conditions. Conversely, lower dilution leads to narrower and taller beads with steeper wetting angles, as the smaller extent of substrate melting allows the deposited metal to retain its original shape more effectively [186]. A thorough understanding and control of the dilution phenomenon are therefore essential for optimizing bead geometry, achieving uniform layer deposition, and ensuring the desired mechanical performance in WAAM-produced parts [187]. Additionally, the process generated a HAZ within the substrate that experienced thermal alteration without full re-melting, as evidenced by its relatively large extent adjacent to the fusion boundary.

Chapter 6

WAAM Fabrication of CuAl8 and ER70S-6 Cubic Structure

Chapter 6

WAAM Fabrication of CuAl8 and ER70S-6 Cubic Structure

6.1. Manufacturing Process of WAAM Samples

In this study, two commercially available alloys, ER70S-6 low-alloy steel (LAS) and CuAl8, were employed using a WAAM system. The chemical composition of both alloys, determined through a quantimeter analysis in accordance with ASTM E1019 standards, is presented in Table 1. All measurements were performed under controlled laboratory conditions (28 °C and 14% relative humidity). Low-alloy steel substrates were selected to evaluate their electrochemical compatibility with CuAl8 and ER70S-6 [188], as these combinations are considered promising for achieving reliable metallurgical bonding and material integration. Both wires had a diameter of 1 mm to ensure high precision in sample fabrication based on Computer-Aided Design (CAD) models.

Table 1. Chemical composition of CuAl8 and ER70S-6 wires used in this study (wt.%).

Element	Cu	Al	Mn	Pb	Si	Zn	C	P	S	Ni	Cr	V	Nb	Ti
CuAl8	Bal	8.5	0.5	0.02	0.19	0.21	0.4	-	-	-	-	-	-	-
ER70S-6	0.2	-	0.9	-	-	-	-	0.035	0.04	0.2	0.15	0.008	0.008	0.025

The WAAM setup consisted of an *ArCreo* system (Italy) integrated with an *iWave 300* power source (Austria). The wire feeding mechanism was mounted on a collaborative robot (Cobot) head, enabling automated deposition of samples following CAD-defined geometries. The entire system was governed by a PC-based controller to ensure accuracy and reproducibility in the manufacturing process (Figure 1a–b). The deposition process utilized a Cold Metal Transfer (CMT) module. For LAS samples, a shielding gas mixture of 92% argon and 8% CO_2 was used, whereas for CuAl8, ultra-high-purity argon (99.999%) was employed to maintain a stable and consistent arc throughout deposition. During the initial commissioning phase, wall structures of LAS and CuAl8 (5 cm × 8 cm) were fabricated at three different orientations 30°, 60°, and 90° relative to the horizontal (X-axis), to evaluate the maximum feasible deposition angle for complex and bulk components (Figure 1c). Each wall was built with a single-pass arc per layer on the substrate.

In the second stage, bulk samples were produced vertically (90° along the Z-axis) with dimensions of 2.5 × 2.5 × 5 cm^3. A linear "snail-pattern" scanning strategy was adopted (Figure 1d), incorporating a 120-second dwell time between successive layers to allow adequate cooling. This approach balanced the solidification rates of both alloys, promoting uniform interlayer bonding and minimizing the occurrence of defects such as porosity. The

selected pattern yielded defect-free samples for both steel and copper, as shown in Figure 1e–f. The corresponding WAAM input parameters for each sample are summarized in Table 2.

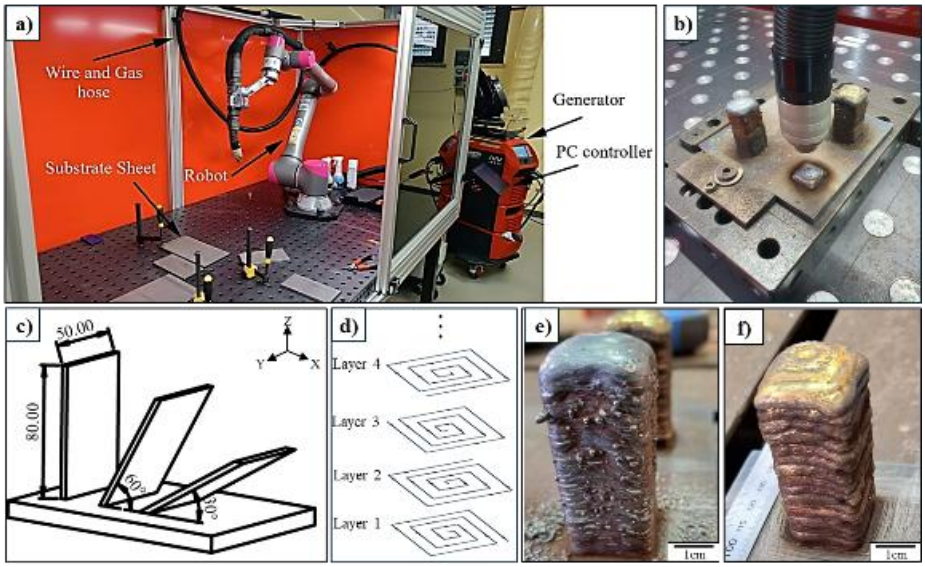

Figure 6-1. WAAM system and sample fabrication steps: (a) Robot and controller; (b) Cobot head; (c) Wall dimensions (mm); (d) Layer fabrication pattern; (e) Steel bulk sample; (f) Copper bulk sample.

Table 2. CMT process parameters used in the WAAM fabrication of ER70S-6 low-alloy steel and CuAl8 samples.

Factors	ER70S-6	CuAl8
Robat Travel speed	10 mm/s	10 mm/s
Wire feeder Rate	4.5 m/min	7 m/min
Voltage	19.9 V (CMT)	12.6 V (CMT)
Current	93 A (CMT)	104 A (CMT)
Wire diameter	1.0 mm	1.0 mm
Type of material	ER70S-6	CuAl8
Type of gas	82%Ar – 18CO2	100 % Ar
Gas flow rate	13.5 l/min	14.0 l/min
Layer thickness	1.5 mm	2 mm
Dwelling time	120 s	120 s
Height of the samples	50 mm	50 mm

6.2. Characterization

A comprehensive set of characterization techniques was employed to evaluate the properties and behavior of the WAAM-fabricated samples. These included microhardness testing, surface roughness analysis, Scanning Electron Microscopy (SEM), advanced electron microscopy, uniaxial tensile testing, and fractographic examination. Together, these analyses provided valuable insights into the microstructural evolution and mechanical performance of the dissimilar materials, supporting further advancements in manufacturing optimization for multi-material WAAM processes.

For metallographic investigations, samples were carefully prepared through standard grinding and polishing procedures, followed by selective chemical etching tailored to each alloy. Optical microscopy was performed using a Keyence VHX-7000 optical microscope to examine the etched microstructures. For steel samples, a 5% Nital solution (5 mL HNO_3 + 95 mL ethanol) was used as the etchant, whereas CuAl8 samples were etched with a ferric chloride-based solution (5 g $FeCl_3$ + 15 mL HCl + 60 mL ethanol) [189].

Advanced electron microscopy analyses were conducted using an FEI Scios 2 HiVac dual-beam microscope equipped with an Oxford AZtecLive Advanced Microanalysis System. This system incorporated an UltiMax 170 large-area analytical silicon drift detector (170 mm^2) for energy-dispersive X-ray spectroscopy (EDS) in combination with Oxford Aztec Energy software. Furthermore, electron backscatter diffraction (EBSD) analysis was carried out using an Oxford Symmetry® S3 detector (1244 × 1024 pixel CMOS sensor) integrated with AZtecHKL software to evaluate the crystallographic orientation and phase distribution.

Mechanical testing included microhardness and tensile property evaluations. Vickers microhardness was measured using a ZwickRoell ZHV30 low-load hardness tester with a 10 g indentation force, following the ASTM E92-17 standard. Uniaxial tensile testing was conducted using an INSTRON 5985 universal testing machine in compliance with ASTM E8-21. Each sample was tested three times to ensure repeatability. The tests employed miniature specimens (25 mm gauge length) and a strain rate of 10^{-3} s^{-1}, with yield strength determined using the 0.2% offset method from the stress–strain curve. Surface roughness measurements were performed using a non-contact optical 3D surface metrology system equipped with a 10× objective lens. This technique evaluates roughness through optical scanning, where variations in reflected light intensity correspond to the topographical features of the surface.

6.3. Microstructural Characterization

6.3.1. Wall Samples

The microstructural examination of the angled-deposited low-alloy steel (LAS) walls provided significant insights into the influence of deposition orientation on the resulting material characteristics. Detailed analyses of macrographs, microstructures, fusion zones, and HAZ were performed to evaluate the thermal effects induced during deposition. Additionally, wetting angle measurements were carried out to determine the optimal deposition orientation for stable layer formation and improved bonding integrity.

Optical micrographs of the ER70S-6 LAS walls deposited at different build angles are presented in Figure 2, illustrating the interfaces between the substrate and the deposited layers as well as the consolidated structure exhibiting a relatively uniform HAZ. The LAS microstructure predominantly consisted of equiaxed and elongated ferrite grains along with dendritic columnar morphologies. At higher magnification (Figure 2-b), the interface displayed a distinct HAZ with an average thickness of approximately 420 μm and a diffusion depth extending up to 1 mm into the substrate. This region reflects the thermal influence of multiple reheating cycles, as the heat from each successive layer affected the microstructure of the previously deposited material.

In the lower layers, the solidification rate was relatively high due to direct thermal conduction into the room-temperature substrate, which acted as a strong heat sink. The rapid cooling promoted the formation of fine columnar dendritic structures, where elongated grains grew parallel to the heat flow direction (Figure 2-c). Such steep thermal gradients and accelerated cooling rates favored columnar grain growth along the solidification direction (Z-axis), corresponding to the 90° build orientation. These columnar grains typically enhance mechanical properties such as strength and directional stiffness [190].

As the number of deposited layers increased, the overall cooling rate gradually decreased. The repeated reheating from subsequent layers raised the temperature of the underlying material, reducing the heat dissipation rate. In addition, limited convection and radiation to the ambient atmosphere contributed to thermal accumulation near the surface [191]. Consequently, a gradual transition from columnar to equiaxed grains occurred in the upper regions of the deposit. Equiaxed grains, characterized by more rounded and randomly oriented structures, form under reduced thermal gradients that allow heat extraction in multiple directions. This microstructural transition is advantageous, as equiaxed grains improve toughness and ductility, properties that are essential for structural reliability in engineering applications [192]. The WAAM process induced complex solid-state transformations in the fusion zone of the 60°-angled LAS wall, as shown in Figure 2-d. The fusion depth measured approximately 1 mm, while the underlying HAZ exhibited a nonuniform thickness of about 480 μm, attributed to the inclined deposition geometry. As illustrated in Figure 2-e, the molten pool dilation area did not maintain the same wetting angle with the substrate. The gravitational influence, combined with surface tension effects, resulted in a slightly wavy wall morphology. The observed variation in HAZ thickness indicates that heat distribution during deposition was uneven, potentially influencing the mechanical performance of the fabricated structure [193, 194].

The characteristics of the HAZ depend primarily on the local heat input, the extent of molten metal dilation, and the maximum temperature reached within the fusion zone. Although the peak temperature during deposition exceeded the critical A_3 temperature, no ferrite-to-austenite transformation was detected. This absence of transformation was likely due to insufficient cooling rates following deposition, which hindered complete austenitic conversion [195]. A closer examination of the conventionally deposited layers revealed the presence of dendritic columnar structures within the fusion zone (Figure 2-f, j). The overall microstructure comprised various ferritic morphologies, including grain boundary ferrite and Widmanstätten ferrite. The coexistence of these features indicates variable cooling rates within different regions of the fusion zone, reflecting localized differences in thermal dissipation and solidification kinetics during the WAAM process [196, 197].

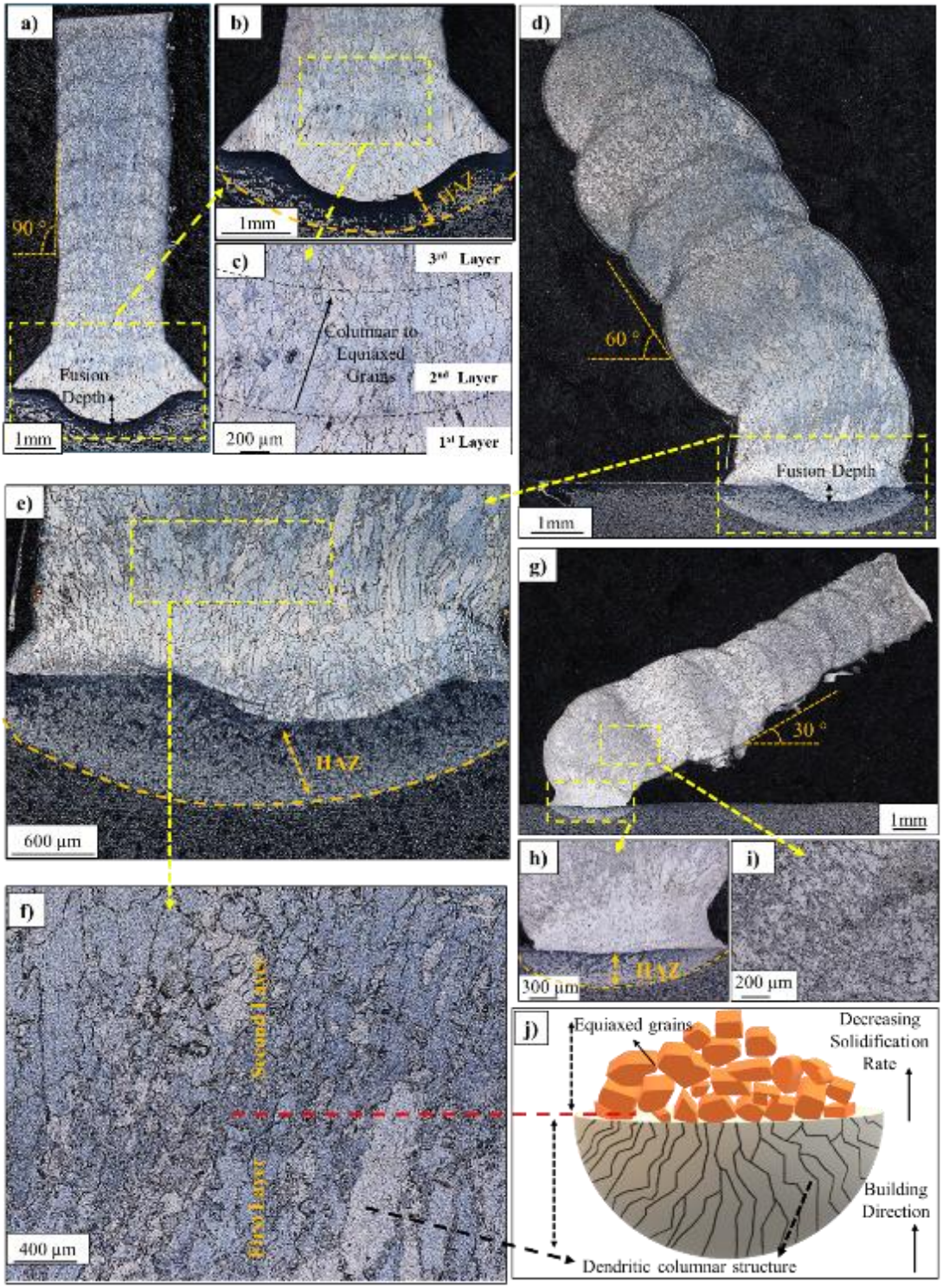

Figure 6-2. Microstructure of the LAS wall samples fabricated via WAAM using ER70S-6 wire:(a) 90° wall sample; (b) HAZ region; (c) Columnar-to-equiaxed grain transition; (d) 60° wall sample; (e) HAZ region and fusion depth; (f) Dendritic columnar structure at first–second layer boundary; (g) 30° wall sample; (h) HAZ and dilation area; (i) Interface between third and fourth layers; (j) Columnar grain formation at first–second layer boundary.

Figure 2-g illustrates the microstructural evolution near the HAZ of the 30° wall sample. In this region, the HAZ closely resembles the fusion zone, exhibiting no signs of plastic deformation or coarse-grained areas. The deposited metal primarily consisted of

Widmanstätten ferrite, non-lamellar pearlite (a mixture of ferrite and carbide aggregates), and grain boundary ferrite, reflecting the influence of the WAAM process parameters on phase formation. These observations align with the findings of Liu et al. [198], who reported similar microstructural features in WAAM-fabricated ER70S-6 steel, identifying Widmanstätten ferrite, non-lamellar pearlite, and grain boundary ferrite as the predominant constituents.

As shown in Figure 2-h, the interface between the first and second deposited layers was free of defects. The solidification morphology indicated that the dendritic columnar grains were oriented along the build direction. However, greater microstructural uniformity was observed in the 90° fabricated wall compared to the 30° and 60° samples. Figure 2-i reveals that the dilation zone in the 30° build was narrower than those observed in the 60° and 90° orientations, which may reduce its ability to withstand high stresses or pressure loads. As deposition progressed, equiaxed grains began to form in the upper layers, corresponding to the reduced solidification rate caused by thermal accumulation. In WAAM processes, each newly deposited layer introduces additional heat to the component, leading to heat buildup that influences process stability, dimensional accuracy, and final material properties. This accumulated heat slows the cooling rate, as the previously deposited layers act as a thermal reservoir, increasing the overall thermal mass of the system [199]. Owing to the low carbon content of the ER70S-6 feedstock wire, the pearlite phase fraction was estimated to be approximately 12% of the total microstructure [200, 201]. Furthermore, the fractions of acicular ferrite and bainite, which tended to form along the fusion boundaries, were negligible in comparison to the dominant ferrite and pearlite phases [202].

The macro and microstructural features of the CuAl8 wall deposited at a 90° build angle are presented in Figure 3-a. Considering the significantly higher thermal conductivity of CuAl8 compared to LAS, rapid solidification occurred during deposition [203]. A similar solidification mechanism to that observed in LAS was evident in CuAl8. The lower region of the sample exhibited a finer microstructure due to rapid cooling facilitated by heat transfer to the cooler substrate [204], while the middle layers displayed comparatively coarser grains resulting from reduced thermal gradients and slower cooling rates.

In Figure 3-b, the absence of darker regions suggests that iron dissolution from the substrate did not occur during deposition. This was achieved by employing a Cold Metal Transfer (CMT) process with a relatively low energy input, preventing excessive melting of

the substrate and thereby avoiding dilution. The reduced energy input also limited wetting between adjacent layers, producing smaller wetting angles as visible in Figure 3-a. Microstructural examination revealed that the CuAl8 deposit consisted primarily of two phases: a β phase (dark regions) distributed along grain boundaries, and an α phase (bright regions) occupying the grain interiors, exhibiting a cellular-dendritic morphology. The α phase possessed a face-centered cubic (FCC) crystal structure, while the β phase exhibited a body-centered cubic (BCC) configuration (Figure 3b–c).

Figure 3-d shows the HAZ within the dilution zone, which extended to a depth of approximately 210 μm. In this region, exposure to elevated temperatures during CuAl8 deposition resulted in localized tempering of the base metal, followed by rapid cooling that produced a fine-grained microstructure. This rapid solidification plays a crucial role in defining the mechanical response of the deposit. The fine-grained structure at the lower region of the sample contributes to increased strength and hardness, attributed to the higher grain boundary density that impedes dislocation motion [205]. Conversely, the coarser grains formed in the mid-layers may slightly reduce strength but enhance ductility, providing a balance between mechanical robustness and deformability [206]. The coexistence of α and β phases indicates a complex microstructural architecture, offering a favorable combination of strength and toughness. The measured HAZ depth of 210 μm further emphasizes the substantial thermal influence of the WAAM process on the substrate, underlining its importance in determining the final performance of additively manufactured CuAl8 components.

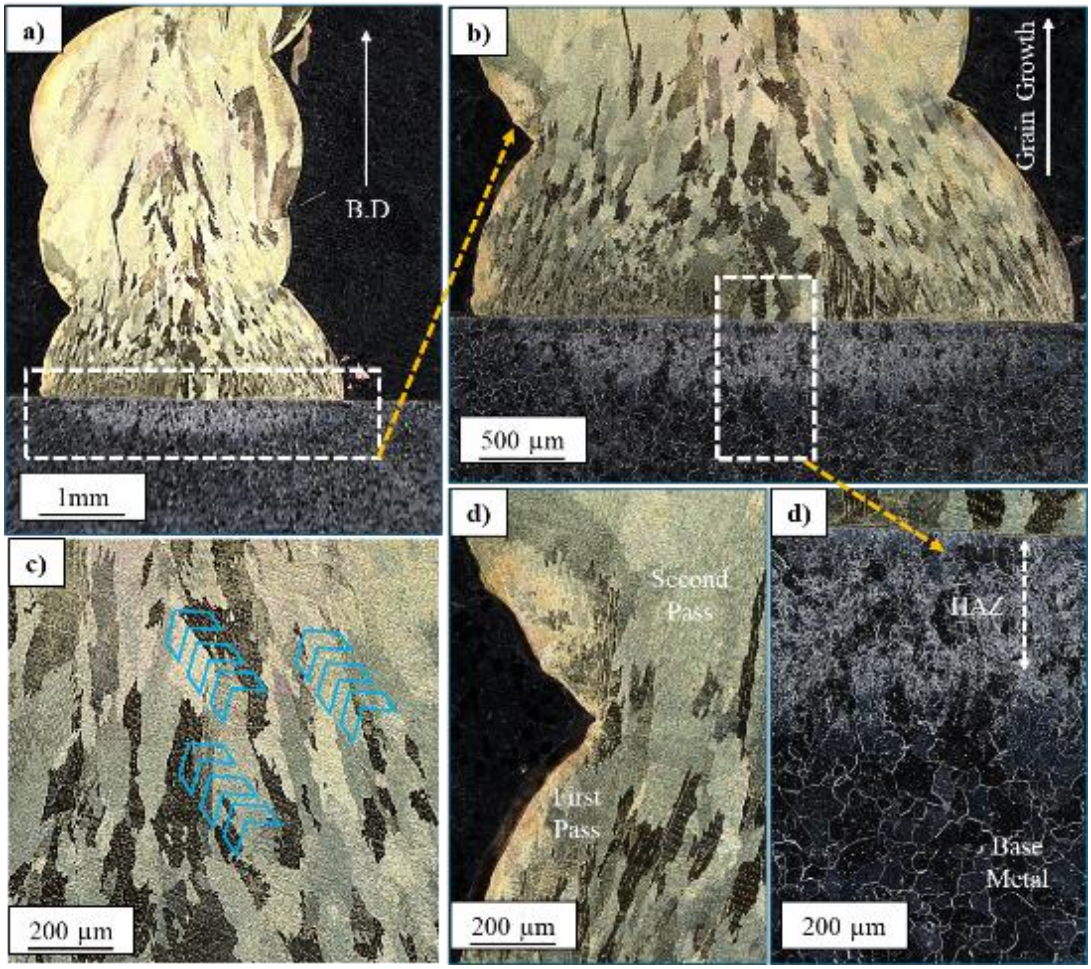

Figure 6-3. Macro- and microstructural analysis of the CuAl8 wall fabricated by WAAM: (a) Macrostructure of CuAl8 wall; (b) Grain growth; (c) Grain formation and phase morphology; (d) Boundary between the first and second deposited layers; (e) Dilution zone and HAZ region.

An increase in voltage and current directly influences the total heat input in the WAAM process, as these parameters determine the electrical power delivered to the arc. Consequently, a higher heat input enhances the thermal energy available for melting and depositing the material [207]. This elevated heat input promotes more extensive melting of the steel, disrupting the crystalline lattice as atoms lose their ordered arrangement at high temperatures. Moreover, the elevated thermal conditions enhance the diffusion of alloying elements, thereby altering both the microstructural evolution and mechanical response of the deposited material. During cooling, rapid solidification can result in the formation of distinct microstructural morphologies, such as dendritic and columnar grains, which critically affect the final mechanical properties of the steel. However, excessive heat input may also enlarge the HAZ, potentially generating residual stresses, microstructural coarsening, and geometrical distortions in the deposited layers [208].

6.3.2. Interface Characterization

The cooling behavior of steel plays a pivotal role in determining its microstructure, with cooling rate and thermal cycling being key controlling factors. Figure 4-a presents the EBSD inverse pole figure (IPF) of the ER70S-6 sample, revealing grain orientation, morphology, and size distributions across the substrate, fusion interface, and deposited regions. During the WAAM process, the high-temperature molten pool partially melts the substrate surface, generating a mixed interfacial region composed of both ER70S-6 and low-alloy steel. This metallurgical mixing zone represents the fusion interface between the deposited and base materials [209, 211]. The EBSD analysis indicates that the average grain size within the HAZ (Zone 1) was approximately 27.8 μm², smaller than that in the middle of the bead (Zone 2 = 50.3 μm²) and in the substrate (Zone 3 = 48.1 μm²). The refined grain structure in the HAZ can be attributed to efficient heat transfer from the molten pool into the substrate, which induced rapid solidification near the interface. The heterogeneity observed within the fusion zone arises from the uneven cooling of the deposited material, resulting from both air convection and heat conduction into the substrate, as well as from incomplete metallurgical mixing of elements with limited mutual solubility. Consequently, grain size distribution in Zone 2 appeared non-uniform, as shown in Figure 4-a [212].

The repeated thermal cycles inherent to the WAAM process significantly influence the microstructure of the HAZ, producing finer grains than those in the consolidated bead or substrate [213, 214]. This grain refinement directly impacts the mechanical behavior, as confirmed by microhardness measurements that revealed higher hardness values in the bead center relative to the adjacent regions. SEM and phase analyses identified the formation of ferritic phases aligned along the Y-axis, contributing to enhanced stability at the critical interface between the deposited layer and the substrate.

The Kernel Average Misorientation (KAM) map (Figure 4-b) further illustrates inhomogeneities in deformation between the substrate and deposited layers. The KAM value was higher in the substrate than in the deposited bead, likely reflecting residual strain induced by solid-state transformations after deposition. Both regions exhibited a face-centered cubic (FCC) crystal structure (Figure 4-c). Pole figure analysis (Figure 4-d) confirmed the absence of significant crystallographic texture variations, as represented by the uniform intensity rings marked by black circles. Following deposition and subsequent air cooling, the grains within the middle region of the fabricated layer exhibited non-uniform alignment, generally

oriented along the direction of heat transfer (Figure 4-e). Vertical samples demonstrated more homogeneous KAM distributions compared to horizontally built samples, indicating uniform strain accommodation and reduced stress concentration in the vertical builds. The KAM values (ranging from 0° to 5°) reflect this uniformity, suggesting that vertical layer deposition leads to more stable mechanical integrity due to consistent thermal histories across multiple layers [215–216].

The {100}, {110}, and {111} pole figures of the WAAM-deposited ER70S-6 sample (Figure 4-d) revealed a weak crystallographic texture with random grain orientations and a maximum intensity of 5.94 above the random background. The KAM map also indicated a high dislocation density surrounding the larger grains within the HAZ. Rapid cooling near the surface in contact with ambient air caused grains to solidify preferentially along the Y-axis, as shown in Figures 4-a and 4-d. Microstructural heterogeneity within the HAZ is evident in Figure 4-a, where most grains in the dilution region exhibit a predominant {100} orientation, consistent with directional heat extraction into the substrate. Elevated local temperatures during deposition facilitated grain boundary migration and localized grain coarsening near the fusion boundary. This effect was most pronounced in the dilution zone, where enhanced thermal interaction with the substrate promoted continued microstructural evolution and modification of grain morphology [217, 218].

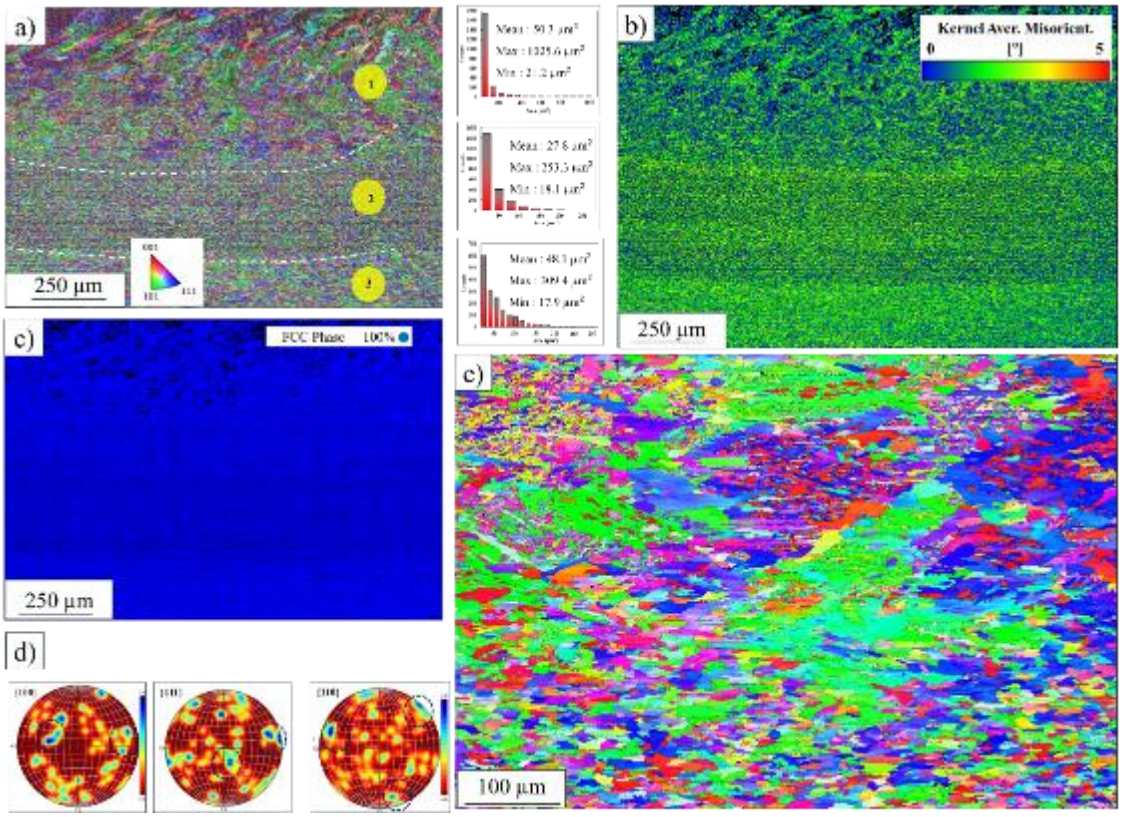

Figure 6-4. EBSD analysis of ER70S-6: (a) Large-area map showing grain sizes in Area 1 (WAAM bead), Area 2 (HAZ), and Area 3 (substrate); (b) Kernel Average Misorientation (KAM) map; (c) Phase detection (FCC); (d) Dilution area image; (e) Pole figures.

Figure 5-a presents the Inverse Pole Figure (IPF) map of the CuAl8 deposition. The deposited layer exhibited larger grain sizes compared to the substrate, primarily due to the slower cooling rate inherent to the WAAM process, which allows more extensive grain growth. This thermal behavior is consistent with heat transfer toward the substrate, resulting in solidification predominantly along the Y-axis, as shown in Figure 5-b. In samples where low-alloy steel (LAS) was used as the substrate for CuAl8 deposition, both materials displayed relatively large grain structures. However, the upper portion of the substrate exhibited finer grains, attributed to localized heat treatment caused by the molten CuAl8 layer. This variation in grain size is likely a result of phase transformations occurring during the copper deposition and subsequent cooling [219, 220].

A 50 µm EDS line scan, starting 25 µm above and ending 25 µm below the CuAl8/steel interface, revealed elemental diffusion across the dilution zone (Figures 5-b and 5-c). The results showed that copper penetrated into the substrate, forming a mixed region with steel. Although the deposition had minimal influence on the microstructure at the center of the CuAl8 bead, it noticeably affected the elemental composition of the fusion zone and dilution area, primarily due to the extent of substrate melting and subsequent elemental diffusion.

EDS analysis at the interface (Figures 5-c and 5-d) indicated greater diffusion of Fe into the deposited layer than Cu into the substrate. This asymmetry arises from the higher affinity of Fe for Al compared to Cu, which facilitates Fe migration toward the substrate [221, 222]. Increased heat accumulation during deposition enlarged the molten pool, prolonged its duration, and intensified convective flow, enhancing Fe–Cu diffusion at the interface and promoting the formation of iron-rich dendritic structures (Figure 5-e).

In the EBSD maps, distinct colors represent different crystallographic orientations, blue for ⟨111⟩, green for ⟨101⟩, and red for ⟨001⟩. The grains in the diffusion zone were smaller than those in the central bead region. This refinement is attributed to rapid solidification along the Y-axis, driven by the cold substrate acting as a heat sink. Analysis of grain boundary orientation differences revealed that most grains near the interface were small-angle grain boundaries (SAGBs) with misorientations <9.5°, whereas the upper bead regions predominantly contained large-angle grain boundaries (LAGBs) exceeding 11.9°. This localized grain refinement and increased dislocation density within the dilution region substantially improved the mechanical strength of the interface [223–225].

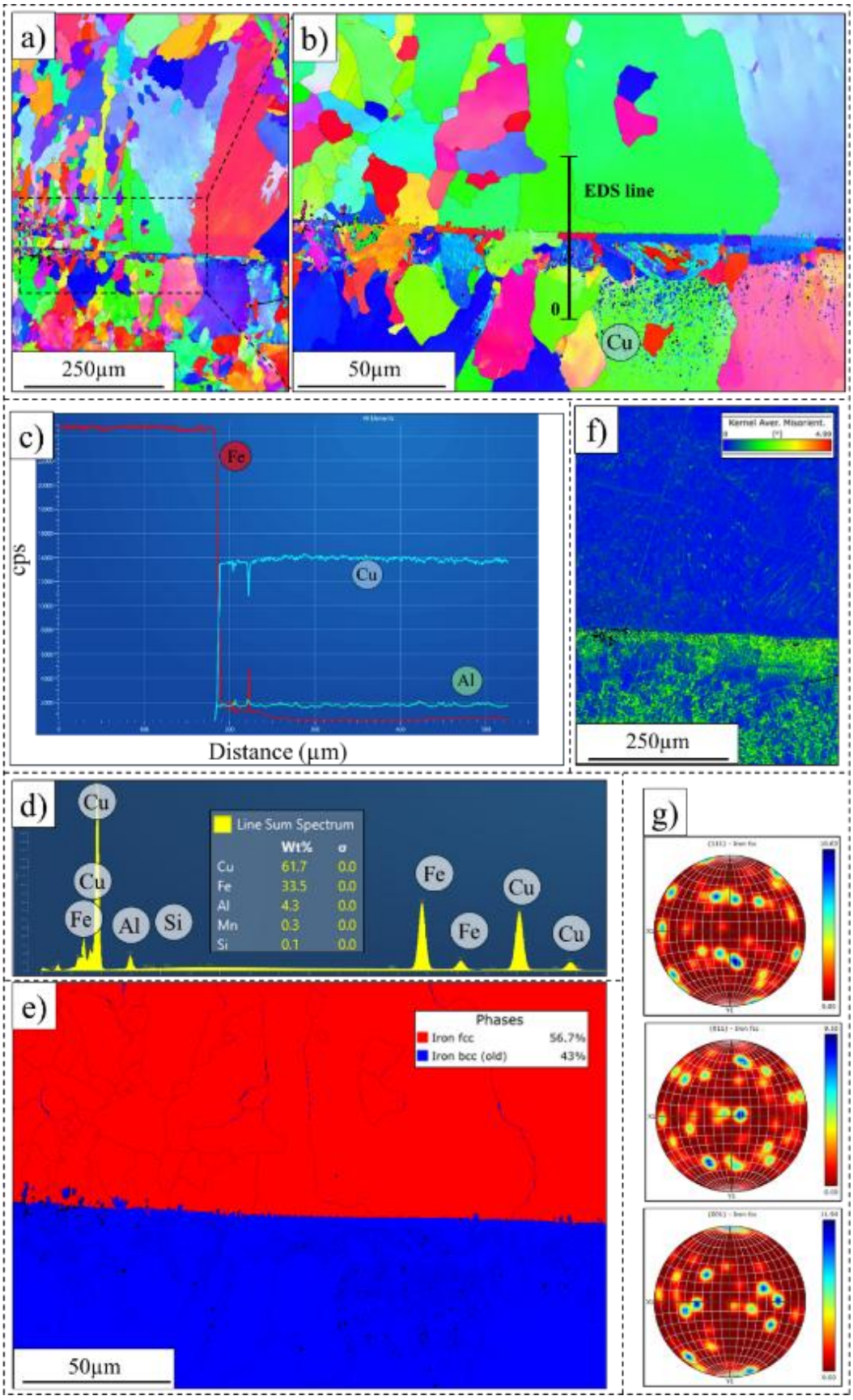

Figure 6-5. EBSD and EDS analysis of CuAl8: (a) Large map image; (b) EDS line-scan direction; (c) Elemental mapping; (d) KAM map; (e) Phase detection; (f) EDS profile; (g) Pole figures.

As illustrated in Figure 5-e, phase distribution mapping revealed that the α-Cu phase (red

regions) with a face-centered cubic (FCC) structure accounted for 56.7% of the total area, while the β (or β′) phase (blue regions) with a body-centered cubic (BCC) structure constituted 43%. The fusion zone was predominantly composed of the α-Cu phase, with minor β(β′) phase fractions. The pole figure of the FCC phase (Figure 5-g) exhibited a maximum polar density of 11.94, suggesting a high degree of anisotropy and a weakly textured grain orientation. The KAM map (Figure 5-f) showed a low misorientation rate within CuAl8, attributed to the predominance of low-angle grain boundaries (LAGBs <10°), which maintain structural coherence. Additionally, the high thermal conductivity of copper relative to steel mitigated thermal stresses and minimized lattice misorientation, promoting improved interlayer bonding and dimensional stability [226, 227].

6.4. Mechanical Characterization

6.4.1. Uniaxial Tensile Testing

Figure 6-a presents the results of uniaxial tensile testing for the steel–steel bulk sample, showing failure occurring in the midsection rather than at the interface, confirming strong metallurgical bonding between the deposited ER70S-6 layers and the steel substrate. Microstructural evaluation of the fractured specimen verified the absence of defects such as pores or cracks in the initial deposited layers of the cubic sample.

The engineering stress–strain curve (Figure 6-b) demonstrated an ultimate tensile strength (UTS) of 371 MPa and an elongation of 35% prior to fracture, indicating good ductility. SEM fractographic analysis (Figures 6-c and 6-d) revealed a uniform fracture morphology with a homogeneous surface texture, suggesting ductile failure dominated by microvoid coalescence. Distinct zones within the fractured surface corresponded to individual deposited layers (see Figure 1-d), while others aligned with interlayer interfaces. The slightly softer regions at these interfaces are attributed to the localized fusion and reheating of adjacent layers during deposition, consistent with typical microstructural transitions in additive manufacturing [228].

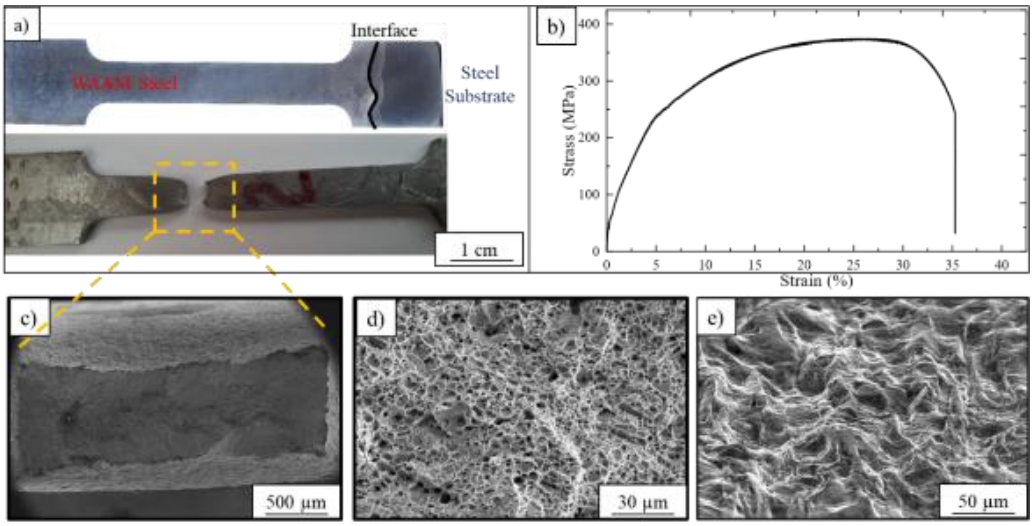

Figure 6-6. Overview of the uniaxial tensile test for the steel–steel WAAM sample: (a) Dog-bone specimens before and after testing; (b) Tensile fracture; (c) Load–extension diagram; (d) Fractography of the steel–steel interface; (e) Central region of the tensile fracture; (f) Edge region of the tensile fracture.

Figure 7-a shows an overview of the uniaxial tensile test conducted on the cubic CuAl8 sample. A comparison between the stress–strain curves of CuAl8 and ER70S-6 (Figure 7-b) reveals that the copper specimen failed at a significantly lower stress of 169 MPa, whereas the steel sample exhibited superior strength. As shown in Figures 7-c, 7-d, and 7-e, the CuAl8 sample displayed a non-uniform fracture surface, with failure propagating across multiple deposited layers. This heterogeneity indicates that fracture occurred along regions of differing metallurgical integrity, likely influenced by the larger grain size of CuAl8 and the weaker interfacial bonding between the copper and steel layers. The latter can be attributed to mismatches in their thermal expansion coefficients, which introduce thermal stresses during solidification.

In contrast, the ER70S-6 steel sample demonstrated a more homogeneous fracture and higher tensile strength, resulting from its finer grain size and stronger metallurgical interface with the low-alloy steel substrate. These findings underscore the critical role of grain morphology, thermal compatibility, and interfacial bonding in defining the mechanical performance of additively manufactured bimetallic components [229, 230].

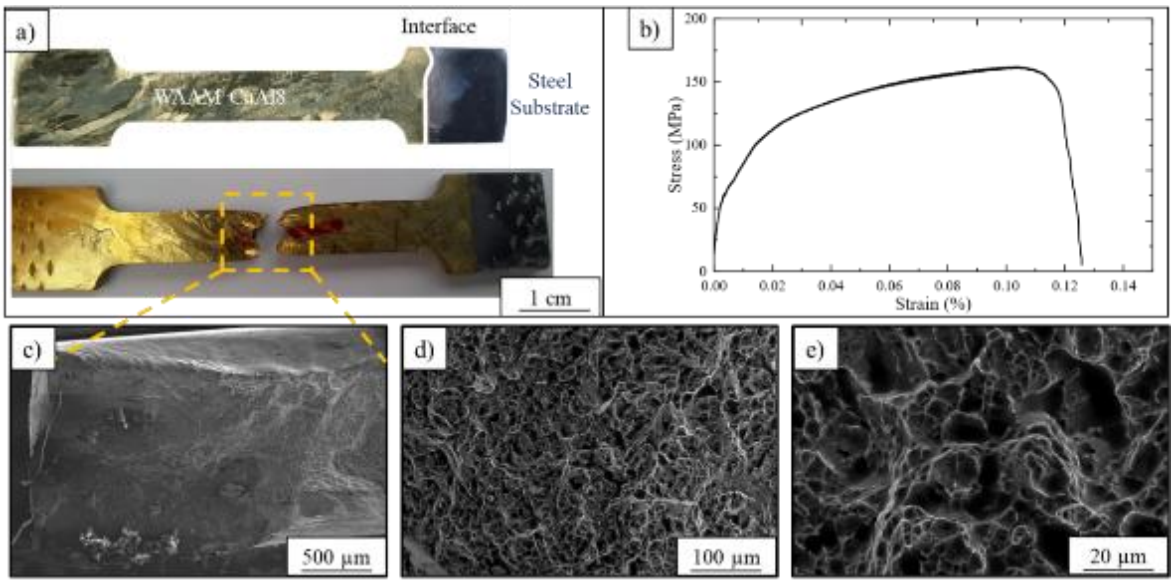

Figure 6-7. Overview of the uniaxial tensile test for CuAl8–steel samples:
(a) Dog-bone specimens before and after testing; (b) Tensile fracture; (c) Load–extension diagram; (d) Fractography of the CuAl8–steel interface; (e) Central region of the tensile fracture; (f) Edge region of the tensile fracture.

6.4.2. Surface Roughness and Microhardness

Considering the arc power and deposition rate, the resulting bead geometry significantly influenced the surface roughness, following a pattern similar to that observed in CMT–WAAM processes. Figure 8-a illustrates the method used to calculate the ideal plane for roughness evaluation, where surface points were fitted using the least-squares method. To ensure precision, each roughness (Ra) measurement was repeated three times in different orientations, and the average value was reported for each condition.

The average surface roughness (Ra) values were 0.61 mm for the CuAl8–steel samples and 0.46 mm for the ER70S-6–steel samples. The higher roughness in CuAl8–steel specimens is attributed to the higher wire feed rate of 7 m/min, compared to 4.5 m/min for steel. Increasing the feed rate resulted in greater material deposition per layer, producing thicker beads and more pronounced peak-to-valley roughness at interlayer interfaces [231, 232]. Conversely, reducing the CuAl8 feed rate to 4.5 m/min caused incomplete deposition and slag formation, particularly in the wall samples.

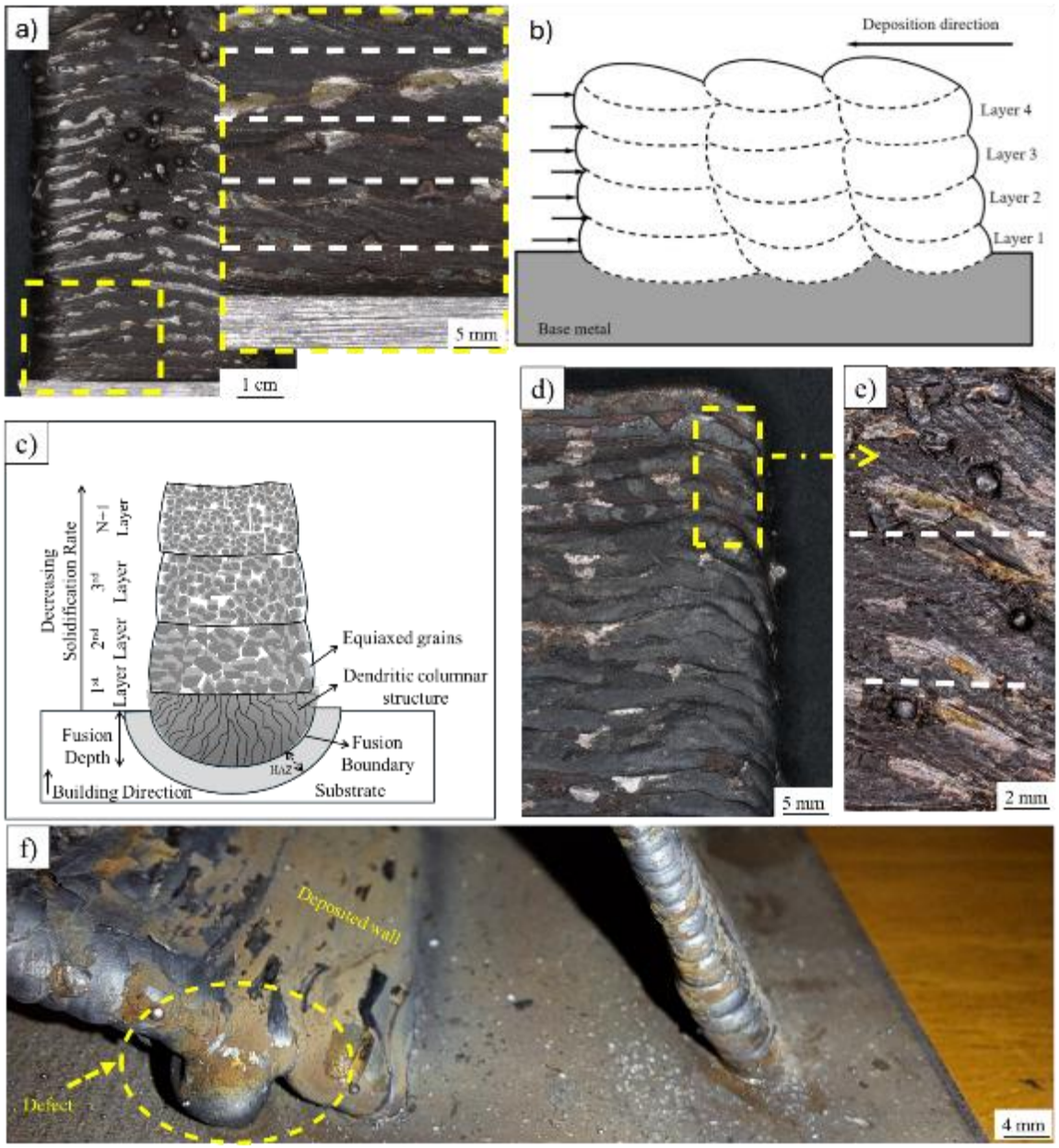

Figure 6-8. (a) Roughness of deposited layers; (b) Wall waviness defects; (c) Schematic of multilayer bead deposition; (d) Top view of steel–steel wall fabrication; (e) Uniform layer formation; (f) Fabrication defects in 60° WAAM deposition.

The deposition pattern also influenced surface uniformity due to the directional nature of bead placement. Improved process parameter control can minimize such variations, as shown in Figure 8-b. The wall waviness at the edges further affected the overall build quality and dimensional precision. The top sections of the walls experienced slower cooling rates, which led to differences in grain formation compared to the underlying layers. Consequently, the top beads exhibited more uniform morphology and reduced solidification rates, resulting in smoother surfaces (Figure 8-c).

Observation of wall fabrication (Figures 8-d and 8-e) confirmed that uniform layer deposition was achieved at a 90° build orientation, while the 60° angled samples displayed

slag-related surface defects caused by gravitational effects and variable cooling rates (Figure 8-f). These process-induced irregularities contributed to increased roughness and waviness, impacting the surface integrity of the manufactured components [233, 234].

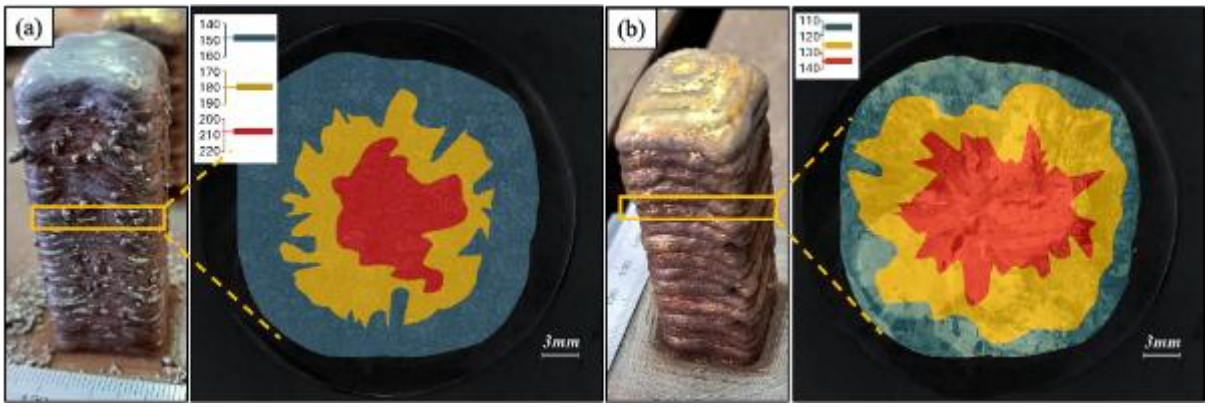

Figure 6-9 Presents the microhardness distribution maps for a) steel–steel b) steel-copper cubic samples fabricated by WAAM

- 140–169 HV (blue),
- 170–199 HV (yellow),
- 200–220 HV (red).

For CuAl8, as shown in Figure 9-b, the hardness ranges were:

- 110–120 HV (blue),
- 121–130 HV (yellow),
- 131–140 HV (red).

The microhardness mapping revealed that both materials exhibited higher hardness values at the cube centers, though distinct differences were observed between the two samples. These variations correspond to differences in solidification dynamics during the WAAM process. EBSD analysis indicated that finer grains concentrated at the cube centers resulted from the transition from columnar dendritic growth to equiaxed grains, driven by the high cooling rates during deposition. This grain refinement enhanced hardness, as smaller grains restrict dislocation motion and improve resistance to plastic deformation [235, 236]. In CuAl8 samples, heat was more effectively distributed toward the center, promoting finer grain formation and thus higher localized hardness. However, due to copper's superior thermal conductivity, the overall cooling rate was higher than that of ER70S-6, leading to a smaller low-hardness region (110–120 HV). This contrast underscores the influence of

thermal conductivity, cooling rate, and grain structure on the hardness distribution in WAAM-fabricated components.

Chapter 7

Laser Hybrid Arc Welding of WAAMed ER70S-6/AISI 308L SS Plates with AISI 316L SS

Chapter 7

Laser Hybrid Arc Welding of WAAMed ER70S-6/AISI 308L SS Plates with AISI 316L SS

7.1. Materials and Fabrication

7.1.1. Base Materials and WAAM Fabrication

Utilizing steel sheets made from AISI 308L stainless steel and ER70S-6 low-alloy carbon steel, fabricated via the WAAM process. The chemical composition of the base steels is provided in Table 1. A collaborative robot (cobot) was employed for precise deposition (Figure 1-c). The resulting plates had a thickness of approximately 3 mm and a height of 96 mm. The additive manufacturing parameters were carefully controlled. For AISI 308L, the settings were 11.1 V, 72 A, and a wire feeder rate of 3.5 m/min. For ER70S-6 steel, the parameters were 14.8 V, 125 A, and a feeder rate of 4.5 m/min. A Fronius welding generator operating in CMT mode was used. To ensure uniform structure and well-bonded beads, the deposition and torch angle were set at 90 degrees (Figure 1-d), the robot speed was maintained at 10 mm/s, and the shielding gas (99.9999% argon) flow rate was fixed at 14.0 l/min. A dwelling time of 120 seconds per layer was implemented to allow for proper solidification (Figure 1-e).

Table 1. The chemical composition of the steels used in this research (Wt.%)

	C	Cu	Ni	Cr	V	Si	P	Nb	Mo	Mn	S	Fe
AISI 316L SS	0.030	-	14	18	-	1.05	0.045	-	-	3.01	0.03	Bal.
ER70S-6	0.135	0.02	-	0.02	0.058	0.01	0.014	0.021	-	0.86	0.11	Bal.
AISI 308L SS	0.020	0.75	10	20	-	0.45	0.020	-	0.4	1.50	-	Bal.

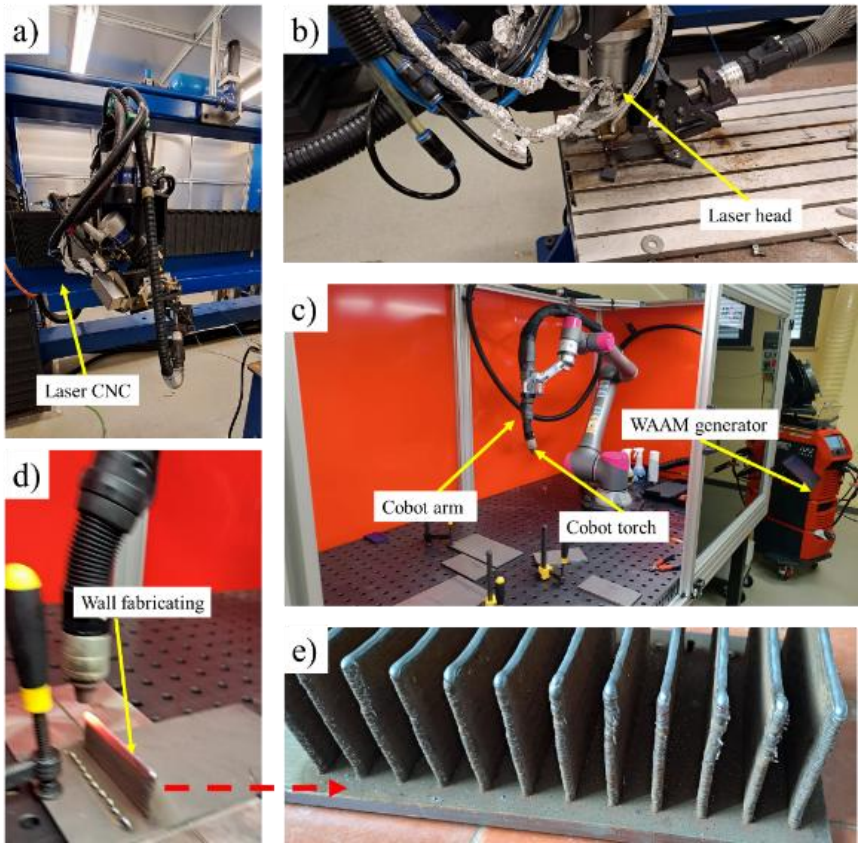

Figure 7-1. a) Laser equipment, b) Laser head set up, c) Wire arc additive manufacturing machine with robotic arm, d) Robot processing the WAAM, e) Fabricated plates.

7.1.2. Pre-Weld Preparation

After fabrication, the WAAM plates were separated from the substrate. Their edges were then milled to create an 80-degree V-groove to facilitate the subsequent laser welding operation. AISI 316L stainless steel, with a thickness of 0.7 mm, was selected as the filler material for the hybrid welding process.

7.2. Laser Hybrid Welding Process

The laser/MIG hybrid welding process was conducted using a 4-kW laser system. Four distinct parameter sets were applied, with laser power ranging from 1000-1500 W and laser scanning speed from 1000-1500 mm/min, as detailed in Table 2. High-purity argon (99.9999%) was used as the shielding gas. The laser head, controlled by a Computer Numerical Control (CNC) system, moved along the X-axis. The steel plates were securely clamped to prevent distortion, and the gap between them was maintained below 0.2 mm for all samples. The stand-off distance between the laser head and the workpiece was set at 18 mm. Preliminary tests were conducted to determine effective parameters and ensure adequate penetration before finalizing the settings for the four main samples.

Table 2. Dissimilar laser hybrid welding parameters on AISI 308L/ER70S-6 WAAM plates

Sample number	Laser speed (mm/min)	Laser power (W)	Arc Voltage (V)	Arc Current (A)	Torch Angle (˚)
#1	1000	1000	20.2	94	41
#2	1500	1000			
#3	1000	1500			
#4	1500	1500			

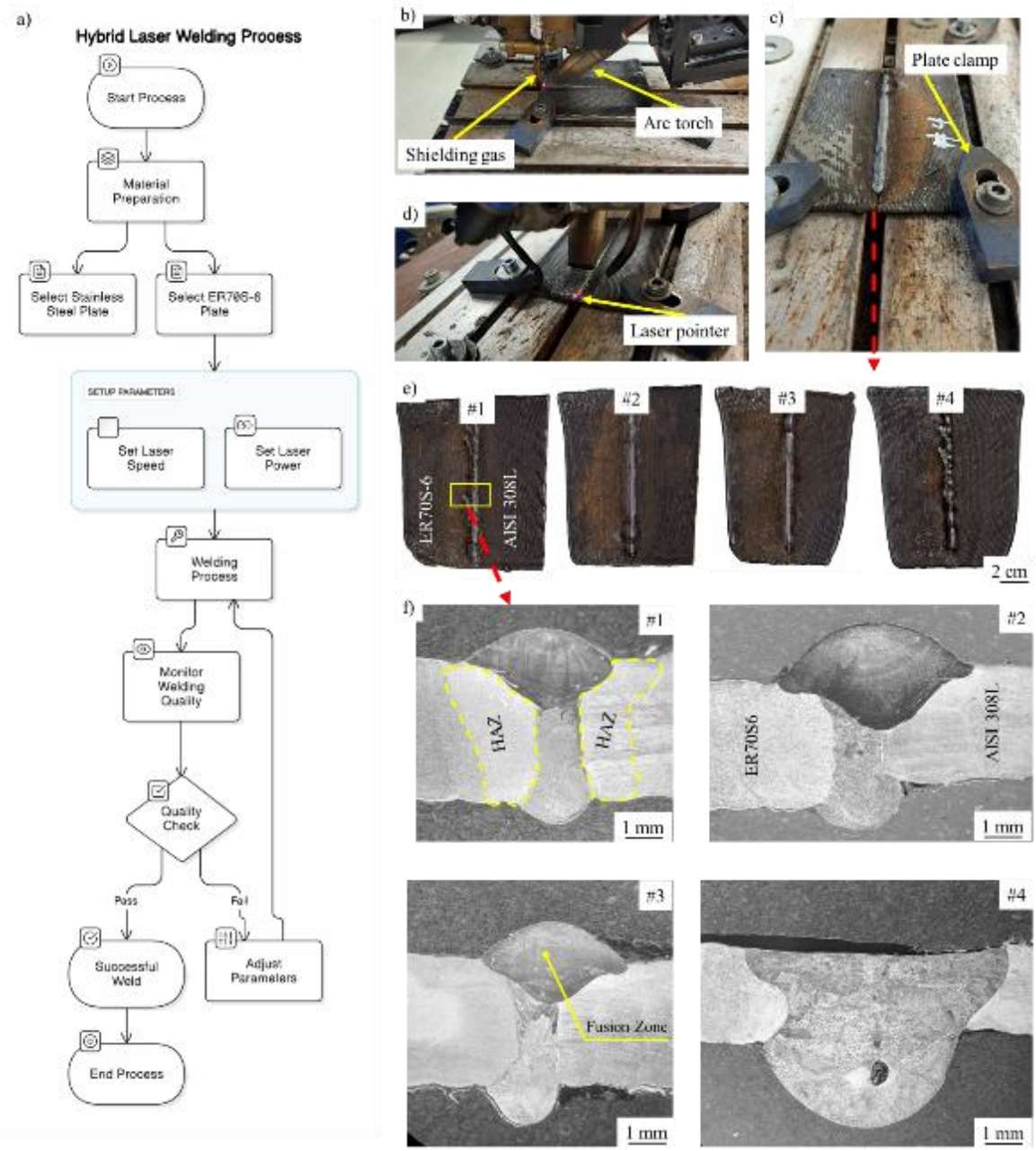

Figure 7-2. a) Flow chart of the welding process, b) Welding process set up, c) Clamping the plates, d) Position of the laser, e) Welded samples, f) Cross section of the welds.

7.3. Material Characterization and Mechanical Testing

7.3.1. Microstructural Analysis

Following welding, cross-sectional samples were extracted from the weld zone, mounted, and polished using abrasive paper with grit sizes from 150 to 2500. The specimens were etched using Carpenter solution and 5% Nital according to standard procedures. Initial microstructural imaging was performed with an Olympus LEXT OLS3000 optical microscope. For detailed analysis, Scanning Electron Microscopy (SEM) was carried out using a Carl Zeiss Merlin microscope equipped with an Energy-Dispersive X-ray Spectroscopy (EDS) detector.

X-ray Diffraction (XRD) analysis was used to determine the phase composition in critical regions like the weld boundary and fusion zone. Electron Backscatter Diffraction (EBSD) was employed to analyze grain orientation and size.

7.3.2. Mechanical Testing

Microhardness measurements were taken across the weld cross-section using a DuraScan G5 Vickers hardness tester with a 200 g load and a 15-second dwell time. Indentations were made at 200 μm intervals. Tensile specimens were prepared according to the ASTM E8:21 standard [237]. Uniaxial tensile tests were conducted using a 25 mm extensometer at a strain rate of 10^{-4}/s. All experimental procedures were performed under controlled laboratory conditions (22 ± 1°C, 45 ± 5% relative humidity) to ensure consistency and prevent environmental influences on the results, as suggested in the literature [238].

7.4. Discussion

7.4.1. Microstructural Analysis of the Weld Zone

7.4.1.1. Weld Bead Morphology and Ferrite Formation

Figure 3-a shows the weld bead peak for Sample #2 (1000 W, 1500 mm/min), where the AISI 316L filler was deposited between the two plates. A magnified view of the top corner (Figures 3-b and c) reveals the presence of lathy ferrite. This needle-like structure forms due to rapid cooling, with its alignment along the cooling direction resulting from directional solidification, which can induce anisotropy in properties like toughness and ductility.

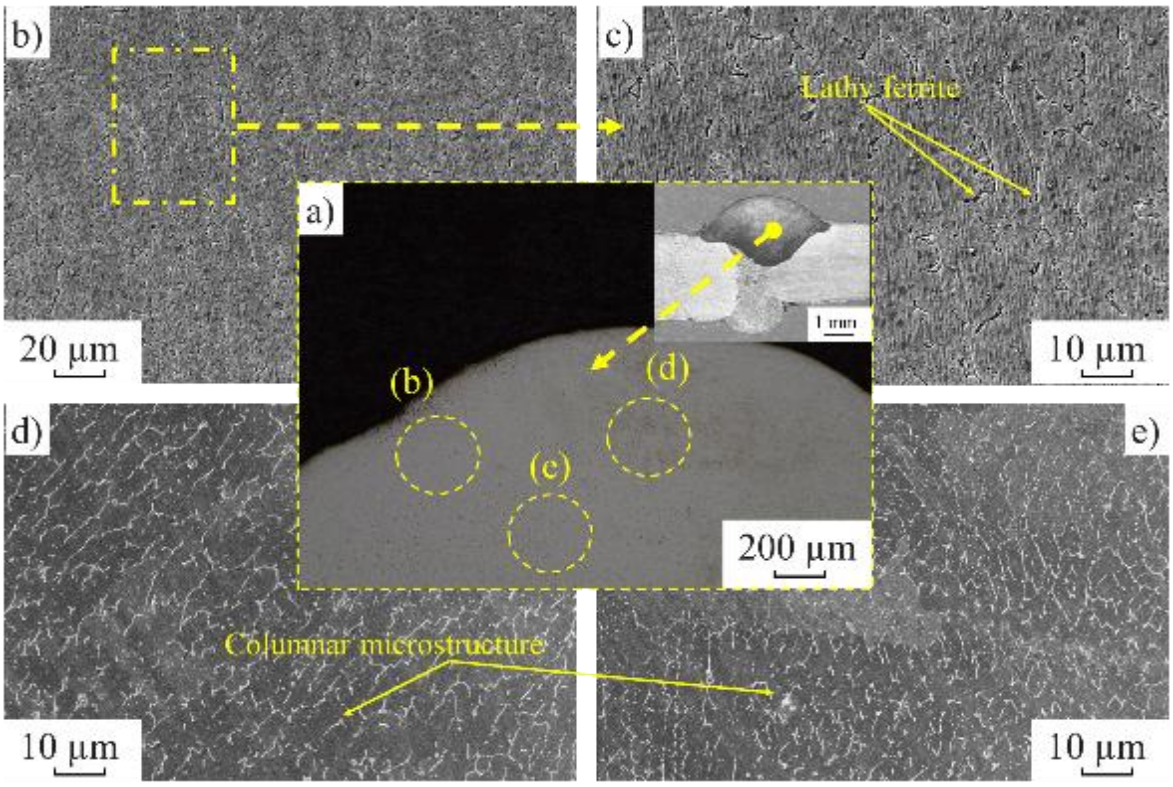

Figure 7-3. a) AISI 316L SS weld peak on sample #2, b) Corner peak weld, c) Lathy ferrite formation, d) Columnar formation in the top center, and e) middle of the bead peak.

7.4.1.2. Columnar Grain Growth

Figures 3-d and e display a columnar microstructure, consisting of elongated grains growing perpendicular to the weld interface from the HAZ towards the weld center. Slight variations in the grain orientation between the figures are attributed to differences in local cooling conditions or weld geometry. This columnar structure leads to anisotropic mechanical properties, where strength is higher parallel to the grain growth direction, though grain boundaries can act as potential sites for cracking.

7.4.1.3. Phase Transformation Analysis via XRD

XRD analysis (Figure 4-c) confirmed the presence of austenite (γ-Fe) and delta-ferrite (δ-Fe) [239, 240]. A comparison between Sample #1 (lower power) and Sample #3 (higher power) revealed distinct phase transformations. In Sample #3, increased intensities for the (111) and (220) γ-Fe peaks indicated a higher austenite fraction, while the decreased (110) δ-Fe peak intensity confirmed a reduction in retained ferrite. This shift is due to extended high-temperature exposure and slower cooling rates at higher heat inputs, promoting the δ → γ transformation (Figure 4-d).

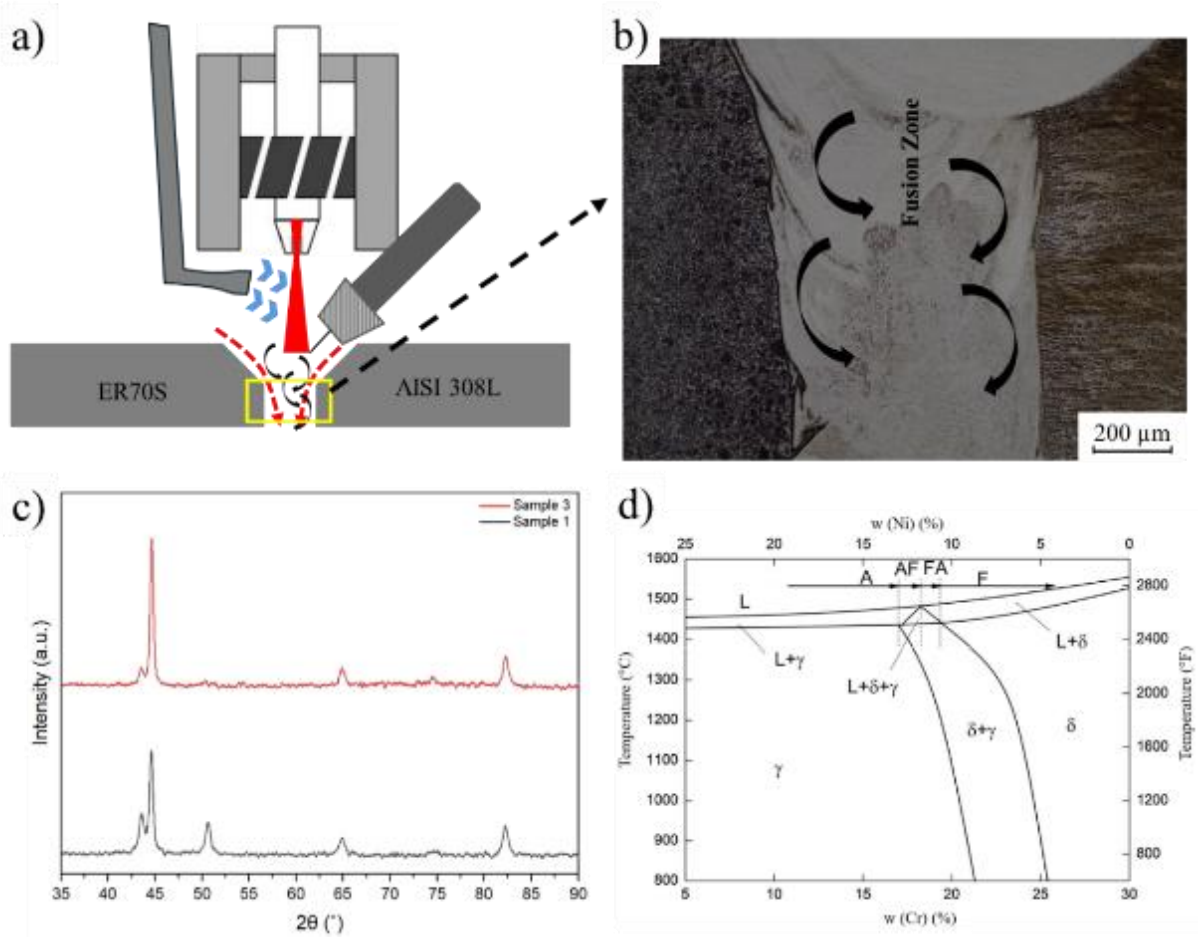

Figure 7-4. a) Schemat of the weld formation, b) Effect of the fusion zone in the formation of the weld zone of Sample #3, c) XRD analysis for sample #1 (Laser scanning speed 1000 mm/min, Laser power 1000 W), and sample #3 (Laser scanning speed 1000 mm/min, Laser power 1500 W), d) W(Cr)-W(Ni)-Temperature diagram for δ → γ.

This microstructural evolution highlights that controlling the austenite/ferrite ratio is crucial for optimizing mechanical properties and corrosion resistance in industrial applications.

7.4.1.4. Microstructural Variations Across the Weld

The cross-section of Sample #2 (Figure 5-a) shows distinct microstructural zones. The HAZ at the ER70S-6/316L interface (Figure 5-b) exhibits a refined grain structure (5–10 µm) due to rapid thermal cycling. In the weld neck region (Figure 5-c), fine cellular dendrites are observed, resulting from high thermal gradients and solidification rates. The dilution zone between AISI 316L filler and AISI 308L substrate (Figure 5-d) shows a mixed microstructure containing vermicular δ-ferrite within an austenitic matrix. The transition zone near the WAAM 308L (Figure 5-e) shows layers of equiaxed and partially recrystallized grains, reflecting the thermal gradient from the weld interface.

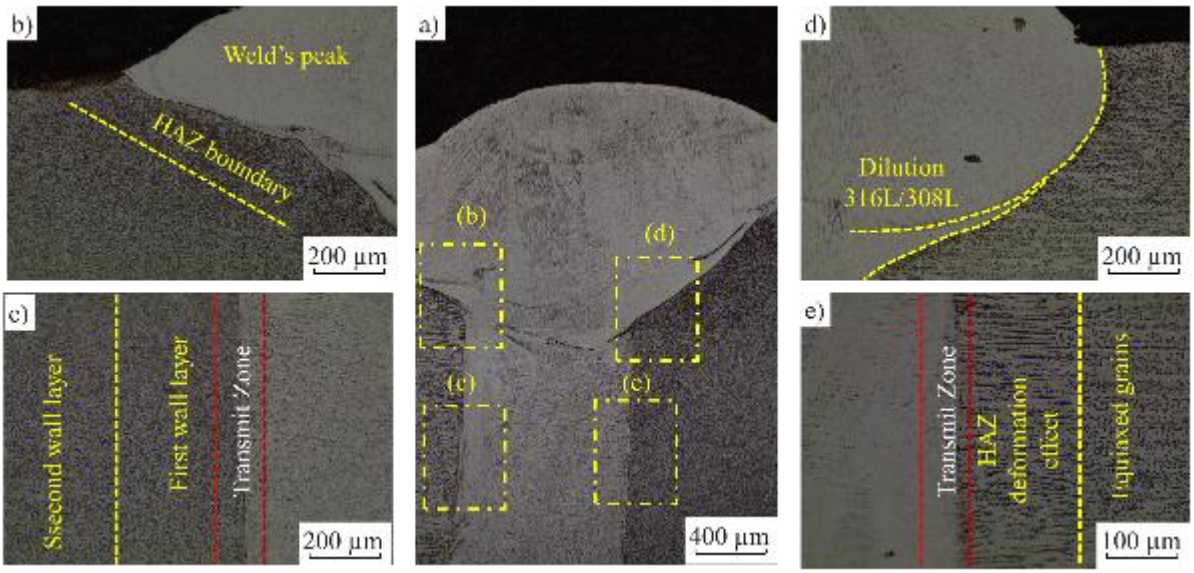

Figure 7-5. a) Cross section of the weld zone of sample #2, b) HAZ's boundary of ER70S-6/AISI 316L weld zone, c) Transmit zone of the weld zone and ER70S-6, d) Dilution area of AISI 316L and AISI 308L, e) Transmit zone of the weld zone and AISI 308L.

7.4.1.5. Defect Formation and Analysis

Figure 6 illustrates various microstructural features and defects. Widmanstätten ferrite plates form in the HAZ of both base materials (Figures 6-a, d) due to intermediate cooling rates. The weld bead center (Figure 6-b) shows lathy ferrite within the AISI 316L matrix, a result of extreme cooling rates. Pore formation mechanisms differed between the interfaces. Pore clusters were found along the AISI 308L fusion boundary (Figure 6-e) due to solidification shrinkage and hydrogen entrapment. In contrast, the ER70S-6/316L interface was largely pore-free (Figure 6-g). A 54 µm spherical cavity was observed in the weld neck (Figures 6-h, i), likely caused by gas entrapment from turbulent melt pool flow.

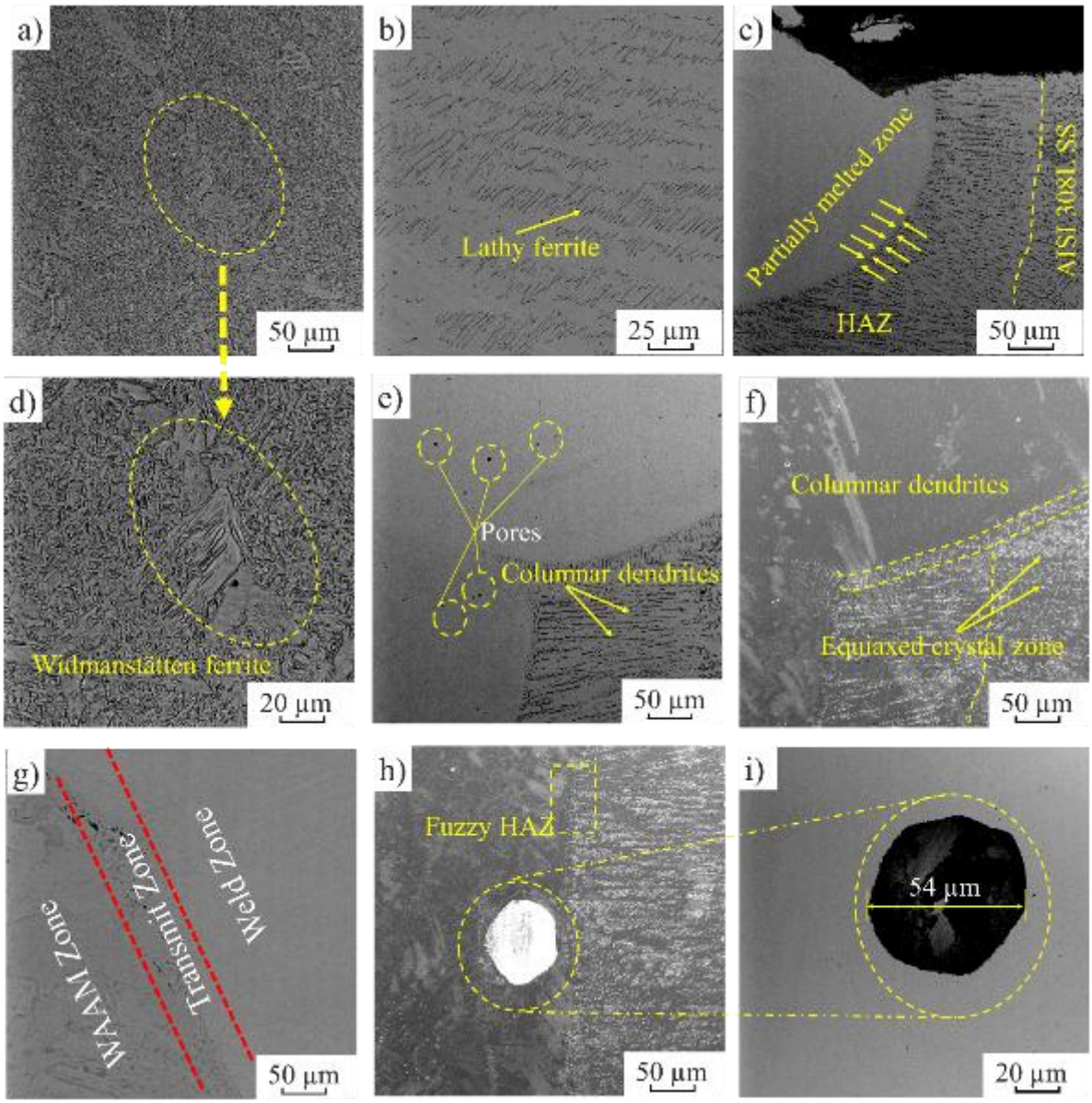

Figure 7-6. a) The HAZ of ER70S-6 in the middle of WZ, b) Peak weld of AISI 316L, c) The boundary of AISI 316L and AISI 308L, d) Widmanstätten ferrite (WF) in the WAAM plate, e) pores positions in the WZ, f) Columnar and equiaxed crystal zones, g) Neck boundary of AISI 316L /AISI 308L, i) 54 µm pore in the WZ.

7.4.2. Crystallographic and Interfacial Analysis

7.4.2.1. AISI 316L/AISI 308L Interface

EBSD analysis of the 316L/308L boundary (Figure 7) revealed a refined grain structure with high Geometrically Necessary Dislocation (GND) densities, resulting from thermal strain incompatibility. The inverse pole figure (Figure 7-f) shows a strong <101> texture aligned with the heat flow direction (Y-axis), indicative of directional solidification.

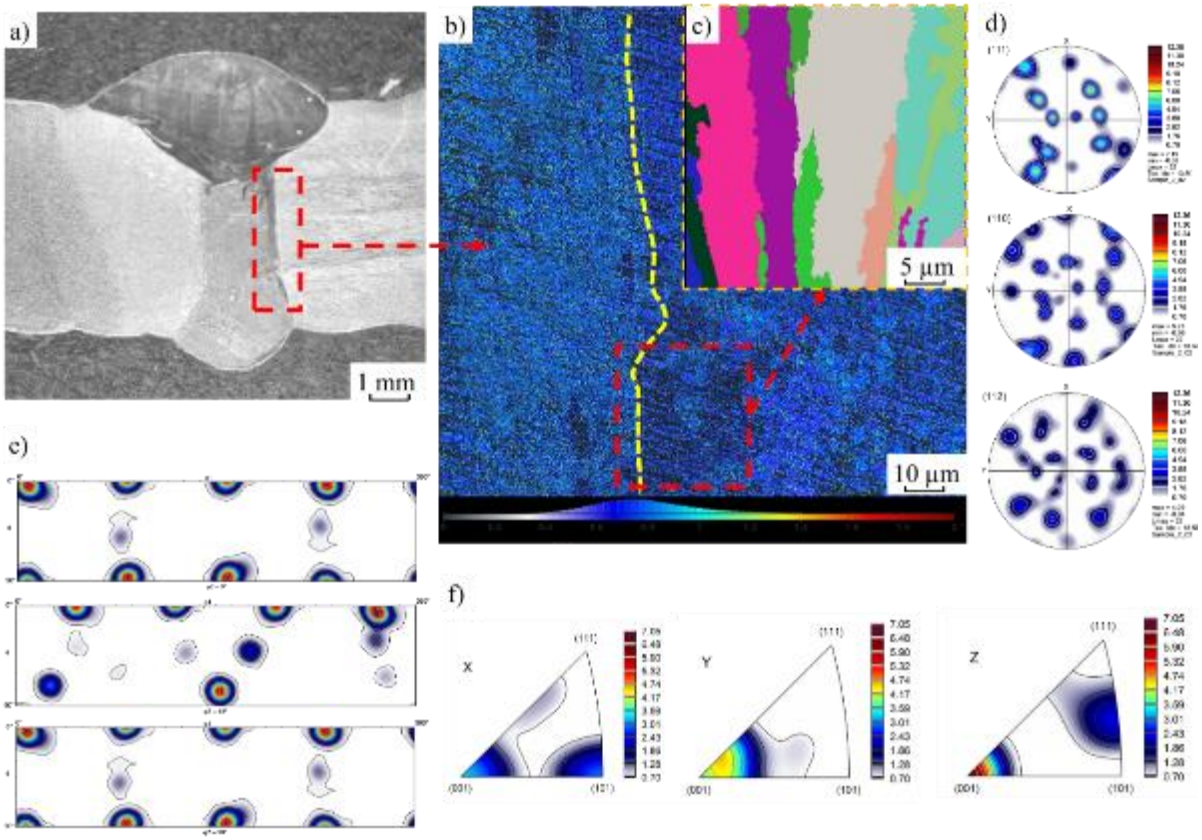

Figure 7-7. a) Position selection of sample #2, b) GND mapping of boundary between AISI 316L and AISI 308L, c) Grains analysis of EBSD, d) Pole figure, e) Presentation of Crystallographic orientations (φ2 = 0° to 360° - Euler space), f) Inverse pole figure.

7.4.2.2. AISI 316L/ER70S-6 Interface

At the 316L/ER70S-6 boundary (Figure 8), significant grain refinement (1–4 µm) was observed due to rapid solidification. The Orientation Distribution Function (ODF) analysis (Figure 8-d, e, f) showed intensified orientations aligned with the thermal gradient, favoring specific slip systems for strain accommodation.

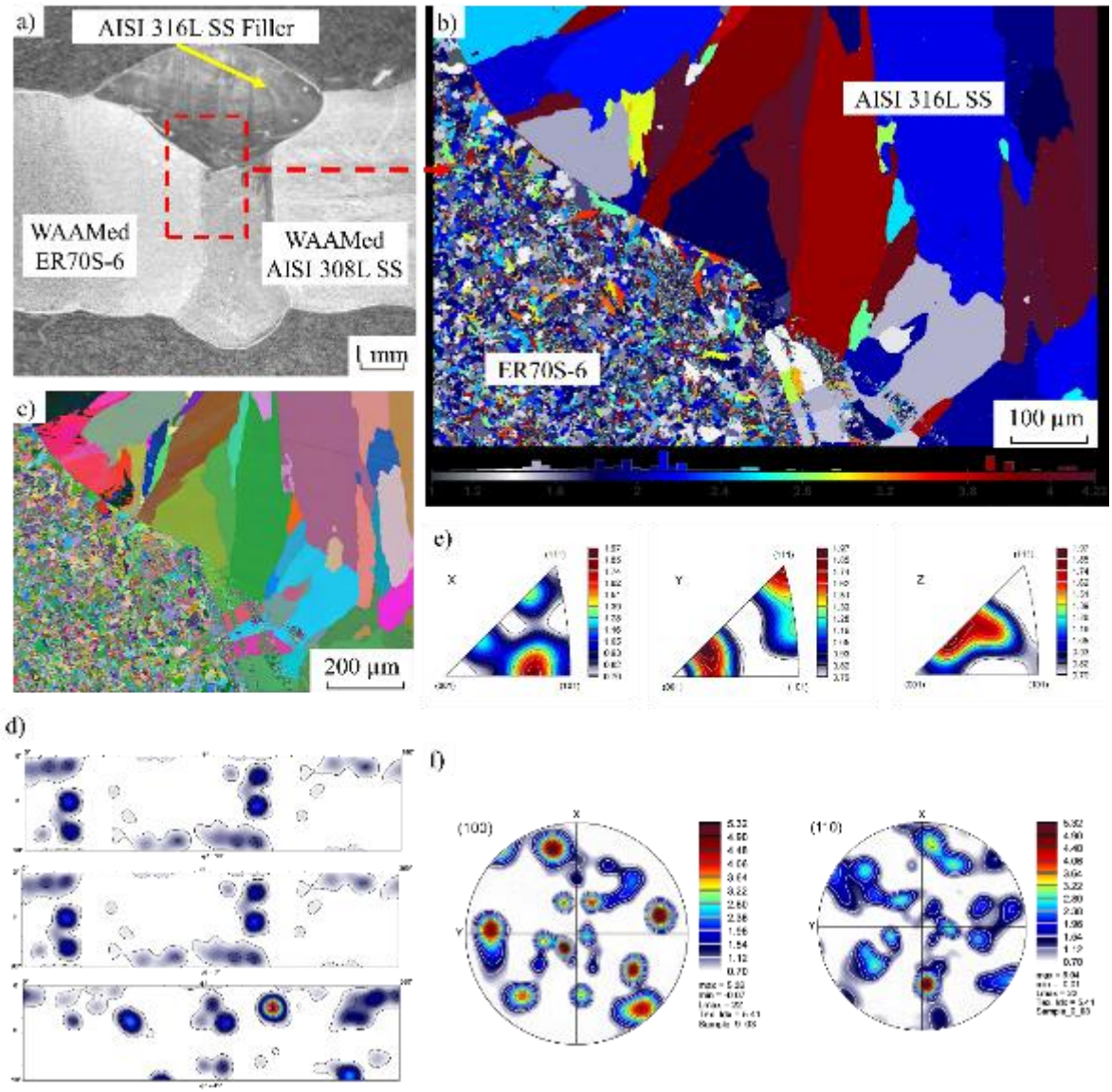

Figure 7-8. a) Position selection of sample #2 b) grain size analysis and phase detection c) EBSD mapping of the weld zone d) Presentation of Crystallographic orientations (φ2 = 0° to 360° - Euler space) e) inverse pole figure f) Pole figures.

7.4.2.3. Phase and Elemental Distribution

Phase mapping (Figure 9-b, c) identified a tripartite microstructure: retained austenite in 316L zones, BCC ferrite in transition regions, and polygonal/acicular ferrite in ER70S-6. EDS analysis (Figures 9-e, f) confirmed elemental redistribution, including Cr depletion and δ-ferrite formation in the dilution zone, governed by the high thermal gradients of the process.

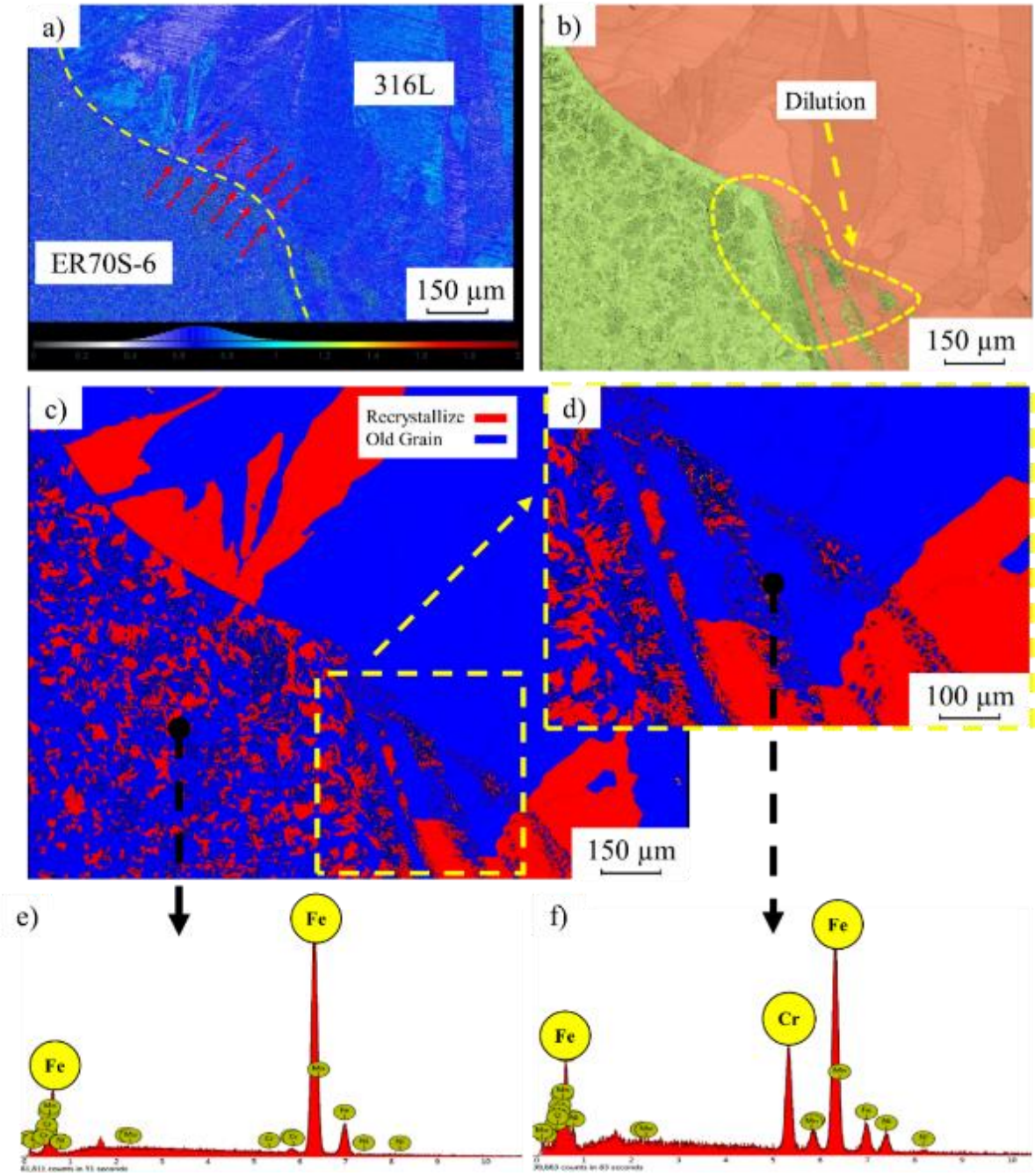

Figure 7-9. a) GND mapping of ER70S-6/AISI 316L b) Area separation of dilution area c) Phase identification of old and recrystallized grains d) Phase identification of dilution area of ER70S-6/AISI 308L e) EDS analysis of ER70S-6 in HAZ f) EDS analysis of AISI 308L in HAZ.

7.4.3. Microhardness Profile

Microhardness mapping revealed a direct correlation with the observed microstructure. The weld center (AISI 316L) showed an average hardness of 245 HV. The HAZ of both base materials exhibited peak hardness values (303 HV in AISI 308L HAZ and 297 HV in ER70S-6 HAZ) due to grain refinement and phase transformations. The Hall-Petch relationship explains this strengthening mechanism, as finer grains offer greater resistance to deformation. Figure 10 illustrates the grain size distribution and corresponding hardness values.

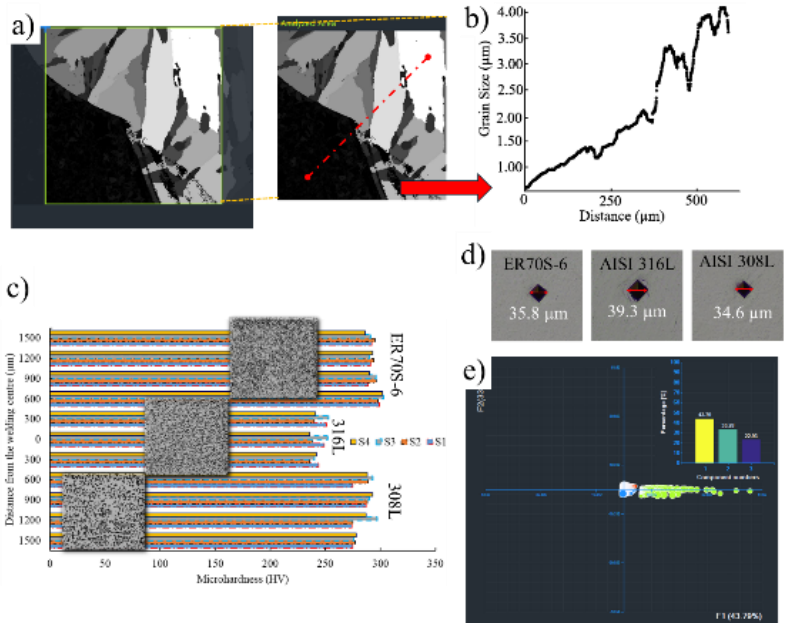

Figure 7-10. a) EBSD selection of the grains b) Measurement's direction for grain analysis c) Microhardness diagram d) Vicker's microhardness indentation of ER70S-6, AISI 308L, and AISI 316L e) Grain concentration map analysis.

7.4.4. Uniaxial Tensile Strength

Dog bone specimens were extracted from the welded plates (Figures 11-a, b). The fracture surface of Sample #3 (Figure 11-d) exhibited a ductile failure mode characterized by micro-void coalescence. The load-extension diagram (Figure 10-e) shows that Sample #3, welded with higher heat input, demonstrated superior tensile performance with both higher strength (11.7 kN vs. 8.2 kN) and greater ductility compared to Sample #1. This is attributed to the synergistic thermo-microstructural interactions, including dynamic recrystallization and a more favorable phase balance.

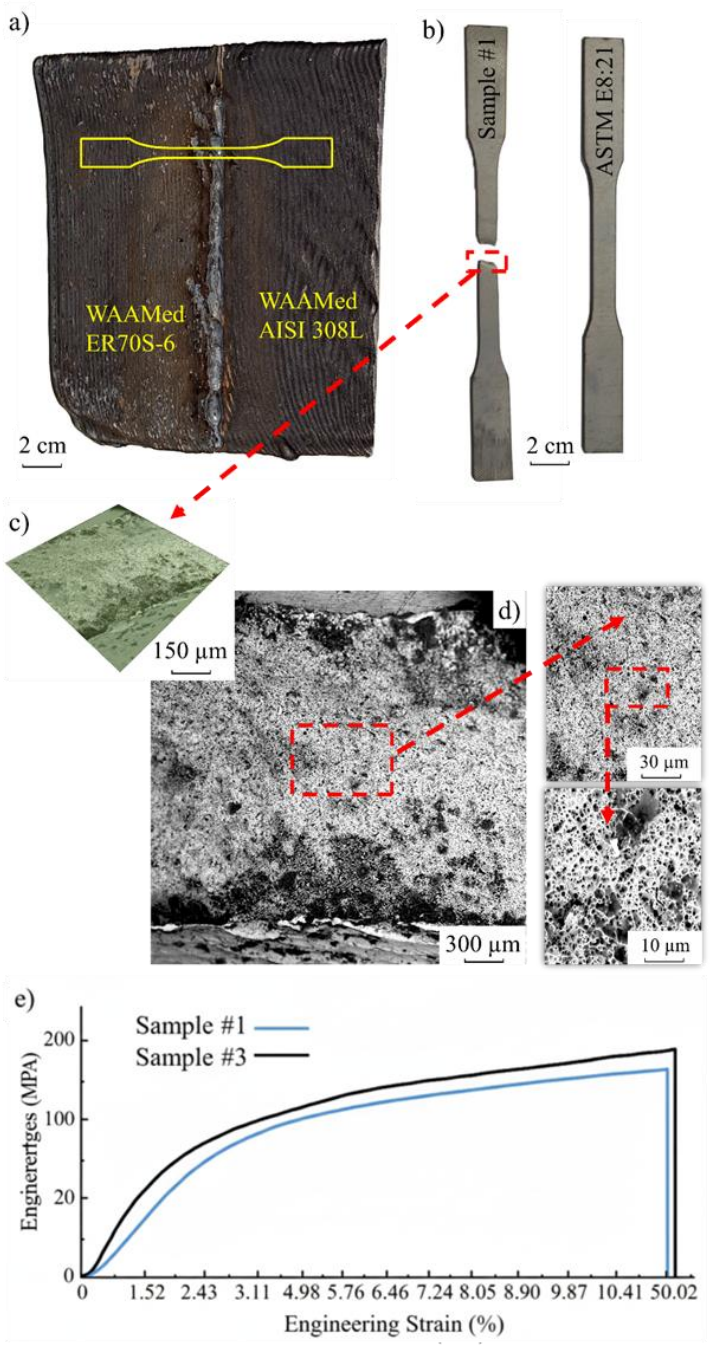

Figure 7-11. a) Welding plates b) Dog bone Uniaxial Tensile Strength c) Fractography selection d) Fractography of sample #3 e) Load-extension diagram of samples #1 and #3.

Chapter 8

Conclusions and Recommendations

Chapter 8

Conclusions and Recommendations

This research presents a comprehensive experimental and numerical investigation into the wire arc additive manufacturing (WAAM) of steels and bimetals, integrating both process structure property relationships and advanced joining methodologies such as laser hybrid welding (LHW). Through a systematic exploration of deposition parameters, wire feed rates, arc powers, and thermal histories, the study provides a unified understanding of WAAM's capability to fabricate and repair structural and functional metallic components with improved metallurgical quality, dimensional accuracy, and mechanical integrity.

8.1. Process parameter microstructure correlation

The experimental studies on AISI 308L and ER70S-6 steels demonstrated that deposition parameters, specifically arc power, deposition speed, and wire feed rate, play a decisive role in determining bead geometry and solidification morphology. For both materials, increased arc power or wire feed rate enhanced melt pool spreading and improved wetting angles while promoting uniform layer formation. Optimal processing windows were established at 1.7 kW and 9 mm/s for 308L and 2.6 kW and 5 mm/s for ER70S-6, ensuring balanced energy input and stable bead geometry. The results confirmed that the cold metal transfer (CMT) mode effectively minimizes spatter, porosity, and oxidation while ensuring near-net-shape deposition.

8.2. Microstructural evolution and mechanical performance

Microstructural characterization via optical microscopy, SEM, EBSD, and FIB revealed refined microstructures with distinct phase distributions in all WAAM-deposited alloys.

- In 308L, the microstructure exhibited *δ-ferrite and γ-austenite* with grain sizes ranging from 5 µm to 16 µm, depending on heat input and location (fusion zone, heat-affected zone, or substrate).
- For ER70S-6, the grain size ranged from 3–11 µm, with significant refinement in the dilution zone due to rapid heat extraction through the substrate.
- The microhardness values reached 310 HV in the heat-affected zone of 308L and 300 HV for ER70S-6, confirming the beneficial influence of controlled cooling and reduced oxidation.

In bimetallic CuAl8/ER70S-6 structures, strong metallurgical bonding was achieved at the Fe–Cu interface with refined grains in the dilution zone. The absence of cracks and voids, combined with a hardness of 131 HV and a failure load near 1.9 kN, demonstrates the feasibility of WAAM for fabricating functional bimetals with tailored mechanical properties.

8.3. Numerical and statistical modeling

A hybrid finite-element and computational-fluid-dynamics (CFD) modeling approach was developed and validated against experimental thermographic and geometrical data. The simulations accurately reproduced the thermal gradients, molten-pool flow, and temperature-time histories, enabling precise prediction of bead width and height within a ±5 % deviation from experimental results. Furthermore, the integration of Response Surface Methodology (RSM) and ANOVA provided statistically optimized process maps, confirming that deposition speed exerts the highest influence on bead height, while arc power most strongly affects bead width and aspect ratio. The models also identified critical correlations between cooling rate, melt-pool dynamics, and defect formation tendencies, forming a robust framework for process optimization.

8.4. Advanced joining via Laser Hybrid Welding (LHW)

To extend WAAM's applicability, Laser Hybrid Welding was employed to join WAAM-fabricated dissimilar steels, AISI 308L and ER70S-6, using an AISI 316L filler. The optimized condition (1500 W laser power, 1000 mm min^{-1} scanning speed) produced joints with fine, equiaxed grains and balanced ferrite–austenite microstructures. Tensile strength increased by 43 % relative to low-power conditions, and microhardness reached 303 HV in the 308L-HAZ. These findings demonstrate that combining WAAM and LHW offers a reliable pathway for producing and repairing high-strength dissimilar steel components, particularly for petrochemical and marine applications.

8.5. Integrated understanding and technological impact

Across all investigations, the synergistic combination of experimental, numerical, and microstructural analysis has established clear relationships between process parameters, thermal history, and resulting material behavior. The outcomes validate that:

- Thermal management through CMT and interlayer dwell times is essential for controlling grain refinement and minimizing residual stresses.
- Process stability depends on optimized deposition paths and feeding strategies that balance heat input and solidification rate.

- Hybrid joining techniques enable functional integration of WAAM-produced parts into complex assemblies without compromising structural reliability.

Collectively, these contributions advance WAAM from a primarily experimental process toward a predictive, simulation-driven manufacturing approach capable of delivering consistent, high-performance metallic components.

8.6. Outlook and future perspectives

The findings of this thesis create a strong foundation for the next generation of intelligent WAAM systems, where real-time monitoring, machine learning, and closed-loop thermal control can be integrated to achieve adaptive manufacturing. Future work should focus on:

- Multi-material and gradient deposition using sensor-based control for microstructure and defect prediction;
- 3D CFD-coupled phase-field modeling to capture solidification front evolution in multilayer builds;
- In-service performance evaluation, including wear, fatigue, and corrosion resistance under operational conditions;
- Development of sustainable WAAM processes through energy-efficient parameter selection and material recycling strategies.

Although remarkable progress has been achieved in WAAM and additive manufacturing, further efforts are necessary to bridge existing gaps related to optimization and simulation. Continuous monitoring of thermal cycles and the molten pool offers valuable potential for correlating these parameters with common defects in the WAAM process, such as porosity and cracking. Since metallic components are fabricated layer by layer, analyzing interfacial regions can provide deeper insight into how artificial intelligence could be employed to establish relationships between interfacial or intra-layer defects and the thermal history of the deposited metal. Future research should also focus on the influence of process parameters, including wire feed speed and power source settings, as well as the use of different filler wire materials, to identify optimal configurations for specific applications. Employing thermal imaging systems to record the temperature evolution during deposition could further enhance understanding of the process. Moreover, 3D computational fluid dynamics (CFD) simulations of molten metal flow may help address key challenges, such as the surface waviness that develops along the sample edges after solidification, which remains

an area requiring refinement [241]. Assessing the performance of WAAM-produced components under realistic service conditions, particularly in terms of wear and corrosion resistance, is essential. Such evaluations will ensure that future WAAM-fabricated parts meet the stringent requirements of industrial applications [242].

References

[1] Wong, K.V. and Hernandez, A., 2012. A review of additive manufacturing. International scholarly research notices, 2012.

[2] Sahafnejad-Mohammadi, I., Karamimoghadam, M., Zolfagharian, A., Akrami, M. and Bodaghi, M., 2022. 4D printing technology in medical engineering: a narrative review. Journal of the Brazilian Society of Mechanical Sciences and Engineering, 44(6), pp.1-26.

[3] Dilberoglu, U.M., Gharehpapagh, B., Yaman, U. and Dolen, M., 2017. The role of additive manufacturing in the era of industry 4.0. Procedia Manufacturing, 11, pp.545-554.

[4] Vayre, B., Vignat, F. and Villeneuve, F., 2012. Designing for additive manufacturing. Procedia CIrP, 3, pp.632-637.

[5] Williams, S.W., Martina, F., Addison, A.C., Ding, J., Pardal, G. and Colegrove, P., 2016. Wire+ arc additive manufacturing. Materials science and technology, 32(7), pp.641-647.

[6] Herzog, D., Seyda, V., Wycisk, E. and Emmelmann, C., 2016. Additive manufacturing of metals. Acta Materialia, 117, pp.371-392.

[7] Bourell, D., Kruth, J.P., Leu, M., Levy, G., Rosen, D., Beese, A.M. and Clare, A., 2017. Materials for additive manufacturing. CIRP annals, 66(2), pp.659-681.

[8] Wohlers, T. and Gornet, T., 2014. History of additive manufacturing. Wohlers report, 24(2014), p.118.

[9] Gao, W., Zhang, Y., Ramanujan, D., Ramani, K., Chen, Y., Williams, C.B., Wang, C.C., Shin, Y.C., Zhang, S. and Zavattieri, P.D., 2015. The status, challenges, and future of additive manufacturing in engineering. Computer-Aided Design, 69, pp.65-89.

[10] Guo, N. and Leu, M.C., 2013. Additive manufacturing: technology, applications and research needs. Frontiers of mechanical engineering, 8(3), pp.215-243.

[11] Bikas, H., Stavropoulos, P. and Chryssolouris, G., 2016. Additive manufacturing methods and modelling approaches: a critical review. The International Journal of Advanced Manufacturing Technology, 83(1), pp.389-405.

[12] Horn, T.J. and Harrysson, O.L., 2012. Overview of current additive manufacturing technologies and selected applications. Science progress, 95(3), pp.255-282.

[13] Calignano, F., Manfredi, D., Ambrosio, E.P., Biamino, S., Lombardi, M., Atzeni, E., Salmi, A., Minetola, P., Iuliano, L. and Fino, P., 2017. Overview on additive manufacturing technologies. Proceedings of the IEEE, 105(4), pp.593-612.

[14] Abdulhameed, O., Al-Ahmari, A., Ameen, W. and Mian, S.H., 2019. Additive manufacturing:

Challenges, trends, and applications. Advances in Mechanical Engineering, 11(2), p.1687814018822880.

[15] Gibson, I., Rosen, D., Stucker, B. and Khorasani, M., 2021. Design for additive manufacturing. In Additive manufacturing technologies (pp. 555-607). Springer, Cham.

[16] Prakash, K.S., Nancharaih, T. and Rao, V.S., 2018. Additive manufacturing techniques in manufacturing-an overview. Materials Today: Proceedings, 5(2), pp.3873-3882.

[17] Ford, S. and Despeisse, M., 2016. Additive manufacturing and sustainability: an exploratory study of the advantages and challenges. Journal of cleaner Production, 137, pp.1573-1587.

[18] Meiabadi, M.S., Moradi, M., Karamimoghadam, M., Ardabili, S., Bodaghi, M., Shokri, M. and Mosavi, A.H., 2021. Modeling the producibility of 3D printing in polylactic acid using artificial neural networks and fused filament fabrication. Polymers, 13(19), p.3219.

[19] Huang, S.H., Liu, P., Mokasdar, A. and Hou, L., 2013. Additive manufacturing and its societal impact: a literature review. The International Journal of Advanced Manufacturing Technology, 67(5), pp.1191-1203.

[20] Gupta, N., Weber, C. and Newsome, S., 2012. Additive manufacturing: status and opportunities. Science and Technology Policy Institute, Washington.

[21] Bourell, D.L., 2016. Perspectives on additive manufacturing. Annual Review of Materials Research, 46.

[22] Jiang, J., Xu, X. and Stringer, J., 2018. Support structures for additive manufacturing: a review. Journal of Manufacturing and Materials Processing, 2(4), p.64.

[23] Gibson, I., Rosen, D., Stucker, B. and Khorasani, M., 2021. Materials for additive manufacturing. In Additive Manufacturing Technologies (pp. 379-428). Springer, Cham.

[24] Kruth, J.P., Leu, M.C. and Nakagawa, T., 1998. Progress in additive manufacturing and rapid prototyping. Cirp Annals, 47(2), pp.525-540.

[25] Gibson, I., Rosen, D., Stucker, B. and Khorasani, M., 2021. Development of additive manufacturing technology. In Additive manufacturing technologies (pp. 23-51). Springer, Cham.

[26] Gu, D., 2015. Laser additive manufacturing (AM): classification, processing philosophy, and metallurgical mechanisms. In Laser additive manufacturing of high-performance materials (pp. 15-71). Springer, Berlin, Heidelberg.

[27] Wang, X., Gong, X. and Chou, K., 2017. Review on powder-bed laser additive manufacturing of Inconel 718 parts. Proceedings of the Institution of Mechanical Engineers, Part B: Journal of Engineering Manufacture, 231(11), pp.1890-1903.

[28] Jiménez, A., Bidare, P., Hassanin, H., Tarlochan, F., Dimov, S. and Essa, K., 2021. Powder-based laser hybrid additive manufacturing of metals: A review. The International Journal of Advanced Manufacturing Technology, 114(1), pp.63-96.

[29] Seepersad, C.C., 2014. Challenges and opportunities in design for additive manufacturing. 3D Printing and Additive Manufacturing, 1(1), pp.10-13.

[30] Oliveira, J.P., Santos, T.G. and Miranda, R.M., 2020. Revisiting fundamental welding concepts to improve additive manufacturing: From theory to practice. Progress in Materials Science, 107, p.100590.

[31] Gasser, A., Backes, G., Kelbassa, I., Weisheit, A. and Wissenbach, K., 2010. Laser additive manufacturing: Laser Metal Deposition (LMD) and Selective Laser Melting (SLM) in turbo-engine applications. Laser Technik Journal, 7(2), pp.58-63.

[32] Boley, C.D., Khairallah, S.A. and Rubenchik, A.M., 2015. Calculation of laser absorption by metal powders in additive manufacturing. Applied optics, 54(9), pp.2477-2482.

[33] Bär, F., Berger, L., Jauer, L., Kurtuldu, G., Schäublin, R., Schleifenbaum, J.H. and Löffler, J.F., 2019. Laser additive manufacturing of biodegradable magnesium alloy WE43: a detailed microstructure analysis. Acta biomaterialia, 98, pp.36-49.

[34] Rajaguru, K., Karthikeyan, T. and Vijayan, V., 2020. Additive manufacturing–State of art. Materials today: proceedings, 21, pp.628-633.

[35] Doubrovski, Z., Verlinden, J.C. and Geraedts, J.M., 2011, January. Optimal design for additive manufacturing: opportunities and challenges. In International design engineering technical conferences and computers and information in engineering conference (Vol. 54860, pp. 635-646).

[36] Hu, D. and Kovacevic, R., 2003. Sensing, modeling and control for laser-based additive manufacturing. International Journal of Machine Tools and Manufacture, 43(1), pp.51-60.

[37] Moradi, M., Karami Moghadam, M. and Asgari, F., 2020. 4D printing additive manufacturing review; Mechanisim, Chalanges, Applications and Future. Modares Mechanical Engineering, 20(4), pp.1063-1077.

[38] Slotwinski, J.A., Garboczi, E.J., Stutzman, P.E., Ferraris, C.F., Watson, S.S. and Peltz, M.A., 2014. Characterization of metal powders used for additive manufacturing. Journal of research of the National Institute of Standards and Technology, 119, p.460.

[39] Lakhdar, Y., Tuck, C., Binner, J., Terry, A. and Goodridge, R., 2021. Additive manufacturing of advanced ceramic materials. Progress in Materials Science, 116, p.100736.

[40] Durakovic, B., 2018. Design for additive manufacturing: Benefits, trends and challenges. Periodicals of Engineering and Natural Sciences (PEN), 6(2), pp.179-191.

[41] Kumar, M.B. and Sathiya, P., 2021. Methods and materials for additive manufacturing: A critical review on advancements and challenges. Thin-Walled Structures, 159, p.107228.

[42] Wu, B., Pan, Z., Ding, D., Cuiuri, D., Li, H., Xu, J. and Norrish, J., 2018. A review of the wire arc additive manufacturing of metals: properties, defects and quality improvement. Journal of Manufacturing Processes, 35, pp.127-139.

[43] Stinson, H., Ward, R., Quinn, J. and McGarrigle, C., 2021. Comparison of Properties and Bead Geometry in MIG and CMT Single Layer Samples for WAAM Applications. Metals, 11(10), p.1530.

[44] Gao, Y., Wu, C., Peng, K., Song, X., Fu, Y., Chen, Q., Zhang, M., Wang, G. and Liu, J., 2021. Towards superior fatigue crack growth resistance of TC4-DT alloy by in-situ rolled wire-arc additive manufacturing. Journal of Materials Research and Technology, 15, pp.1395-1407.

[45] Dharmendra, C., Shakerin, S., Ram, G.J. and Mohammadi, M., 2020. Wire-arc additive manufacturing of nickel aluminum bronze/stainless steel hybrid parts–Interfacial characterization, prospects, and problems. Materialia, 13, p.100834.

[46] Liu, R., Wang, Z., Sparks, T., Liou, F. and Newkirk, J., 2017. Aerospace applications of laser additive manufacturing. In Laser additive manufacturing (pp. 351-371). Woodhead publishing.

[47] Froes, F.H. and Boyer, R. eds., 2019. Additive manufacturing for the aerospace industry. Elsevier.

[48] Pinkerton, A.J., 2016. Lasers in additive manufacturing. Optics & Laser Technology, 78, pp.25-32.

[49] Meng, L., McWilliams, B., Jarosinski, W., Park, H.Y., Jung, Y.G., Lee, J. and Zhang, J., 2020. Machine learning in additive manufacturing: a review. Jom, 72(6), pp.2363-2377.

[50] Najmon, J.C., Raeisi, S. and Tovar, A., 2019. Review of additive manufacturing technologies and applications in the aerospace industry. Additive manufacturing for the aerospace industry, pp.7-31.

[51] Pereira, T., Kennedy, J.V. and Potgieter, J., 2019. A comparison of traditional manufacturing vs additive manufacturing, the best method for the job. Procedia Manufacturing, 30, pp.11-18.

[52] Seow, C.E., Zhang, J., Coules, H.E., Wu, G., Jones, C., Ding, J. and Williams, S., 2020. Effect of crack-like defects on the fracture behaviour of Wire+ Arc Additively Manufactured nickel-base Alloy 718. Additive Manufacturing, 36, p.101578.

[53] Zeng, Y., Wang, X., Qin, X., Hua, L. and Xu, M., 2021. Laser Ultrasonic inspection of a Wire+ Arc Additive Manufactured (WAAM) sample with artificial defects. Ultrasonics, 110, p.106273.

[54] Hauser, T., Reisch, R.T., Breese, P.P., Lutz, B.S., Pantano, M., Nalam, Y., Bela, K., Kamps, T., Volpp, J. and Kaplan, A.F., 2021. Porosity in wire arc additive manufacturing of aluminium alloys.

Additive Manufacturing, 41, p.101993.

[55] Gierth, M.; Henckell, P.; Ali, Y.; Scholl, J.; Bergmann, J.P. Wire Arc Additive Manufacturing (WAAM) of Aluminum Alloy AlMg5Mn with Energy-Reduced Gas Metal Arc Welding (GMAW). Materials 2020, 13, 2671.

[56] Y. Wang, B. Qi, B. Cong, M. Yang, F. Liu, Arc characteristics in double-pulsed VPGTAW for aluminum alloy, J. Mater. Process. Technol. 249 (2017) 89–95.

[57] Ding, J., et al., Thermo-mechanical analysis of Wire and Arc Additive Layer Manufacturing process on large multi-layer parts. Computational Materials Science, 2011. 50(12): p. 3315-3322.

[58] Wang, F., et al., Microstructure and Mechanical Properties of Wire and Arc Additive Manufactured Ti-6Al-4V. Metallurgical and Materials Transactions A, 2012. 44(2): p. 968-977.

[59] Ding, D., et al., A tool-path generation strategy for wire and arc additive manufacturing. The International Journal of Advanced Manufacturing Technology, 2014. 73(1-4): p. 173-183.

[60] Shen, C., et al., Fabrication of iron-rich Fe–Al intermetallics using the wire-arc additive manufacturing process. Additive Manufacturing, 2015. 7: p. 20-26.

[61] Ding, D., et al., Fabricating Superior NiAl Bronze Components through Wire Arc Additive Manufacturing. Materials (Basel), 2016. 9(8).

[62] Dong, B., et al., Fabrication of Copper-Rich Cu-Al Alloy Using the Wire-Arc Additive Manufacturing Process. Metallurgical and Materials Transactions B, 2017. 48(6): p. 3143-3151.

[63] Ge, J., et al., Characterization of wire arc additive manufacturing 2Cr13 part: Process stability, microstructural evolution, and tensile properties. Journal of Alloys and Compounds, 2018. 748: p. 911-921.

[64] Graf, M., et al., Thermo-Mechanical Modelling of Wire-Arc Additive Manufacturing (WAAM) of Semi-Finished Products. Metals, 2018. 8(12).

[65] Wu, B., et al., Effects of heat accumulation on microstructure and mechanical properties of Ti6Al4V alloy deposited by wire arc additive manufacturing. Additive Manufacturing, 2018. 23: p. 151-160.

[66] Oyama, K., et al., Heat source management in wire-arc additive manufacturing process for Al-Mg and Al-Si alloys. Additive Manufacturing, 2019. 26: p. 180-192.

[67] Yangfan, W., C. Xizhang, and S. Chuanchu, Microstructure and mechanical properties of Inconel 625 fabricated by wire-arc additive manufacturing. Surface and Coatings Technology, 2019. 374: p. 116-123.

[68] Bambach, M., et al., Hybrid manufacturing of components from Ti-6Al-4V by metal forming

and wire-arc additive manufacturing. Journal of Materials Processing Technology, 2020. 282.

[69] Dong, B., et al., Wire arc additive manufacturing of Al-Zn-Mg-Cu alloy: Microstructures and mechanical properties. Additive Manufacturing, 2020. 36.

[70] Suárez, A., et al., Wire arc additive manufacturing of an aeronautic fitting with different metal alloys: From the design to the part. Journal of Manufacturing Processes, 2021. 64: p. 188-197.

[71] Yuan, L., et al., Fabrication of metallic parts with overhanging structures using the robotic wire arc additive manufacturing. Journal of Manufacturing Processes, 2021. 63: p. 24-34.

[72] Yu, L., et al., Microstructures and mechanical properties of NiTi shape memory alloys fabricated by wire arc additive manufacturing. Journal of Alloys and Compounds, 2022. 892.

[73] Chen, X., Kong, F., Fu, Y., Zhao, X., Li, R., Wang, G. and Zhang, H., 2021. A review on wire-arc additive manufacturing: typical defects, detection approaches, and multisensor data fusion-based model. The International Journal of Advanced Manufacturing Technology, 117(3), pp.707-727.

[74] Naksuk, N., Poolperm, P., Nakngoenthong, J., Printrakoon, W. and Yuttawiriya, R., 2022. Experimental investigation of hot-wire laser deposition for the additive manufacturing of titanium parts. Materials Research Express.

[75] L. Wang, M. Gao, C. Zhang, X. Zeng, 2016, Effect of oscillating beam pattern on weld characterization of laser welding of AAA6061-T6 aluminum alloy, Materials and Design, DOI: 10.1016 / j.matdes.2016.07.053

[76] V. Kancharla, M. Mendes, M. Grupp, B. Baird, 2018, Recent advances in fiber laser welding

[77] J. Li, Q. Sun, Y. Liu, Z. Zhen, Q. Sun, J. Feng, 2020, Melt flow and microstructural characteristics in beam oscillation superimposed laser welding of 304 stainless steel, Journal of Manufacturing Processes

[78] K. Hao, G. Li, M. Gao, X. Zeng, 2015, Weld formation mechanism of fi ber laser oscillating welding of austenitic stainless steel, Journal of Material Processing Technology

[79] Z. Wang, JP Oliveira, Z. Zeng, X. Bu, B. Peng, X. Shao, 2019, Laser beam oscillating welding of 5A06 aluminum alloys: Microstructure, porosity and mechanical properties, Optics and Laser Technology

[80] S. Li, G. Mi, C. Wang, A study on laser beam oscillating welding characteristics for the 5083 aluminum alloy: Morphology, microstructure, and mechanical properties, 2020, Journal of Manufacturing Processes

[81] Brandl, E., Palm, F., Michailov, V., Viehweger, B. and Leyens, C., 2011. Mechanical properties of additive manufactured titanium (Ti–6Al–4V) blocks deposited by a solid-state laser and wire. Materials & Design, 32(10), pp.4665-4675.

[82] Brandl, E., Schoberth, A. and Leyens, C., 2012. Morphology, microstructure, and hardness of titanium (Ti-6Al-4V) blocks deposited by wire-feed additive layer manufacturing (ALM). Materials Science and Engineering: A, 532, pp.295-307.

[83] Fu, J., Gong, L., Zhang, Y., Wu, Q., Shi, X., Chang, J. and Lu, J., 2017. Microstructure and mechanical properties of Ti-6Al-4V fabricated by vertical wire feeding with axisymmetric multi-laser source. applied sciences, 7(3), p.227.

[84] Demir, A.G., 2018. Micro laser metal wire deposition for additive manufacturing of thin-walled structures. Optics and Lasers in Engineering, 100, pp.9-17.

[85] Elmer, J.W., Vaja, J., Carpenter, J.S., Coughlin, D.R., Dvornak, M.J., Hochanadel, P., Gurung, P., Johnson, A. and Gibbs, G., 2019. Wire-based additive manufacturing of stainless steel components. Welding Journal, 99(LLNL-JRNL-771645; LA-UR-19-23147).

[86] Yuan, D., Sun, X., Sun, L., Zhang, Z., Guo, C., Wang, J. and Jiang, F., 2021. Improvement of the grain structure and mechanical properties of austenitic stainless steel fabricated by laser and wire additive manufacturing assisted with ultrasonic vibration. Materials Science and Engineering: A, 813, p.141177.

[87] Yuan, D., Shao, S., Guo, C., Jiang, F. and Wang, J., 2021. Grain refining of Ti-6Al-4V alloy fabricated by laser and wire additive manufacturing assisted with ultrasonic vibration. Ultrasonics Sonochemistry, 73, p.105472.

[88] Liang, L., Hu, R., Wang, J., Huang, A. and Pang, S., 2021. A thermal fluid mechanical model of stress evolution for wire feeding-based laser additive manufacturing. Journal of Manufacturing Processes, 69, pp.602-612.

[89] Bassis, M., Kotliar, A., Koltiar, R., Ron, T., Leon, A., Shirizly, A. and Aghion, E., 2021. The Effect of a Slow Strain Rate on the Stress Corrosion Resistance of Austenitic Stainless Steel Produced by the Wire Laser Additive Manufacturing Process. Metals, 11(12), p.1930.

[90] Sun, W., Shan, F., Zong, N., Dong, H. and Jing, T., 2021. A simulation and experiment study on phase transformations of Ti-6Al-4V in wire laser additive manufacturing. Materials & Design, 207, p.109843.

[91] Da Silva, A., Frostevarg, J., Volpp, J. and Kaplan, A.F., 2021. Additive Manufacturing by laser-assisted drop deposition from a metal wire. Materials & Design, 209, p.109987.

[92] Huang, W., Chen, S., Xiao, J., Jiang, X. and Jia, Y., 2021. Laser wire-feed metal additive manufacturing of the Al alloy. Optics & Laser Technology, 134, p.106627.

[93] Mortello, M. and Casalino, G., 2021. Transfer mode effects on Ti6Al4V wall building in wire laser additive manufacturing. Manufacturing Letters, 28, pp.17-20.

[94] Jamnikar, N.D., Liu, S., Brice, C. and Zhang, X., 2022. In situ microstructure property prediction by modeling molten pool-quality relations for wire-feed laser additive manufacturing. Journal of Manufacturing Processes, 79, pp.803-814.

[95] Wang, Y., Chen, C., Liu, X., Wang, J., Zhang, Y., Long, W., Guan, S. and Peng, L., 2022. Cross-Scale Simulation Research on the Macro/Microstructure of TC4 Alloy Wire Laser Additive Manufacturing. Metals, 12(6), p.934.

[96] Zhang, W., Xu, Y., Shi, Y., Su, G., Gu, Y. and Volodymyr, K., 2022. Intergranular corrosion characteristics of high-efficiency wire laser additive manufactured Inconel 625 alloys. Corrosion Science, 205, p.110422.

[97] Cui, X., Qi, E., Sun, Z., Jia, C., Zeng, Y. and Wu, S., 2022. Wire oscillating laser additive manufacturing of 2319 aluminum alloy: optimization of process parameters, microstructure, and mechanical properties. Chinese Journal of Mechanical Engineering: Additive Manufacturing Frontiers, 1(3), p.100035.

[98] Alagha, A.N., Hussain, S. and Zaki, W., 2021. Additive manufacturing of shape memory alloys: A review with emphasis on powder bed systems. Materials & Design, 204, p.109654.

[99] Wang, C., Suder, W., Ding, J. and Williams, S., 2021. Wire based plasma arc and laser hybrid additive manufacture of Ti-6Al-4V. Journal of Materials Processing Technology, 293, p.117080.

[100] Gong, M., Meng, Y., Zhang, S., Zhang, Y., Zeng, X. and Gao, M., 2020. Laser-arc hybrid additive manufacturing of stainless steel with beam oscillation. Additive Manufacturing, 33, p.101180.

[101] Shen, H., Jin, J., Liu, B. and Zhou, Z., 2021. Measurement and evaluation of laser-scanned 3D profiles in wire arc hybrid manufacturing processes. Measurement, 176, p.109089.

[102] Kapil, A., Suga, T., Tanaka, M. and Sharma, A., 2022. Towards hybrid laser-arc based directed energy deposition: Understanding bead formation through mathematical modeling for additive manufacturing. Journal of Manufacturing Processes, 76, pp.457-474.

[103] Hirohata, M., Chen, G., Morioka, K., Hyoma, K., Matsumoto, N. and Inose, K., 2022. An investigation on laser-arc hybrid welding of one-pass full-penetration butt-joints for steel bridge members. Welding in the World, 66(3), pp.515-527.

[104] Sefene, E.M., Hailu, Y.M. and Tsegaw, A.A., 2022. Metal hybrid additive manufacturing: state-of-the-art. Progress in Additive Manufacturing, pp.1-13.

[105] Omiyale, B.O., Olugbade, T.O., Abioye, T.E. and Farayibi, P.K., 2022. Wire arc additive manufacturing of aluminium alloys for aerospace and automotive applications: a review. Materials Science and Technology, 38(7), pp.391-408.

[106] Ma, Z.X., Cheng, P.X., Ning, J., Zhang, L.J. and Na, S.J., 2021. Innovations in Monitoring, Control and Design of Laser and Laser-Arc Hybrid Welding Processes. Metals, 11(12), p.1910.

[107] Näsström, J., Brueckner, F. and Kaplan, A.F., 2019. Laser enhancement of wire arc additive manufacturing. Journal of Laser Applications, 31(2), p.022307.

[108] Ma, S., Jiang, M., Chen, X., Li, B., Jiang, N., Chen, Y., Wu, S., Liang, J., Li, B., Lei, Z. and Chen, Y., 2022. Macro/micro-structure and mechanical properties of Al-6Mg-0.3 Sc alloy fabricated by oscillating laser-arc hybrid additive manufacturing. Journal of Alloys and Compounds, 929, p.167325.

[109] Liu, M., Ma, G., Liu, D., Yu, J., Niu, F. and Wu, D., 2020. Microstructure and mechanical properties of aluminum alloy prepared by laser-arc hybrid additive manufacturing. Journal of Laser Applications, 32(2), p.022052.

[110] Gong, M., Zhang, S., Lu, Y., Wang, D. and Gao, M., 2021. Effects of laser power on texture evolution and mechanical properties of laser-arc hybrid additive manufacturing. Additive Manufacturing, 46, p.102201.

[111] Ma, S., Jiang, M., Chen, X., Li, B., Jiang, N., Chen, Y., Wu, S., Liang, J., Li, B., Lei, Z. and Chen, Y., 2022. Macro/micro-structure and mechanical properties of Al-6Mg-0.3 Sc alloy fabricated by oscillating laser-arc hybrid additive manufacturing. Journal of Alloys and Compounds, 929, p.167325.

[112] Vander Voort, G.F., Lampman, S.R., Sanders, B.R., Anton, G.J., Polakowski, C., Kinson, J., Muldoon, K., Henry, S.D. and Scott Jr, W.W., 2004. ASM handbook. Metallography and microstructures, 9, pp.44073-0002.

[113] Bilmes, P., Gonzalez, A., Llorente, C. and Solari, M., 1996. Effect of δ ferrite solidification morphology of austenitic stainless steel weld metal on properties of welded joints. Welding international, 10(10), pp.797-808.

[114] Hunko, W.S., 2018. Cold Metal Transfer-Gas Metal Arc Welding (CMT-GMAW) Wire+ Arc Additive Manufacturing (WAAM) Process Control Implementation (Doctoral dissertation, Auburn University).

[115] Ali, A. and Bhadeshia, H.K.D.H., 1991. Microstructure of high strength steel refined with intragranularly nucleated Widmanstätten ferrite. Materials science and technology, 7(10), pp.895-903.

[116] Li, J., Shi, C., Li, J. and Shi, C., 2021. Effect of Heat Treatment on the Carbide in Steel. Carbide in Special Steel: Formation Mechanism and Control Technology, pp.143-203.

[117] Vishakha Shukla, Vikash Kumar, Ankit Dixit. Microstructural characteristics and tensile

properties of ER70S-6 manufactured by Robotic CMT wire-and-arc additive manufacturing. Materials today: proceedings. In Press, Corrected Proof. https://doi.org/10.1016/j.matpr.2023.02.011

[118] Sixin Zhao, Na Min, and Wei Li. Formation of Widmanstätten Ferrite and Grain Boundary Ferrite in a Hypereutectoid Pearlitic Steel. Metals 2022, 12(3), 493; https://doi.org/10.3390/met12030493

[119] Bodnar, R.L. and Hansen, S.S., 1994. Effects of Widmanstätten ferrite on the mechanical properties of a 0.2 pct C-0.7 pct Mn steel. Metallurgical and Materials Transactions A, 25, pp.763-773. https://doi.org/10.1007/BF02665453

120 Karamimoghadam, M., Aghayar, Y., Forooghi, F., Mohammadi, M., Contuzzi, N. and Casalino, G., 2024, August. Effect of Manufacturing Strategy on Microstructure of a Low-Carbon Steel Alloy Fabricated with Wire-Arc Additive Manufacturing. In Conference of Metallurgists (pp. 109-112). Cham: Springer Nature Switzerland. https://doi.org/10.1007/978-3-031-67398-6_23.

[121] Das, B., Panda, B.N. and Dixit, U.S., 2024. Effects of Heat Treatment on the Mechanical Properties of Fe-Based ER70S-6 Cladding on Aluminum Substrate Using Cold Metal Transfer Process. Journal of Materials Engineering and Performance, 33(1), pp.173-193. https://doi.org/10.1007/s11665-023-07975-6.

[122] Zhai, W., Aishwarya, Shandro, R. and Zhou, W., 2024. Microstructure and mechanical properties of the wire arc additively manufactured 316L/ER70S-6 bimetal structure. Virtual and Physical Prototyping, 19(1), p.e2375105. https://doi.org/10.1080/17452759.2024.2375105.

[123] da Silva, L.J., Souza, D.M., de Araújo, D.B., Reis, R.P. and Scotti, A., 2020. Concept and validation of an active cooling technique to mitigate heat accumulation in WAAM. The International Journal of Advanced Manufacturing Technology, 107, pp.2513-2523.

[124] Derekar, K.S., Addison, A., Joshi, S.S., Zhang, X., Lawrence, J., Xu, L., Melton, G. and Griffiths, D., 2020. Effect of pulsed metal inert gas (pulsed-MIG) and cold metal transfer (CMT) techniques on hydrogen dissolution in wire arc additive manufacturing (WAAM) of aluminium. The International Journal of Advanced Manufacturing Technology, 107, pp.311-331.

[125] Derekar, K.S., 2018. A review of wire arc additive manufacturing and advances in wire arc additive manufacturing of aluminium. Materials science and technology, 34(8), pp.895-916. https://doi.org/10.1080/02670836.2018.1455012.

[126] Bellamkonda, P.N., Sudersanan, M. and Visvalingam, B., 2022. Mechanical properties of wire arc additive manufactured carbon steel cylindrical component made by cold metal transferred arc welding process. Materials Testing, 64(2), pp.260-271. https://doi.org/10.1515/mt-2021-2051.

[127] Fattahi, M., Nabhani, N., Hosseini, M., Arabian, N. and Rahimi, E., 2013. Effect of Ti-containing inclusions on the nucleation of acicular ferrite and mechanical properties of multipass

weld metals. Micron, 45, pp.107-114.

[128] Abson, D.J., 2018. Acicular ferrite and bainite in C–Mn and low-alloy steel arc weld metals. Science and Technology of Welding and Joining, 23(8), pp.635-648.

[129] Yang, J.R. and Chang, L.C., 1997. The effect of stress on the Widmanstätten ferrite transformation. Materials Science and Engineering: A, 223(1-2), pp.158-167.

[130] Cullity, B.D. and Smoluchowski, R., 1957. Elements of X-ray Diffraction. Physics Today, 10(3), pp.50-50. https://doi.org/10.1063/1.3060306.

[131] Yang, J.R. and Chang, L.C., 1997. The effect of stress on the Widmanstätten ferrite transformation. Materials Science and Engineering: A, 223(1-2), pp.158-167. https://doi.org/10.1016/S0921-5093(96)10475-5.

[132] Rosli, N.A., Alkahari, M.R., bin Abdollah, M.F., Maidin, S., Ramli, F.R. and Herawan, S.G., 2021. Review on effect of heat input for wire arc additive manufacturing process. Journal of Materials Research and Technology, 11, pp.2127-2145. https://doi.org/10.1016/j.jmrt.2021.02.002.

[133] Bui, M.C. and Nguyen, T.D., 2023. On the connection of the heat input to the forming quality in wire-and-arc additive manufacturing of stainless steels. Vacuum, 209, p.111807. https://doi.org/10.1016/j.vacuum.2023.111807.

[134] Yin, Y., Zhang, J., Pan, S., Xing, Y., Yue, X. and Chang, W., 2023. Room-and elevated-temperature mechanical property of selective laser melting-fabricated Hastelloy X with different heat treatments. Materials Science and Engineering: A, 886, p.145697. https://doi.org/10.1016/j.msea.2023.145697.

[135] Chi, Y., Pan, S., Liese, M., Liu, J., Murali, N., Soemardy, E. and Li, X., 2023. Wire-arc directed energy deposition of aluminum alloy 7075 with dispersed nanoparticles. Journal of Manufacturing Science and Engineering, 145(3), p.031010. https://doi.org/10.1115/1.4056257.

[136] Dinovitzer, M., Chen, X., Laliberte, J., Huang, X., & Frei, H. (2019). Effect of wire and arc additive manufacturing (WAAM) process parameters on bead geometry and microstructure. Additive Manufacturing, 26, 138–146. https://doi.org/10.1016/j.addma.2018.12.013

[137] Mahmood, M.A., Popescu, A.C., Hapenciuc, C.L. et al. Estimation of clad geometry and corresponding residual stress distribution in laser melting deposition: analytical modeling and experimental correlations. Int J Adv Manuf Technol 111, 77–91 (2020). https://doi.org/10.1007/s00170-020-06047-6

[138] Gemming, S., Schreiber, M. (2007). Theoretical Investigation of Interfaces. In: Gemming, S., Schreiber, M., Suck, JB. (eds) Materials for Tomorrow. Springer Series in Materials Science, vol 93. Springer, Berlin, Heidelberg. https://doi.org/10.1007/978-3-540-47971-0_4

[139] Zhao, W., Wei, Y., Long, J., & others. (2021). Modeling and simulation of heat transfer, fluid flow and geometry morphology in GMAW-based wire arc additive manufacturing. Welding in the World, 65, 1571–1590. https://doi.org/10.1007/s40194-021-01123-1

[140] Jia, J., Zhao, Y., Dong, M., & Wu, A., & Li, Q. (2020). Numerical simulation on residual stress and deformation for WAAM parts of aluminum alloy based on temperature function method. China Welding, 29(2), 1–8. https://doi.org/10.12073/j.cw.20191101002

[141] Fang, X., Ren, C., Zhang, L., Wang, C., Huang, K., & Lu, B. (2021). A model of bead size based on the dynamic response of CMT-based wire and arc additive manufacturing process parameters. Rapid Prototyping Journal, 27(4), 741–753. https://doi.org/10.1108/RPJ-03-2020-0051

[142] Liu B, Lan J, Liu H, Chen X, Zhang X, Jiang Z, Han J. The Effects of Processing Parameters during the Wire Arc Additive Manufacturing of 308L Stainless Steel on the Formation of a Thin-Walled Structure. Materials. 2024; 17(6):1337. https://doi.org/10.3390/ma17061337

[143] Feng, Y., & Fan, D. (2024). Investigating the forming characteristics of 316 stainless steel fabricated through cold metal transfer (CMT) wire and arc additive manufacturing. Materials, 17(10), 2184. https://doi.org/10.3390/ma17102184

[144] Oliari, S., D'Oliveira, A. S., & Schulz, M. (2017). Additive manufacturing of H11 with wire-based laser metal deposition. Soldagem & Inspeção, 22, https://doi.org/10.1590/0104-9224/si2204.06

[145] Ramírez-Argáez, M., Conejo, A., & López-Cornejo, M. (2015). Mathematical modeling of the melting rate of metallic particles in the EAF under multiphase flow. ISIJ International, 55(1), 117-125. https://doi.org/10.2355/isijinternational.55.117

[146] Kozamernik, N., Bračun, D., & Klobčar, D. (2020). WAAM system with interpass temperature control and forced cooling for near-net-shape printing of small metal components. The International Journal of Advanced Manufacturing Technology, 110, 1955–1968. https://doi.org/10.1007/s00170-020-05958-8

[147] Baier, D., Wolf, F., Weckenmann, T., & others. (2022). Thermal process monitoring and control for a near-net-shape wire and arc additive manufacturing. Production Engineering, 16, 811–822. https://doi.org/10.1007/s11740-022-01138-7

[148] Kiran, A., Li, Y., Koukolíková, M., Brázda, M., Hodek, J., Urbánek, M., Džugan, J., & Raghavan, S., Odehnal, J. (2022). Elevated temperature baseplate effect on microstructure, mechanical properties, and thermal stress evaluation by numerical simulation for austenite stainless steel 316L fabricated by directed energy deposition. Materials, 15(12), 4165. https://doi.org/10.3390/ma15124165

[149] Chaturvedi, M., Scutelnicu, E., Rusu, C. C., Mistodie, L. R., Mihailescu, D., & Subbiah, A. V.

(2021). Wire arc additive manufacturing: Review on recent findings and challenges in industrial applications and materials characterization. Metals, 11(6), 939. https://doi.org/10.3390/met11060939

[150] Kang M, Ahn Y, Kim C. Gas Metal Arc Welding Using Novel CaO-Added Mg Alloy Filler Wire. Metals. 2016; 6(7):155. https://doi.org/10.3390/met6070155

[151] Tippanna, R., Mishra, R., Imam, M., Chinthapenta, V., & Vineesh, K. P. (2023, July 11). Temperature evolution in WAAM process without overlapping weld beads. AIP Conference Proceedings, 2745(1), 030002. https://doi.org/10.1063/5.0143318

[152] Di, Y. Y., et al. (2022). IOP Conference Series: Materials Science and Engineering, 1270, 012084. https://doi.org/10.1088/1757-899X/1270/1/012084

[153] Montevecchi, F., Venturini, G., Grossi, N., Scippa, A., & Campatelli, G. (2018). Heat accumulation prevention in Wire-Arc-Additive-Manufacturing using air jet impingement. Manufacturing Letters, 17, 14-18. https://doi.org/10.1016/j.mfglet.2018.06.004

[154] Jorge, V. L., Teixeira, F. R., & Scotti, A. (2022). Pyrometrical interlayer temperature measurement in WAAM of thin wall: Strategies, limitations, and functionality. Metals, 12(5), 765. https://doi.org/10.3390/met12050765

[155] Da Silva Viola, R. (2023). Additive manufacturing: Process modelling of WAAM and expression of performance indicators. Université Clermont Auvergne.

[156] Zhao, W., Wei, Y., Long, J., & others. (2021). Modeling and simulation of heat transfer, fluid flow and geometry morphology in GMAW-based wire arc additive manufacturing. Welding in the World, 65, 1571–1590. https://doi.org/10.1007/s40194-021-01123-1

[157] Sana Shahoveisi, Mohammad Vahab, Babak Shahbodagh, Sascha Eisenträger, Nasser Khalili, Phase-field modelling of dynamic hydraulic fracturing in porous media using a strain-based crack width formulation, Computer Methods in Applied Mechanics and Engineering, Volume 429, 2024, 117113, ISSN 0045-7825, ttps://doi.org/10.1016/j.cma.2024.117113.

[158] Junxiang Yang, Junseok Kim, A phase-field model and its efficient numerical method for two-phase flows on arbitrarily curved surfaces in 3D space, Computer Methods in Applied Mechanics and Engineering, Volume 372, 2020, 113382, ISSN 0045-7825, https://doi.org/10.1016/j.cma.2020.113382.

[159] Charles Mareau, A thermodynamically consistent formulation of the Johnson–Cook model, Mechanics of Materials, Volume 143, 2020, 103340, ISSN 0167-6636, https://doi.org/10.1016/j.mechmat.2020.103340.

[160] Fang, X., Ren, C., Zhang, L., Wang, C., Huang, K., & Lu, B. (2021). A model of bead size based on the dynamic response of CMT-based wire and arc additive manufacturing process

parameters. Rapid Prototyping Journal, 27(4), 741–753. https://doi.org/10.1108/RPJ-03-2020-0051

[161] Saleh, B., Fathi, R., Tian, Y. et al. Fundamentals and advances of wire arc additive manufacturing: materials, process parameters, potential applications, and future trends. Archiv.Civ.Mech.Eng 23, 96 (2023). https://doi.org/10.1007/s43452-023-00633-7

[162] Fang, X., Ren, C., Zhang, L., Wang, C., Huang, K. and Lu, B. (2021), "A model of bead size based on the dynamic response of CMT-based wire and arc additive manufacturing process parameters", Rapid Prototyping Journal, Vol. 27 No. 4, pp. 741-753. https://doi.org/10.1108/RPJ-03-2020-0051

[163] Malcolm Dinovitzer, Xiaohu Chen, Jeremy Laliberte, Xiao Huang, Hanspeter Frei, Effect of wire and arc additive manufacturing (WAAM) process parameters on bead geometry and microstructure, Additive Manufacturing, Volume 26, 2019, Pages 138-146, ISSN 2214-8604, https://doi.org/10.1016/j.addma.2018.12.013.

[164] Xiangfang Xu, Jialuo Ding, Supriyo Ganguly, Chenglei Diao, Stewart Williams, Oxide accumulation effects on wire+arc layer-by-layer additive manufacture process, Journal of Materials Processing Technology, Volume 252, 2018, Pages 739-750, ISSN 0924-0136, https://doi.org/10.1016/j.jmatprotec.2017.10.030.

[165] Singh S, Jinoop AN, Tarun Kumar GTA, Palani IA, Paul CP, Prashanth KG. Effect of Interlayer Delay on the Microstructure and Mechanical Properties of Wire Arc Additive Manufactured Wall Structures. Materials (Basel). 2021 Jul 27;14(15):4187. doi: 10.3390/ma14154187. PMID: 34361378; PMCID: PMC8347272.

[166] Saadatmand, M., Talemi, R., Study on the thermal cycle of Wire Arc Additive Manufactured (WAAM) carbon steel wall using numerical simulation, Frattura ed Integrità Strutturale, 52 (2020) 98-104.

[167] Voropaev A, Korsmik R, Tsibulskiy I. Features of Filler Wire Melting and Transferring in Wire-Arc Additive Manufacturing of Metal Workpieces. Materials (Basel). 2021 Sep 5;14(17):5077. doi: 10.3390/ma14175077. PMID: 34501167; PMCID: PMC8434615.

[168] Resnina, N., Palani, I.A., Belyaev, S. et al. Influence of Substrate Temperature on Structure and Functional Properties of NiTi Walls Produced by WAAM. Trans Indian Inst Met 77, 987–995 (2024). https://doi.org/10.1007/s12666-023-03193-9

[169] Nor Ana Rosli, Mohd Rizal Alkahari, Mohd Fadzli bin Abdollah, Shajahan Maidin, Faiz Redza Ramli, Safarudin Gazali Herawan, Review on effect of heat input for wire arc additive manufacturing process, Journal of Materials Research and Technology, Volume 11, 2021, Pages 2127-2145, ISSN 2238-7854, https://doi.org/10.1016/j.jmrt.2021.02.002.

[170] Zeng J, Nie W, Li X. The Influence of Heat Input on the Surface Quality of Wire and Arc

Additive Manufacturing. Applied Sciences. 2021; 11(21):10201. https://doi.org/10.3390/app112110201

[171] Zhang, R., Jiang, F. & Xue, L. Experimental Study on Wire Melting Control Ability of Twin-Body Plasma Arc. Chin. J. Mech. Eng. 37, 30 (2024). https://doi.org/10.1186/s10033-024-01006-8

[172] Luo L, Qian E, Lu T, Pan J, Liu M, Liu C, Guo Y, Bi L. Vision-Based Estimation of Force Balance of Near-Suspended Melt Pool for Drooping and Collapsing Prediction. Sensors (Basel). 2024 May 21;24(11):3270. doi: 10.3390/s24113270. PMID: 38894064; PMCID: PMC11174812.

[173] Kukla, Christian & Duretek, Ivica & Schuschnigg, Stephan & Gonzalez-Gutierrez, Joamin & Gooneie, Ali & Holzer, Clemens. (2015). Study of rheological behaviour of stainless steel feedstock taking into account the thermal effects.

[174] F. Montevecchi, G. Venturini, N. Grossi, A. Scippa, G. Campatelli, Heat accumulation prevention in Wire-Arc-Additive Manufacturing using air jet impingement, Manufacturing Letters, 17 (2018) 14-18, https://doi.org/10.1016/j.mfglet.2018.06.00

[175] Saadatmand, M., Talemi, R., Study on the thermal cycle of Wire Arc Additive Manufactured (WAAM) carbon steel wall using numerical simulation, Frattura ed Integrità Strutturale, 52 (2020) 98-104.

[176] Hackenhaar, W., Mazzaferro, J.A.E., Mazzaferro, C.C.P. et al. Effects of different WAAM current deposition modes on the mechanical properties of AISI H13 tool steel. Weld World 66, 2259–2269 (2022). https://doi.org/10.1007/s40194-022-01342-0

[177] Müller, J., Hensel, J. WAAM of structural components, building strategies for varying wall thicknesses. Weld World 67, 833–844 (2023). https://doi.org/10.1007/s40194-023-01481-y

[178] Ayed, Achraf and Valencia, Amélie and Bras, Guénolé and Bernard, H. and Michaud, Pierre and Balcaen, Yannick and Alexis, Joël Effects of WAAM Process Parameters on Metallurgical and Mechanical Properties of Ti-6Al-4V Deposits. (2019) In: Advances in Materials, Mechanics and Manufacturing. Springer, Cham, Switzerland, 26-35. ISBN 978-3-030-24246-6

[179] Mohd. Gufran, Avinash Mishra, Rabesh Kumar Singh, Anuj Kumar Sharma, Ankit Dixit, Ashiv Shah, Dependence of process planning strategy on deposition ratio in wire arc additive manufacturing, Materials Today: Proceedings, Volume 62, Part 6, 2022, Pages 3468-3472, ISSN 2214-7853, https://doi.org/10.1016/j.matpr.2022.04.290.

[180] Graf, Marcel & Hälsig, Andre & Höfer, Kevin & Awiszus, Birgit & Mayr, Peter. (2018). Thermo-Mechanical Modelling of Wire-Arc Additive Manufacturing (WAAM) of Semi-Finished Products. Metals. 8. 1009. 10.3390/met8121009.

[181] D. Bonn, J. Eggers, J. Indekeu, J. Meunier, Wetting and spreading, Rev. Mod. Phys., 81

(2009), pp. 739-805, 10.1103/RevModPhys.81.739

[182] Sergio Ríos, Paul A. Colegrove, Filomeno Martina, Stewart W. Williams, Analytical process model for wire + arc additive manufacturing, Additive Manufacturing, Volume 21, 2018, Pages 651-657, ISSN 2214-8604, https://doi.org/10.1016/j.addma.2018.04.003.

[183] Zhang H, Huang J, Liu C, Ma Y, Han Y, Xu T, Lu J, Fang H. Fabricating Pyramidal Lattice Structures of 304 L Stainless Steel by Wire Arc Additive Manufacturing. Materials. 2020; 13(16):3482. https://doi.org/10.3390/ma13163482

[184] Jorge, V. L., Teixeira, F. R., Wessman, S., Scotti, A., & Henke, S. L. (2024). The Impact of Multiple Thermal Cycles Using CMT® on Microstructure Evolution in WAAM of Thin Walls Made of AlMg5. Metals, 14(6), 717. https://doi.org/10.3390/met14060717

[185] Kumar P, Sharma SK, Singh RKR. Heat input and shielding environment effect on CMT-WAAM of IN718. Proceedings of the Institution of Mechanical Engineers, Part C: Journal of Mechanical Engineering Science. 2024;238(20):10026-10044. doi:10.1177/09544062241262217

[186] Kumar P, Singh RKR, Sharma SK. Effect of welding parameters on bead characteristics and mechanical properties of wire and arc additive manufactured inconel 718. Proceedings of the Institution of Mechanical Engineers, Part C: Journal of Mechanical Engineering Science. 2023;237(7):1668-1691. doi:10.1177/09544062221133035

[187] Kumar, P., Raj Singh, R.K. and Sharma, S.K. (2025), "Effect of process parameters on wire-arc direct energy deposited Inconel 718 superalloy", Rapid Prototyping Journal, Vol. ahead-of-print No. ahead-of-print. https://doi.org/10.1108/RPJ-05-2023-0176

[188] Bouchoucha, A., Zaidi, H., Kadiri, E.K. and Paulmier, D., 1997. Influence of electric fields on the tribological behaviour of electrodynamical copper/steel contacts. Wear, 203, pp.434-441.

[189] Vander Voort, G.F., Lampman, S.R., Sanders, B.R., Anton, G.J., Polakowski, C., Kinson, J., Muldoon, K., Henry, S.D. and Scott Jr, W.W., 2004. ASM handbook. Metallography and microstructures, 9, pp.44073-0002.

[190] Xia, C., Pan, Z., Polden, J., Li, H., Xu, Y. and Chen, S., 2022. Modelling and prediction of surface roughness in wire arc additive manufacturing using machine learning. Journal of Intelligent Manufacturing, 33(5), pp.1467-1482.

[191] DebRoy, T., Wei, H.L., Zuback, J.S., Mukherjee, T., Elmer, J.W., Milewski, J.O., Beese, A.M., Wilson-Heid, A.D., De, A. and Zhang, W., 2018. Additive manufacturing of metallic components–process, structure and properties. Progress in materials science, 92, pp.112-224.

[192] Chena, P., Liua, S., Suna, X., Hock, A.J., Dua, Z. and Chewa, Y., Effect of Inter-Layer Cooling on Microstructure of Low-Carbon Steel Fabricated by Wire Arc Additive Manufacturing.

[193] Balasubramani, N., Venezuela, J., StJohn, D., Wang, G. and Dargusch, M., 2023. A review of the origin of equiaxed grains during solidification under mechanical stirring, vibration, electromagnetic, electric-current, and ultrasonic treatments. Journal of Materials Science & Technology, 144, pp.243-265.

[194] Zhai, W., Aishwarya, Shandro, R. and Zhou, W., 2024. Microstructure and mechanical properties of the wire arc additively manufactured 316L/ER70S-6 bimetal structure. Virtual and Physical Prototyping, 19(1), p.e2375105.

[195] Guo, Y., 2025. Microstructures and mechanical properties of ER70S-6 steel fabricated by wire arc additive manufacturing.

[196] Fan, Y., Wang, K., Wang, X.Y., Cao, X.Y., Liu, T.G., Xin, L. and Lu, Y.H., 2021. Microstructures and mechanical properties of the fusion zone of 316L-316LN stainless steel multi-pass gas tungsten arc welded joint. Journal of Materials Science, 56(30), pp.17306-17318.

197 Wang, W., Luo, T., Liu, Z., Luo, S. and Zhu, M., 2023. Influences of cooling rate on solidification microstructure and carbide of GCr15 bearing steel. Metallurgical and Materials Transactions B, 54(2), pp.776-792.

[198] İpekoğlu, G., Küçükömeroğlu, T., Aktarer, S.M., Sekban, D.M. and Çam, G., 2019. Investigation of microstructure and mechanical properties of friction stir welded dissimilar St37/St52 joints. Materials Research Express, 6(4), p.046537.

[199] Liu, S., Chen, P., Xianchong, S., Hock, A.J., Yao, X., Zhenglin, D. and Chew, Y., 2022. Mechanical Performance of ER70S-6 Low-Carbon Steel Fabricated by Wire Arc Additive Manufacturing. Asian Society for Precision Engineering and Nanotechnology (ASPEN 2022), Research Publishing Services, pp.79-85.

[200] Yildiz, A.S., Davut, K., Koc, B. and Yilmaz, O., 2020. Wire arc additive manufacturing of high-strength low alloy steels: study of process parameters and their influence on the bead geometry and mechanical characteristics. The International Journal of Advanced Manufacturing Technology, 108, pp.3391-3404.

[201] Herian, J. and Sulkowski, R., 2008. Quantitative evaluation of the structure and properties of hot rolled products of continuous ingots made of low-carbon steels. Journal of Achievements in Materials and manufacturing Engineering, 28(1), pp.15-18.

[202] Lin, Z., Goulas, C., Ya, W. and Hermans, M.J., 2019. Microstructure and mechanical properties of medium carbon steel deposits obtained via wire and arc additive manufacturing using metal-cored wire. Metals, 9(6), p.673.

[203] Wen, C., Wang, Z., Deng, X., Wang, G. and Misra, R.D.K., 2018. Effect of heat input on the microstructure and mechanical properties of low alloy ultra-high strength structural steel welded

joint. steel research international, 89(6), p.1700500.

[204] Duarte, V.R., Rodrigues, T.A., Schell, N., Miranda, R.M., Oliveira, J.P. and Santos, T.G., 2022. In-situ hot forging directed energy deposition-arc of CuAl8 alloy. Additive Manufacturing, 55, p.102847.

[205] Cui, J., Yuan, L., Commins, P., He, F., Wang, J. and Pan, Z., 2021. WAAM process for metal block structure parts based on mixed heat input. The International Journal of Advanced Manufacturing Technology, 113, pp.503-521.

[206] Nemani, A.V., Ghaffari, M., Bokati, K.S., Valizade, N., Afshari, E. and Nasiri, A., 2024. Advancements in additive manufacturing for copper-based alloys and composites: a comprehensive review. Journal of Manufacturing and Materials Processing, 8(2), p.54.

[207] Boczkal, S., Korczak, P., Żyłka, K., Limanówka, K., Płonka, B., Remsak, K., Szymański, W. and Leśniak, D., 2024. Effects of Copper Content and Thermo-Mechanical Treatment on Microstructure and Mechanical Properties of AlMgSi (Cu) Alloys. Crystals, 14(12), p.1027.

[208] Andreazza, P., Gericke, A., Klötzer-Freese, C. and Henkel, K.M., 2023, June. Investigations on WAAM using copper-based alloys for ship propeller manufacturing. In ISOPE International Ocean and Polar Engineering Conference (pp. ISOPE-I). ISOPE.

[209] Wu, Y., Zeng, D., Liu, Z., Qiu, W., Yu, H., Zhong, X., Li, S. and Ma, Y., 2012. Microstructure and sliding wear behavior of pseudo-alloy PS45/CuAl8 composite coating sprayed by HVAA technique. Rare Metals, 31, pp.204-208.

[210] Magnabosco, I., Ferro, P., Bonollo, F. and Arnberg, L., 2006. An investigation of fusion zone microstructures in electron beam welding of copper–stainless steel. Materials Science and Engineering: A, 424(1-2), pp.163-173.

[211] Kujanpää, V., 2014. Thick-section laser and hybrid welding of austenitic stainless steels. Physics Procedia, 56, pp.630-636.

[212] Oliveira, J.P., Santos, T.G. and Miranda, R.M., 2020. Revisiting fundamental welding concepts to improve additive manufacturing: From theory to practice. Progress in Materials Science, 107, p.100590.

[213] Yang, K.V., Shi, Y., Palm, F., Wu, X. and Rometsch, P., 2018. Columnar to equiaxed transition in Al-Mg (-Sc)-Zr alloys produced by selective laser melting. Scripta Materialia, 145, pp.113-117.

[214] Chen, W., Guo, S., Xuan, Y., Xu, J., Li, S., Fang, W., Zhou, Q. and Wang, K., 2024. Influence of different deposition strategies on the microstructure and mechanical properties of the laminated heterostructured material with ER130S-G HSS and 316 L SS fabricated by WAAM. Materials Characterization, 210, p.113838.

[215] Argumedo, J.G., Mahmoudiniya, M., Reinton, T.E., Kestens, L.A.I., Hermans, M.J.M. and Popovich, V.A., 2024. Functional grading of low alloy steel to 316 L by wire arc additive manufacturing–Microstructural and mechanical characterization of bi-metal interface. Journal of Materials Processing Technology, 325, p.118305.

[216] Biscuola, V.B. and Martorano, M.D.A., 2008. Mechanical blocking mechanism for the columnar to equiaxed transition. Metallurgical and Materials Transactions A, 39, pp.2885-2895.

[217] Taylor, M., Mozumder, Y.H., Smith, A.D., Davis, A.E., Scenini, F., Prangnell, P.B. and Pickering, E.J., 2024, August. In-Situ EBSD Study of Austenitisation in a Wire-Arc Additively Manufactured High-Strength Steel. In IOP Conference Series: Materials Science and Engineering (Vol. 1310, No. 1, p. 012001). IOP Publishing.

[218] Chi, Y., Pan, S., Liese, M., Liu, J., Murali, N., Soemardy, E. and Li, X., 2023. Wire-arc directed energy deposition of aluminum alloy 7075 with dispersed nanoparticles. Journal of Manufacturing Science and Engineering, 145(3), p.031010.

[219] Yin, Y., Zhang, J., Pan, S., Xing, Y., Yue, X. and Chang, W., 2023. Room-and elevated-temperature mechanical property of selective laser melting-fabricated Hastelloy X with different heat treatments. Materials Science and Engineering: A, 886, p.145697.

[220] Ou, W., Mukherjee, T., Knapp, G.L., Wei, Y. and DebRoy, T., 2018. Fusion zone geometries, cooling rates and solidification parameters during wire arc additive manufacturing. International Journal of Heat and Mass Transfer, 127, pp.1084-1094.

[221] Srivastava, M., Rathee, S., Tiwari, A. and Dongre, M., 2023. Wire arc additive manufacturing of metals: A review on processes, materials and their behaviour. Materials Chemistry and Physics, 294, p.126988.

[222] Cai, X., Wang, Z., Dong, L., Yang, M., Zhou, J. and Xue, F., 2022. Advanced mechanical properties of nickel-aluminum bronze/steel composite structure prepared by wire-arc additive manufacturing. Materials & Design, 221, p.110969.

[223] Zykova, A., Panfilov, A., Chumaevskii, A., Vorontsov, A., Moskvichev, E., Nikonov, S., Gurianov, D., Savchenko, N., Kolubaev, E. and Tarasov, S., 2023. In-situ dispersion hardened aluminum bronze/steel composites prepared using a double wire electron beam additive manufacturing. Progress in Additive Manufacturing, 8(5), pp.1067-1082.

[224] Xu, Z., Li, X., Li, S., Jiang, R., Hua, P. and Liu, D., 2025. Wire arc additive manufacturing of CuAl8Ni2/42CrMo bimetallic deposition: microstructure and properties. Journal of Materials Science, pp.1-17.

[225] Wang, L., Tan, Z., Wang, S., Liu, W., Hao, J., Zhang, X., Deng, S., Yu, C., Zheng, H., Zeng, Z. and Lu, H., 2023. Atomization gases dependent mechanical properties in the laser powder bed

fusion manufactured 304L stainless steel. Journal of Materials Processing Technology, 316, p.117966.

[226] Zhang, L., Zhai, W., Zhao, K., Bi, G., Zhou, W., Lu, G. and Xu, S., 2024. Enhanced quasi-static and dynamic tensile properties of stainless steel 316L produced by laser aided additive manufacturing in controlled argon environment. Materials Science and Engineering: A, 895, p.146255.

[227] Chen, Y., Zhang, X., Ding, D., Wang, X., Zhang, K., Liu, Y., Lu, T. and Tu, S., 2023. Integration of interlayer surface enhancement technologies into metal additive manufacturing: A review. Journal of Materials Science & Technology, 165, pp.94-122.

[228] Serrati, D.S., Machado, M.A., Oliveira, J.P. and Santos, T.G., 2023. Non-destructive testing inspection for metal components produced using wire and arc additive manufacturing. Metals, 13(4), p.648.

[229] Zhao, Z., Perini, M. and Pellizzari, M., 2025. Solidification cracking in steel/copper alloy multi-material structures deposited by laser-based directed energy deposition. Journal of Materials Science, pp.1-21.

[230] Mansoura, A., Omidi, N., Barka, N., Karganroudi, S.S. and Dehghan, S., 2024. Selective laser melting of stainless steels: a review of process, microstructure and properties. Metals and materials International, 30(9), pp.2343-2371.

[231] Nandhakumar, R. and Venkatesan, K., 2023. A process parameters review on selective laser melting-based additive manufacturing of single and multi-material: Microstructure, physical properties, tribological, and surface roughness. Materials Today Communications, 35, p.105538..

[232] Wang, J., Zhao, B., Liu, Y., Zhao, J. and Ma, G., 2024. Research Progress in Shape-Control Methods for Wire-Arc-Directed Energy Deposition. Materials, 17(23), p.5704.

[233] Srivastava, M., Rathee, S., Tiwari, A. and Dongre, M., 2023. Wire arc additive manufacturing of metals: A review on processes, materials and their behaviour. Materials Chemistry and Physics, 294, p.126988.

[234] Shah, A., Aliyev, R., Zeidler, H. and Krinke, S., 2023. A review of the recent developments and challenges in wire arc additive manufacturing (WAAM) process. Journal of Manufacturing and Materials Processing, 7(3), p.97.

[235] Liu, R., Dang, X., Peng, Y. and Wu, T., 2022. Microstructure and Wear Behavior of Laser Cladded CoCrNiMox Coatings on the Low Carbon Steel. Crystals, 12(9), p.1229.

[236] Sharma, G., Rathore, S., Kumar, H. and Yadav, K.K., 2024. Wear Properties of Wire and Arc Additive Manufacturing Components: A review on recent developments on Processes, Materials and

Parameters. Library of Progress-Library Science, Information Technology & Computer, 44(3).

[237] ASTM International Committee E-28 on Mechanical Testing, 2021. Standard test methods for tension testing of metallic materials. ASTM international.

[238] Adin, M.Ş., 2025. Investigation of the effects of machining parameters on kerf widths during laser beam machining of medium carbon steels. Journal of Materials Engineering and Performance, pp.1-12.

[239] Kou, S. (2003). Welding Metallurgy. John Wiley & Sons. https://onlinelibrary.wiley.com/doi/book/10.1002/0471434027.

[240] Adin, M.Ş., 2024. A study on additive manufacturing processes, standards and mechanical properties. In Post-Processing of parts and components fabricated by fused deposition modeling (pp. 213-231). CRC Press.

[241] de Rubeis, T., Ciccozzi, A., Giusti, L. and Ambrosini, D., 2024. On the use of 3D printing to enhance the thermal performance of building envelope–A Review. Journal of Building Engineering, p.110284.

[242] Sharma, G., Rathore, S., Kumar, H. and Yadav, K.K., 2024. Wear Properties of Wire and Arc Additive Manufacturing Components: A review on recent developments on Processes, Materials and Parameters. Library of Progress-Library Science, Information Technology & Computer, 44(3).

Appendix

Publications

Metal Wire Additive Manufacturing: A Comparison between Arc Laser and Laser/Arc Heat Sources

https://doi.org/10.3390/inventions8020052

inventions

MDPI

Perspective

Metal Wire Additive Manufacturing: A Comparison between Arc Laser and Laser/Arc Heat Sources

Giuseppe Casalino *, Mojtaba Karamimoghadam and Nicola Contuzzi

Department of Mechanics, Mathematics and Management, Polytechnic University of Bari, Via Orabona 4, 70125 Bari, Italy
* Correspondence: giuseppe.casalino@poliba.it

Abstract: In this paper, the authors introduce the reader to the state of the art of Metal Wire Additive Manufacturing (MWAM) and provide a comparison between Wire Arc Additive Manufacturing (WAAM), Wire Laser Additive Manufacturing (WLAM), and Laser Arc Hybrid Wire Deposition (LAHWD) based on their characteristics and potential future applications, since MWAM is expected to have a promising future in various areas, such as aerospace, automotive, biomedical, and energy fields. A detailed discussion of the benefits and drawbacks of each Metal Wire Additive Manufacturing process can help to improve our understanding of the unique characteristics of metal wire application. Therefore, this paper offers a comprehensive analysis that can serve as a reference for upcoming industrial projects and research initiatives, with the aim of helping industries choose the most appropriate WAM technique for their specific applications.

Keywords: wire arc additive manufacturing; laser wire additive manufacturing; laser arc hybrid wire deposition; perspectives

check for updates

Citation: Casalino, G.; Karamimoghadam, M.; Contuzzi, N. Metal Wire Additive Manufacturing: A Comparison between Arc Laser and Laser/Arc Heat Sources. *Inventions* **2023**, *8*, 52. https://doi.org/10.3390/inventions8020052

Academic Editor: Zhengyi Jiang

Received: 30 January 2023
Revised: 21 February 2023
Accepted: 24 February 2023
Published: 1 March 2023

1. Introduction

The use of materials such as nickel, steel, titanium, and aluminum is widespread in the additive manufacturing industry. Metal feedstocks, which are melted by directed energy deposition (DED) methods into the desired part, have either powder or wire shapes [1]. With respect to wire, wire arc additive manufacturing (WAAM) and wire laser additive manufacturing (WLAM) are available for directed energy deposition. The operating windows of WAAM and WLAM can be complementary and alternative. In fact, WAAM can provide a high deposition rate, and WLAM enables sufficient control to build medium to small features with near-net shape characteristics. Laser arc hybrid wire deposition (LAHWD) is a hybrid additive manufacturing process that combines wire arc additive manufacturing (WAAM) and laser metal deposition (LMD) processes. WAAM was the first to appear with WLAM and WLAHM being recently introduced options for WAM [2]. To date, many different methods have been used for additive manufacturing, each having advantages and disadvantages regarding the experimental environments, the materials used, and the devices installed [1]. Based on the use of unique parts for particular applications, AM methods have been used to find specific solutions to 3D-printing problems to achieve maximum productivity [3]. In the additive manufacturing (AM) industry, wire arc additive manufacturing (WAAM) and wire laser additive manufacturing (WLAM) are both forms of additive manufacturing that use wire as a material feedstock.

The main difference is the type of energy used to melt the wire. WAAM uses an electric arc, while WLAM uses a laser source. WAAM tends to be faster and more efficient than WLAM, but the latter produces parts with higher precision and surface quality. Additionally, WLAM is more versatile as it can be used with various materials, while WAAM primarily uses aluminum.

However, a serious challenge the laser material processing industry faces is how to ensure careful preparation of the edges of AM parts while minimizing defects due to the

Experimental, statistical and numerical study of the single laser spot condition and influence parameters of a Neodymium-Doped Yttrium Lithium Fluoride laser

https://doi.org/10.1016/j.optlastec.2025.113202

Progress in Additive Manufacturing
https://doi.org/10.1007/s40964-025-01108-2

CORRESPONDENCE

Experimental and numerical study of the effects of deposition speed and arc power on a single AISI 308L WAAM bead

Alexandra Morvayova[1] · Mojtaba Karamimoghadam[1] · Nicola Contuzzi[1] · Vito Denora[1] · Laura Fabbiano[1] · Giuseppe Casalino[1]

Received: 10 January 2025 / Accepted: 5 April 2025

Abstract
This paper investigates the impact of deposition speed and arc power on the geometry of a single AISI 308L bead deposited by wire arc additive manufacturing (WAAM). The study reveals that bead width and wetting angles are significantly influenced by arc power. Optimal bead geometry, with good wetting angle and aspect ratio, was achieved by 1700 W arc power and 9 mm/s deposition speed. The complex dynamics of the process are probably too intricate and cannot be adequately captured by a second-order polynomial in the response surface methodology. Otherwise, the numerical model introduced in this paper accurately simulates the drop formation and its influence on bead geometry under various process conditions. It suggests that high arc power enhances the melt rate and drop growth, causing better melt pool spreading and improving bead geometry. The numerical model was calibrated by thermography and shows that the deposition speed affects the dependency thermal curves.

Keywords Wire arc additive manufacturing · Fabricated geometry · Numerical model · Cold metal transfer · Deposition speed · Arc power

1 Introduction

Metal wire additive manufacturing is a promising technology for rapid and precise metal additive manufacturing [1]. Among wire additive manufacturing options, the arc has become increasingly popular due to its high productivity, versatility with various materials, and ability to produce large, complex components [2]. Wire arc additive manufacturing (WAAM) is notably used in aerospace, automotive, and rail industries as well as the oil and gas sector for manufacturing pipeline components and pressure vessels. Beyond prototyping and low-volume production, in addition, WAAM is employed to repair and refurbish existing parts, resulting in material savings and extended equipment lifespan [3–5].

The fundamental principles of WAAM involve depositing arc-melted, continuously fed metal wire onto a substrate [6]. Despite the apparent simplicity, the process involves complex physical phenomena such as heat transfer, fluid flow, surface tension, electromagnetic effects, phase changes, microstructural evolution, and residual stresses [7, 8]. The dynamics of WAAM are influenced by parameters like deposition velocity, wire feed rate, filler material characteristics, and arc properties, which significantly affect the geometry, defects, porosity, and microstructure of the deposited beads [9, 10].

To enhance the precision and reliability of this manufacturing technique, researchers are investigating the interplay between WAAM parameters and the properties of the manufactured components using experimental and numerical methods [11–13]. Nguyen et al. [14] found that

✉ Mojtaba Karamimoghadam
m.karamimoghadam@phd.poliba.it

Alexandra Morvayova
alexandra.morvayova@poliba.it

Nicola Contuzzi
nicola.contuzzi@poliba.it

Vito Denora
v.denora@phd.poliba.it

Laura Fabbiano
laura.fabbiano@poliba.it

Giuseppe Casalino
giuseppe.casalino@poliba.it

[1] Polytechnic University of Bari, Bari, Italy

Published online: 05 May 2025

Analysis of wire arc additive manufacturing of ER70S-6 steel beads through experimental, statistical, and numerical analysis

https://doi.org/10.1177/09544062251351162

Manufacture

Institution of MECHANICAL ENGINEERS

Journal of MECHANICAL ENGINEERING SCIENCE

Proc IMechE Part C:
J Mechanical Engineering Science
2025, Vol. 239(18) 7430–7443

DOI: 10.1177/09544062251351162
journals.sagepub.com/home/pic
Sage

Analysis of wire arc additive manufacturing of ER70S-6 steel beads through experimental, statistical, and numerical analysis

Alexandra Morvayová, Mojtaba Karamimoghadam, Nicola Contuzzi, Vito Denora, Laura Fabbiano and Giuseppe Casalino

Abstract

This study investigates the Wire Arc Additive Manufacturing (WAAM) process for fabricating single beads from ER70S-6 steel under varying deposition speed and arc power. A combined experimental, statistical, and FEM approach is employed to evaluate the effects of arc power and deposition speed on bead geometry, specifically bead width, height, aspect ratio, and wetting angle. Using a Design of Experiments (DOE) methodology, nine single-layer beads were deposited at arc power levels of 1616, 2434, and 2839 W and deposition speeds of 5, 7, and 9 mm/s. The previously mentioned characteristics were analyzed using Analysis of Variance (ANOVA) and Response Surface Methodology (RSM). Furthermore, a FEM model based on Computational Fluid Dynamics (CFD) and a two-phase field approach provided insights into the molten metal flow behavior and thermal evolution during deposition. A statistical optimization identified process parameters (arc power of 2592 W and deposition speed of 5 mm/s) that yield an aspect ratio and wetting angle close to literature-reported optimal values (2.50 and 60°, respectively). Experimental validation demonstrated strong agreement between predicted and measured values (aspect ratio: 2.70 vs 2.50; wetting angle: 58.80° vs 60.79°), confirming the accuracy of the developed statistical model.

Keywords

Wire Arc Additive Manufacturing, Cold Metal Transfer (CMT), response surface methodology analysis, FEM analysis

Date received: 9 December 2024; accepted: 1 June 2025

Introduction

Wire Arc Additive Manufacturing (WAAM) presents several significant advantages over other metal-based additive manufacturing techniques, including higher deposition rates, improved material efficiency, and the capability to produce large-scale components.[1,2] However, WAAM-deposited parts often demonstrate lower precision compared to methods such as Laser Powder Bed Fusion (LPBF) or Electron Beam Melting (EBM).[3] To broaden the range of applications for WAAM, it is essential to develop methodologies that enhance the precision of components produced through this technique.[4]

Recent studies have shown that the heat source type used in WAAM significantly affects the precision and geometry of the manufactured parts. Different heat sources can lead to modifications in heat accumulation, thermal history, energy input, and metal transfer modes, all of which play critical roles in the final product's characteristics.[5–7] Among the various techniques, Cold Metal Transfer (CMT) has emerged as the most effective for achieving uniform and fine bead geometry.[8,9] This effectiveness is attributed to its reduced spattering, lower heat input, and minimized thermal distortions. Unlike conventional Gas Metal Arc Welding (GMAW), CMT operates in a short-circuit transfer mode, utilizing a digitally controlled servomotor to reverse the filler wire's motion once it contacts the melt pool. This reverse motion severs the molten metal droplet while maintaining a

Department of Mechanics, Mathematics and Management, Polytechnic University of Bari, Bari, Italy

Corresponding author:
Mojtaba Karamimoghadam, Department of Mechanics, Mathematics and Management, Polytechnic University of Bari, Via Orabona 4, Bari 70125, Italy.
Email: m.karamimoghadam@phd.poliba.it

Wire arc additive manufacturing of low alloyed steels, copper aluminum alloys, and their bimetals

https://doi.org/10.1007/s00170-025-16436-4

The International Journal of Advanced Manufacturing Technology
https://doi.org/10.1007/s00170-025-16436-4

ORIGINAL ARTICLE

Wire arc additive manufacturing of low alloyed steels, copper aluminum alloys, and their bimetals

Mojtaba Karamimoghadam[1,2] · Yahya Aghayar[2] · Foroozan Forooghi[2] · Vito Denora[1] · Mohsen Mohammadi[2] · Nicola Contuzzi[1] · Giuseppe Casalino[1]

Received: 1 April 2025 / Accepted: 20 August 2025

Abstract
This study investigates the mechanical performance and microstructure of wire arc additive manufactured (WAAM) components using ER70S-6 low-alloy steel (LAS), CuAl8 aluminum bronze, and their bimetallic combination. WAAM was employed to fabricate both wall and bulk samples using a CMT (cold metal transfer) system. For LAS, the deposited microstructure featured Widmanstätten ferrite and grain boundary ferrite, with a maximum microhardness of 259 HV and a failure load of 4726 N. The CuAl8 alloy exhibited a β-phase along grain boundaries and α-phase within grains, achieving a maximum hardness of 137 HV and a failure load of 1690 N. In the bimetallic configuration (CuAl8–steel), strong metallurgical bonding was achieved at the interface, with refined grains in the dilution zone contributing to enhanced local hardness. The bimetallic samples demonstrated a maximum microhardness of 131 HV and a failure load of 1939 N. These findings highlight the potential of WAAM for fabricating monolithic and bimetallic parts suitable for marine and structural applications requiring localized strength.

Keywords Additive manufacturing · Microstructure · Mechanical properties · ER70S-6 alloy steel · Copper/steel bimetals

1 Introduction

With the continued growth of the metal processing industry, the demand for high-precision and rapid manufacturing methods has intensified [1]. Traditional fabrication techniques often struggle with limitations in cost, complexity, and scalability, especially when producing large or geometrically complex components [2–4]. In response, additive manufacturing (AM) technologies have emerged as efficient alternatives that can reduce lead times, minimize waste, and offer greater design flexibility [5, 6].

Among various AM techniques, wire arc additive manufacturing (WAAM) has gained significant traction due to its ability to deposit large volumes of metal with relatively high deposition rates and low material cost [7, 8]. WAAM uses a wire feedstock melted by an electric arc to fabricate metallic parts layer by layer, similar to welding processes [9, 10]. Key process parameters, such as current, voltage, travel speed, and wire feed rate, must be carefully controlled to ensure proper melting, deposition uniformity, and mechanical integrity [11–13]. WAAM's microstructural control is essential in determining the final mechanical properties of fabricated parts. Cooling rates, heat input, and deposition strategies significantly influence grain structure, phase formation, and defect generation (e.g., porosity, cracking, or delamination between layers) [14–17]. For instance, high heat input or improper arc control may lead to columnar grain growth or residual stresses, while optimized deposition strategies can promote refined, equiaxed microstructures and enhanced mechanical performance [13, 18, 19].

Recent research efforts have explored the application of WAAM in producing functionally graded materials (FGMs) and bimetals, where two dissimilar metals are combined to tailor material properties along the build direction [20–22]. One of the most promising yet challenging systems involves iron (Fe) and copper (Cu). Steel offers high mechanical strength and durability, while copper provides excellent

✉ Mojtaba Karamimoghadam
m.karamimoghadam@phd.poliba.it

[1] Department of Mechanics, Mathematics and Management, Polytechnic University of Bari, Via Edoardo Orabona 4, 70125 Bari, Italy

[2] Marine Additive Manufacturing Center of Excellence (MAMCE), University of New Brunswick, Fredericton, NB E3B5A1, Canada

Published online: 30 August 2025

Impact of feed rate and arc power in wire arc additive manufacturing of AISI 308L stainless steel

https://doi.org/10.1007/s43452-025-01274-8

Archives of Civil and Mechanical Engineering (2025) 25:220

ORIGINAL ARTICLE

Impact of feed rate and arc power in wire arc additive manufacturing of AISI 308L stainless steel

Mojtaba Karamimoghadam[1] · Mohammad Rezayat[2,3] · Nicola Contuzzi[1] · Vito Denora[1] · Antonio Mateo[2,3] · Giuseppe Casalino[1]

Received: 4 March 2025 / Revised: 25 May 2025 / Accepted: 6 July 2025 / Published online: 15 July 2025

Abstract
In this study, the process of wire arc additive manufacturing (WAAM) by cold metal transfer (CMT) operation has been investigated for AISI 308L austenitic stainless steel. The wire feeder rate (WFR) was set between 3.5 and 7.0 m/min, while the current ranged from 72 to 115 A and the voltage from 11.1 to 12.6 V, as determined by the generator. Additionally, the robot speed was maintained at 7 mm/min for all samples. Microstructural and mechanical analyses have been conducted to improve the dilution area by considering having a different range of the width of the deposited part. Optical microscopy (OM) has been used for scanning the cross-section of the fabricated parts, and scanning electron microscopy (SEM), together with electron back scatter diffraction (EBSD), for monitoring the microstructure of the substrate, heat-affected zone (HAZ), and deposited metal. Energy-dispersive X-ray (EDX) analysis was applied to reveal the dilution area. Moreover, to link the oxidation of the peak deposition to the surface roughness, a focused ion beam (FIB) was used to remove a tiny volume of the peak surface. The results indicate that increasing the voltage and current in the WAAM process directly influences both microhardness and bead width. Microhardness reached up to 310 HV in the heat-affected zone (HAZ), while the width of the deposited bead increased from 2.9 mm at 799 W to 6.2 mm at 1449 W. Additionally, surface roughness along the deposited lines decreased with a higher wire feeder rate, with the lowest roughness recorded at 20.1 µm. Finally, FIB analysis revealed that the oxide layer was approximately 1 µm thick, with chromium penetration observed within the layer.

Keywords Additive manufacturing · Wire arc additive manufacturing · Process parameters · AISI 308L · Wire feeder rate

1 Introduction

The demand for rapid, efficient, and inexpensive fabrication and repair of parts of complex geometries has expanded the use of portable equipment and advanced manufacturing technologies [1–4]. Among these, additive manufacturing is the most promising one because it opens advantages in several ways compared to conventional methods of manufacturing [5–9]. Assisted by CAD, and using sophisticated control systems, the AM techniques manufacture complex parts layer by layer, reducing waste, and minimizing material consumption [5–9].

WAAM is one of the most used AM techniques for repairing and manufacturing large-scale components. A continuous deposition of molten wire onto a substrate is done with the help of a robotic arm, which enables the creation of complex and customized parts [10, 11]. Material versatility further extends the capabilities of

Effect of wire feed rate on ER70S-6 microstructure of wire arc additive manufacturing process

https://doi.org/10.1007/s00170-025-15334-z

The International Journal of Advanced Manufacturing Technology (2025) 137:2947–2961
https://doi.org/10.1007/s00170-025-15334-z

ORIGINAL ARTICLE

Effect of wire feed rate on ER70S-6 microstructure of wire arc additive manufacturing process

Mojtaba Karamimoghadam[1] · Mohammad Rezayat[2,3] · Nicola Contuzzi[1] · Vito Denora[1] · Antonio Mateo[2,3] · Giuseppe Casalino[1]

Received: 11 November 2024 / Accepted: 27 February 2025 / Published online: 11 March 2025

Abstract
This study investigates the manufacturing and characterization of ER70S-6 single line-wire arc additive manufacturing (WAAM) using a cobot to produce defect-free samples. Adjusting the wire feed rate aims to improve efficiency in fabricating steel frames for building structures. In this regard, 1-mm-diameter ER70S-6 wire samples were fabricated with feeder rates ranging from 4.5 to 6.5 m/min, maintaining a constant robot speed of 7 m/min. The voltage and current of the WAAM machine were controlled between 14.8–16 V and 125–159 A, respectively. Microhardness profiles and grain sizes at grain dilution of the area were systematically compared to monitor the solidification behavior after the process. Electron backscatter diffraction (EBSD) analysis assessed the crystallographic orientations and calculated the grain sizes. Optical microscopy and scanning electron microscopy (SEM) revealed uniform, defect-free surfaces of metal mixing during the WAAM process in the 100 ± 10 µm upper than dilution area. As a result of two types of cooling processes following WAAM, transferring heat into the substrate and environment, the formation of Widmanstätten ferrite on top of the beads' peaks was more extensive. The grain size in the middle of the bead ranged from approximately 8.6 to 11.6 µm, while at the dilution area, it decreased to 3 to 5.6 µm. This variation influenced the microhardness, which reached 300 ± 15 HV.

Keywords Additive manufacturing · Wire arc additive manufacturing · Microstructure · ER70S-6 · Wire feed rate

1 Introduction

Wire arc additive manufacturing is considered one of the innovative metal additive manufacturing methods and has received considerable attention in recent years. WAAM employs an electric arc as its thermal source and wire as the feedstock material [1–4] to build sizable, high-strength metallic parts in a successive layer-manufacturing process [5–10]. This technique differs from other additive manufacturing methods because it makes complex geometries using economically viable materials (steels, copper, aluminum, etc.) [11–14] at a relatively fast deposition rate. These advantages make WAAM very attractive for industries like aerospace, automotive, oil and gas, and shipbuilding, which have an increasing demand for high-performance, large metallic parts. These components can be used in structural applications, with one major advantage being the mobility of WAAM equipment. This allows it to be deployed directly to construction sites where large structures can be fabricated in situ based on the provided design [15–18].

Control over input parameters, such as voltage, current, wire feed rate, and speed, is crucial because each metal has a specific melting temperature that needs to be carefully regulated within the machine [19, 20]. For example, ER70S-6 low-carbon steel samples were successfully produced using WAAM with a gas metal arc welding (GMAW) torch and a six-axis robotic arm in surface tension transfer (STT) mode [21]. The resulting microstructure primarily consisted of fine ferrite and some bainite. Additionally, Yildiz et al. [22]

✉ Mojtaba Karamimoghadam
m.karamimoghadam@phd.poliba.it

[1] Department of Mechanics, Mathematics and Management, Polytechnic University of Bari, Via Orabona 4, 70125 Bari, Italy

[2] Center for Structural Integrity, Micromechanics, and Reliability of Materials (CIEFMA), Department of Materials Science and Engineering, Universitat Politècnica de Catalunya-BarcelonaTECH, 08019 Barcelona, Spain

[3] Barcelona Research Center in Multiscale Science and Engineering, Politècnica de Catalunya-BarcelonaTECH, 08019 Barcelona, Spain

Laser Hybrid Welding of WAAM-Fabricated Dissimilar Steels: Microstructural Evolution and Mechanical Performance of AISI 308L and ER70S-6 Joints with 316L Filler

https://doi.org/10.1007/s11665-025-12265-4

JMEPEG
https://doi.org/10.1007/s11665-025-12265-4

1059-9495/$19.00

ORIGINAL RESEARCH ARTICLE

Laser Hybrid Welding of WAAM-Fabricated Dissimilar Steels: Microstructural Evolution and Mechanical Performance of AISI 308L and ER70S-6 Joints with 316L Filler

Mojtaba Karamimoghadam, Mohammad Rezayat, Vito Denora, Nicola Contuzzi, Antonio Mateo, and Giuseppe Casalino

Submitted: 9 June 2025 / Revised: 7 August 2025 / Accepted: 1 September 2025

In this study, dissimilar stainless steel (AISI 308L stainless steel) and low-alloy steel (ER70S-6) plates fabricated via Wire Arc Additive Manufacturing were joined using Laser Hybrid Welding with AISI 316L stainless steel filler wire. Four welding parameter sets were tested by varying laser power (1000-1500 W) and Laser scanning speed (1000-1500 mm/min). Microstructural analysis using Scanning Electron Microscopy, Electron Backscatter Diffraction, and x-ray Diffraction revealed significant phase transformations in the weld zone, including the formation of δ-ferrite and γ-austenite, with retained δ-ferrite decreasing at higher laser powers. The welds exhibited refined grain structures, especially at the fusion boundaries and heat-affected zone, with Electron Backscatter Diffraction measured grain sizes of 5.13 ± 1 μm (ER70S-6 heat-affected zone), 16.33 ± 5 μm (316L weld), and 10.09 ± 6 μm (weld center). Maximum microhardness values reached 303 HV in the heat-affected zone of 308L, 297 HV in ER70S-6, and 245 HV in the weld center. Tensile testing showed a 43% increase in strength for the sample welded at 1500 W and 1000 mm/min compared to lower heat input conditions, confirming improved ductility and joint integrity. These findings demonstrate the feasibility and effectiveness of Laser Hybrid Welding for producing robust joints between wire arc additive manufacturing-fabricated dissimilar steels with enhanced mechanical and microstructural performance.

Keywords laser hybrid welding, laser material processing, low-alloy steel, stainless steel, wire arc additive manufacturing

Abbreviations

Wt.% (%)	Weight percent
LS (mm/min)	Laser speed
LP (W)	Laser power
AV (V)	Arc voltage
AC (A)	Arc current
LHW	Laser hybrid welding
AM	Additive manufacturing
WAAM	Wire arc additive manufacturing
CMT	Cold metal transfer
GMAW	Gas metal arc welding
EBSD	Electron backscatter diffraction
SEM	Scanning electron microscopy
EDS	Energy-dispersive x-ray spectroscopy
HAZ	Heat-affected zone
GND	Geometrically necessary dislocation
OM	Optical microscopy
XRD	X-ray diffraction
Cr	Chromium
Ni	Nickel
Fe	Iron
UTS	Ultimate tensile strength
FZ	Fusion zone
CNC	Computer numerical control
DED	Directed energy deposition
CTE	Coefficient of thermal expansion

This invited article is part of a special topical issue of the *Journal of Materials Engineering and Performance* on Advances in Dissimilar Welding. The issue was organized by Dr. Chandan Pandey, Indian Institute of Technology, Jodhpur; Dr. Sachin Sirohi, SRM Institute of Science and Technology Delhi, NCR Campus; Prof. Dariusz Fydrych, Gdańsk University of Technology; and Dr. Shailesh Mani Pandey, National Institute of Technology, Patna.

Mojtaba Karamimoghadam, Vito Denora, Nicola Contuzzi, and **Giuseppe Casalino**, Department of Mechanics, Mathematics and Management, Polytechnic University of Bari, Via Orabona 4, 70125 Bari, Italy; **Mohammad Rezayat**, Center for Structural Integrity, Micromechanics, and Reliability of Materials (CIEFMA), Department of Materials Science and Engineering, Universitat Politècnica de Catalunya BarcelonaTECH, 08019 Barcelona, Spain; Barcelona Research Center in Multiscale Science and Engineering, Politècnica de Catalunya BarcelonaTECH, 08019 Barcelona, Spain; and Fundacio Privada Centre CIM, C/ Llorens i Artigas, 12, 08028 Barcelona, Spain; **Antonio Mateo**, Center for Structural Integrity, Micromechanics, and Reliability of Materials (CIEFMA), Department of Materials Science and Engineering, Universitat Politècnica de Catalunya BarcelonaTECH, 08019 Barcelona, Spain; and Barcelona Research Center in Multiscale Science and Engineering, Politècnica de Catalunya BarcelonaTECH, 08019 Barcelona, Spain. Contact e-mail: m.karamimoghadam@phd.poliba.it.

Journal of Materials Engineering and Performance

Published online: 06 October 2025

Effect of manufacturing strategy on microstructure of a low-carbon steel alloy fabricated with wire-arc additive manufacturing

https://doi.org/10.1007/978-3-031-67398-6_23

Effect of Manufacturing Strategy on Microstructure of a Low-Carbon Steel Alloy Fabricated with Wire-Arc Additive Manufacturing

Mojtaba Karamimoghadam, Yahya Aghayar, Foroozan Forooghi, Mohsen Mohammadi, Nicola Contuzzi, and Giuseppe Casalino

Abstract

In recent times, wire-arc additive manufacturing (WAAM) has emerged as a versatile and highly productive method for producing various structural materials. This innovative technique has garnered significant attention across multiple industrial sectors, owing to its adaptability and efficiency. In this study, St-52 alloy steel samples were manufactured by the WAAM method on St-37 alloy steel substrate employing different fabricating angles of 60°, and microstructure was investigated. Observing the melt-pools has yielded valuable insights into the impact of the arc's heat on the substrate microstructure. This occurs during the entire cycle of wire melting and subsequent solidification in the WAAM process, with consistent process parameters maintained across all samples. Notably, finer microstructures were observed in the top layers across all strategies. However, as the angle of the initial additive layer decreased, there was a significant increase in heat effects on the substrate, leading to a broader area impacted by the arc's heat input. Moreover, in the recrystallized microstructure, the grain size at the interfaces transformed into the subsequent layer until the layer's manufacturing concluded.

Keywords

Additive manufacturing · Wire-arc additive manufacturing · Low carbon steel alloy · Microstructure · Manufacturing strategy

1 Introduction

Additive manufacturing (AM) has revolutionized various industries with its advantages of enhanced sample quality, reduced production time, and intricate geometry creation [1–4], making metals crucial in the process across medical, educational, and industrial sectors [5–8]. A recent breakthrough in AM technology, Wire Arc Additive Manufacturing (WAAM), inspired by arc welding processes, utilizes a millimeter-sized wire melted through an arc to construct metal samples on a small to large scale. WAAM's key advantages include the fabrication of large-scale samples, flexibility in material selection, and the capacity for remote control accessibility [9, 10]. WAAM's potential is underlined by its ability to improve mechanical properties through careful metallic material selection and meticulous control over process parameters, including temperature. This precision in thermal aspects significantly contributes to the overall quality of manufactured parts. The process involves monitoring and controlling the temperature during metal deposition to mitigate defects such as porosities, lack of fusion, and cracks. Additionally, various input parameters like voltage, current, deposition pattern, wire feeder speed, and wire diameter directly impact the efficiency and outcome of the additive manufacturing process. As a revolutionary advancement, WAAM

M. Karamimoghadam (✉) · N. Contuzzi · G. Casalino
Department of Mechanics, Mathematics and Management, Polytechnic University of Bari, Bari, Italy
e-mail: m.karamimoghadam@phd.poliba.it

Y. Aghayar · F. Forooghi · M. Mohammadi
Marine Additive Manufacturing Center of Excellence (MAMCE), University of New Brunswick, Fredericton, NB, Canada

Proceedings of the 63rd Conference of Metallurgists, COM 2024, https://doi.org/10.1007/978-3-031-67398-6_23